Spectral Characteristics of Blazars: A Detailed Study of Mkn 421 and S5 0716+714

A thesis submitted to

University of Calicut

in partial fulfillment of the requirements

for the award of the degree of

Doctor of Philosophy in Physics

under the Faculty of Science

by

Baheeja C

Department of Physics
University of Calicut
Kerala, India
December 2024

CERTIFICATE

This is to certify that the thesis entitled "**Spectral Characteristics of Blazars: A Detailed Study of Mkn 421 and S5 0716+714**" submitted to the Department of Physics, University of Calicut by **Miss. Baheeja C** in partial fulfilment of the requirements for the award of the degree of **Doctor of Philosophy** is the original work carried out by her under my supervision and guidance at the Department of Physics, University of Calicut. No part of this thesis has been included previously for the award of any other degree, either in this university or in any other institution. The thesis has been checked for plagiarism, using *iThenticate* software, at the CHMK library, University of Calicut and the similarity index is found within the permissible limit. Also the corrections recommended by the adjudicators have been incorporated, and the contents of the thesis and the soft copy are the same.

Supervisor:
Dr. C. D. Ravikumar
Professor
Department of Physics
University of Calicut

DECLARATION

I hereby declare that the thesis titled **“Spectral Characteristics of Blazars: A Detailed Study of Mkn 421 and S5 0716+714”** is an authentic record of research work carried out by me at the Department of Physics, University of Calicut under the supervision of Dr. C. D. Ravikumar. No part of this thesis has been included previously for the award of any other degree, either in this university or in any other institution. The thesis has been checked for plagiarism, using *iThenticate* software, at the CHMK library, University of Calicut and the similarity index is found within the permissible limit. I also declare that the thesis is free from AI-generated content.

Date:

Baheeja C
Research scholar
Department of Physics
University of Calicut

Dedicated to my Mother

Acknowledgement

During my Ph.D. journey, I have received invaluable support and encouragement from many people, and I am deeply grateful for the opportunity to express my thanks to them all.

It is a great privilege for me to convey my deepest respect and heartfelt gratitude to my Ph.D. supervisor, Dr. C. D. Ravikumar. His continuous guidance, insightful advice, and support have helped me complete this thesis successfully. I have greatly benefited from his guidance and learned a lot from him. As a mentor, he excels by giving his students the freedom to explore and grow in their studies.

I am deeply grateful to my collaborator, Dr. Sunder Sahayanathan (Scientist, Astrophysical Science Division, BARC Mumbai), for his unwavering commitment and dedication, which greatly contributed to the successful completion of this thesis. I learned the fundamentals of blazar physics from Dr. Sunder Sahayanathan, who always nurtured my growth as a researcher. Whenever I faced confusion, he patiently simplified complex concepts for me. I am deeply grateful for his constructive criticism, inspiring ideas, and unwavering mental support throughout my research journey. It has been a true blessing to have the opportunity to be one of his students. I would also like to express my heartfelt gratitude to my collaborator, Dr. Frank M. Rieger (Institute for Theoretical Physics, University Heidelberg, Germany), for his insightful comments and valuable suggestions, which have significantly enriched my research work. I am extremely grateful to Prof. Nilay Bhat (BARC), who was always available for discussions whenever I needed. My heartfelt thanks to Dr. Vaidehi S. Paliya (IUCAA) for his valuable academic interactions and helpful insights.

I would like to extend my heartfelt gratitude to my research seniors Dr. Sitha K Jagan and Dr. Vinod K. T. for their intense academic support and constant encouragement throughout this journey. Their willingness to share their knowledge and expertise has helped me a lot. Beyond their academic assistance, their moral support and encouragement have been a source of strength, helping me stay motivated and focused during difficult times. I thank you both for your selfless contributions and for being such an integral part of academic and personal growth. I am truly grateful to my colleague Aminabi for her care and support during times when I needed it the most. I am so happy to be a part of Blazar group including Zahir Shah, Pranju, Rukaiya, Sitha, Amal, Aminabi, Zahoor, Aaqib, Athar, Soumya, Athira, Sajad, Reshma and Naseef. Thanks to my friends Nicemon, Athira Unni, Arjun Jayaraj, Parvathy, Swapna and Jinu, who always stood with me in my ups and downs. I would like to express my special appreciation to Parvathy, Swapna, Gayathri and Fara for their invaluable help during challenging times. I would like to extend my sincere thanks to all of the former HOD's, faculty members, non-teaching staff and all the research scholars of our department for their support over the entire Ph.D. period. I am so thankful to CSIR for the financial support during the research period.

I am deeply grateful to all my family members for their unconditional love, support, and encouragement throughout this journey. Their belief in me have always been my greatest source of strength.

List of Publications

Publications relevant to this thesis:

1. **C. Baheeja**, S. Sahayanathan, F. M. Rieger, S. K. Jagan, and C. D. Ravikumar, “Do radiatiave losses determine the characteristic emission of the blazar Mkn 421?”, *Monthly Notices of Royal Astronomical Society*, Volume 514, 3074-3081 (2022).

2. **C. Baheeja**, S. Sahayanathan, F. M. Rieger, and C. D. Ravikumar, “Signature of Particle Diffusion on the X-ray Spectra of the blazar Mkn 421”, *Physical Review D*, Volume 109, 103039 (2024).

3. **C. Baheeja**, Aminabi Thekkoth, Sunder Sahayanathan, C. D. Ravikumar and Nilay Bhatt, “Long term multi-wavelength spectral variations of blazar S5 0716+714”, *Publications of the Astronomical Society of Australia*, Volume 41 (2024).

Publications not used in this thesis:

1. K. T. Vinod, **C. Baheeja**, S. Aswathy and C. D. Ravikumar, “Study of Central Intensity Ratio of Seyfert Galaxies in Nearby Universe”, *Research in Astronomy and Astrophysics* , Volume 23, 045008 (2023).

2. K. T. Vinod, **C. Baheeja**, and C. D. Ravikumar, “Connections between Central Intensity Ratio and hot gas properties of early-type galaxies”, *Monthly Notices of the Royal Astronomical Society* , Volume 528, 2040-2045 (2024).

3. Aminabi Thekkoth, **C. Baheeja**, S. Sahayanathan, Ravikumar C.D., “Gamma-ray variability and multi-wavelength insights into the unprecedented outburst from 4C 31.03”, *Journal of High Energy Astrophysics*, Volume 42 (2024).

4. Naseef Mohammed PN, Aminabi T, **C. Baheeja**, Sunder Sahayanathan, Vaidehi S Paliya, C.D. Ravikumar, “Deciphering the Multi-Wavelength Flares of the Most Distant Very High-Energy (>100 GeV) γ-ray Emitting Blazar” *Journal of High Energy Astrophysics*, Volume 47 (2025).

List of conference presentations

1. “Understanding the Spectral features of Blazars” International Conference on Theoretical and Experimental Physics, Farook College, Calicut University, February 2024.
2. “The Physics behind the X-ray spectral curvature in blazars” 41^{st} meeting of Astronomical Society of India (ASI), IIT Indore, March 2023.
3. “What decides the characteristic emission of blazars” IUCAA sponsored Three Day Southern Regional Astronomers Meeting on Research in Astronomy: Opportunities, RSET, Cochin, Kerala, February 2023.
4. “Probing the characteristic emission of blazars” International Astronomical Union Symposia 375: “The Multimessenger Chakra of Blazar Jets”, Kathmandu, Nepal, December 2022.
5. “Characteristic emission of the blazar MKN 421” IUCAA sponsored 4^{th} National Conference on “High Energy Emission from AGN”, Farook College, Calicut University, August 2022.
6. IUCAA sponsored Two-Day Workshop on “High Energy Emission from AGN”, Farook College, Calicut University, August 2022.
7. “Probing the origin of Synchrotron spectral peak of the blazar 1ES 1959+650” 40^{th} meeting of Astronomical Society of India (ASI), IIT Roorkee, Uttarakhand, March 2022.
8. VHE Data Analysis using Open Source Packages, Kashmir University, Srinagar, participation, February 2022.

9. “Does Radiative Loss decide the Characteristic emission of the blazar Mkn 421?” Theoretical Aspects of High Energy Emission from AGN, Kashmir University, Srinagar, July 2021.
10. “Infra-red Central Intensity Ratio of Type 1 Active Galaxies” 38^{th} Meeting of the Astronomical Society of India (ASI),IISER Tirupati, February 2020.
11. “Studies of central light distribution in Active galaxies” 32^{th} Kerala Science Congress, Yuvakshetra Institute of Management Studies, Palakkad, January 2020.

Abstract

The broadband SED of blazars is often modeled by a broken power-law function, indicating that the underlying electron distribution follows a broken power-law shape. However, one of the long-standing problems has been that the observed difference in the spectral index could not be explained solely by the radiative loss interpretation of the broken power-law electron distribution. Additionally, high-resolution observations have revealed curvature in the X-ray spectra of high-energy-peaked blazars. In the first part of the thesis, we aim to thoroughly investigate the radiative loss interpretation of the broken power-law electron distribution by studying the blazar spectrum around the synchrotron peak. We conduct a detailed analysis of the characteristic photon energy of blazar Mkn 421, where the spectral index changes significantly. Our findings indicate the presence of a strong anti-correlation between the spectral indices before and after this characteristic photon energy. This result contradicts the interpretation based on simple radiative loss for the characteristic photon energy, and alternative scenarios are thus discussed. Further, we carried out a detailed analysis on the observed curvature in the broadband X-ray spectrum of blazar Mkn 421. The curvature in the blazar spectrum can provide insights into the particle dynamics within jets. Our study suggests that the curvature in the X-ray spectra are consistent with a scenario where particle acceleration is governed by Bohm-type diffusion, and the spectra beyond the synchrotron peak are modulated by the radiative loss process.

The latter part of this thesis focuses on a long-term, multi-wavelength spectral study of another blazar S5 0716+714. All available observations in optical/UV, X-ray, and gamma-ray wavebands of the source by *Swift*-UVOT/XRT or *Fermi*-LAT from April 2005 to January 2023 were used, and the spectra in each energy band were explored using power-law/log-parabola functions. A detailed correlation study between the best-fit parameters was performed, and our results suggest that the spectral changes observed during high flux states could be associated with the spectral energy distribution shifting towards the blue end. Furthermore, the broadband SED during two distinct flux states can be successfully fitted by considering synchrotron, synchrotron self-Compton, and external Compton emission processes. The flux enhancement of the source is predominantly associated with an increase in the bulk Lorentz factor. Additionally, we find that the model curves corresponding to variations in the bulk Lorentz factor have the potential to explain the observed correlations between the spectral parameters. Our study thereby suggests that the spectral variations of blazar S5 0716+714 are primarily associated with changes in the bulk Lorentz factor of the jet.

Contents

Acknowledgement vii

List of Publications ix

List of conference presentations xi

1 Introduction 3

- 1.1 Structure of an AGN 3
- 1.2 Classification of AGNs 4
- 1.3 Relativistic jets 7
- 1.4 Blazars 9
  - 1.4.1 Broadband spectral energy distribution of blazars 10
  - 1.4.2 Blazar sequence 11
- 1.5 Particle acceleration: Fermi mechanism 13
  - 1.5.1 Stochastic acceleration: Fermi second-order mechanism 16
  - 1.5.2 Shock acceleration: Fermi first-order mechanism 16
  - 1.5.3 Diffusive shock acceleration 18
- 1.6 Radiative Processes 19
  - 1.6.1 Synchrotron emission 19
  - 1.6.2 Inverse Compton emission 23
  - 1.6.3 Hadronic processes 25
- 1.7 Modeling high energy emission from blazars 27
- 1.8 Radiative cooling of a power-law electron spectrum 32
- 1.9 Empirical modeling of blazar spectrum 34
- 1.10 Multi-wavelength variability in blazars 36

1.11 Aim of the thesis and Outline 40

2 Multi-wavelength observatories and data analysis 43

2.1 *Swift* 44

2.1.1 X-Ray Telescope (XRT) 45

2.1.2 Ultraviolet/Optical Telescope (UVOT) 46

2.2 *NuSTAR* 49

2.3 *Fermi* 51

2.3.1 Large Area Telescope (LAT) 51

3 The characteristic emission of blazar Mkn 421 55

3.1 Introduction 55

3.2 Observation and Data analysis 59

3.3 X–ray spectral fit 59

3.4 Discussion and Summary 64

4 Study of X-ray spectral curvature of blazar Mkn 421 75

4.1 Introduction 75

4.2 Observation and Data analysis 78

4.2.1 *NuSTAR* 79

4.2.2 *Swift*-XRT 79

4.3 X–ray spectral analysis and results 80

4.3.1 *NuSTAR* (3-79 keV) regime 80

4.3.2 Combined *NuSTAR* and *Swift*-XRT regime 90

4.3.3 Probing a power-law with modified exponential cutoff 93

4.4 Summary 94

5 Multi-wavelength spectral variations of blazar S5 0716+714 97

5.1 Introduction 97

5.2 Observation and Data analysis 99

5.2.1 *Swift*-XRT 100

5.2.2 *Swift*-UVOT 100

5.2.3 *NuSTAR* 103

5.2.4 *Fermi*-LAT 103

- 5.3 Multi-wavelength analysis 105
  - 5.3.1 Flux-Index Correlation 105
  - 5.3.2 Flux-Flux Correlation 108
  - 5.3.3 Index-Index Correlation 110
  - 5.3.4 Distribution of fluxes and indices 115
  - 5.3.5 Broadband Spectral Energy Distribution 119
- 5.4 Discussion 123
- 5.5 Summary 126

6 Summary and Future Prospects **131**
- 6.1 Future plans 134

7 Recommendations **137**

A Appendix 1 **139**

B Appendix 2 **149**

List of Tables

2.1 The *Swift*-UVOT filter characteristics. 48

3.1 Best fit parameters of spectral fitting using *eplogpar* model and *sbpl* model 63
3.2 Best fit parameters of combined (*Swift*-XRT and *NuSTAR*) spectral fitting using *sbpl* model 71

4.1 Details of simultaneous *Swift*-XRT and *NuSTAR* observations. 79
4.2 Fit parameters of *NuSTAR* (3-79 keV) spectra as modeled with PL, LP and CPL. 82
4.3 The best-fit parameters of combined spectrum from *Swift*-XRT and *NuSTAR* with a LP and a simple CPL model. 87
4.4 Best fit parameters using the MCPL model (cooled p=2) for the energy range ϵ_p-79 keV. 92

5.1 Table showing best-fit parameters of power-law spectral fitting of *Swift*-XRT observations. 101
5.2 Table showing best-fit parameters of selected *Swift*-XRT observations using log-parabola model. 101
5.3 Table showing best-fit parameters of power-law spectral fitting of *Swift*-UVOT observations. 102
5.4 Table showing best-fit parameters of spectral fitting using a power-law model (along with TS values) for selected γ-ray observational data (2-day bins from *Fermi*-LAT) simultaneous with *Swift* observations. 105

5.5 Spearman correlation coefficient (r_s) and corresponding null hypothesis probability (p_s) of various relations among fluxes and indices. . . 114
5.6 Anderson Darling test results of index/flux distributions in optical/UV, X-ray and γ-ray bands. 118
5.7 Best fit parameter values of the probability density functions fitted to the logarithm of flux and spectral indices in optical/UV, X-ray, and γ-ray. 118
5.8 Best fit values of the model parameters from broadband SED fitting. 129
5.9 Best fit values of the model parameters from broadband SED fitting for the epoch MJD 59640–59699 with $\theta = 2$ degree. 130

A.1 Best fit parameters of spectral fitting using *eplogpar* model and *sbpl* model 140

B.1 Table showing the best-fit parameters of power-law fitting of *Swift*-XRT observations. 150
B.2 Table showing the best-fit parameters of selected *Swift*-XRT observations using log-parabola model. 160
B.3 Best-fit parameters for power-law fitting of *Swift*-UVOT observations. 161
B.4 Best-fit parameters of spectral fitting using a power-law model for selected gamma-ray observational data (2-day bins) simultaneous with *Swift* observations. 166

List of Figures

1.1 Schematic representation of an AGN. 5

1.2 Classification of AGNs based on the observer's viewing angle. 7

1.3 Schematic view of the blob of plasma moving at a relativistic speed. . 9

1.4 SED of blazar Mkn 421. 11

1.5 The blazar sequence by Ghisellini et al. (2017). 13

1.6 Illustration of Fermi acceleration. 14

1.7 Synchrotron power function $F\left(\frac{\nu}{\nu_c}\right)$ peaking at frequency $\nu \sim 0.29\nu_c$. 21

2.1 A visual representation of *Swift* telescope and the payloads on-board 44

2.2 *Swift*-XRT images of Mkn 421 in both PC and WT observation modes. 45

2.3 The plot of effective area of XRT as a function of energy 47

2.4 The plot of effective area of UVOT filters as a function of wavelength. 48

2.5 Schematic diagram of the *NuSTAR* telescope. 50

2.6 The plot compares the effective collecting area of *NuSTAR* with other focusing telescopes. 50

2.7 Schematic diagram of *Fermi*-LAT 52

3.1 The scatter plot between β and ϵ_p obtained from *eplogpar* (top panel) and between β and the integrated 0.3–10.0 keV flux (lower panel) for different epochs. 65

3.2 The scatter plot between ϵ_p and $\epsilon_{p,sbpl}$ along with the identity line . . 66

3.3 The scatter plot beween Γ_{low} and Γ_{high}. 67

3.4 Left panel: scatter plot between Γ_{low} and curvature parameter β, 0.3–10.0 keV flux and ϵ_p; Right panel: scatter plot between Γ_{high} and curvature parameter β, 0.3–10.0 keV flux and ϵ_p. 68

3.5 The scatter plot between ϵ_p and $\epsilon_{p,sbpl}$ using combined *Swift*-XRT and *NuSTAR* data, along with the identity line. 72
3.6 Example of 0.3-10 keV specta around the synchrotron SED peak modeled with *sbpl* function. 74

4.1 Spectral fits (*NuSTAR* alone) using the models PL, CPL and LP for the ObsIDs 60002023018 (low-flux state) and 60002023027 (high-flux state) 83
4.2 Scatter plots (*NuSTAR* alone) showing flux, along with reduced chi-square values for the PL fit (left), and LP curvature values β (right) . 84
4.3 Scatter plots between the reduced chi-square values of *NuSTAR* data fitted with the PL, LP, and CPL models, along with the identity line. 84
4.4 Scatter plots (*NuSTAR* alone) showing LP index α, along with **(a)** spectral curvature β, and **(b)** flux in the 3-79 keV range. 85
4.5 Scatter plots (*NuSTAR* alone) showing best-fit CPL model parameters 86
4.6 Scatter plots between the parameters obtained from LP fitting of combined *Swift*-XRT and *NuSTAR* data 89
4.7 Spectral fit from ϵ_p-79 keV using the MCPL model 91
4.8 Scatter plots between best-fit parameters for the MCPL model 92

5.1 Multi-wavelength light curve of S5 0716+714 106
5.2 Plot of spectral indices in optical/UV, X-ray and γ-ray energy bands corresponding to the observations shown in Figure 5.1 107
5.3 Scatter plots of the fluxes and indices in optical/UV, X-ray and γ-ray energies. 109
5.4 Scatter plots between fluxes in optical/UV, X-ray and γ-ray energies. 111
5.5 Scatter plots between the spectral indices $\alpha_{\rm X}$, $\alpha_{\rm O/UV}$ and α_γ 113
5.6 The demonstration of shift of the SED towards the bluer and/or redder ends as the source becomes brighter 114
5.7 Histograms of logarithmic flux (left) and spectral index (right) in optical/UV (top panel), X-ray (middle panel) and γ-ray bands 120
5.8 The broadband SED fitting of S5 0716+714 for the epochs MJD 59640–59699 (low-flux state) and MJD 57045–57048 (high-flux state) 128

5.9 The broadband SED fitting of S5 0716+714 during the epoch MJD 59640–59699 with viewing angle, $\theta = 2$ degree 129

Chapter 1

Introduction

Galaxies are considered the largest and most fundamental building blocks of our Universe. A galaxy is a system of stars ($\sim 10^{9-11}$), stellar remnants, interstellar gas, dust, and dark matter held together by gravity. A relatively small fraction of galaxies ($\sim$ 5%) exhibits a luminous galactic core with luminosity $\geq 10^{44}$ erg s^{-1}. This luminosity surpasses the collective radiance emitted from rest of the host galaxy. These galaxies are known as Active galaxies, and their nucleus is termed as Active Galactic Nucleus (AGN). AGN is very compact compared to the size of a galaxy, but emits immense power that cannot be elucidated by conventional thermonuclear reactions occurring in stars. The emissions from AGNs exhibit a broad energy spectrum, ranging from radio to very high energy gamma-ray frequencies.

1.1 Structure of an AGN

Observing AGNs across various wavelengths throughout the electromagnetic spectrum provides a broader picture of AGN. Significant advancements have been made in our perception of AGNs in the last few decades. There is a widespread acceptance that a **supermassive black hole** (SMBH) of mass $\sim 10^{6-10}\mathrm{M}_{\odot}$ resides at the centre of AGNs, accreting matter from the surroundings through its strong gravitational force (Shakura & Sunyaev, 1973). The infalling matter spirals around the SMBH due to its inherent angular momentum and results in an optically thick disk known as **accretion disk**. The angular momentum of the accreted matter is lost through viscous and turbulent processes, causing the accretion disk to heat up to high temperatures and emit a significant amount of thermal radiation, predominantly in the optical and ultraviolet (UV) wavebands. Furthermore, the photons from the accretion disk can undergo scattering by a **corona** of hot material located above the disk, producing X-ray emissions through the inverse Compton (IC) process. The **Broad Line Region (BLR)** is one of the AGN structures, typically located at a distance of $0.1 - 1$ pc from the SMBH. High-density cold gas clouds (number density $\sim 10^{10}\,\mathrm{cm}^{-3}$) form this structure, which is ionized by radiations from the accretion disk and re-emits in line spectrum. The broadening of emission lines is attributed to the Doppler broadening as the gas clouds move rapidly at large velocities ($\sim 1000 - 5000$ km/s) around the SMBH. The central region of an AGN (comprising SMHB, accretion disk and BLR) is surrounded by an optically thick obscuring **dusty torus** (Nenkova et al., 2002) along the equatorial plane, located at a distane of $1 - 10$ pc from the central black hole and it grabs a fraction of the radiation from the accretion disk and re-emits them in the infrared (IR) band. The narrow line features in the AGN spectrum are believed to be originated from the **Narrow Line Region (NLR)**, located at a distance $\sim$ 10 pc to 1 kpc from the SMBH (Peterson, 1997). NLR clouds are relatively less dense ($\sim 10^{3}\,\mathrm{cm}^{-3}$), and their velocity is relatively smaller than that of the BLR clouds ($\sim$ 500 km/s). Another important structure of AGN is the relativistic **jets**, highly collimated, bipolar outflows of matter and radiation, launched from the vicinity of the central engine. They are directed along the rotational axis of the black hole and extends up to kiloparsec (kpc) or megaparsec (Mpc) scales. Figure 1.1 represents the basic structure of an AGN according to the classification scheme by Urry & Padovani (1995).

1.2 Classification of AGNs

AGNs have been divided into several subgroups based on their characteristics observed in different wavebands. They are broadly divided into two major classes: *radio-loud* and *radio-quiet* AGNs, based on their radio and optical emissions. AGNs with a radio-loudness factor (the ratio of radio luminosity at 5 GHz to the optical luminosity at B-band (4850Å)) greater than 10 are categorized as radio-loud, while rest are classified as radio-quiet (Kellermann et al., 1989). Most of the AGNs hosted

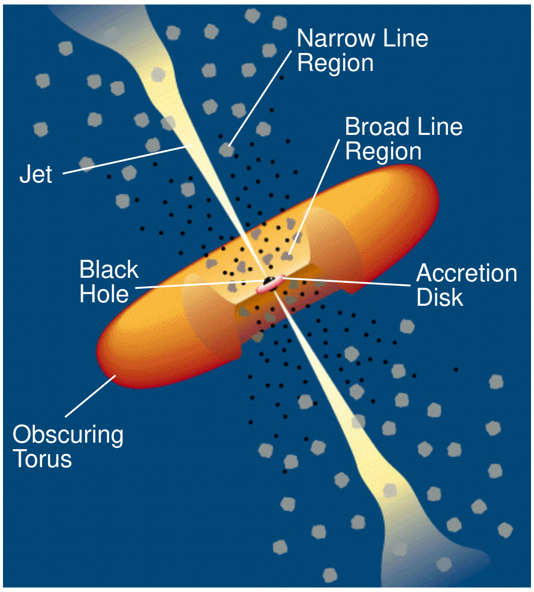

Figure 1.1: Structure of an AGN. Image Courtesy: `https://heasarc.gsfc.nasa.gov`.

in elliptical galaxies are radio-loud, whereas those in spiral galaxies tend to be radio-quiet. The key observational contrast between these two categories lies in whether powerful relativistic jets are present or absent. Radio-loud AGNs are characterized by strong collimated relativistic jets extending up to kpc or Mpc scales in some cases (Bagchi et al., 2014), whereas jet-related emissions are absent or weak in radio-quiet AGNs (Miller et al., 1993). Despite their differences, these sources exhibit similar thermal emissions, featured by emission-line spectra in the optical-UV range and continuum emissions in the infrared and soft X-ray spectra. This thermal emission is attributed to the black hole mass and the Eddington ratio according to the black hole accretion model (Rees, 1984). This suggests that, for both classes, the black hole mass and the Eddington ratio are nearly identical. However, since relativistic jets are thought to be initiated by the magnetic flux surrounding the black hole (Sikora & Begelman, 2013) and powered by the rotation of black hole; the magnetic field and the spin of the black hole may differentiate between radio-loud and radio-quiet sources. About 10–15% of AGNs are radio-loud, where radio emission is dominated by the relativistic jets (Kellermann et al., 1989). AGNs (both *radio-loud* and *radio-quiet*) are also classified into *Type 1* and *Type 2* based on the strength of emission lines in their optical spectra. The emission lines are believed to result from the recombination process by the ions of different elements. The optical spectrum of *Type 1* AGNs is characterized by both narrow (FWHM $\sim$ 1000 km/s) and broad (FWHM up to $\sim$ 10000 km/s) emission lines, whereas *Type 2* objects contain only narrow emission lines.

The radio-quiet AGNs mainly include Seyfert galaxies and radio-quiet quasars. Seyfert galaxies, the first identified distinct class of AGNs (Seyfert, 1943), differ from quasars in that their host galaxies are clearly visible. The majority of Seyfert galaxies are spirals with less power compared to radio-quiet quasars. Seyfert galaxies are classified into *Seyfert 1* and *Seyfert 2* based on the width of emission lines in their optical spectra. *Seyfert 1* have broad (coming from BLR) and narrow (coming from NLR) emission line features, whereas only narrow emission line features are present in *Seyfert 2*. Thus, *Seyfert 1* and *Seyfert 2* belong to the *Type 1* and *Type 2* categories, respectively. Radio-loud AGNs include radio-loud quasars, radio galaxies, and blazars. Giant elliptical galaxies that show strong radio emission are called radio galaxies. Radio galaxies are further divided into two categories based on their emission lines in optical/UV spectra: Broad Line Radio Galaxies (BLRG; *Type 1*) and Narrow Line Radio Galaxies (NLRG; *Type 2*). AGNs with relativistic jets pointing towards the line of sight of the observer at small angles are classified as *blazars*. They are compact radio objects with unresolved radio emissions. Blazars are subdivided into flat-spectrum radio quasars (FSRQs) and BL Lacertae-type objects (BL Lacs) based on whether emission lines are present or absent in their optical spectra, respectively. Typically, FSRQs are more luminous than BL Lac objects. The alignment of the jet toward the observer's line of sight results in significant Doppler boosting of the blazar emissions. This thesis mainly focuses on blazars.

The unification hypothesis proposes that different types of AGNs can be interpreted as a single population observed under different circumstances. Orientation effects can play a vital role in interpreting observations from various classes of AGNs; i.e., different orientations of the object with respect to the line of sight can explain the observed differences between various types of AGNs (Antonucci, 1993; Urry & Padovani, 1995). The key factors contributing to various manifestations are axis-symmetric dusty torus, bipolar relativistic jets and the luminosity. Figure 1.2 represents the classification of AGNs based on the observer's viewing angle.

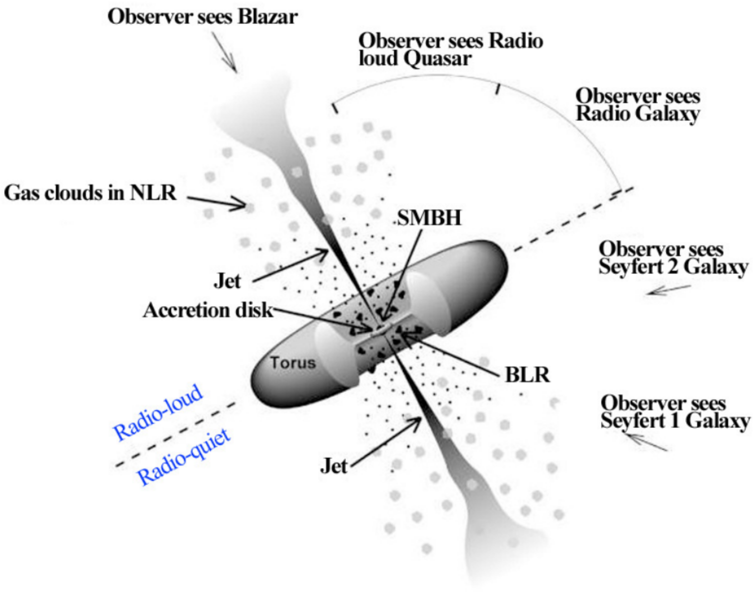

Figure 1.2: Classification of AGNs based on the observer's viewing angle. Credit: `https://fermi.gsfc.nasa.gov/science/eteu/agn/`.

1.3 Relativistic jets

High-resolution radio maps reveal the existence of well-collimated jets in many AGNs, with patterns moving at superluminal velocities. The launching of astrophysical jets in AGNs from the system near the central engine is a highly complex phenomenon. The highly collimated jets, occurring at various scales ranging from a few parsecs to megaparsecs, can be seen as an efficient mechanism for transporting highly energetic particles in strong helical magnetic fields varying from $\sim$ 1 mG - 10 G, through the bulk motion of plasma moving at relativistic speeds (Martí-Vidal et al., 2015). The relativistic motion of the jet can be understood through observed properties such as the superluminal pattern, gamma-ray transparency, and rapid variability of the source (e.g., Rees, 1966; Begelman et al., 1984; Guilbert et al., 1983; Ghisellini et al., 1993). The rapid variability observed in blazar jets suggest that the emission region is very close to the central engine, with bulk acceleration taking place within a radius of approximately 10 parsecs (Dondi & Ghisellini, 1995). Though the physics behind jet launching, collimation, and plasma acceleration are not well understood, theoretical models anticipate that the jets are expelled from the accreting supermassive black holes and are powered either by the accretion process (Blandford & Payne, 1982) or by the spinning black hole (Blandford & Znajek, 1977). Thus, the direction of the jet emission will be determined by either the spin axis of the black hole or the angular momentum axis of the accretion disk. Nevertheless, the estimated jet power contradicts the accretion power for most blazars (Ghisellini et al., 2014).

- ## Superluminal motion:

The relativistic beaming (Doppler boosting) effects become more pronounced when the blobs of plasma within the jet moves at close to the speed of light along a trajectory slightly angled with the observer's line of sight. As a consequence, the blobs of plasma appear to move faster than the velocity of light (Blandford & Königl, 1979). This phenomenon is known as superluminal motion (Rees, 1966). The apparent velocity of the superluminal jet flow is given by

$$\beta_{app} = \frac{\beta_1 \, \sin\theta}{1 - \beta_1 \, \cos\theta} \, , \tag{1.1}$$

where β_1 $(= v/c)$ is the dimensionless velocity of the blob of plasma, and θ is the angle between the jet flow and the observer's line of sight. The radiation emitted will be collimated in the direction of motion (Figure 1.3), forming a cone with an opening angle of $\phi = \frac{1}{\Gamma}$ $(\Gamma = (1 - \beta_1^2)^{-1/2}$ is the bulk Lorentz factor), and hence Doppler boosting will enhance the intensity of the radiation in the direction of motion. The Doppler factor (δ) corresponding to Γ can be given by

$$\delta = \frac{1}{\Gamma\,(1 - \beta_1 \, \cos\theta)} \, . \tag{1.2}$$

The blazar emission is enhanced by relativistic motion when observed at a small angle, and this enhancement is governed by the Doppler or beaming factor δ.

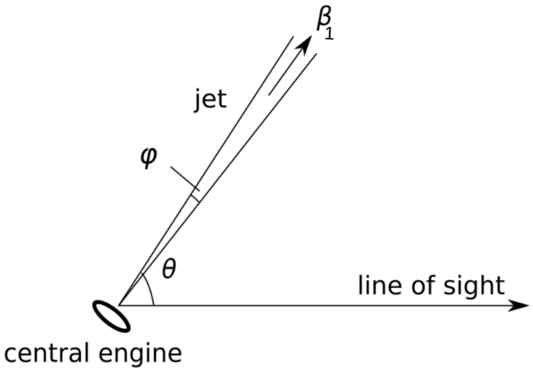

Figure 1.3: Schematic representation of the blob of plasma moving at a relativistic speed β_1 ($= v/c$) at an angle θ with respect to the observer's line of sight. ϕ is the jet opening angle.

1.4 Blazars

Blazars are radio-loud AGNs characterized by one of the relativistic jets directed towards the observer's line of sight (Urry & Padovani, 1995). Emissions from blazars cover the entire electromagnetic spectrum, primarily arising from the jet and being predominantly non-thermal. Key features of blazar emissions include Doppler boosting, rapid variability, and high polarization (Wagner et al., 1996; Heidt & Wagner, 1996; Takalo et al., 1994; Fan et al., 1997). Blazars are divided into Flat Spectrum Radio Quasars (FSRQs) and BL Lacertae-type objects (BL Lacs), based on the presence or absence of strong emission lines in their optical spectra. BL Lacs exhibit weak or no emission lines, while FSRQs show strong broad optical emission lines (Fan, 2003; Urry & Padovani, 1995). More specifically, if the equivalent width (EW) of the lines is > 5Å, the blazar source is classified as an FSRQ; whereas if the EW < 5Å, it is classified as a BL Lac object (Urry & Padovani, 1995). The presence or absence of these lines may relate to accretion mechanisms, as ionizing photons responsible for broad line emission are generated by the accretion disk. Radiatively efficient accretion processes can yield strong and broad emission lines, while a low accretion rate may result in weak or no emission lines due to the lack of significant contribution from the BLR. FSRQs are generally more luminous than BL Lac objects and are typically found at higher redshifts. Ghisellini et al. (2011) proposed another method for the classification of FSRQs and BL Lacs based on measuring the luminosity of broad lines (L_{BLR}) in units of the Eddington luminosity (L_{Edd}), stating that $L_{BLR} \geq 10^{-3}\, L_{Edd}$ for FSRQs and $L_{BLR} < 10^{-3}\, L_{Edd}$ for BL Lacs.

1.4.1 Broadband spectral energy distribution of blazars

The blazar emission covers almost the entire electromagnetic spectrum, from radio to gamma-ray energies. The distribution of power radiated by the source at different frequencies is known as the spectral energy distribution (SED). The SED of blazars typically exhibits two prominent peaks: the low-energy component peaks between IR and soft X-ray energies, while the high energy component peaks in the gamma-ray region (see Figure 1.4). The low-energy component is well understood as synchrotron emission produced by the gyration of relativistic electrons around the jet magnetic field. However, the origin of the high-energy component is not well understood. In the leptonic scenario, it is generally modeled as the emission from inverse Compton (IC) scattering of low-energy photons by the same population of electrons responsible for the synchrotron emission (Dermer et al., 1992; Dermer & Schlickeiser, 1993). The seed photons for IC can be either synchrotron photons themselves, commonly known as synchrotron self-Compton (SSC) (Marscher & Gear, 1985a; Costamante & Ghisellini, 2002), or the photons from sources external to the jet, such as the accretion disk, the broad-line region, and the dusty torus. This is commonly referred to as external Compton (EC) (Dermer et al., 1992; Sikora et al., 1994). In the hadronic scenario, the high-energy component is explained by emission through hadronic scenarios, such as proton-synchrotron and proton-photon interactions processes (Abdo et al., 2011; Böttcher et al., 2013; Weidinger & Spanier, 2015).

In FSRQs, the low-energy SED component peaks within the radio to infrared range, while in BL Lacs, the peak falls between IR/optical and X-ray energies. BL Lacs are further categorized based on the position of the synchrotron peak frequency (ν_{sp}). They are divided into low-energy peaked BL Lac objects (LBL: $\nu_{\mathrm{sp}} < 10^{14}$ Hz), intermediate energy peaked BL Lac objects (IBL: $10^{14} < \nu_{\mathrm{sp}} < 10^{15}$ Hz), and high energy peaked BL Lac objects (HBL: $\nu_{\mathrm{sp}} > 10^{15}$ Hz) (Fan et al., 2016; Abdo et al., 2010).

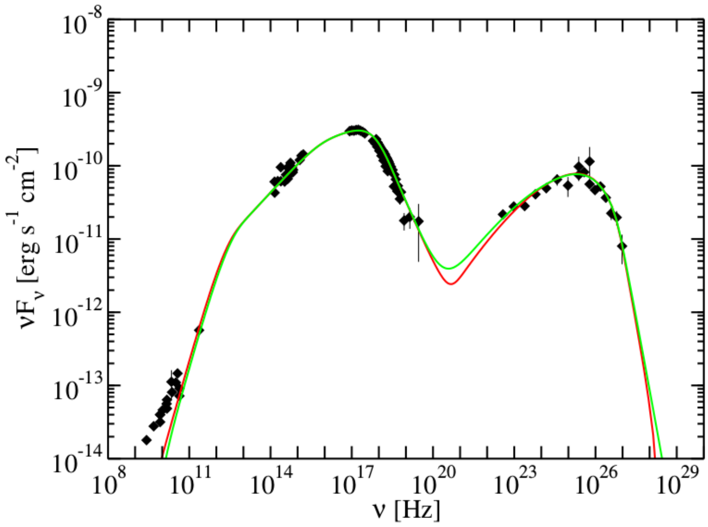

Figure 1.4: SED of blazar Mkn 421 (Abdo et al., 2011).

1.4.2 Blazar sequence

Fossati et al. (1998) introduced the concept of the blazar sequence by analyzing a sample of 126 bright blazars, 33 of which were detected in the γ-ray band by EGRET. To generate the average SED, these sources were categorized into bins based on their radio luminosity at 5 GHz, and their luminosities were averaged at selected frequencies. It was observed that a shift in SED towards lower frequencies is associated with an increase in bolometric luminosity of blazars, regardless of whether they are FSRQs or BL Lac sources. The peak frequencies of low and high energy components are also found to be correlated. The strong anti-correlation between SED peak frequencies and the source luminosity leads to a sequence from HBL → LBL → FSRQ, known as the *blazar sequence*. Additional observational characteristics of this blazar sequence reveal that as luminosity increases, the IC component becomes dominant over the synchrotron component, a feature known as *Compton dominance*. Figure 1.5 describes the blazar sequence, where HBLs have the lowest luminosities and highest peak frequencies, while FSRQs exhibit the highest luminosities and lowest peak frequencies. IBL and LBL class blazars fall between HBLs and FSRQs. An alternative perspective on the blazar sequence suggests that gamma-ray slopes soften and X-ray slopes harden as luminosity increases.

Ghisellini et al. (1998) proposed an explanation for the observed trends in the blazar sequence based on the rate of radiative cooling of electrons undergoing emission. As the luminosity increases, the electron collision rate also increases due to the high radiation energy density, resulting in fast cooling of electrons. Subsequently, the maximum frequency of the synchrotron component decreases because of the reduction in the maximum attainable particle energy of the electron distribution. In the blazar sequence, FSRQs are recognized as the most luminous ones. The contribution of the external radiation field is also dominant in the case of FSRQs. Consequently, the fast radiative cooling prevents electrons from attaining high energies, resulting in a synchrotron peak at lower energies. On the other hand, HBLs, characterized by the lowest intrinsic power, have the least contribution of external radiation field. Consequently, the cooling of particles in HBLs is less efficient and their energy can reach high enough to cause synchrotron emission peaking at UV or X-ray frequencies. LBLs, positioned between FSRQs and HBLs in terms of luminosity, typically have their synchrotron peak in optical/IR region.

Ghisellini et al. (2017) revisited the *blazar sequence* by conducting an extensive study of a large sample of *Fermi* blazars. The sample consists of 299 BL Lacs and 448 FSRQs from the third AGN catalogue of *Fermi*-LAT (Ackermann et al., 2015). These sources were divided into six different bins based on gamma-ray luminosity, and SEDs were constructed using archival data. The average SED of blazars in each luminosity bin was produced for a comparison with the blazar sequence by Fossati et al. (1998), confirming that this sample also follows the original blazar sequence (Figure: 1.5). When FSRQs and BL Lacs were analysed separately, it was found that (i) FSRQs form a sequence only in Compton dominance and X-ray slope, and (ii) The brighter the BL Lacs, the redder they become, whereas FSRQs do not become redder at high luminosities. The blazar sequence is still an open question, with several outliers being identified. If the blazar sequence reflects an inherent physical characteristic of blazars, it could significantly enhance our understanding of the mechanisms shaping the SEDs.

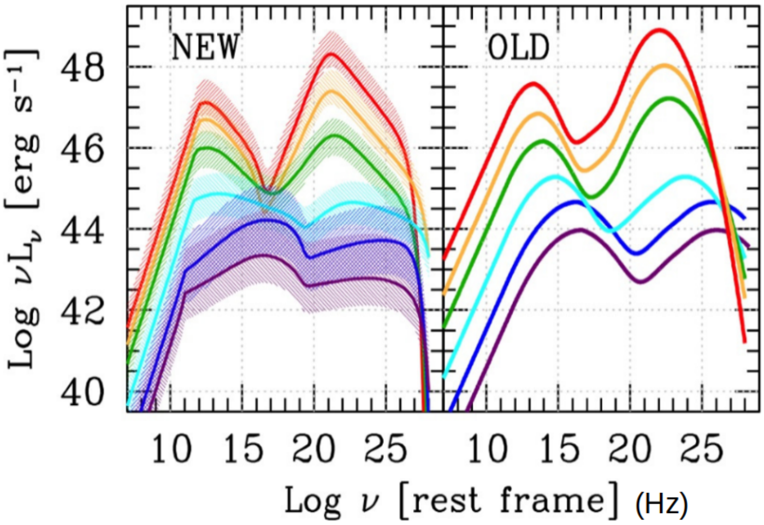

Figure 1.5: **Left** : The revised blazar sequence (NEW) presented by Ghisellini et al. (2017) based on different gamma-ray luminosity bins, showing FSRQs at the top and BL Lacs in the middle. **Right**: The original blazar sequence (OLD) from Fossati et al. (1998) is based on radio luminosity bins and illustrates the transition from FSRQs in red to LBLs, IBLs and HBLs in blue.

1.5 Particle acceleration: Fermi mechanism

The broadband SED of blazars, reaching GeV/TeV energies, indicates the presence of extremely relativistic particles in AGN jets. Furthermore, the observed spectra covering a broad range of wavelengths, from radio to gamma-ray, support a power-law model, suggesting that jet emission is predominantly driven by non-thermal mechanisms. It is widely believed that the Fermi acceleration mechanism plays a significant role in generating non-thermal power-law particle distributions (Fermi, 1949a). Enrico Fermi proposed that charged particles could undergo acceleration to higher energies through repeated scattering by magnetic irregularities, as they traverse through the galactic interstellar space, with a minor energy change occurring during each interaction (Fermi, 1949a). To understand this process, consider a scenario involving a cloud of mass M in motion at velocity V and a particle of mass m traveling at velocity v. Let us assume that the particle collides with the massive cloud, its initial direction forming an angle θ with the normal to the surface of the cloud (Figure 1.6). If the cloud is very massive compared to that of the particle and

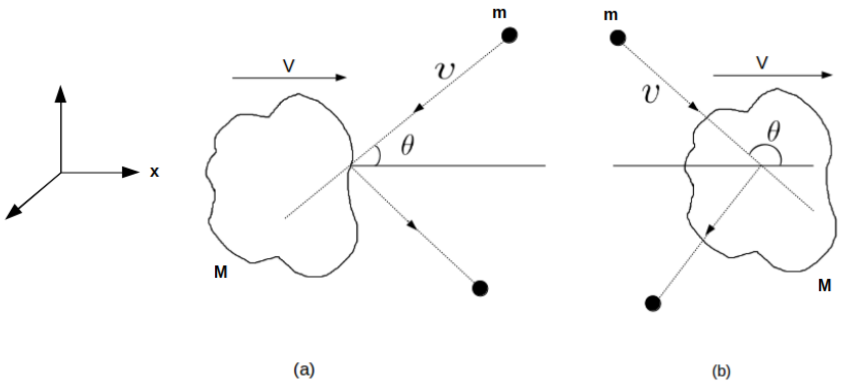

Figure 1.6: Illustration of Fermi acceleration: Collision of a particle of mass m and velocity v with a cloud of mass M and velocity V. (a) Head-on collison; (b) Follow-on collision.

its velocity remains unchanged even after the collision, this indicates that the center of mass frame (CM-frame) coincides with the cloud's frame itself. Using Lorentz transformation, we can express the energy and momentum equations of the particle before scattering, as observed from the CM-frame (Longair, 2011).

$$E' = \Gamma_{\rm c} \left(E - V p_{\rm x}\right) \,, \tag{1.3}$$

$$p'_{\rm x} = \Gamma_{\rm c} \left(p_{\rm x} - \frac{VE}{c^2}\right) \,, \tag{1.4}$$

where $\Gamma_{\rm c} = \left(1 - \frac{V^2}{c^2}\right)^{-1/2}$ is the Lorentz factor of the moving cloud, E and $p_{\rm x}$ are the energy and x-component of momentum of the particle in the observer's frame, while these quantities in the CM-frame are indicated with a prime (E' and $p'_{\rm x}$). Given that the CM-frame aligns with that of the scatterer, we obtain the condition of energy and the momentum (along the x-axis) before collision ($E'_{\rm b}$, $p'_{\rm x,b}$) and after collision ($E'_{\rm a}$, $p'_{\rm x,a}$) as

$$E'_{\rm a} = E'_{\rm b} = E' \tag{1.5}$$

$$p'_{\mathrm{x,a}} = -p'_{\mathrm{x,b}} = -p'_{\mathrm{x}} \,. \tag{1.6}$$

In the observer's frame, the scattered energy will be,

$$E_{\mathrm{a}} = \Gamma_{\mathrm{c}} \left(E' - V p'_{\mathrm{x}} \right) \,. \tag{1.7}$$

subtituiting equations (1.3) and (1.4) in (1.7), we can write

$$E_{\mathrm{a}} = \Gamma_{\mathrm{c}}^2 \left[E - 2V p_{\mathrm{x}} + \left(\frac{V^2}{c^2} \right) E \right] \,. \tag{1.8}$$

Using the formula for particle momentum with a velocity v along the x-axis represented as $p_{\mathrm{x}} = \frac{E v_{\mathrm{x}}}{c^2}$, we determine the scattered particle energy to be,

$$E_{\mathrm{a}} = \Gamma_{\mathrm{c}}^2 E \left(1 - \frac{2V v_{\mathrm{x}}}{c^2} + \frac{V^2}{c^2} \right) \,. \tag{1.9}$$

Assuming $V \ll c$, the change in particle energy after the collision will be

$$\Delta E = E_{\mathrm{a}} - E \,, \tag{1.10}$$

by neglecting the higher terms in (V/c) which go beyond the second order, we find

$$\Delta E \approx E \left[- \frac{2V v_{\mathrm{x}}}{c^2} + 2 \left(\frac{V}{c} \right)^2 \right] \,. \tag{1.11}$$

From figure (1.6), we can write $v_{\mathrm{x}} = -v \cos\theta$

$$\frac{\Delta E}{E} = \frac{2V}{c^2} \left(v \cos\theta + V \right) \,. \tag{1.12}$$

The fractional energy change may either be positive or negative. In a head-on collision where $\cos\theta$ is positive, the particle gains energy, while in a tail-on collision where $\cos\theta$ is negative, the particle loses energy. Since the probability for head-on collisions is higher than that for tail-on collisions, there will always be a gain in particle energy.

1.5.1 Stochastic acceleration: Fermi second-order mechanism

In stochastic acceleration, particles gain energy through random collisions with magnetized clouds or magnetohydrodynamic waves. In this process, the collision probability between the particle and the scatterer is anisotropic, therefore, the mean gain in energy can be obtained by averaging over the angle θ in the equation (1.12)

Assuming particles move relativistically with $v \approx c$, and by averaging over angle θ, from 0 to π, the angle-dependent term in equation (1.12) can be expressed as:

$$\left\langle \frac{\Delta E}{E} \right\rangle \approx \frac{2V}{c^2} \left\langle (c \cos\theta + V) \right\rangle \ , \tag{1.13}$$

$$\langle \cos\theta \rangle \approx \frac{\int_0^\pi \cos\theta \left[1 + (V/c)\cos\theta\right] \ \sin\theta \ d\theta}{\int_0^\pi \left[1 + (V/c)\cos\theta\right] \ \sin\theta \ d\theta} = \frac{1}{3}\left(\frac{V}{c}\right) \ , \tag{1.14}$$

$$\left\langle \frac{\Delta E}{E} \right\rangle \approx \frac{2V}{c^2}\left(\frac{V}{3} + V\right) \approx \frac{8}{3}\left(\frac{V}{c}\right)^2 \ . \tag{1.15}$$

The average energy increase is second-order in V/c ($\approx (V/c)^2$); therefore, this stochastic acceleration process is also referred to as the second-order Fermi acceleration mechanism.

1.5.2 Shock acceleration: Fermi first-order mechanism

Acceleration of charged particles becomes more efficient when a shock moves through the plasma, and particles repeatedly cross the shock front. Shock acceleration refers to the acceleration of charged particles in the vicinity of a shock, which is expected in various astrophysical contexts, such as supernova explosions in the interstellar medium, accreting X-ray binaries, and stellar winds. A shock results from disturbance in a supersonic fluid flow, creating a discontinuity. The plasma on either side of the shock exists in distinct equilibrium states, categorized as upstream (the plasma ahead of the shock front) and downstream (the plasma behind the shock front), but remains connected by conservation equations. If we suppose that in the upstream plasma, the particle possesses energy E and momentum p_x along the x-axis (perpendicular to the shock front), then the particle's energy in the downstream plasma, E' will be:

$$E' = E + p_x V\,, \tag{1.16}$$

where V is defined as the velocity of the downstream plasma relative to the downstream direction. Let θ be the angle between the momentum of particle and the shock normal, then $p_x \approx \frac{E\cos\theta}{c}$. Hence, the increase in particle energy in the downstream will be

$$\Delta E = E' - E = E\left(\frac{V}{c}\right)\cos\theta\,. \tag{1.17}$$

The probability of a particle crossing the shock front and transitioning into the downstream within the angle range from θ to $\theta + d\theta$ is directly proportional to $\sin\theta\cos\theta\, d\theta$. Therefore, the net gain in energy on crossing the shock front is given by,

$$\frac{\Delta E}{E} = \frac{2}{3}\left(\frac{V}{c}\right)\,. \tag{1.18}$$

When we account for both the upstream-to-downstream and downstream-to-upstream flows of particles crossing the shock front, the average fractional energy gain during one complete trip is given by

$$\frac{\Delta E}{E} = \frac{4}{3}\left(\frac{V}{c}\right)\,. \tag{1.19}$$

As seen in above equation (1.19), the average energy gain is first order of (V/c). Thus, shock acceleration is also termed as the First-order Fermi acceleration mechanism. Additionally, shock acceleration is considered more efficient for particle energization compared to stochastic acceleration.

1.5.3 Diffusive shock acceleration

The supersonic outflows in a blazar jet naturally produce shocks, which may serve as the primary region where the kinetic energy of the jet flow is dissipated through the acceleration of electrons to relativistic energies, enabling the emission of X-rays and gamma-rays. Diffusive shock acceleration (DSA) is a highly efficient mechanism for generating energetic particles from a flow containing strong shocks (Kirk et al., 1998) and is considered a significant acceleration process in blazars (e.g., Bell, 1978; Blandford & Ostriker, 1978; Blandford & Eichler, 1987). Fermi acceleration at non-relativistic shocks produces a power-law particle spectrum

$$N(\gamma) \propto \gamma^{-s_1} \,,$$

where γ is the electron Lorentz factor, and s_1 the spectral index, which depends only on the shock compression ratio $r_1 = u_u/u_d$ (where u_u and u_d are the velocities of upstream and downstream flows, respectively).

$$s_1 = \frac{r_1 + 2}{r_1 - 1} \,,$$

where $1 < r_1 \leq 4$. For strong shocks, $r_1 = 4$, and thus $s_1 = 2$.

The electrons are accelerated at the shock front and then drift into the downstream region, where they emit most of their energy. The acceleration time-scale for DSA will have the following form (Kirk & Dendy, 2001)

$$t_{acc} \approx \frac{3\,\kappa}{u_{sh}^2} \,, \tag{1.20}$$

where u_{sh} represents the shock speed measured in the upstream frame, and κ denotes the spatial diffusion coefficient and is given by

$$\kappa = \frac{\lambda\, c}{3} \,, \tag{1.21}$$

where λ is the particle's mean free path. A fundamental physical limit of diffusive particle transport is Bohm diffusion, which occurs when the scattering mean free path is approximately equal to the gyro-radius (r_g) of the particle. In this scenario, the diffusion coefficient is expressed as

$$\kappa = \kappa_B = \frac{r_g\, c}{3} \quad \text{with } r_g = \frac{\gamma\, m_e\, c^2}{e\, B}\,. \tag{1.22}$$

Bohm diffusion results in the fastest acceleration due to the minimal mean free path, enabling frequent shock crossings and efficient energy gain. From equations 1.20 and 1.22, t_{acc} will be

$$t_{acc} \approx \frac{\gamma\, m_e\, c}{eB} \left(\frac{c}{u_{sh}}\right)^2 . \tag{1.23}$$

As we know, Fermi acceleration at non-relativistic shocks produces power-law particle spectra. However, the interplay between acceleration and escape (and/or cooling) from the shock region can lead to more complex spectral shapes (e.g., Zirakashvili & Aharonian, 2007).

1.6 Radiative Processes

The SED of blazars extends over the entire range of the electromagnetic spectrum. The observation of a power-law spectrum across a wide range of energies in blazars suggest that non-thermal processes predominantly govern their emission mechanisms. The non-thermal continuum emission suggests the presence of a non-thermal population of particles that can emit photons across the whole electromagnetic spectrum. Under the leptonic scenario, the main radiative mechanisms are considered to be synchrotron and inverse Compton processes of relativistic electrons, whereas the radiative processes associated with protons and nuclei are considered in the hadronic scenario.

1.6.1 Synchrotron emission

The key ingredients of the blazar jets are believed to be highly relativistic charged particles and magnetic fields. The primary radiation mechanism in blazar jets is advised as synchrotron emission, where the acceleration of relativistic electrons is considered in the presence of a magnetic field. Relativistic charged particles undergoing acceleration in a helical motion by gyrating around a magnetic field emit synchrotron radiation. The M87 jet is the first astrophysical source where synchrotron emission was identified (Burbidge, 1956).

The synchrotron power emitted by an electron moving with relativistic velocity $\beta_1 (= v/c)$ in a uniform magnetic field B at pitch angle α_1 (angle between the magnetic field and particle velocity) is defined following Rybicki & Lightman (1986) as

$$P_{\rm syn} = 2\, c\gamma^2 \beta_1^2 r_{\rm e}^2 B^2 \sin^2\alpha_1\,, \tag{1.24}$$

where γ is the electron Lorentz factor ($\gamma = (1-{\beta_1}^2)^{-1/2}$) and $r_{\rm e}(=\frac{e^2}{m_e c^2})$ is the electron radius. The total radiated power from an isotropic electron distribution can be obtained on averaging equation (1.24) over α_1, and the total power is

$$P_{\rm syn} = \frac{4}{3} c\gamma^2 \beta_1^2 \sigma_{\rm T} U_{\rm B}\,, \tag{1.25}$$

where $\sigma_{\rm T}$ is the Thomson cross section and $U_{\rm B}(= B^2/8\pi)$ is the magnetic field energy density. Thus the radiated power at frequency ν by a relativistic electron of energy $\gamma\, m_e\, c^2$ (m_e is mass of the electron), with a pitch angle α_1 in a magnetic field B, will have the following form (Blumenthal & Gould, 1970)

$$P_{\rm syn}(\gamma,\nu) = \frac{\sqrt{3} e^3 B \sin\alpha_1}{m_{\rm e} c^2} F\left(\frac{\nu}{\nu_{\rm c}}\right)\,, \tag{1.26}$$

where ν is the frequency of emitted photon and $\nu_{\rm c}$ is the critical frequency given by

$$\nu_{\rm c} = \frac{3eB\gamma^2}{4\pi m_{\rm e} c} \sin\alpha_1\,. \tag{1.27}$$

The synchrotron spectral shape is decided by the power function $F\left(\frac{\nu}{\nu_{\rm c}}\right)$, which is given by

$$F\left(\frac{\nu}{\nu_c}\right) = \frac{\nu}{\nu_c} \int_{\frac{\nu}{\nu_c}}^{\infty} K_{5/3}(\xi_1) d\xi_1\,, \tag{1.28}$$

where $K_{5/3}(\xi_1)$ is the modified Bessel function of order 5/3. Considering the peaked

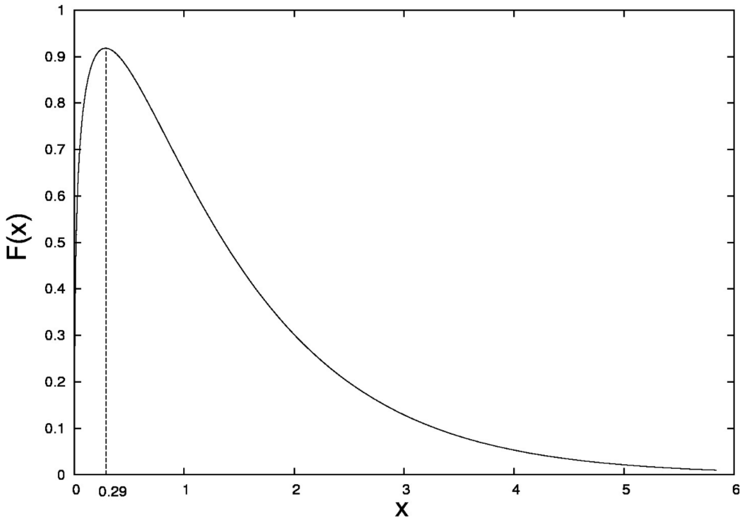

Figure 1.7: Synchrotron power function $F\left(\frac{\nu}{\nu_c}\right)$ peaking at frequency $\nu \sim 0.29\nu_c$.

nature of the synchrotron power function, an analytical solution for the single-particle emission spectrum can be approximated using equation 1.25 as (Shu, 1991)

$$P_{syn}(\gamma, \nu) = \frac{4}{3}\,\beta_1^2\,\gamma^2\,c\,\sigma_T\,U_B\,\Psi_\nu(\gamma)\,, \tag{1.29}$$

where the function $\Psi_\nu(\gamma)$ satisfies the condition

$$\int_0^\infty \Psi_\nu(\gamma)\;d\nu = 1\,. \tag{1.30}$$

$\Psi_\nu(\gamma)$ can be further approximated as a Dirac-delta function since the synchrotron emissivity for a single particle is peaked.

$$\Psi_\nu(\gamma) \to \delta(\nu - \gamma^2 \nu_L)\,, \tag{1.31}$$

where $\nu_L = eB/2\pi m_e\,c$, is the Larmor frequency.

For an isotropic power-law particle distribution of the form $N(\gamma) = k\,\gamma^{-s}$ (s is the particle spectral index) with $\gamma_{min} < \gamma < \gamma_{max}$ (γ_{min} and γ_{max} are the Lorentz factors corresponding to minimum and maximum energy of the electron, respectively), the energy of emitted radiation per second per frequency can be expressed following Blumenthal & Gould (1970) as

$$\frac{dW}{d\nu dt} \approx \frac{4\pi\, k\, e^3\, B^{(s+1)/2}}{m_e\, c^2} \left(\frac{3\, e}{4\pi\, m_e\, c}\right)^{(s-1)/2} a(s)\, \nu^{-(s-1)/2}\,, \tag{1.32}$$

where $a(s)$ is a function of particle spectral index s. For a power-law particle distribution, it suggests that the emitted synchrotron spectrum will also follow a power-law form, with an index $\frac{s-1}{2}$.

The synchrotron emissivity resulting from an isotropic electron distribution is given by

$$j_{\rm syn}(\nu) = \frac{1}{4\pi} \int_{\gamma_{min}}^{\gamma_{max}} P_{syn}(\gamma, \nu)\, N(\gamma)\; d\gamma\,. \tag{1.33}$$

The synchrotron flux $F_{syn}(\nu)$ recieved by the observer on Earth can be derived by accounting for the relativistic and cosmological factors (Begelman et al., 1984)

$$F_{\rm syn}(\nu) \approx \frac{\delta^3(1+z)}{d_{\rm L}^2}\, V\, j_{\rm syn}\left(\frac{(1+z)}{\delta}\nu\right)\,, \tag{1.34}$$

where δ is the Doppler factor, z the redshift, d_L the luminosity distance, and V is the volume of the emission region.

Synchrotron emission process can be followed by an absorption process known as *Synchrotron Self Absorption* (SSA). In this process, a charged particle absorbs a photon and get energized in the presence of magnetic field. The absorption coefficient for SSA process is given by (Ghisellini & Svensson, 1991)

$$\kappa_\nu = -\frac{1}{8\pi\, m_e\, \nu^2} \int \frac{N(\gamma)}{\gamma^2} \frac{d}{d\gamma}\, [\gamma^2\, P_{syn}(\gamma, \nu)] d\gamma\,. \tag{1.35}$$

For a power-law particle distribution $N(\gamma) = k\,\gamma^{-s}$, the SSA coefficient will be (Shu, 1991)

$$\kappa_\nu \propto B^{(s+2)/2}\; \nu^{-(s+4)/2}\,. \tag{1.36}$$

A frequency-dependent absorption coefficient with a negative power implies that the source can be optically thick (optical depth, $\tau_\nu > 1$) at low frequencies and optically thin ($\tau_\nu < 1$) at high frequencies. For an optically thick region, the source function S_ν will have a power-law form (Rybicki & Lightman, 1986)

$$S_\nu = \frac{j_{syn}(\nu)}{\kappa_\nu} \propto \nu^{5/2} \,. \tag{1.37}$$

As the radiation from the source is optically thick at low frequencies and thin at high frequencies, the total synchrotron spectrum will have a broken power-law shape. The spectrum deviates from a $\nu^{5/2}$ dependence at low frequencies to $\nu^{-(s-1)/2}$ at high frequencies. The frequency at which the index shifts is termed as the synchrotron self-absorption frequency. Furthermore, the synchrotron spectral index for the optically thick region is independent of the particle energy distribution, whereas for the optically thin region, the synchrotron spectral index depends on the electron energy distribution index s.

1.6.2 Inverse Compton emission

Photons generated in astrophysical processes have the potential to be scattered by electrons, and this scattering significantly impacts the observed spectrum. In a scattering event, if the energy of a high-energy photon transferred to a low-energy electron is termed as Compton scattering, whereas when the energy from a high-energy electron is transferred to a low-energy photon, causing the photon to undergo upscattering, this process is termed inverse Compton (IC) scattering. Based on the energies of incident photons in the rest frame of the electron, inverse Compton scattering can be categorized into two regimes: the Thomson regime and the Klein-Nishina regime.

If the energy of the incoming photon in the electron's rest frame is significantly smaller than the rest mass energy of the electron ($m_e\, c^2$), the recoil of an electron will be negligible. Consequently, the photon energy remains unchanged in the electron's rest frame after scattering. This scattering process is governed by the Thomson cross-section, and the differential cross-section is expressed as

$$\frac{d\sigma}{d\Omega} = \frac{1}{2} r_e^2 \,(1 + \cos^2\theta)\,, \tag{1.38}$$

where r_e stands for the classical electron radius, while θ indicates the scattering angle (angle between the incident and scattered photon directions). Thomson scattering can be described within the framework of classical electrodynamics. When the energy of the incoming photon in the electron's rest frame becomes comparable or exceeds the rest mass energy of the electron, the recoil of the electron becomes significant, causing the scattering process to deviate from the Thomson regime. Under these conditions, a quantum treatment is required, known as the Klein-Nishina regime. In this scenario, the differential cross-section can be expressed in relation to the energies of the incident and scattered photons (ϵ_i and ϵ_s, respectively) as follows:

$$\frac{d\sigma}{d\Omega} = \frac{\epsilon_s^2 r_e^2}{2\epsilon_i^2} \left(\frac{\epsilon_i}{\epsilon_s} + \frac{\epsilon_s}{\epsilon_i} - \sin^2\theta \right) . \tag{1.39}$$

The conditions for the Thomson and Klein-Nishina regimes can also be expressed based on the incident photon energy, such that $\gamma\epsilon_i << m_e c^2$ for the Thomson regime and $\gamma\epsilon_i >> m_e c^2$ for the Klein-Nishina regime (Rybicki & Lightman, 1986; Blumenthal & Gould, 1970). Furthermore, the scattered photon energy is $\epsilon_s \approx \gamma^2\,\epsilon_i$ for the scattering process in the Thomson regime, whereas it will be $\epsilon_s \approx \gamma\, m_e\, c^2$ under the extreme Klein-Nishina case (Blumenthal & Gould, 1970). In the Thomson regime, the increase in photon energy is quite small, resulting in only a minor loss of energy for the electron with each scattering event. Conversely, in the Klein-Nishina regime, the electron transfers nearly all of its energy to the photon in a single scattering event.

In the Thomson regime, when considering a power-law distribution of particles with power-law index s ($N(\gamma) = k\,\gamma^{-s}$), the resulting emitted photon spectrum will be (Blumenthal & Gould, 1970)

$$\begin{aligned} \frac{dW}{dt d\epsilon_s} &= \pi\, r_e^2\, c\, k\, 2^{s+3}\, \frac{s^2 + 4\,s + 11}{(s+3)^2\,(s+1)(s+5)}\, \epsilon_s^{-(s-1)/2} \\ &\times \int \epsilon_i^{(s-1)/2}\, n(\epsilon_i)\, d\epsilon_i\,, \end{aligned} \tag{1.40}$$

where $n(\epsilon_i)$ is the number density of the soft target photons. In the extreme Klein-Nishina limit, the emitted photon spectrum for the same power-law particle distribution will be

$$\begin{aligned}\frac{dW}{dtd\epsilon_s} &= \pi\, r_e^2\, c\, k\, (m_e\, c^2)^{s+1}\, \epsilon_s^{-s} \\ &\times \int \frac{d\epsilon_i}{\epsilon_i}\, n(\epsilon_i) \left(\ln \frac{\epsilon_i\, \epsilon_s}{m_e^2\, c^4} + C(s) \right) ,\end{aligned} \tag{1.41}$$

where $C(s)$ is a parameter of order unity (Blumenthal & Gould, 1970). We observe that the photon spectrum emitted by both the synchrotron and inverse Compton processes in the Thomson regime can be represented by a power-law with the same index of $(s-1)/2$ (equations 1.32 and 1.40). However, the inverse Compton spectrum in the extreme Klein-Nishina limit is considerably steeper than that of the Thomson limit (equation (1.41)).

1.6.3 Hadronic processes

AGN jets are believed to consist of electron-proton plasma. Accelerating protons to ultra-relativistic energies requires strong magnetic fields, typically several tens of Gauss. When protons are accelerated to high energies, they can lose energy through proton synchrotron radiation and hadronic interactions. Proton emission is generally weaker than that of electrons and a significant emission from proton demands high magnetic field and high proton density. The primary hadronic interactions through which protons can lose energy are proton-proton collision and proton-photon interaction. The proton-proton collisions are limited due to the low matter density in jets. Unlike elecrons, protons within a jet interact with low-energy photons and primarily undergo Bethe-Heitler pair production and photo-meson production.

- Bethe–Heitler process

  In this process, the protons interact with photons ($h\nu$) and generate electron-positron pair

$$p + h\nu \rightarrow p^{'} + e^{+} + e^{-} , \tag{1.42}$$

where $p^{'}$ indicates protons in the excited state. This process requires photon to have a threshold energy of about 1.022 MeV in the proton's rest frame and the pair can lose energy through synchrotron process and IC scattering with the soft photons.

- Photo-meson process

  When protons undergo interactions with high-energy photons, they generate both neutral and charged pions.

$$\begin{aligned} &p + h\nu \rightarrow n + \pi^{+} \\ &p + h\nu \rightarrow p' + \pi^{0} \\ &p + h\nu \rightarrow p' + \pi^{+} + \pi^{-} \end{aligned} \tag{1.43}$$

  The neutral and charged pions then decay primarily as

$$\begin{aligned} &\pi^{0} \rightarrow 2\gamma \\ &\pi^{+}(\pi^{-}) \rightarrow \mu^{+}(\mu^{-}) + \nu_{\mu}(\bar{\nu}_{\mu}) \\ &\mu^{+}(\mu^{-}) \rightarrow e^{+}(e^{-}) + \nu_{e}(\bar{\nu}_{e}) + \bar{\nu}_{\mu}(\nu_{\mu}) \end{aligned} \tag{1.44}$$

  The threshold energy of photons for this photo-meson or photo-pion reaction $\approx$ 145 MeV.

1.7 Modeling high energy emission from blazars

The observations of high energy (HE; E $>$ 100 MeV) and very high energy (VHE; E $>$ 100 GeV) gamma-rays from blazars have proven that the blazar jets are capable of accelerating particles upto ultra-relativistic energies. The number of blazar sources detected at HE/VHE gamma-rays has risen significantly with the advancements in the current generation ground based imaging atmospheric cherenkov telescopes (IACTs) such as high energy stereoscopic system (HESS), major atmospheric gamma imaging cherenkov telescopes (MAGIC) and very energetic radiation imaging telescope array system (VERITAS), major atmospheric cherenkov experiment telescope (MACE), first G-APD cherenkov telescope (FACT) and cherenkov telescope array observatory (CTAO) and the space based high sensitive *Fermi*-Large Area Telescope (LAT). The Large-Sized Telescope (LST) at CTAO recently detected VHE emission from FSRQ OP 313 (z = 0.997) above 100 GeV. This marks the first VHE detection from a distant AGN, making OP 313 the most distant AGN and the second farthest source detected at such energies (Cortina & CTAO LST Collaboration, 2023). VHE observations of blazars provide a means to study the extragalactic background light (EBL), as the high energy gamma-ray radiation is absorbed by the EBL via pair production process on its path to the observer. At higher redshifts, VHE flux is heavily attenuated by the EBL, making the observed spectra steeper than the intrinsic ones. Observations of distant blazars exhibiting hard intrinsic spectra at relatively high energies have posed challenges in understanding their emission; however, efforts have been made to account for these hard VHE spectra. High energy gamma-ray observations in blazars also exhibit pronounced time variability, ranging from days to minutes.

The modeling of blazar SED at high energies primarily involves two types of models: leptonic and hadronic. Below, a brief discussion of these models are provided.

Leptonic models

In leptonic models, the radiative output is mainly dominated by electrons and/or electron-positron pairs in the jet. The HE/VHE gamma-ray emission is believed to be produced via inverse Compton scattering of soft photons by relativistic electrons. The production of high energy gamma-rays must overcome gamma-gamma absorption and pair production to successfully escape the emission region. In the leptonic approach, it is widely believed that jets likely contain mildly relativistic or non-relativistic protons, and these protons contribute little to the radiative output due to their significantly larger mass. Leptonic models generally require magnetic field strengths approximately 0.1 to 10 Gauss.

In the inverse Compton process, low-energy photons may originate from different sources. They can either be low-energy synchrotron photons, in which case the process is termed synchrotron self-Compton, or they can be externally sourced. If the source of the target photons is located external to the jet, the emission process is termed external Compton.

- **Synchrotron Self Compton (SSC)**

  If the low-energy synchrotron photons undergo further upscattering by the same electron distribution responsible for the synchrotron emission, this process is termed synchrotron self-Compton. The one-zone SSC model is the simplest method for describing steady multi-wavelength emission in the absence of external photon fields. One can describe the emission region to be a spherical blob embedded with a tangled magnetic field and is populated homogeneously by a broken power-law/log-parabola electron distribution. Despite the simplicity of one-zone SSC model it succeeds in the broadband SED modeling of many blazars, mostly HBLs. The single-particle Compton emissivity resulting from the scattering of isotropic synchrotron photons can be determined (from Klein-Nishina formula) as (Blumenthal & Gould, 1970; Jones, 1968):

  $$P_{\rm ssc}(\gamma, \nu_s) = \frac{3\pi\sigma_T\nu_s}{\gamma^2}\int\limits_{\rm x_1}^{\rm x_2} \frac{I_{\rm syn}(\nu_i)}{\nu_i^2} f(\nu_i, \nu_s, \gamma)\, d\nu_i\,, \tag{1.45}$$

  where $\nu_{\rm i}$ and $\nu_{\rm s}$ are the frequency of the incident and the scattered photon, $\rm I_{syn}(\nu_i)$ is the synchrotron intensity, $\rm x_1 = MAX\left[\nu_{syn}^{min}, \frac{\nu_s}{4\gamma^2(1-h\nu_s/\gamma m_e c^2)}\right]$, $\rm x_2 = MIN\left[\nu_{syn}^{max}, \frac{\nu_s}{(1-h\nu_s/\gamma m_e c^2)}\right]$ with $\nu_{\rm syn}^{\rm max(min)} \approx 1.29 \times 10^6 \gamma^2_{\rm max(min)} B$, with $\gamma_{\rm min}$ and $\gamma_{\rm max}$ are the minimum and maximum available electron energies, respectively, and

$$f(\nu_i, \nu, \gamma) = 2r \log r + (1 + 2r)(1 - r) + \frac{\psi^2 r^2 (1 - r)}{2(1 + \psi r)} \,,$$

where $\mathrm{r} = \frac{\nu_\mathrm{s}}{4\nu_\mathrm{i}\gamma^2(1 - \mathrm{h}\nu_\mathrm{s}/\gamma \mathrm{m_e c^2})}$ and $\psi = \frac{4\mathrm{h}\nu_\mathrm{i}\gamma}{\mathrm{m_e c^2}}$.

The SSC emissivity resulting from an isotropic electron distribution is given by

$$j_\mathrm{ssc}(\nu) = \frac{1}{4\pi} \int_{\gamma_{min}}^{\gamma_{max}} P_{ssc}(\gamma, \nu)\, N(\gamma)\, d\gamma \tag{1.46}$$

After taking into account of the relativistic and cosmological effects, the SSC flux recieved on earth can be obtained by replacing j_syn in equation (1.34) with j_ssc.

- **External Compton (EC)**

  The region around SMBH is extremely bright and contains various photon fields that can undergo inverse Compton scattering with the relativistic electrons besides the synchrotron photons in the jet. The plausible soft photons in the external inverse Compton process can be thermal photons from the accretion disk, optical emission from broad line region, X-ray emission from corona and/or IR photons from the dusty torus. Additionally, they may result from interactions with the cosmic microwave background (CMB) radiation. External Compton process strongly depends on location of the emitting region from the SMBH and the properties of the external photon field. As the jet's plasma moves away at high speeds, Doppler deboosting limits inverse Compton emission from accretion disk photons (Dermer & Schlickeiser, 1993). If the plasma in the jet moves away with a Lorentz factor Γ, the energy density of the disk photon field is greatly diminished by a factor of Γ^{-3}. However, the disk photons can contribute significantly to the HE emission if the emission region is close to the disk. The BLR emits bright lines, with Ly-α being the most prominent one and serving as a target soft photon field for the IC process. Additionally, a second radiative contribution from the BLR comes from the accretion disk photons, which can be Thomson-scattered by electrons in the BLR. The dusty torus emits thermal radiations and is well described by a black-body distribution at a temperature about 1000 K. Inverse Compton scattering of CMB radiation is significant for the sources at high redshifts, since the intensity of CMB is proportional to $(1+z)^4$ (Schwartz, 2002). Also, CMB is relatively inefficient near the SMBH because stronger photon fields dominate, but it can become a significant mechanism for HE emission from jets at larger distances.

The calculation of EC component begins with transforming the external photon field distribution into the frame of the jet, followed by a process similar to that of the SSC calculation. The incorporation of external Compton emission along with the SSC radiation makes it possible for the reproduction of the high Compton dominance seen in high luminous blazar (e.g., Sikora et al., 1994). In the case of an isotropic external photon field, the EC emissivity will be (Dermer & Schlickeiser, 1993; Dermer & Menon, 2009; Finke, 2016)

$$j_{\mathrm{ec}}(\nu) = \frac{3}{8}\nu c \beta_\Gamma \sigma_T \int_0^\infty d\nu_{i*} \int_{\gamma_{min}}^{\gamma_{max}} d\gamma \, \frac{N(\gamma)}{\gamma^2} \, \frac{U_{\mathrm{ph}*}(\nu_{i*})}{\nu_{i*}^2} \, \phi(\gamma, \nu, \nu_i') \,, \tag{1.47}$$

where $\beta_\Gamma = \sqrt{1 - 1/\Gamma^2}$, $\nu_i' \approx \Gamma\gamma(1+\beta_1)\nu_{i*}$, and ν_{i*} and $U_{\mathrm{ph}*}$ are the frequency and energy density of the target photon field in the AGN frame, respectively.

$$\phi(\gamma, \nu_s, \nu_i') = \left[y + \frac{1}{y} + \frac{\nu_s^2}{\gamma^2 \nu_i'^2 y^2} - \frac{2\nu_s}{\gamma \nu_i' y} \right] \quad \text{where} \quad y = 1 - \frac{h\nu_s}{\gamma m_e c^2} \,. \tag{1.48}$$

Considering the relativistic and cosmological effects, the observer on Earth can acquire the EC flux by replacing j_{syn} in equation 1.34 with j_{ec}.

Hadronic models

It is possible that the protons in the jet accelerated to ultra-relativistic energies along with electrons and positrons. In hadronic models, the high energy emission from blazars is believed to be as a result of the processes such as proton-synchrotron radiation and/or hadronic interactions. Proton-synchrotron models often demand very high magnetic field (> 30 G) compared to the leptonic models. The prominent hadronic interactions through which proton can lose most of their energies are explained in Section 1.6.3. The probability of photon-proton processess (photopair and photo-meson production) generally surpasses that of a proton-proton interaction since the central parsecs of AGNs are abundant in radiation but contain relatively poor baryonic matter. The target photons for photo-meson process can be the electron synchrotron photon and/or the external photons. The photo-meson process can result in the production of high-energy γ-rays as a result of decay of π^0 mesons produced in these reactions. Also, the decay of charged pions result in the production of secondary relativistic $e^{\pm}$ pairs and neutrinos ($\pi^+(\pi^-) \rightarrow \mu^+(\mu^-) + \nu_\mu(\bar{\nu}_\mu)$, $\mu^+(\mu^-) \rightarrow e^+(e^-) + \nu_e(\bar{\nu}_e) + \bar{\nu}_\mu(\nu_\mu)$). The decay products, $e^{\pm}$ pairs and γ-ray photons can initiate an electromagnetic cascade by producing further γ-rays and pairs. Thus electrons/positrons (primary and secondary), protons, photons and neutrinos can be considered as the stable populations in the emission region of blazar. In this models the low energy bump is attributed to the synchrotron radiation from the primary and secondary electrons.

Leptonic and hadronic models: Successes and Limitations

Leptonic emission models effectively reproduce the rapid variabilities/flares observed in blazars at broad energies because of the fast acceleration time-scale and cooling time-scale of electrons. The correlations between high-energy and the low-energy fluxes are often interpreted as supporting a leptonic scenario for the high-energy emission, as the same electron population is responsible for both low-energy photons through synchrotron processes and high-energy photons through inverse Compton processes. Eventhough the leptonic model is successful in explaining broadband SED of many blazars (mostly HBLs), they are challenging to explain the observed orphan X-ray and gamma-ray flares in many blazars. Other main challenges of this model include the observed hard VHE spectra and the detection of neutrinos.

Hadronic models have become more attractive for the modeling of HE/VHE emission from blazars especially with detection of neutrino events. TXS 0506 + 056 is the first blazar source to be associated with the neutrino from IceCube-170922A (IceCube Collaboration et al., 2018). Unlike leptonic process, neutrinos are also produced with high energy gamma-rays in the hadronic interactions (pp and $p\gamma$) as a result of charged pion decay present in the reaction products (see Section 1.6.3).

This model is successful in explaining the observed orphan flares and also the hard VHE spectra. However, the hadronic framework for high-energy emissions faces two key challenges; the rapid variability and the jet power. The observed rapid variability at high energies is difficult to explain with protons due to their much longer acceleration time-scales and cooling time-scale compared to electrons. If the hadronic processes significantly contribute to HE/VHE emissions, the required jet power tends to be extremely large. Also, hadronic models often necessitate higher magnetic fields, typically ranging from approximately 10 to 100 G (Cerruti, 2020).

Considering the successes and limitations of both models, a combination of leptonic and hadronic scenarios is widely used today (e.g., Sahakyan, 2018; Gasparyan et al., 2022; Rodrigues et al., 2024).

1.8 Radiative cooling of a power-law electron spectrum

In the preceding section, we discussed how the non-thermal electrons responsible for blazar emissions are accelerated through Fermi processes. Now, let us consider a scenario where the medium of jet is loosely divided into two spatial zones: the particle acceleration region (AR) and the emission/cooling region (ER). In the acceleration region, particles are injected at low energy and undergo continuous acceleration, emitting very little radiation during this process. The non-thermal electrons responsible for blazar emissions are accelerated to relativistic energies at a shock front (i.e., in the acceleration region). These high-energy particles then diffuse into the cooling region, where they radiate most of their energy through processes like synchrotron and inverse Compton (Kirk et al., 1998; Sahayanathan, 2008). The kinetic equation describing the evolution of particle in the acceleration region can be written as (Kardashev, 1962)

$$\frac{\partial N(\gamma,t)}{\partial t}+\frac{\partial}{\partial\gamma}\left[\left(\frac{\gamma}{t_a}-A\gamma^2\right)N(\gamma,t)\right]+\frac{N(\gamma,t)}{t_e}=Q\delta(\gamma-\gamma_0)\,, \tag{1.49}$$

where t_a and t_e are the electron acceleration timescale and escape timescale, respectively. The terms γ/t_a and $A\gamma^2$ represent the electron acceleration rate and the radiative loss rate, respectively. The injection of particles into the acceleration region is assumed to be monoenergetic, $Q(\gamma) = Q\delta(\gamma - \gamma_0)$. Electrons in the acceleration region will attain their maximum energy when the rate of acceleration and radiative loss are equal. Thus, the maximum attainable Lorentz factor of the accelerated electrons will be $\gamma_{max} = \frac{1}{At_a}$. Under steady state, equation (1.49) for $\gamma > \gamma_0$ will be,

$$\frac{d}{d\gamma}\left[\left(\frac{\gamma}{t_a} - A\gamma^2\right)N(\gamma)\right] + \frac{N(\gamma)}{t_e} = 0\,. \tag{1.50}$$

Assuming energy independence for both t_a and t_e, the solution to the equation above yields a power-law electron distribution (Kirk et al., 1998; Sahayanathan, 2008)

$$N(\gamma) \propto \gamma^{-\left(1+\frac{t_a}{t_e}\right)}\left(1 - \frac{\gamma}{\gamma_{max}}\right)^{\frac{t_a}{t_e}-1}. \tag{1.51}$$

for $\gamma \ll \gamma_{max}$

$$N(\gamma) \propto \gamma^{-p} \quad ; p = \left(1 + \frac{t_a}{t_e}\right). \tag{1.52}$$

After escaping from the acceleration region to the emission region, the evolution of the particle in the emission region is governed by

$$\frac{\partial n(\gamma,t)}{\partial t} - \frac{\partial}{\partial\gamma}[B\gamma^2 n(\gamma,t)] = \frac{N(\gamma,t)}{t_e} - \frac{n(\gamma,t)}{\tau_e}, \tag{1.53}$$

where $B\gamma^2$ describes the rate of radiative loss in the emission region, and τ_e is the escape timescale of electrons from the emission region. The steady state solution of the equation (1.53) is a broken power law with a break at energy (energy at which the cooling timescale equals τ_e), $\gamma_b = 1/B\tau_e$,

$$n(\gamma) = \begin{cases} \gamma^{-\left(1+\frac{t_a}{t_e}\right)} & \gamma < \gamma_{\rm b} \\ \gamma^{-\left(2+\frac{t_a}{t_e}\right)} & \gamma > \gamma_{\rm b}\,, \end{cases} \tag{1.54}$$

where $\left(1 + \frac{t_a}{t_e}\right)$ and $\left(2 + \frac{t_a}{t_e}\right)$ are the indices of broken power-law, differed by unity by derivation.

As the radiative loss rate is proportional to γ^2, the resulting synchrotron spectrum will again be a broken power law with indices $\frac{t_a}{2t_e}$ and $\frac{(t_a+t_e)}{2t_e}$, respectively. Here, the photon indices are expected to differ by 0.5. However, SED modeling of blazars often does not support this inference and the difference in index is usually found to be significantly larger than 0.5 (e.g., Mankuzhiyil et al., 2012). In **Chapter 3**, we discuss a comprehensive analysis of the radiative loss interpretation of the broken power-law electron distribution by studying the photon spectrum around the synchrotron peak.

1.9 Empirical modeling of blazar spectrum

Below, we discuss the general models employed for fitting the spectra of blazars:

- Power-law

$$F(\epsilon) = K\,\epsilon^{-\Gamma_1}\,, \tag{1.55}$$

where ϵ is the photon energy, and Γ_1 represents the power-law index

- Cutoff power-law

$$F(\epsilon) = K\,\epsilon^{-p}\exp[-(\epsilon/\epsilon_c)]\,, \tag{1.56}$$

where p represents the power-law index, and ϵ_c characterizes the position of the cutoff energy.

- Broken power-law

$$F(\epsilon) = \begin{cases} K & \begin{array}{ll} \epsilon^{-\Gamma_1} & \text{for}\,\epsilon \le \epsilon_b \\ \epsilon_b^{\Gamma_2-\Gamma_1}\epsilon^{-\Gamma_2} & \text{for}\,\epsilon > \epsilon_b\,, \end{array} \end{cases} \tag{1.57}$$

where Γ_1 and Γ_2 are the power law photon indices for $\epsilon < \epsilon_b$ and $\epsilon > \epsilon_b$ respectively, and ϵ_b is the break energy.

- Log-parabola

$$F(\epsilon) = K \left(\frac{\epsilon}{\epsilon_0}\right)^{-\alpha-\beta\log(\epsilon/\epsilon_0)}, \tag{1.58}$$

where α is the spectral index at energy ϵ_0, and β is the spectral curvature. An aternative SED representation of logparabola function is

$$F(\epsilon) = K \times 10^{-\beta[\log(\epsilon/\epsilon_p)]^2}/\epsilon^2\,, \tag{1.59}$$

where ϵ_p is the spectral peak in $\epsilon^2 F(\epsilon)$ representation.

Spectral curvature

An important feature of the non-thermal emission from AGNs is that a power-law function describes their spectra across a broad energy range. However, several blazar sources show significant curvature in their narrow band photon spectrum. The presence of curvature, even within a narrow energy band, suggests that the underlying electron distribution may be intrinsically curved. The increased availability of highly sensitive X-ray observations of blazars allows us to probe their spectral characteristics. It is well recognized that the X-ray spectra of HBLs often exhibit mild to strong curvature, typically milder than what would be expected from an exponential cutoff. The log-parabola model is widely used to fit these spectra, although in some instances the power-law model also provides an acceptable fit. A log-parabolic photon spectrum suggests the underlying electron distribution to also follow a log-parabola. This type of electron distribution can be achieved from a statistical acceleration scenario with an energy-dependent acceleration probability (Massaro et al., 2004). This situation can arise, for example, when the probability of a particle being confined by a magnetic field within the acceleration region decreases with an increase in the gyration radius. It is then expected that the photon index α and curvature parameter β are expected to be linearly correlated (Massaro et al., 2004). In fact, under certain conditions, the electron distribution resulting from stochastic particle acceleration could also resemble a log-parabola (Tramacere et al., 2011). This model predicts an anti-correlation between the peak energy (ϵ_p) and the peak curvature (Tramacere et al., 2007a). However, recent studies using *Swift*–XRT/*NuSTAR* observations report no significant correlation between α and β (Sinha et al., 2015; Kapanadze et al., 2017; Kapanadze et al., 2018b), and between ϵ_p and β (Kapanadze et al., 2018b,a; Kapanadze et al., 2020; Sinha et al., 2015; Baheeja et al., 2022). In this context, we perform a dedicated study to investigate the spectral curvature in the X-ray spectra of blazar Mkn 421 in **Chapter 4**. We are particularly interested to understand whether the observed X-ray spectral characteristics allow some inferences on the turbulent properties in the jet.

1.10 Multi-wavelength variability in blazars

An important feature of blazar emission is the flux variability on timescales ranging from minutes to years across the entire electromagnetic spectrum. When the variability timescale spans from a few minutes to less than a day, it is termed intra-day variability. Similarly, variability lasting from days to weeks is referred to as short-term variability, while variability lasting from months to years is termed as long-term variability. Studies on the temporal variability can provide insights into the physical conditions of the system, such as emission region properties (location and size), disk-jet connections, the mechanisms of particle acceleration and radiative cooling, etc.

A clear optical variability with a timescale of 1.5 hours was observed from BL Lacertae for the first time in 1987 (Miller et al., 1989), followed by discoveries of intra-day variability in the optical band of other blazars (e.g., OQ 530, OJ 287, 4C 29.45, AO 0235+164, 0109+22 etc.) in the subsequent years (Carini et al., 1990, 1992; Noble & Miller, 1996). The flux variation, with doubling timescales of the order of a few minutes, has been observed in the X-ray band of Mkn 421 (Sembay et al., 2002). Similar flux variability has been detected in different wavebands of 3C 279 (Soldi et al., 2008). With the introduction of the highly sensitive *Fermi*-Large Area Telescope (LAT), minute-scale variability at γ-ray energies was observed from the blazar 3C 279 in 2015 (Ackermann et al., 2016). The variability amplitudes are typically frequency-dependent, with higher frequencies exhibiting larger amplitudes at shorter variability timescales (Böttcher & Dermer, 2010).

The rapid flux variability (in timescales of days, hours, and/or even minutes) of blazars is believed to be associated with the Doppler boosting of the jet emission. Sometimes, large Doppler factors are necessary to interpret the observed minute-scale variabilities (e.g., Begelman et al., 2008). Further, this rapid variations also suggest that the emission region within the jet is highly compact, and the region size (R) can be constrained from the shortest variability time-scale (t_{var}) as $R \leq \frac{\delta\, c\, t_{var}}{1+z}$.

Light curves that span months to years are typically referred to as long-term light curves. Blazars, with their emission spanning the entire electromagnetic spectrum, have become the primary focus of multi-wavelength campaigns, especially with the advancements in multi-wavelength astronomy. The study of long-term multi-wavelength light curves of blazars is used to understand correlated flux variability. Correlated variability across different wavebands suggests a co-spatial origin for their emission. However, orphan flares have also been detected in multi-wavelength light curves of blazars, raising questions about the validity of the co-spatial origin of their emission.

In most cases, the narrow-band energy spectra of blazars in different wavebands can be modeled using a simple power-law function, whereas a log-parabola function is typically used to model the spectrum near the peaks of the SEDs. Studying the correlation between flux and spectral index in multi-wavelength observations reveals whether a source exhibits *harder when brighter* or *softer when brighter* trend in each waveband. A negative correlation between the spectral index and flux indicates *harder when brighter*, while a positive correlation signifies *softer when brighter* trend in that specific waveband. These observed *harder when brighter* or *softer when brighter* trends in different wavebands may be associated with the shifting of the SED toward higher frequencies (bluer) or lower frequencies (redder) with changes in brightness. The shifting of the SED toward higher frequencies with increasing brightness is known as *bluer when brighter* behavior, whereas the shifting of the SED toward lower frequencies with increasing brightness is referred to as *redder when brighter*. The *bluer when brighter* or *redder when brighter* behavior of blazars can also be analyzed by studying the correlation between the SED peak energy and flux. A positive correlation between peak energy and flux indicates *bluer when brighter* behavior, while a negative correlation signifies *redder when brighter* behavior of the source. The study of long-term multi-wavelength spectral variations of blazars can probe the underlying physical processes responsible for these variations. In **Chapter 5**, we perform a long-term multi-wavelength (in optical/UV, X-ray, and gamma-ray wavebands) spectral study of blazar S5 0716+714. A detailed study of the long-term spectral variations of the source in different wavelengths has the potential to shed more light on the physics behind these spectral variations. We further investigate the dominant source parameter responsible for the spectral variations.

Log-normal variability of blazar emission

Studying the long-term flux distributions can provide possible hints about the mechanism behind the variations in blazar light curves. Studies have been conducted on blazar light curves across various energy bands, and largely support a log-normal (Gaussian in logarithm) variability of fluxes (Romoli et al., 2018; Sinha et al., 2018; Rieger, 2019; Khatoon et al., 2020). The flux variation in blazar emission is generally stochastic in nature. According to the central limit theorem, if the flux variations result from additive processes, one should expect a Gaussian/normal distribution of fluxes. On the other hand, flux variations follow a log-normal distribution when the underlying process responsible for the variation is multiplicative (Uttley et al., 2005). BL Lacertae is the first blazar source in which a log-normal flux distribution was observed in X-rays (Giebels & Degrange, 2009). The moving perturbation in the accretion disk (multiplicative process) can explain the observed log-normal variability. However, flux variations occurring on minute timescales in many blazars suggest that the variability likely originates within the jet.

While examining the flux distribution at high energies, Biteau & Giebels (2012) demonstrated that a large ensemble of mini-jets within the blazar jet could also account for the log-normal behavior. Alternatively, for a power-law spectrum, a log-normal variability in flux can be an outcome of normal variation in the photon index (Sinha et al., 2018; Khatoon et al., 2020).

For a power-law spectrum

$$F(\nu) \propto \nu^{-\alpha}. \tag{1.60}$$

or

$$\log \mathrm{F}(\nu) \propto -\alpha \log \nu. \tag{1.61}$$

$$\Delta \log \mathrm{F}(\nu) \propto -\Delta\alpha \log \nu\,. \tag{1.62}$$

This suggests that a Gaussian variation in the index of a power-law spectrum will result in a log-normal variation in the flux. Thus the observed log-normal variability in blazars may be associated with Gaussian variation in the spectral indices. In **Chapter 5**, we perform a long-term distribution study of fluxes and indices of blazar S5 0716+714 in optical/UV, X-ray, and gamma-ray wavebands.

1.11 Aim of the thesis and Outline

Modeling the broadband SED of blazars often suggests that the emitting electron distribution follows a broken power-law. However, one of the long-standing problem is that the observed difference in spectral index cannot be explained by the radiative loss interpretation of the broken power-law electron distribution. Additionally, high-resolution observations have revealed curvature in the X-ray spectra of high-energy-peaked blazars. This observed spectral curvature implies the necessity for modification in the underlying particle distribution. In the first part of the thesis, we aim to thoroughly investigate the radiative loss interpretation of the broken power-law electron distribution by studying the blazar spectrum around the synchrotron peak. Further, a dedicated study is carried out to understand the spectral curvature in the X-ray spectrum of the blazar. The latter part of this thesis focuses on a long-term, multi-wavelength spectral study of a blazar. Using simultaneous optical/UV, X-ray, and gamma-ray data, we aim to understand the underlying physical mechanisms responsible for the spectral variations of the blazar. Here is a brief description of each chapter.

- We have used data from the space-based X-ray telescopes *Swift*-XRT and *NuSTAR* for a detailed study of the X-ray spectra of the blazars. Additionally, we employed the instruments *Swift*-UVOT for optical/UV data and *Fermi*-LAT for gamma-ray data to perform a multi-wavelength study of blazar. In **Chapter 2**, we discuss the details about these telescopes used for the studies presented in the thesis.
- In **Chapter 3**, we performed a detailed analysis of the X-ray spectrum of blazar around the synchrotron peak. The radiative loss interpretation for the broken power-law spectra of blazars is often questioned since the difference between the observed photon spectral indices does not support this inference. Using the blazar Mkn 421 as a case study, we perform a detailed analysis of its characteristic photon energy where the spectral index changes significantly. Our study show that the spectral indices before and after the characteristic photon energy are strongly anti-correlated. This

anti-correlation infact, does not support a simple radiative loss interpretation for the characteristic photon energy, and alternative scenarios are discussed (Baheeja et al., 2022).

- In **Chapter 4**, we thoroughly investigate the spectral curvature of the blazar to explore the signature of particle diffusion on the X-ray spectra. The curvature in blazar spectrum has the potential to understand the particle dynamics in jets. Our spectral analysis of Mkn 421 reveals that, the hard X-ray spectrum exhibits significant curvature during its high flux states. To investigate this, we explore plausible diffusion processes facilitating shock acceleration in the emission region that can contribute to the observed spectral curvature. We find that the X-ray spectra of Mkn 421 are consistent with a scenario where particle acceleration is mediated through Bohm-type diffusion and the spectra beyond the synchrotron peak is modulated by the radiative loss process (Baheeja et al., 2024).
- In **Chapter 5**, we present a long-term multi-wavelength spectral study of blazar S5 0716+714. In particular, we analyze the simultaneous optical/UV, X-ray, and gamma-ray observations of the source, spanning a period of $\sim$ 18 years, and perform a statistical analysis to identify the possible reasons for the spectral variations. A detailed correlation study between the best-fit parameters were performed. Our results suggest that the spectral changes observed during high flux states could be associated with the spectral energy distribution shifting towards the bluer end. We also explore the long-term flux and spectral index distributions of the source in optical/UV, X-ray, and gamma-ray bands. A broadband spectral study of the source, utilizing synchrotron, SSC, and EC processes, is also performed. We further investigate the dominant source parameter responsible for the flux variations using the best-fit model SED. We find that the model curves corresponding to variations in the bulk Lorentz factor have the potential to explain the observed correlations between the spectral parameters (Baheeja et al., 2024).
- In **Chapter 6**, we conclude by summarizing the findings and discussing the open problems that could be addressed in the future. The main find-

ings include that the evolution of the spectral indices around the SED peak of the synchrotron component of blazar Mkn 421 is inconsistent with a simple radiative loss interpretation of the broken power-law electron distribution. Further a detailed investigation of spectral curvature beyond the synchrotron peak provides an insight to the diffusion processes in the jet. A long-term multi-wavelength spectral study of blazar S5 0716+714 suggests that the spectral variations are primarily associated with changes in the bulk Lorentz factor of the jet.

Chapter 2

Multi-wavelength observatories and data analysis

Most of our comprehension regarding AGN jets originates from observations carried out across various energy bands, such as radio, optical/UV, X-ray, and gamma-rays. To understand the spectral features and temporal variations of blazar emissions, it is essential to conduct observational studies across the entire electromagnetic spectrum and supplement them with theoretical analysis to unravel the fundamental physical mechanisms. In this Chapter we discuss the details about the telescopes used for the study presented in the thesis. Chapter 3 of the thesis mainly focus on the X-ray spectra around the synchrotron peak of blazar Mkn 421. For this study, we have used the X-ray data in 0.3 to 10 keV energy range from the X-ray telescope *Swift*-XRT. A dedicated study of broadband X-ray spectrum of the source Mkn 421 in 0.3 to 79 keV by using data from *Swift*-XRT and *NuSTAR* is presented in Chapter 4. These space-based high-sensitivity instruments *Swift*-XRT and *NuSTAR*, provide a wide range of X-ray spectra to probe the spectral features at these energies. In Chapter 5, we present a multi-wavelength study of the blazar S5 0716+714 utilizing data from the instruments *Swift*-XRT/UVOT, *NuSTAR*, and *Fermi*-LAT. With the advent of *Fermi*-LAT, blazars are now continuously monitored in gamma-rays. In this chapter, we provide a brief overview of all these instruments as well as their data reduction and analysis procedures.

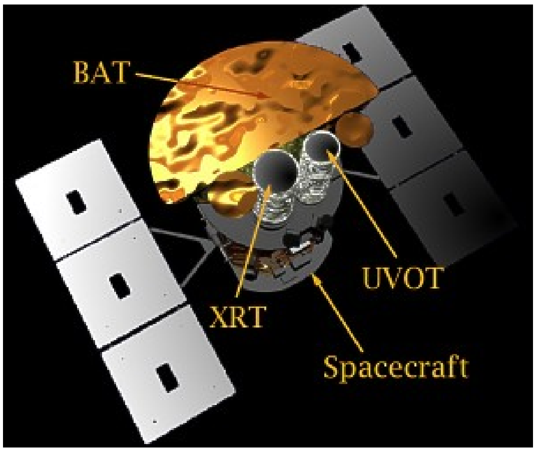

Figure 2.1: A visual representation depicting the *Swift* telescope and the payloads on-board. Credit: `https://www.swift.psu.edu/`

2.1 *Swift*

Swift is a pioneering multi-wavelength observatory dedicated specifically to the study of gamma-ray burst (GRB) phenomena. On November 20, 2004, it was launched into a low Earth orbit as a part of NASA's Medium Explorer (MIDEX) program. *Swift* has a notable repository of gamma-ray bursts, with consistent monitoring of X-ray/UV/optical afterglows and prompt follow-up observations by other observatories. Though the satellite is primarily dedicated to detecting and studying GRBs, it has also played a significant role in blazar studies. *Swift* is equipped with three co-aligned instruments operating in different energy bands: the Burst Alert Telescope (BAT, 15–150 keV), the X-Ray Telescope (XRT, 0.2–10 keV), and the Ultraviolet/Optical Telescope (UVOT, 170–650 nm). The BAT (Barthelmy et al., 2005) is a highly sensitive coded aperture imaging instrument with a large field of view (FoV) of 1.4 steradians. Its main purpose is to survey a significant portion of the sky for GRBs in the energy range of 15 – 150 keV and precisely determine their position. However, for our research, we utilized *Swift* data obtained from the XRT and UVOT instruments. Detailed descriptions of these instruments are presented in the following sections. Figure 2.1 shows a visual representation of the satellite along with its payloads.

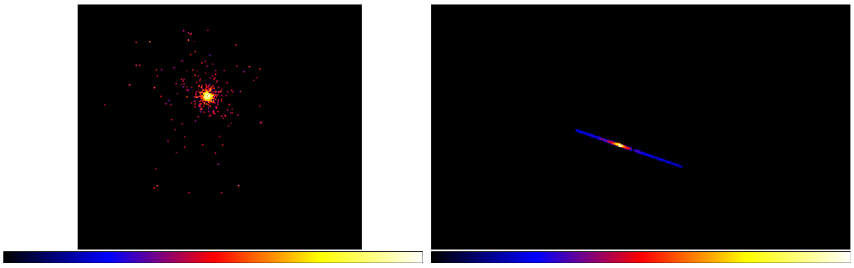

Figure 2.2: *Swift*-XRT images of Mkn 421 in both (left) Photon Counting (PC) and (right) Windowed Timing (WT) observation modes.

2.1.1 X-Ray Telescope (XRT)

The *Swift* X-ray telescope (Burrows et al., 2005) is a focusing telescope that operates in the soft X-ray energy region from 0.2 to 10 keV. It has an effective area of 120 cm^2, a field of view of 23.6 × 23.6 arcmin, and a resolution of 18 arcsec at an energy of 1.5 keV. It employs a 3.5-meter grazing incidence telescope (Wolter 1) to focus X-rays onto a Charge-Coupled Device (CCD). The complete mirror module comprises X-ray mirrors, a mirror collar, a thermal baffle, and an electron deflector. The CCD consists of an image area featuring a 600 × 602 array of 40 mm × 40 mm pixels, where each pixel corresponds to 2.36 arcsecs. The full width at half maximum (FWHM) energy resolution of the CCDs decreases from approximately 190 eV at 10 keV to around 50 eV at 0.1 keV.

In XRT, there are four readout modes: Imaging (IM), Photon Counting (PC), Windowed Timing (WT), and Photodiode (PD). Additionally, it autonomously selects the appropriate readout mode to utilize. In Imaging mode, an integrated image is generated that measures the total energy deposited per pixel and does not allow for spectroscopy, while spectroscopy is possible with PC, WT, and PD modes. The Photodiode mode is presently unavailable, although it was used to obtain high timing accuracy for rapidly varying flux from a bright source. The switching between PC and WT modes depends on the measurement of count rate. PC mode is the most sensitive one, and it retains complete spatial information and spectroscopic resolution, albeit with a time resolution of only 2.5 seconds. XRT is operated in PC mode for faint (low flux) sources, below 10 mCrab, whereas WT mode is usually used for high count rates. WT mode provides high timing resolution of 2.2 ms with 1-D position information.

All *Swift* data are publicly available through NASA's HEASARC interface. The XRT data is processed using the XRT Data Analysis Software (XRT-DAS) package, which is available in the X-ray reduction package HEASOFT. Observations are conducted in both PC and WT modes, and standard procedures are followed to process the telemetry data. The *xrtpipeline* tool is used to generate the cleaned event files for each observation. The raw data are reprocessed using the latest calibration files (`https://heasarc.gsfc.nasa.gov/docs/heasarc/caldb/swift/`) and standard screening criteria.

Usually, the source region is chosen as a circle centered on the source position with a radius of 20 pixels (approximately 47 arcseconds), encompassing about 90% of the Point Spread Function (PSF). For the background, a nearby circular region of 40 pixels is chosen, ensuring it is free from source contamination. The choice of the source region is also influenced by the brightness of the source. If the source count rate exceeds 0.5 counts/s in PC mode and 100 counts/s in WT mode, thorough examination of the data is necessary. In such cases, annular regions should be selected to avoid pile-up effects, with the size of the annular region varying according to the brightness of the source. Finally, the source and background spectra are produced using the *xrtproducts* task with proper selection of the source and background regions. The *xrtmkarf* task is used for producing the auxiliary response files (ARFs), and the response matrix files (RMFs) can be taken from the *Swift* calibration database (CALDB).

2.1.2 Ultraviolet/Optical Telescope (UVOT)

The UVOT is a diffraction-limited 30 cm (12 arcsec aperture) Ritchey-Chrétien reflector with a FOV of 17×17 arcmin, co-aligned with XRT (Roming et al., 2005). It operates in photon counting mode in the 170–650 nm wavelength range and is sensitive up to magnitude B=22.3 in a 17-minute exposure. Its filter wheel comprises of seven broadband filters. Among these filters, three operate within the optical range (V, B, and U), while the remaining three

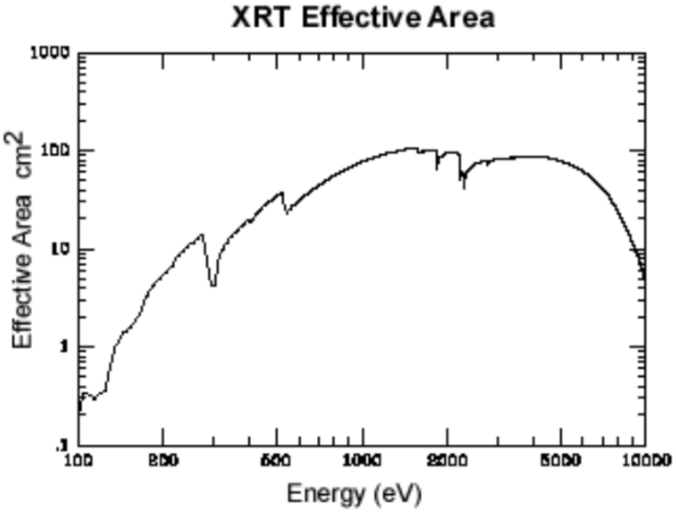

Figure 2.3: The plot of effective area of XRT as a function of energy. Credit: `https://swift.gsfc.nasa.gov/about_swift/xrt_desc.html`.

operate within the UV range (UVW1, UVM2, and UVW2), and one provides white light covering the entire UV/optical wavelength range. The wavelengths at which each filter operates are given in Table 2.1. The plot of effective area of UVOT filters as a function of wavelength is given in Figure 2.4. In order to attain a temporal resolution of 11 ms, a micro-channel-plate intensified, photon-counting CCD detector with fast readout capability is used.

The UVOT data are publicly available at the HEASARC data archive. The *uvotimsum* tool is used to sum the extensions within an image to analyze faint sources. Furthermore, the images in each filter from different observation can be combined using the the ftool *fappend*. The *uvotsource* tool is used to perform aperture photometry on images in each filter. Typically, a circular region (with a radius of approximately 5 arcseconds), centered on the source, is chosen as the source region, while for the background, either a circular region with a larger radius (approximately 20 arcseconds), free from source contamination, or an annular region, is selected to perform photometry. The obtained magnitudes are then corrected for reddening and Galactic extinction and subsequently converted to fluxes using photometric zero-points and conversion factors.

Table 2.1: The *Swift*-UVOT filter characteristics.

Filter	Central wavelength (Å)	FWHM (Å)
V	5468	769
B	4392	975
U	3465	785
UVW1	2600	693
UVM2	2246	498
UVW2	1928	657

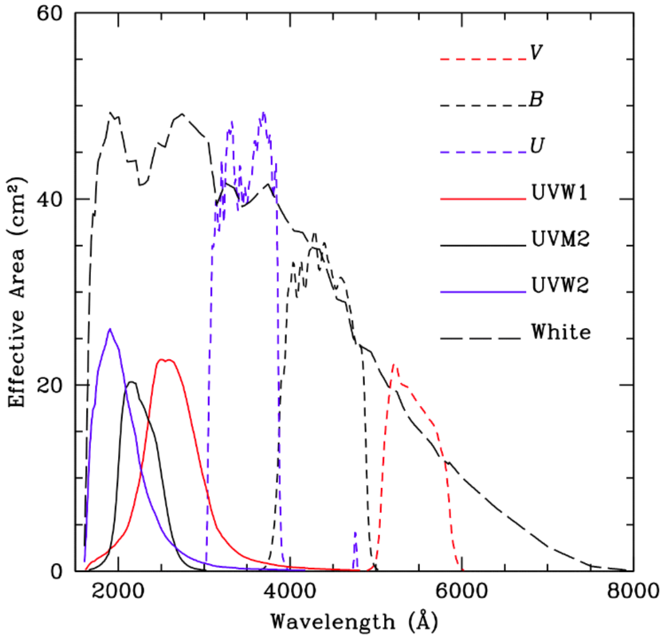

Figure 2.4: The plot of effective area of UVOT filters as a function of wavelength. Credit: `https://www.swift.ac.uk/analysis/uvot/filters.php`.

2.2 *NuSTAR*

The Nuclear Spectroscopic Telescope Array (*NuSTAR*) mission, launched under the NASA Small Explorer satellite program (SMEX-11) on June 13, 2012, marks a significant breakthrough as the first focusing high-energy X-ray telescope in orbit. *NuSTAR* operates in the 3 to 79 keV energy band, with excellent sensitive observations far beyond $\sim$ 10 keV. *NuSTAR* utilizes a new generation of hard X-ray optics and solid-state detector technologies, allowing it to probe the hard X-ray sky with a 100-fold improvement in sensitivity compared to collimated or coded mask instruments that have been previously employed in this energy range. *NuSTAR* features an unprecedented temporal resolution of 2 microseconds and an angular resolution of $\sim$ 18 arcminutes (FWHM). The observatory comprises of two co-aligned, independent telescopes: FPMA and FPMB (Focal Plane Modules A and B), facilitating parallel observations. Each set of co-aligned focal plane detectors consists of four Cadmium-Zinc-Telluride (CZT) detectors shielded by Cesium-Iodide (CsI) crystals. These detectors employ a conical approximation to the Wolter-I design and are coated with a multi-layer structure. A comprehensive explanation of the optics/electronics can be found in (Harrison et al., 2013). Figure 2.6 shows a comparison of the effective collecting area of *NuSTAR* with other focusing telescopes. *NuSTAR* not only offers excellent overlap with soft X-ray observatories but also extends its focusing capabilities up to 79 keV.

Archival data from *NuSTAR* are available through NASA's HEASARC interface. The NuSTARDAS package, accessible within HEASOFT, generates cleaned and calibrated event files. NuSTARDAS includes the data analysis tools *nupipeline* and *nuproduct*. The *nupipeline* tool is employed to generate cleaned event files, ancillary response files (ARFs), and response matrice files (RMFs) from the telemetry data. A circular region (with a radius of about 30 arcseconds), centered around the source, is utilized to extract the source spectrum. The background is estimated from a circular region with a larger radius (about 50 arcseconds), devoid of source contamination. With these selections of source and background regions, the *nuproduct* tool is used to produce the spectrum for each observation.

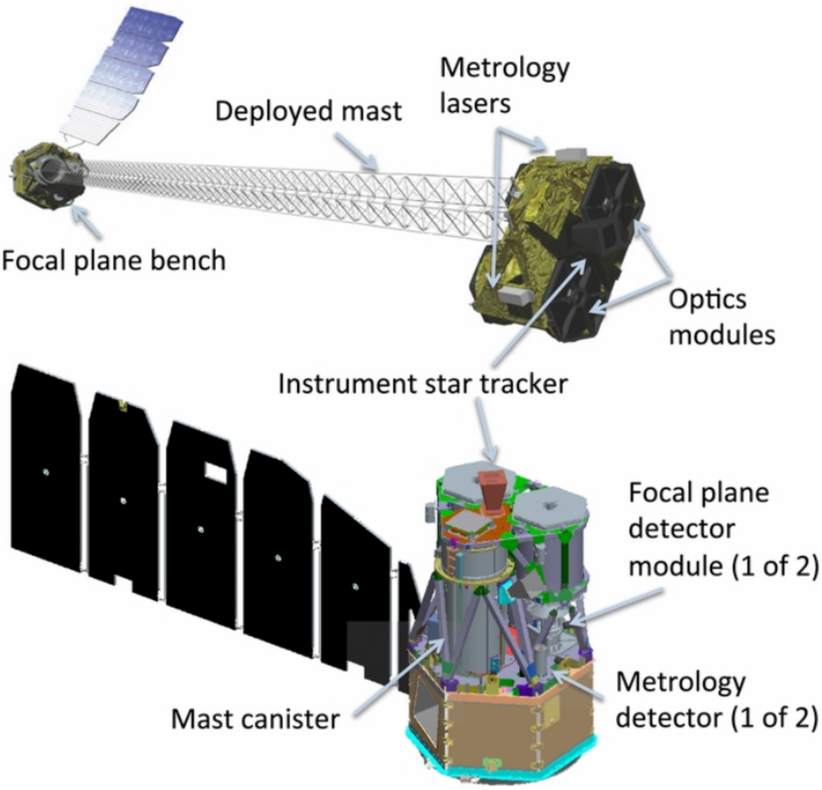

Figure 2.5: Schematic diagram of the *NuSTAR* telescope (Harrison et al., 2013).

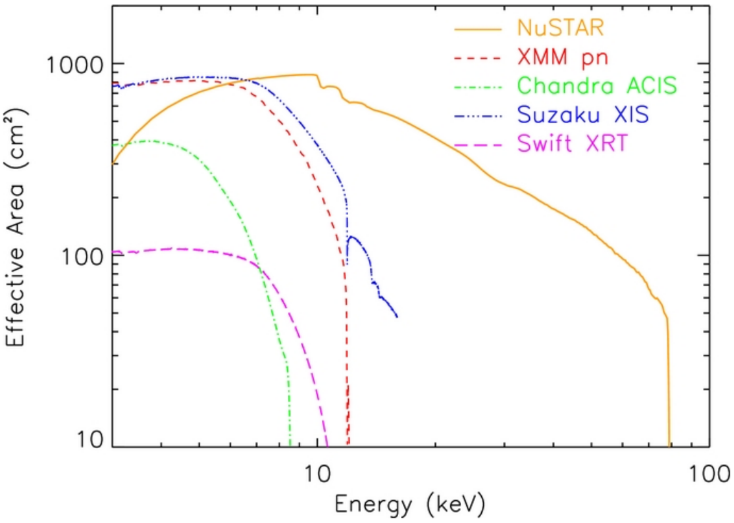

Figure 2.6: The plot compares the effective collecting area of *NuSTAR* with other focusing telescopes (Harrison et al., 2013).

2.3 *Fermi*

The *Fermi* Gamma-ray Space Telescope was launched into a lower Earth orbit on June 11, 2008, and was previously known as the Gamma Ray Large Area Telescope (GLAST). It orbits Earth at an altitude of approximately 550 km, completing one orbit in about 96 minutes. *Fermi* comprises of two scientific payloads: the GLAST Burst Monitor (GBM) and the Large Area Telescope (LAT). LAT serves as the principal scientific instrument, operating in the energy range of MeV to GeV, while GBM, operating in the 8 keV to 40 MeV energy range, serves as the secondary instrument. The main purpose of GBM is to identify sudden gamma-ray flares generated by Gamma Ray Bursts (GRBs) and solar flares.

2.3.1 Large Area Telescope (LAT)

The LAT, which covers the energy range from $\sim$ 20 MeV to 300 GeV (Atwood et al., 2009), is designed to measure the energy, time of arrival, and direction of incoming gamma-ray photons. It has a wide field of view of 2.4 sr, allowing it to survey 20% of the sky at all times, and it can complete a full scan of the entire sky every 3 hours. It features an effective area exceeding $> 8000\,\mathrm{cm}^2$ and a point source sensitivity $< 6 \times 10^{-9}\,\mathrm{phs\,cm^{-2}\,s^{-1}}$ at energies above 100 MeV. LAT is basically an electron-positron pair conversion gamma-ray detector, and the schematic diagram of the instrument is shown in Figure 2.7. LAT is shielded by the anti-coincidence detector (ACD) to effectively filter out background cosmic rays. The γ-ray photons pass through the ACD, undergo pair production, and generate electron-positron pairs as a result of interaction with the thin tungsten foils inside the detector. The trackers are employed to determine the direction of electron-positron pairs and, consequently, the direction of incident gamma-ray photons, while the calorimeter measures the energy of the incident gamma-ray photons.

We can access the *Fermi*-LAT archival data from the Fermi Science Tools (FST) webpage. LAT data becomes publicly accessible $\sim$ 12 hours after its observation. Details of the LAT data analysis procedure are available on the

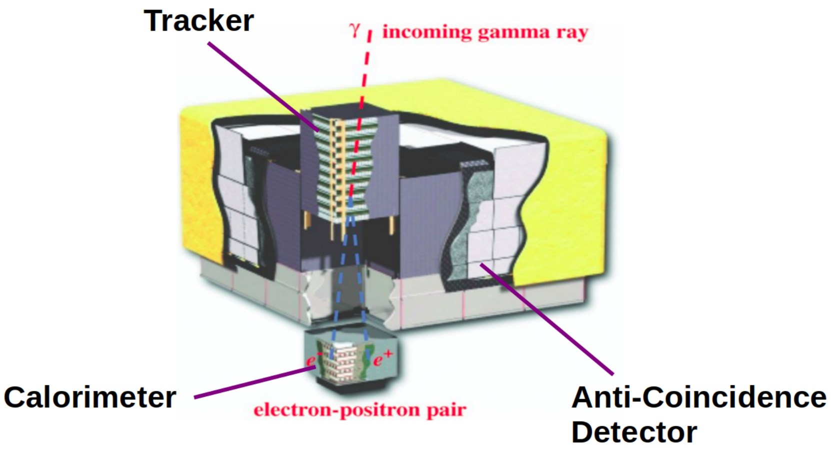

Figure 2.7: Schematic diagram of *Fermi*-LAT (Atwood et al., 2009).

FST webpage. The standard software tools for the analysis are based on the maximum likelihood optimization method (e.g., Mattox et al., 1996). For analyzing *Fermi*-LAT data, both "unbinned" and "binned" likelihood analyses are available. The binned likelihood analysis is favored when the source is very bright or observed for long duration, while the unbinned method is recommended for faint sources or for short duration observations. Both methods are executed through a set of tasks that are compatible with Python and are available in the LAT Science Tools software package `https://fermi.gsfc.nasa.gov./ssc/data/analysis/scitools/`.

When performing LAT data analysis with the unbinned likelihood method, it is preferable to specify a region of interest (ROI) with a radius of around 10 degrees, centered on the source of interest; for binned likelihood analysis, a larger ROI (15 degrees) is recommended. While modeling, sources from a region larger than the ROI can be included, and this area is referred to as the "Source Region" (ROI+5 degree).

The tool *gtselect* is used for the selection of photon events based on various criteria such as the source's position (R.A. and Dec), observation time (start time and stop time of the observation in MET (mission elapsed time)), energy bins (minimum and maximum event energy in MeV), zenith angle, etc. The data are filtered by applying a 90-degree zenith angle cut to eliminate strong background gamma-rays. Photons arriving at zenith angles greater than 90 degrees are barred to minimize Earth's limb gamma-ray contamination. The spacecraft files are used to compute good time intervals (GTIs) with the tool *gtmktime*. The *gtltcube* tool is used to calculate the livetime (which refers to the time during which the LAT observes a specific position on the sky at a particular inclination angle) of the ROI, while the *gtexpmap* tool is employed for generating the exposure map. The *gtdiffrsp* tool calculates the responses for diffuse sources. In the last stage of LAT data analysis, likelihood fitting is performed using the *gtlike* tool to determine the best-fit model parameters from the input model and observed data. The input model includes spectral parameters and source positions within the "Source Region". The significance of the gamma-ray event is determined using the maximum likelihood test statistic (TS), defined as $\mathrm{TS} = 2\ \Delta\ \log(\mathrm{L})$, where L is the likelihood function comparing models with and without a point source at the source of interest. During likelihood fitting, spectral parameters for all sources within the ROI are allowed to vary, while for sources outside the ROI but within the "Source Region", parameters are fixed to catalog values. Typically, sources with $\mathrm{TS} < 9$ (approximately 3σ) are excluded, followed by a maximum likelihood analysis with the remaining sources.

All the X-ray and Optical/UV data used in this thesis are publicly available from the HEASARC archive at `https://heasarc.gsfc.nasa.gov/` and gamma-ray data from `https://Fermi.gsfc.nasa.gov/`. In the next chapter, we conduct a dedicated X-ray spectral study of blazar Mkn 421, around the synchrotron SED peak.

Chapter 3

Do radiative losses determine the characteristic emission of blazar Mkn 421?

3.1 Introduction

The non-thermal emission observed from blazars is believed to originate from the radiative cooling of relativistic particle distributions within highly Doppler-boosted jets. The BL Lac object Mkn 421 is one of the nearest ($z = 0.031$) and extensively studied blazars with a non-thermal spectrum extending from radio to very high energy gamma-rays (Acciari et al., 2009; Abdo et al., 2011; Aleksić et al., 2012; Baloković et al., 2016; Bartoli et al., 2016). The source exhibits rapid flux and spectral variability, suggesting the emission to originate from a relativistic moving jet aligned close to the line of sight (Dondi & Ghisellini, 1995). Its broadband spectral energy distribution is characterized by two broad peaks, where the low-energy component is interpreted as synchrotron emission from a relativistic electron population (Celotti & Ghisellini, 2008) while the high-energy component is usually attributed to inverse Compton scattering of the synchrotron photons by the same electron population (e.g., Aleksić et al., 2012; Abdo et al., 2011; Acciari et al., 2011).

In general, different types of non-thermal electron distributions, mostly involving a power-law regime (e.g., broken power-law and power-law with exponential cut-off), have been used to account for the broadband SED of blazars (e.g., Sinha et al., 2017; Kataoka & Stawarz, 2016; Yan et al., 2013; Tramacere et al., 2007b; Krawczynski et al., 2004). On the other hand, since the narrow band X-ray spectrum can deviate significantly from a simple power-law, the photon number distribution is often represented by a log-parabolic function

$$F(\epsilon) \propto \left(\frac{\epsilon}{\epsilon_0}\right)^{-\alpha-\beta \log(\frac{\epsilon}{\epsilon_0})} \quad , \tag{3.1}$$

where ϵ is the photon energy, α is the spectral slope at energy ϵ_0 and β is the curvature parameter (Massaro et al., 2004; Tramacere et al., 2007b). In case of Mkn 421, the peak energy ϵ_p of the synchrotron SED component falls into the soft X-ray regime and the hard X-ray energy band probes the decline of the synchrotron spectral component. The spectrum at these energy regimes individually can be reproduced by a log-parabolic function, though this approach is not very successful in explaining the combined optical/UV and X-ray spectra (Massaro et al., 2004; Tramacere et al., 2009; Sinha et al., 2015)

The characteristic peak photon energy (ϵ_p) of Mkn 421, at which the synchrotron spectral component carries maximum power, can vary significantly depending on the state of the source. For instance, using *Swift*-XRT observations Kapanadze et al. (2020) showed that ϵ_p varies from less than 0.1 keV to greater than 15 keV during different flux states. Such large variation in ϵ_p for Mkn 421 is also reported by various authors using *RXTE*, *BeppoSAX*, *XMM-Newton* observations (e.g., Massaro et al., 2004; Tramacere et al., 2007a). The spectral shape around ϵ_p is usually well represented by a log-parabola function. Correlation studies between the fit parameters on the other hand, are often contradictory or inconclusive. For example, ϵ_p and β obtained through a log-parabolic spectral fit of *BeppoSAX*, *RXTE*, *XMM-Newton* and *Swift*-XRT observations of Mkn 421 during 1997–2006 were found to be anti-correlated (Tramacere et al., 2007a; Massaro et al., 2008; Tramacere et al., 2009, 2011). However, no significant correlation between these quantities was witnessed in case of *Swift*-XRT observation during 2005–2008 (Kapanadze et al., 2018b), 2009–2012 (Kapanadze et al., 2018a), 2015–2018 (Kapanadze et al., 2020), and also in combination with *NuSTAR* observations during April 2013 (Sinha et al., 2015). Similarly, Massaro et al. (2004) have reported a strong positive correlation between the spectral index at 1 keV and the curvature parameter using *BeppoSAX* observations (0.1−100 keV) of Mkn 421 during May 1999 and April−May 2000. However, *Swift*-XRT observations and combined *Swift*-XRT/*NuSTAR* spectra did not show an appreciable correlation (Sinha et al., 2015; Kapanadze et al., 2017; Kapanadze et al., 2018b). In spite of this seemingly contradictory results, in many observations the enhancement in flux is associated with a spectral hardening commonly referred to as *harder when brighter* trend (Kapanadze et al., 2016; Kapanadze et al., 2017; Kapanadze et al., 2018b,a; Kapanadze et al., 2020).

The power-law/log-parabolic photon spectra demand the emitting electron distribution to be also power-law/log-parabola type (Kardashev, 1962; Massaro et al., 2004; Tramacere et al., 2009). It is also established that a power-law electron distribution can be readily achieved under Fermi acceleration (e.g., Rieger et al., 2007), while a log-parabolic electron distribution may indicate an energy-dependence in the particle acceleration and/or diffusion process (Massaro et al., 2004; Jagan et al., 2018; Goswami et al., 2018; Goswami et al., 2020). In particular, when the electron escape time-scale from the main particle acceleration site becomes mildly energy-dependent (referred to as 'energy dependent diffusion model', hereafter EDD), the resultant electron distribution has been shown to follow a log-parabola function (Jagan et al., 2018). On the other hand, when the energy-dependence is strong, the shape deviates from a log-parabola. The latter case is witnessed in the hard X-ray spectra of Mkn 421 (Goswami et al., 2018; Goswami et al., 2020) observed by *NuSTAR*. The spectra corresponding to different flux states can be well fitted by synchrotron emission originating from an electron distribution obtained in an EDD model with a strong energy-dependent escape time-scale. Incidentally, the hard X-ray spectra can also be explained by a log-parabolic electron distribution and hence, a single spectrum fitted separately with these two models does not allow one to differentiate between the models. However, the fit parameters of the EDD model (spectral curvature (which is associated with the electron diffusion time-scale) and the spectral index at a given energy) corresponding to the different flux states indicate a strong positive correlation, while this is not the case with a log-parabolic electron distribution.

The peak energy ϵ_p of the photon spectrum can be translated to a break or peak energy, $E_b = \gamma_b m_e c^2$, of the emitting electron energy distribution[1] under synchrotron theory. The system deposits most of its power to the electrons at this energy, and hence identifying the process that determines γ_b (or ϵ_p) is important to understand the dynamics of the source. Radiative cooling (synchrotron and/or inverse Compton) of a power-law electron distribution can give rise to a broken power law electron distribution with power-law indices differing by unity (Kardashev, 1962). Correspondingly, the photon spectrum will also be a broken power-law with a difference of 0.5 between high and low energy spectral indices (Rybicki & Lightman, 1986). However, SED modeling of blazars often does not support this inference and the index difference is frequently found to be significantly larger than 0.5 (e.g., Mankuzhiyil et al., 2012). On the other hand, radiative cooling of a log-parabolic electron distribution can transform the distribution into a broken log-parabolic form. This could probably explain the large differences between spectral indices (Jagan et al., 2018). Under this interpretation, the increase or decrease in the spectral slope at low energies ($< \epsilon_p$) will be associated with a similar spectral slope change at high energies ($> \epsilon_p$). In principle, the assumption of multiple acceleration processes is also capable of producing broken power-law electron distributions (e.g., Sahayanathan, 2008). The low and high energy indices would then be governed by the associated acceleration rates.

In this chapter, we examine the radiative loss origin of ϵ_p in the high energy peaked blazar Mkn 421. For this, we use long term observations of the source by *Swift*-XRT spanning from January 2008 to December 2019. The spectral resolution of *Swift*-XRT is appreciable within the energy range 0.3 to 10.0 keV, encompassing a broad range of ϵ_p, and hence, represents a suitable experiment to perform this study. The X-ray spectrum is well represented by a

---

[1] The electron energy distribution is represented by $E^2 N(E)$, where $N(E)$ is the specific electron number density. Most of the electron energy resides at E_b when the broken power law indices before and after E_b are greater than -2 and less than -2, respectively.

log-parabola function which allows one to constrain ϵ_p. The spectral indices before and after ϵ_p are obtained by refitting the spectrum with a smooth broken power-law. We then study the correlation between these quantities to explore the possible origin of ϵ_p.

3.2 Observation and Data analysis

We analysed the *Swift*-XRT (Burrows et al., 2005) observations of Mkn 421 during 2008–2019. The data were retrieved from NASA's HEASARC interface and processed using XRTDAS software package (Version 3.0.0) included within HEASOFT package (Version 6.22.1). We used only those observations which were performed in Windowed Timing (WT) mode and selected events with 0–2 grades. Standard procedures employing *xrtpipeline* (Version 0.13.4) were used for calibration and data cleaning.

A circular region of radius about 20–30 pixels centred at the source was used to extract the source spectrum, while another circular region of about 30–40 pixel radius, free from the source contamination, was used to extract the background spectrum. For observations with pileup, the source spectra were extracted by excluding the central circular aperture of 2–3 pixel radius. The final spectrum was produced using *xrtproducts* (Version 0.4.2). The ancillary response files (ARFs) were generated using the *xrtmkarf* task and the response matrices files (RMF) were used from the *Swift* CALDB. To ensure better χ^2 statistics, the spectra were grouped to 20 photons per bin using the tool *grppha* (Version 3.0.1). We rejected some observations that were strongly biased due to the dead columns on the CCD.

3.3 X–ray spectral fit

The X-ray spectra in the $0.3 - 10.0$ keV energy band encompass or are close to ϵ_p, and hence are significantly curved. The reduced data is analysed with the XSPEC package (Arnaud, 1996) using a log-parabolic function while fixing the hydrogen column density to the Galactic value $N_H = 1.92 \times 10^{20}\mathrm{cm}^{-2}$ (Kalberla et al., 2005) for all the observations. Since our aim is to understand the origin of ϵ_p, we used the *eplogpar* model (Tramacere et al., 2009) to perform the spectral fit. The log-parabolic function under this model is expressed in terms of ϵ_p as

$$F(\epsilon) \propto \frac{10^{-\beta\left(\log(\frac{\epsilon}{\epsilon_p})\right)^2}}{\epsilon^2}. \tag{3.2}$$

We excluded observations having reduced chi-square, $\chi^2_{\mathrm{red}} > 1.2$. However, for some observations IDs (observation with high exposure time and significant variation in the count rate) we have extracted spectra from individual orbits (O1, O2, ..) to obtain a better fit. Certain observations corresponding to a single orbit were also divided segment-wise (S1, S2, ..) to improve the χ^2_{red}. The details of the observation are shown in Table 3.1. For many observations, the obtained ϵ_p lied outside the $0.3 - 10.0$ keV range. These estimates are not reliable, since they fall outside the spectral energy range of *Swift*-XRT and are thus excluded. This leaves 258 spectra with ϵ_p between 0.4 to 7.0 keV for the present study. The X-ray spectra in this energy region can be well fitted by a log-parabola, which is consistent with the literature (Massaro et al., 2004; Tramacere et al., 2007a; Kapanadze et al., 2016; Kapanadze et al., 2017). In Table 3.1 (column 4−5), we provide the fit results and in Figure 3.1 (upper panel) we show the scatter plot between ϵ_p and β. The Spearman rank correlation study between ϵ_p and β yields correlation coefficient, $r_s = -0.28$ with a null hypothesis probability (p_s) of 1.35×10^{-05}. This result is consistent with earlier studies where a weak or no correlation was observed (Kapanadze et al., 2018b,a; Sinha et al., 2015).

The radiative loss interpretation of ϵ_p predicts the spectral slopes at energies $\epsilon \ll \epsilon_p$ and $\epsilon \gg \epsilon_p$ to be positively correlated. To examine this, we fitted the spectra with a smooth broken power-law (*sbpl*) function defined by

$$F(\epsilon) \propto \left[\left(\frac{\epsilon}{\epsilon_{\mathrm{b}}}\right)^{\Gamma_{\mathrm{low}}} + \left(\frac{\epsilon}{\epsilon_{\mathrm{b}}}\right)^{\Gamma_{\mathrm{high}}}\right]^{-1}, \tag{3.3}$$

where $\Gamma_{\rm low}$ and $\Gamma_{\rm high}$ are the indices before and after the break energy ϵ_b. The peak of the smooth broken power-law function in $\epsilon^2\, F(\epsilon)$ representation is

$$\epsilon_{\rm p,sbpl} = \epsilon_{\rm b} \left(\frac{\Gamma_{\rm high} - 2}{2 - \Gamma_{\rm low}} \right)^{\frac{1}{\Gamma_{\rm low} - \Gamma_{\rm high}}} . \tag{3.4}$$

For typical values of $\Gamma_{\rm high}$ (~ 2.5) and $\Gamma_{\rm low}$ (~ 1.5), $\epsilon_{\rm b} \approx \epsilon_{\rm p,sbpl}$. The function (3.3) was added as a local model (*sbpl*) in XSPEC and the $0.3 - 10.0$ keV *Swift*-XRT observations of Mkn 421 were refitted. However, the narrow-band X-ray spectra do not allow us to sufficiently constrain all parameters of the model. Hence, we performed a fitting with ϵ_b fixed to the value ϵ_p obtained from the *eplogpar* spectral fit. A subsequent inspection shows that $\epsilon_{p,sbpl}$ estimated from equation (3.4) using the so obtained best fit $\Gamma_{\rm low}$ and $\Gamma_{\rm high}$ does not differ much from ϵ_p (Figure 3.2), suggesting that our choice of ϵ_b does not strongly affect the outcome. We consider only those *Swift*-XRT observations with 0.4 keV $< \epsilon_p <$ 7.0 keV since estimation of $\Gamma_{\rm low}$ and $\Gamma_{\rm high}$ demands ϵ_p to be within the spectral energy range of *Swift*-XRT. The resultant best fit values for $\Gamma_{\rm low}$ and $\Gamma_{\rm high}$ are given in Table 3.1 (column 7−8), while the scatter plot between these quantities is shown in Figure 3.3. The correlation study between these quantities yields a linear correlation coefficient $r = -0.95$ with significance, $s > 99.99$ per cent (Press et al., 1992). This strong anti-correlation between $\Gamma_{\rm low}$ and $\Gamma_{\rm high}$ poses a serious challenge to a simple radiative cooling interpretation of ϵ_p. A linear fit to $\Gamma_{\rm low}$ and $\Gamma_{\rm high}$ results in

$$\Gamma_{\rm high} = (-0.89 \pm 0.05)\Gamma_{\rm low} + (3.83 \pm 0.08) \tag{3.5}$$

with a goodness of fit (q-value) of 0.99. The inability of the simple radiative loss interpretation to successfully account for the origin of ϵ_p can be visualized further by studying the correlation between $\Gamma_{\rm low}$ or $\Gamma_{\rm high}$ with the curvature parameter β obtained from *eplogpar* model. In Figure 3.4 (bottom panel), we show the scatter plot between these quantities. The strong linear correlation of $\Gamma_{\rm high}$ with β ($r = 0.96$, $s > 99.99$ per cent) and anti-correlation of $\Gamma_{\rm low}$ with β ($r = -0.92$, $s > 99.99$ per cent) are consistent with the anti-correlation observed between $\Gamma_{\rm low}$ and $\Gamma_{\rm high}$. A softening of the high energy index is associated with a hardening of the low energy index. Correspondingly, high curvature β will be associated with hard Γ_{low} and steep Γ_{high} (narrowing of the synchrotron spectral component).

We did not find any appreciable correlation between Γ_{low} or Γ_{high} with the $0.3 - 10.0$ keV integrated flux ($F_{0.3-10.0\,\text{keV}}$, middle panel of Figure 3.4). This indicates that the narrowing of the synchrotron component of the SED of Mkn 421 is not associated with flux state. This is also consistent with the weak correlation observed between β and $F_{0.3-10.0\,\text{keV}}$ (lower panel of Figure 3.1). Similarly, no significant correlation is witnessed between ϵ_p and Γ_{low} or Γ_{high} (top panel of Figure 3.4). Hence, the narrowing of the SED cannot be attributed to *bluer when brighter* trend of Mkn 421.

Table 3.1: Best fit parameters of spectral fitting using *eplogpar* model and *sbpl* model

ObsID	Date of Obs.	Exposure	*eplogpar*			*sbpl*			$\mathrm{Flux}_{0.3-10.0\,\mathrm{kev}}$
		(sec)	ϵ_p (keV)	β	χ^2_{red} (dof)	Γ_{low}	Γ_{high}	χ^2_{red} (dof)	$(10^{-10}\mathrm{erg\,cm^{-2}s^{-1}})$
(1)	(2)	(3)	(4)	(5)	(6)	(7)	(8)	(9)	(10)
30352053-O2	2008-01-16	575.100	$0.42^{+0.07}_{-0.08}$	0.28±0.05	1.04 (305)	1.36±0.12	2.54±0.02	1.06 (305)	20.00±0.28
30352054	2008-01-16	1134.085	$0.42^{+0.04}_{-0.05}$	0.30±0.03	1.08 (394)	1.33±0.10	2.57±0.01	1.12 (394)	15.26±0.15
30352056	2008-01-17	944.126	$0.43^{+0.05}_{-0.07}$	0.34±0.04	0.95 (322)	1.29±0.12	2.61±0.02	1.00 (322)	13.54±0.17
30352055-O1	2008-01-17	394.900	$0.64^{+0.07}_{-0.08}$	0.45±0.08	1.11 (227)	1.29±0.12	2.69±0.04	1.12 (227)	10.00±0.21
30352055-O2	2008-01-17	362.600	$0.60^{+0.05}_{-0.04}$	0.49±0.06	1.09 (260)	1.22±0.10	2.73±0.03	1.12 (260)	15.04±0.26
30352058	2008-01-18	889.108	$0.57^{+0.04}_{-0.04}$	0.33±0.04	1.07 (378)	1.38±0.07	2.59±0.02	1.10 (378)	14.88±0.16
30352059	2008-01-19	919.112	$0.43^{+0.04}_{-0.04}$	0.34±0.04	1.04 (359)	1.22±0.12	2.62±0.01	1.06 (359)	13.73±0.15
30352060	2008-02-06	753.060	$0.60^{+0.05}_{-0.06}$	0.26±0.03	1.13 (429)	1.48±0.06	2.51±0.02	1.15 (429)	24.33±0.24
30352066	2008-02-10	1174.100	$0.74^{+0.03}_{-0.03}$	0.30±0.03	1.17 (467)	1.46±0.04	2.55±0.02	1.18 (467)	20.85±0.18
30352068	2008-02-11	1868.208	$0.46^{+0.03}_{-0.05}$	0.25±0.02	1.10 (495)	1.44±0.06	2.52±0.01	1.14 (495)	18.61±0.14
30352069	2008-02-11	949.085	$0.48^{+0.04}_{-0.06}$	0.28±0.03	0.96 (422)	1.4±0.08	2.54±0.01	0.98 (422)	18.53±0.18
30352071-S1	2008-02-12	699.700	$0.50^{+0.08}_{-0.07}$	0.24±0.04	1.14 (381)	1.49±0.09	2.49±0.02	1.17 (381)	18.90±0.22
30352071-S2	2008-02-12	763.700	$0.50^{+0.08}_{-0.07}$	0.23±0.03	1.10 (394)	1.49±0.08	2.48±0.02	1.12 (394)	19.17±0.21
30352072	2008-02-13	979.112	$0.41^{+0.06}_{-0.07}$	0.23±0.03	1.05 (412)	1.45±0.10	2.49±0.01	1.07 (412)	18.91±0.20
30352073	2008-02-13	629.107	$0.54^{+0.07}_{-0.09}$	0.25±0.04	0.98 (352)	1.47±0.09	2.51±0.02	1.00 (352)	19.13±0.25
30352074-O1	2008-02-14	790.900	$0.63^{+0.08}_{-0.11}$	0.20±0.04	1.05 (378)	1.56±0.08	2.44±0.03	1.06 (378)	22.21±0.28
30352074-O2	2008-02-14	422.700	$0.74^{+0.11}_{-0.14}$	0.24±0.06	0.93 (273)	1.51±0.10	2.49±0.04	0.93 (273)	22.38±0.45
30352075	2008-02-14	1529.124	$0.66^{+0.05}_{-0.06}$	0.23±0.03	1.10 (489)	1.53±0.05	2.47±0.02	1.11 (489)	18.30±0.15
30352077	2008-02-15	1589.125	$0.72^{+0.07}_{-0.09}$	0.24±0.04	0.93 (375)	1.51±0.07	2.48±0.03	0.93 (375)	17.03±0.21

(Table is available in its entirety in Appendix A, Table A.1).

3.4 Discussion and Summary

The observed anti-correlation between $\Gamma_{\rm low}$ and $\Gamma_{\rm high}$ is inconsistent with a simple radiative loss interpretation of ϵ_p. To examine alternate explanations, we consider the case where the synchrotron spectral component is governed by a power-law with an exponential cut-off. Such a spectral shape could be possible when the underlying particle distribution has a sharp cut-off at the maximum achievable electron energy. The high-energy end of the synchrotron spectrum will then be governed by the exponential decay of the synchrotron single particle emissivity function. To mimic this, we assume a synchrotron spectral shape as

$$F(\epsilon) \propto \epsilon^{-\psi} {\rm exp}\left(-\frac{\epsilon}{\epsilon_c}\right) . \tag{3.6}$$

The SED peak in $\epsilon^2\, F(\epsilon)$ representation will be

$$\epsilon_{p,{\rm exp}} = (2-\psi)\epsilon_c \, , \tag{3.7}$$

so that the spectral slope of the photon distribution around $\epsilon_{p,{\rm exp}}$ can be expressed as

$$\Gamma_{\rm exp}(\epsilon) = \psi + \frac{\epsilon}{\epsilon_{p,{\rm exp}}}\,(2-\psi) \ . \tag{3.8}$$

In this case, the spectral slopes at energies $\epsilon < \epsilon_{p,{\rm exp}}$ and $\epsilon > \epsilon_{p,{\rm exp}}$ will be anti-correlated. If we set $\epsilon_{p,{\rm exp}} = 1.14$ keV corresponding to the average value of ϵ_p estimated from all the observations, the dependence of $\Gamma_{\rm exp}(0.3\,{\rm keV}) = \Gamma_{\rm low}$ and $\Gamma_{\rm exp}(10.0\,{\rm keV}) = \Gamma_{\rm high}$ can be studied for different values of ψ. In Figure 3.3, we show this dependence as red solid line and the red shaded region represents its 1-σ deviation. Though this interpretation supports the anti-correlation between the indices, it deviates largely from the best fit line obtained from the observed $\Gamma_{\rm low}$ and $\Gamma_{\rm high}$ (using *sbpl*).

Another possible explanation for ϵ_p could be, when the underlying particle distribution exhibits a gradual decline at the maximum electron energy rather

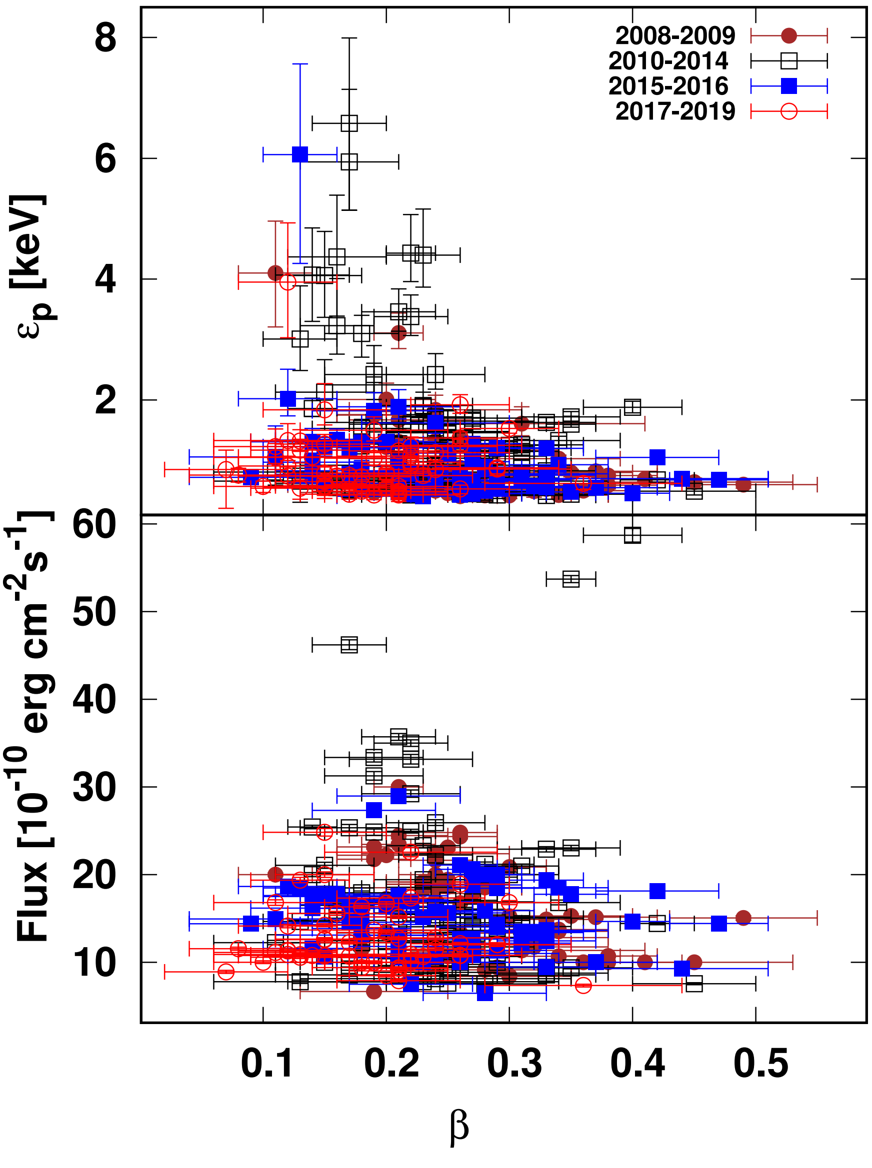

Figure 3.1: The scatter plot between β and ϵ_p obtained from *eplogpar* (top panel) and between β and the integrated 0.3–10.0 keV flux (lower panel) for different epochs.

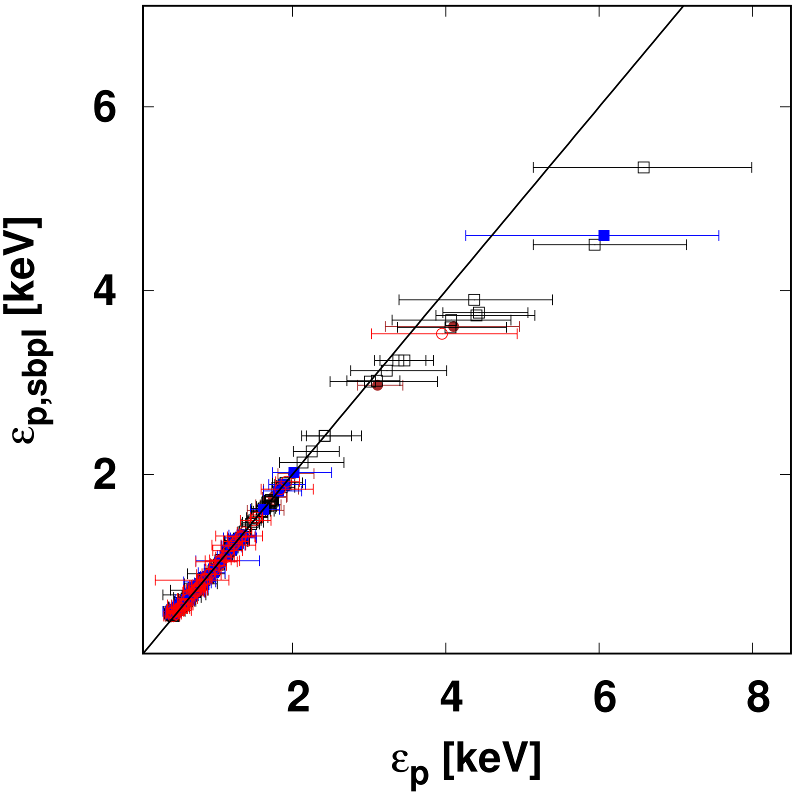

Figure 3.2: The scatter plot between ϵ_p and $\epsilon_{p,sbpl}$ along with the identity line (see text). The symbols are as shown in Figure 3.1.

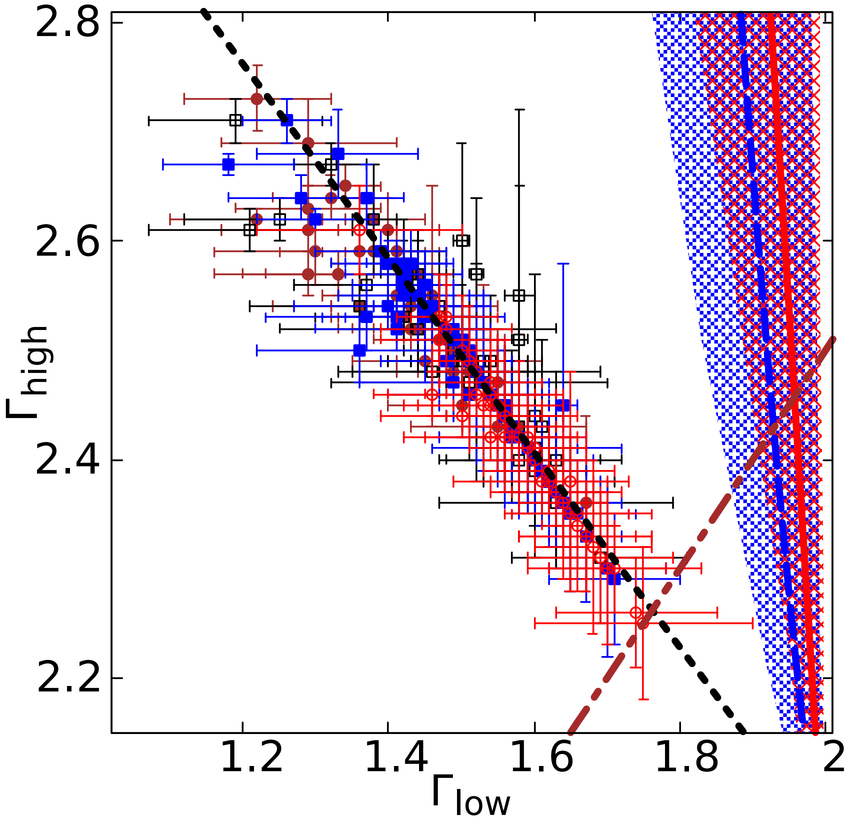

Figure 3.3: The scatter plot between $\Gamma_{\rm low}$ and $\Gamma_{\rm high}$: black dotted line represents the best fit line showing variation between $\Gamma_{\rm low}$ and $\Gamma_{\rm high}$. The red solid line corresponds to the synchrotron spectrum of an electron distribution following power-law with an exponential cut-off for $1.75 < \psi < 2.0$, and the red shaded region represents its 1-σ deviation. The blue dashed line correspond to the synchrotron spectrum of the electron distribution with a gradual decline at the maximum electron energy by varying ϕ between 1.3 and 2.0, and the blue shaded region represents its 1-σ deviation. The brown dotted dash line represents the cooling break. The symbols are as shown in Figure 3.1.

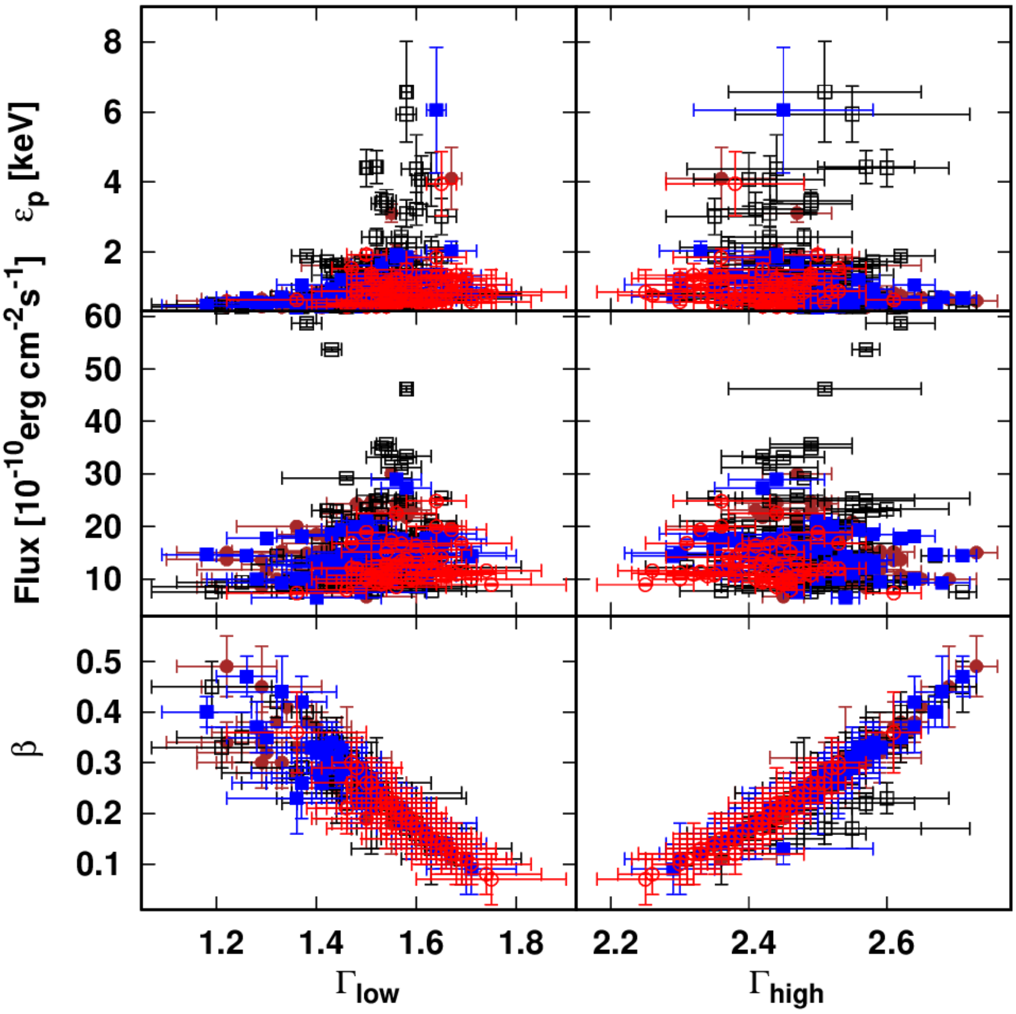

Figure 3.4: Left panel: scatter plot between $\Gamma_{\rm low}$ and curvature parameter β, 0.3–10.0 keV flux and ϵ_p; Right panel: scatter plot between $\Gamma_{\rm high}$ and curvature parameter β, 0.3–10.0 keV flux and ϵ_p. The symbols are as shown in Figure 3.1.

than a sharp cut-off, that dominates the spectral shape around ϵ_p. To examine this possibility, we use the electron distribution accelerated at a shock front assuming constant acceleration time-scale and escape time-scale (Kirk et al., 1998)

$$N(\gamma) \propto \gamma^{-(1+\phi)} \left(1 - \frac{\gamma}{\gamma_{\max}}\right)^{\phi-1} , \tag{3.9}$$

where γ is the Lorentz factor of the electron, $\gamma_{\max}$ is the Lorentz factor corresponding to the maximum electron energy, and ϕ is the ratio of the acceleration time-scale to escape time-scale. The observed synchrotron spectrum will then be (Rybicki & Lightman, 1986)

$$F(\epsilon) \propto \frac{1}{4\pi} \int\limits_{\gamma_{\min}}^{\gamma_{\max}} P_{\rm syn}(\gamma, \epsilon^*)\, N(\gamma)\, d\gamma\,, \tag{3.10}$$

where $P_{\rm syn}$ is the synchrotron single particle emissivity and ϵ^* is the photon energy in the comoving frame of the emitting region carried by the blazar jet (e.g., Begelman et al., 1984). The integration in equation (3.10) is performed numerically using Gaussian quadrature, and we study the spectral shape around the peak. Again setting ϵ_p at 1.14 keV, the spectral index at 0.3 keV and 10 keV can be studied for different values of ϕ. In Figure 3.3, we show the plot between these indices as blue solid line and the blue shaded region represents the 1-σ deviation of the line. This interpretation for ϵ_p also supports an anti-correlation between $\Gamma_{\rm low}$ and $\Gamma_{\rm high}$; however, it still deviates significantly from the best fit line.

An alternative scenario which could be capable of reproducing the best fit straight line besides explaining the observed anti-correlation between $\Gamma_{\rm low}$ and $\Gamma_{\rm high}$ is when the synchrotron spectral component is a superposition of multiple broken power-law components. This would implicitly assume that the emission region is not reducible to a single homogeneous zone. The dominant broken power-law component then determines ϵ_p and with proper choice of break energy and/or the normalisation one could possibly reproduce the observed best fit straight line. However, unless some fine tuning occurs, one would also expect ϵ_p or the flux to be correlated with Γ_{low} or Γ_{high}. The apparent absence of such correlations (top and middle panels of Figure 3.4) would again seem to disfavour simple variants of such a scenario.

As shown above, the curvature in the electron distribution introduced by the simplistic assumptions of constant acceleration time-scale and escape time-scale is unable to account for the observed properties. Probably, relaxing these assumptions, by including more complex energy-dependent acceleration time-scale and escape time-scale, could modify the correlation and reduce the deviation.

Multiple particle acceleration scenarios (e.g., shock acceleration and stochastic acceleration) are also capable, in principle, of producing electron distributions that could imitate a broken power-law (e.g., Sahayanathan, 2008). In this case, the indices are governed by the ratio of acceleration time-scale to escape time-scale of the associated acceleration processes. The dominant acceleration processes in the blazar jet are assumed to be shock- and stochastic-type. Since the rate of acceleration by both these processes depends on the nature of particle diffusion into the jet medium, the corresponding particle power-law indices may be correlated. However, the exact nature of this correlation and comparison with observations would demand a detailed study/simulation of AGN jets considering these acceleration processes.

An important uncertainty in the present work is related to the choice of ϵ_b used in spectral fitting with the *sbpl* model. Since this parameter was frozen to ϵ_p obtained from the log parabola spectral fit, this could introduce an additional bias which may be reflected in the parameters Γ_{high} and Γ_{low}. In order to explore this, we performed a combined spectral fit using simultaneous/near-simultaneous *NuSTAR* observations of the source. The *NuSTAR* data were downloaded from the online data archive[2] and standard data reducing techniques were employed using the latest software provided[3]. The spectral fit is then performed using *sbpl* model on simultaneous/near-simultaneous *Swift*-XRT (0.3–10.0 keV) and *NuSTAR* (3.0 to 30.0 keV) X-ray spectra with all

---

[2] `https://heasarc.gsfc.nasa.gov/`

[3] `https://heasarc.gsfc.nasa.gov/docs/nustar/analysis/`

Table 3.2: Best fit parameters of combined (*Swift*-XRT and *NuSTAR*) spectral fitting using *sbpl* model

Swift-XRT ObsID	*Nu*STAR ObsID	$\epsilon_{p,sbpl}$	$\Gamma_{\rm low}$	$\Gamma_{\rm high}$	χ^2_{red} (dof)
80050019-O1	60002023027	$2.08^{+0.07}_{-0.07}$	$1.58^{+0.03}_{-0.03}$	$3.04^{+0.03}_{-0.03}$	1.06 (1303)
80050019-O5	60002023027	$1.85^{+0.05}_{-0.05}$	$1.68^{+0.02}_{-0.02}$	$3.08^{+0.03}_{-0.03}$	1.05 (1438)
35014065-O3	60002023035	$1.99^{+0.09}_{-0.09}$	$1.82^{+0.02}_{-0.02}$	$3.00^{+0.05}_{-0.05}$	1.01 (1563)
34228110-O3	60202048002	$1.49^{+0.10}_{-0.10}$	$1.70^{+0.04}_{-0.07}$	$2.78^{+0.05}_{-0.07}$	1.09 (1211)
34228110-O5	60202048002	$1.37^{+0.10}_{-0.10}$	$1.73^{+0.04}_{-0.07}$	$2.79^{+0.05}_{-0.07}$	1.04 (1201)
81926001	60202048004	$1.46^{+0.15}_{-0.12}$	$1.84^{+0.03}_{-0.04}$	$2.98^{+0.06}_{-0.08}$	1.03 (1240)

parameters kept free. It may be noted that, only four *Nu*STAR observations were simultaneous with *Swift*-XRT; dividing the later orbit-wise we obtain six spectra. The best spectral fit parameters are given in Table 3.2. We find that the $\epsilon_{\rm p,sbpl}$ obtained through the combined spectral fit matches reasonably well with ϵ_p got from the log parabolic fit of *Swift*-XRT observations. The scatter plot between these quantities along with the identity line is shown in Figure 3.5. Though this result can be viewed as supporting our choice of ϵ_b, it may be noted that this is based on only a small number of data points. To improve on this and to be able to draw a more firm conclusion on the nature of ϵ_p, further simultaneous broadband X-ray observations of the source are clearly desirable. Nevertheless, the fact that all data points in Figure 3.3 lie above the cooling break line (brown dotted dash line) clearly disfavours a radiative loss interpretation of the considered, characteristic photon energy in Mkn 421.

A similar finding to the one presented here has also been reported by Abdo et al. (2011) based on broadband SED modelling of the source observed in 2009. Their modelling results show that the required spectral break is significantly larger than the one inferred from a simple radiative cooling scenario. As a possible explanation the authors suggest that source inhomogeneities might be responsible for the large spectral break (e.g., Reynolds, 2009). Using a large number of *Swift-XRT* observations corresponding to different flux states, we have shown here that a simple cooling break interpretation for the characteristic photon energy of Mkn 421 is inconsistent with the observations. Our statistical analysis reveals a strong anti-correlation between $\Gamma_{\rm low}$ and $\Gamma_{\rm high}$. While simple scenarios can reproduce part of the observed properties, a deeper

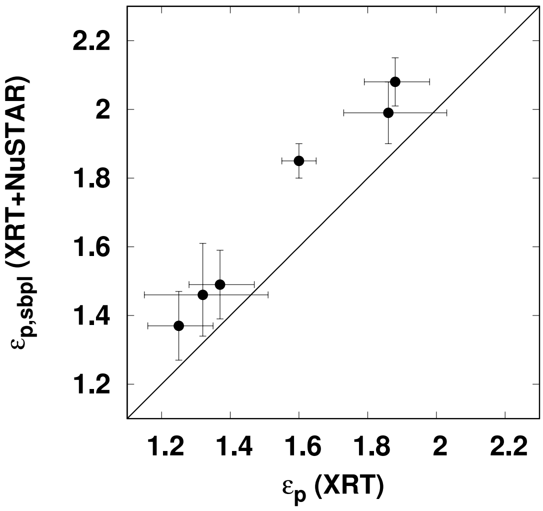

Figure 3.5: The scatter plot between ϵ_p and $\epsilon_{p,sbpl}$ using combined *Swift*-XRT and *NuSTAR* data, along with the identity line.

understanding of the origin and evolution of the radiating particle distribution is needed to satisfactorily match the observed results.

The correlation between the indices around the spectral peak might also be present for the high energy Compton spectral component if the same electron distribution is responsible for the emission at these energies and scattering occurs in the Thomson regime. However, the curvature could differ depending on the spectral shape of the target photons responsible for Compton emission. This could be further complicated if the Compton spectral peak is governed by the transition of the scattering process from the Thomson to the Klein-Nishina regime. We note that Chen (2014) has performed a detailed spectral study of a sample of *Fermi* bright blazars by fitting their synchrotron and Compton spectral components (one SED data set for each source) log-parabola and broken power-law functions. Comparing the sources in this sample, a significant correlation between the peak frequency and the curvature was found for the synchrotron spectral components, while the Compton spectral components did not show such a behaviour. This seems at variance with our findings based on multiple observations of a single source where no such correlation has been seen for the synchrotron spectral component. In principle, this could suggest that correlation results obtained from a single source cannot be easily generalised to the entire set of blazars. On the other hand, the results for the Compton emission are still less certain given the (then) limited observational characterisation of the Compton spectrum, and an updated analysis might be helpful to clarify the situation.

Earlier studies interpreting the blazar sequence in terms of radiative loss suggested FSRQs to undergo significant losses compared to BL Lacs (e.g., Ghisellini et al., 2002). This results in a rather low characteristic (peak) photon energy for FSRQs compared to BL Lacs, though FSRQs are more luminous. However, the present study indicates that the characteristic photon energy is not readily related to radiative losses, at least in the case of Mkn 421, and hence this inference does not apply. Therefore, a definite explanation of the characteristic photon energy along with a study based on an increased number of sources will have the potential to decipher the mystery behind the blazar sequence.

E_{peak} = 0.72 keV (ObsID 30352077)

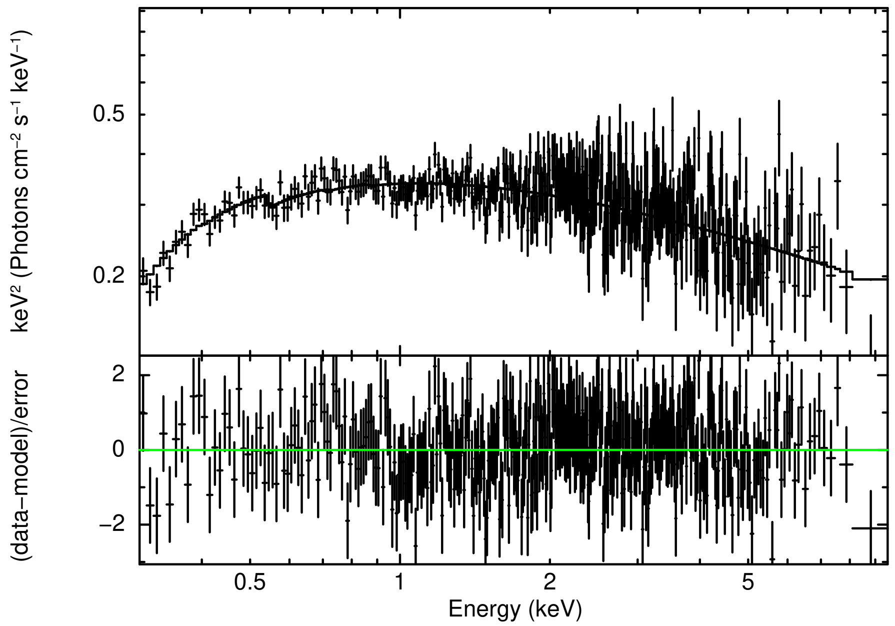

E_{peak} = 1.50 keV (ObsID 30352226)

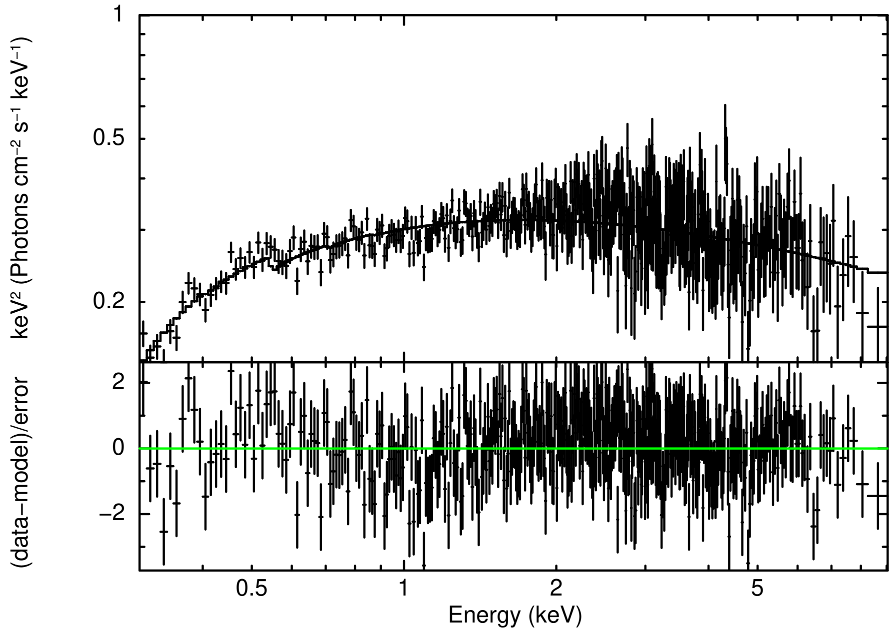

Figure 3.6: Example of 0.3-10 keV specta around the synchrotron SED peak modeled with *sbpl* function.

Chapter 4

Signature of Particle Diffusion on the X-ray Spectra of blazar Mkn 421

4.1 Introduction

The broadband synchrotron spectral component of blazars often suggests the emitting electron distribution to be a broken power-law (Sambruna et al., 1994; Tavecchio et al., 1998; Fossati et al., 2000). In principle, a power-law electron distribution could be produced by Fermi-type particle acceleration (e.g., Fermi, 1949b; Lemoine, 2019), where particles gain energy as they are scattered by magnetic turbulent structures embedded in the jet. When electrons are scattered by the turbulent structures across a shock front, Fermi acceleration will be efficient and is commonly referred to as shock acceleration (e.g., Kirk et al., 1998; Rieger et al., 2007). Synchrotron cooling of a power-law electron distribution then results in a broken power-law distribution of electrons with power-law indices differing by one. The corresponding synchrotron photon spectrum would follow a broken power-law with indices differing by half (Kardashev, 1962; Rybicki & Lightman, 1986). However, broadband SED modeling of blazars often fails to support such an interpretation (e.g., Mankuzhiyil et al., 2012). In particular, our earlier study of the blazar Mkn 421 reported a strong anti-correlation between the spectral indices measured before and after the synchrotron spectral peak, disfavouring a simple radiative loss origin of the synchrotron peak (Baheeja et al., 2022).

Narrow-band spectral analysis of blazars frequently reveals significant curvature around the peak of the synchrotron component, that is formally well represented by a log-parabola function (Landau et al., 1986; Massaro et al., 2004; Tramacere et al., 2007b; Chen, 2014). However, such a function fails to explain the combined optical-UV and X-ray spectrum (Massaro et al., 2004; Tramacere et al., 2009; Sinha et al., 2015; Jagan et al., 2018). Instead, a smooth broken power-law or a power-law particle distribution with an exponential cutoff is often capable of explaining this broadband spectral component (Sinha et al., 2017; Kirk et al., 1998). Recent studies with high-resolution observations have revealed significant spectral curvature even beyond the synchrotron peak (Bhagwan et al., 2014; Sinha et al., 2015; Gaur et al., 2017).

A simple description of first-order Fermi acceleration, assuming an energy-independent acceleration time-scale and escape time-scale, naturally produces a power-law electron distribution. However, when radiative losses are taken into account and an energy-dependence is incorporated into the acceleration time-scale and/or escape time-scale, the resulting particle distribution can deviate from a power-law and can exhibit curvature towards high energies (Kirk et al., 1998). Similarly, a log-parabolic photon spectrum suggests the underlying electron distribution to be log-parabolic, which could be interpreted in terms of a statistical acceleration scenario with an energy-dependent acceleration probability (Massaro et al., 2004). In fact, under specific conditions, the electron distribution resulting from a stochastic particle acceleration could mimic a log-parabola (Tramacere et al., 2011). It is then expected that the synchrotron peak energy anti-correlates with spectral curvature (Tramacere et al., 2007a). During the period of 1997−2006, an anti-correlation between the synchrotron peak energy and the spectral curvature was indeed found through log-parabolic spectral fitting of the X-ray data from Mkn 421 and other TeV BL Lacs, seemingly supportive of a stochastic acceleration scenario

(Tramacere et al., 2007a, 2009; Massaro et al., 2008; Tramacere et al., 2011). However, recent studies using *Swift*–XRT/*NuSTAR* observations report no significant correlation between these quantities (Kapanadze et al., 2018b,a; Kapanadze et al., 2020; Sinha et al., 2015; Baheeja et al., 2022). On the other hand, a curved spectrum could also be the outcome of an energy-dependent escape from the acceleration region. When this energy-dependence is mild, the resulting electron distribution closely follows a log-parabolic shape (Jagan et al., 2018) but deviates significantly otherwise. Synchrotron emission by an electron distribution originating in a model with a strong energy-dependent escape time-scale has been used to fit the spectra of Mkn 421 during different flux states (Goswami et al., 2018, 2020).

Particle acceleration at non- or mildly relativistic shock fronts has been considered for long as one of the preferred mechanisms for generating the non-thermal particle distributions seen in AGN jets (e.g., Marscher & Gear, 1985b; Kirk et al., 1998; Rieger et al., 2007; Zech & Lemoine, 2021; Di Gesu et al., 2022, 2023). The highest energy achieved by the accelerated particles, as well as the shape of the spectrum around the maximum energy, are influenced by the balance among the rates of acceleration, escape and the radiative energy loss. In the presence of synchrotron losses, shock acceleration (for example) can result in a power-law particle distribution with a modified exponential cutoff, $\propto \exp[-(\gamma/\gamma_c)^{\beta_e}]$, where β_e is dependent on the underlying turbulence/diffusion properties (e.g., Zirakashvili & Aharonian, 2007). Formally, $\beta_e = (1 + a)$ is related to the momentum index a of the spatial diffusion coefficient, $\kappa = (1/3)\lambda\, c \propto \gamma^a$, that facilitates the particle transport. Here, λ is the particle mean free path and γ is the particle Lorentz factor. In particular, one may have $\beta_e = 1$ (or $a = 0$) in the case of "idealized" hard-sphere scattering (energy-independent diffusion), and $\beta_e = 2$ (or $a = 1$) for Bohm type diffusion (where $\lambda \sim r_g$, the gyroradius). Since the corresponding particle acceleration time-scale, $t_{\rm acc}$ is proportional to λ, Bohm diffusion typically yields the fastest acceleration rate (i.e., the highest $\gamma_{\rm e,max}$ when balanced with synchrotron losses). The resultant synchrotron spectra can exhibit some extended curvature at high energies. In particular, an electron distribution with exponential cutoff index β_e will result in a synchrotron spectrum which can be significantly smoother (sub-exponential) $j_\nu \propto \exp\left[-(\nu/\nu_c)^\zeta\right]$ with $\zeta \equiv \frac{\beta_e}{\beta_e+2}$, e.g., $\zeta = 1/2$ in the case of Bohm-type diffusion (Fritz, 1989).

The BL Lac object Mkn 421, that we focus on here, is the nearest (z = 0.031) and one of the most well-studied TeV blazars. Mkn 421 belongs to the high-frequency BL Lac (HBL) class, as its synchrotron spectral component peaks in the X-ray regime. The X-ray spectrum around the synchrotron peak exhibits significant curvature that has been interpreted in terms of a log-parabola function. X-ray spectral analysis of Mkn 421 using *NuSTAR* (3-79 keV) observations, reveals that during the low-flux state of the source in January 2013, the hard X-ray spectra were well represented by a steep power-law model with a photon index saturating at ~ 3 (Kataoka & Stawarz, 2016; Baloković et al., 2016). However, the observed X-ray spectrum also shows a significant curvature during its high-flux states in April 2013 (Sinha et al., 2015). This curvature persists even in hard X-rays, which makes it (in spite of the fact that some blending of components cannot be excluded) challenging to attribute this solely to the spectral transition occurring at the peak of the synchrotron component (Fossati et al., 2008; Horan et al., 2009). To explore this further, we have performed a detailed spectral study on the X-ray data of the source. We are particularly interested to understand whether the observed X-ray spectral characteristics allow some inferences on the turbulent properties in the jet.

4.2 Observation and Data analysis

Mkn 421 has been observed by *NuSTAR* and *Swift*-XRT in both flaring as well as quiescent flux states. For the current study we have selected all the available simultaneous *Swift*-XRT and *NuSTAR* observations till 2018 (details are given in Table 4.1). This allows us to analyse the source over a wide range of X-ray energies, from 0.3 to 79 keV. The strategies for analysing these observations are detailed below.

Table 4.1: Details of simultaneous *Swift*-XRT and *NuSTAR* observations.

Swift Obs.ID	Date & time	Exposure (s)	*NuSTAR* Obs.ID	Date & time	Exposure (s)
35014034	2013-01-15 02:09:59	3958.859	60002023006	2013-01-15 00:56:07	24181
80050003	2013-02-06 01:20:59	9506.827	60002023010	2013-02-06 00:16:07	19302
80050006	2013-02-17 00:03:59	9201.642	60002023014	2013-02-16 23:36:07	17356
80050007	2013-03-04 23:34:25	984.609	60002023016	2013-03-04 23:06:07	17251
80050011	2013-03-11 23:58:59	8425.937	60002023018	2013-03-11 23:01:07	17472
80050013	2013-03-17 01:22:59	8880.740	60002023020	2013-03-17 00:11:07	16554
80050014	2013-04-02 21:01:59	1644.569	60002023022	2013-04-02 17:16:07	24767
80050016	2013-04-11 00:30:59	1118.631	60002023024	2013-04-10 21:26:07	5757
80050019	2013-04-12 21:53:58	9546.279	60002023027	2013-04-12 20:36:07	7629
32792002	2013-04-14 00:38:59	6327.071	60002023029	2013-04-13 21:36:07	16508
35014062	2013-04-15 23:07:59	534.621	60002023033	2013-04-15 22:01:07	17276
35014065	2013-04-17 00:46:59	8842.132	60002023035	2013-04-16 22:21:07	20278
35014066	2013-04-18 00:49:59	6887.219	60002023037	2013-04-18 00:16:07	17795
35014067	2013-04-19 00:52:59	6132.768	60002023039	2013-04-19 00:31:07	15958
34228110	2017-01-04 00:06:57	6021.027	60202048002	2017-01-03 23:51:09	23691
81926001	2017-01-31 23:27:57	1009.619	60202048004	2017-01-31 23:46:09	21564
34228145	2017-02-28 22:46:56	44.620	60202048006	2017-02-28 22:11:09	23906

4.2.1 *NuSTAR*

The *NuSTAR* observations were taken from the HEASARC interface by NASA and the data were processed with NuSTARDAS package (Version 2.1.1) available within HEASOFT (Version 6.29). The source spectrum is extracted from a circular region with a radius of 50 arcsec centered on the source, while the background is estimated from another circular region with a radius of 70 arcsec that is free from any contamination by the source, but near it. The *nuproduct* (Version 0.3.3) task was used to obtain source and background spectra after running *nupipeline* (Version 0.4.9) on each observation. The FPMA and FPMB source spectra were then individually grouped to 30 photons per bin using the tool *grppha* to ensure improved χ^2 statistics.

4.2.2 *Swift*-XRT

The *Swift*-XRT observations were also retrieved from HEASARC interface and the data were processed using the XRTDAS software package (Version 3.6.1) available within HEASOFT. We used the observations performed in Windowed Timing (WT) mode and the events with 0-2 grades have been considered in the analysis. The event files were cleaned and calibrated using standard procedures with the *xrtpipeline* (Version 0.13.6) task. A circular region of 30 pixel radius centred at the source was used to extract the source spectrum, and a circular region of same size devoid of source contamination was used to extract the background spectrum. An annular region with inner and outer radii of 2 and 30 pixels, respectively, was used as source and background regions for the observation with pileup. The tool *xrtproducts* (Version 0.4.2) was used to generate the final spectrum. The *xrtmkarf* (Version 0.6.3) task was employed to generate the auxiliary response files (ARFs), and the response matrice files (RMFs)were taken from the *Swift* CALDB. The source spectra were then grouped using the *grppha* tool ensuring a minimum of 20 counts/bin.

4.3 X–ray spectral analysis and results

4.3.1 *NuSTAR* (3-79 keV) regime

To investigate the curvature in the hard X-ray regime, we fitted the *NuSTAR* observations (3-79 keV) of the source, using three models available in XSPEC namely, power-law (PL), log-parabola (LP), and a power-law with an exponential cutoff (CPL). These models are defined as

$$F(\epsilon) \propto \epsilon^{-\Gamma_1} \qquad (\mathrm{PL})\,, \tag{4.1}$$

where ϵ is the photon energy, and Γ_1 represents the power-law index.

$$F(\epsilon) \propto \left(\frac{\epsilon}{\epsilon_0}\right)^{-\alpha-\beta\log(\epsilon/\epsilon_0)} \qquad (\mathrm{LP})\,, \tag{4.2}$$

where α is the spectral index at energy ϵ_0, and β is the spectral curvature, and

$$F(\epsilon) \propto \epsilon^{-p}\exp[-(\epsilon/\epsilon_{\mathrm{c}})] \qquad (\mathrm{CPL})\,, \tag{4.3}$$

where p represents the power-law index, and ϵ_c characterizes the position of the cutoff energy. The spectral peak ($\epsilon^2 F(\epsilon)$ representation) of the log-parabola function is obtained from

$$\epsilon_p = \epsilon_0 \, 10^{\left(\frac{2-\alpha}{2\beta}\right)} \, . \tag{4.4}$$

Table 4.2: Fit parameters of *NuSTAR* (3-79 keV) spectra as modeled with PL, LP and CPL.

NuSTAR	Flux	PL		LP(ϵ_0=5 keV)			CPL		
Obs.ID	(3-79 keV)	Γ_1	χ^2_{red} (DOF)	α	β	χ^2_{red} (DOF)	p	ϵ_c (keV)	χ^2_{red} (DOF)
60002023006	-9.954±0.004	3.03±0.01	1.05 (563)	2.95±0.02	0.31±0.06	0.92 (562)	2.82±0.05	$35.12^{+9.75}_{-6.47}$	0.94 (562)
60002023010	-9.842±0.004	2.95±0.01	1.32 (570)	2.83±0.02	0.41±0.06	1.04 (569)	2.64±0.05	$24.99^{+4.49}_{-3.41}$	1.06 (569)
60002023014	-10.187±0.007	3.02±0.02	1.06 (419)	3.00±0.03	0.11±0.09	1.05 (418)	–	–	–
60002023016	-9.779±0.004	3.01±0.01	1.11 (557)	2.95±0.02	0.25±0.06	1.01 (556)	2.85±0.05	$44.97^{+16.44}_{-9.80}$	1.03 (556)
60002023018	-9.906±0.005	3.09±0.02	1.04 (509)	3.04±0.02	0.20±0.07	0.99 (508)	2.96±0.05	$53.64^{+31.18}_{-14.91}$	1.00 (508)
60002023020	-9.731±0.005	2.77±0.01	1.18 (595)	2.68±0.02	0.28±0.05	1.04 (594)	2.58±0.04	$40.77^{+10.57}_{-7.19}$	1.06 (594)
60002023022	-9.343±0.002	2.74±0.01	1.51 (898)	2.64±0.01	0.30±0.03	1.03 (897)	2.52±0.02	$38.28^{+3.89}_{-3.29}$	1.06 (897)
60002023024	-9.201±0.003	2.90±0.01	1.47 (620)	2.78±0.02	0.39±0.05	1.11 (619)	2.61±0.04	$27.88^{+4.20}_{-3.33}$	1.14 (619)
60002023027	-8.624±0.002	2.62±0.01	2.63 (1023)	2.45±0.01	0.44±0.02	0.94 (1022)	2.29±0.02	$26.4^{+1.36}_{-1.26}$	1.01 (1022)
60002023029	-9.085±0.002	2.79±0.01	2.06 (917)	2.65±0.01	0.42±0.02	0.98 (916)	2.48±0.02	$26.67^{+1.83}_{-1.64}$	1.08 (916)
60002023033	-9.014±0.002	2.59±0.01	1.86 (1019)	2.46±0.01	0.33±0.02	1.01 (1018)	2.34±0.02	$35.89^{+2.50}_{-2.23}$	1.02 (1018)
60002023035	-8.934±0.002	2.39±0.01	2.33 (1182)	2.25±0.01	0.35±0.02	1.07 (1181)	2.13±0.01	$35.77^{+1.90}_{-1.74}$	1.1 (1181)
60002023037	-9.835±0.004	2.85±0.01	1.31 (568)	2.72±0.02	0.40±0.06	1.05 (567)	2.55±0.05	$26.61^{+4.85}_{-3.67}$	1.05 (567)
60002023039	-9.868±0.005	2.94±0.02	0.98 (519)	2.88±0.02	0.22±0.06	0.91 (518)	2.79±0.05	$50.09^{+23.58}_{-12.58}$	0.92 (518)
60202048002	-9.269±0.003	2.45±0.01	1.39 (1006)	2.36±0.01	0.22±0.02	1.10 (1005)	2.29±0.02	$60.22^{+7.58}_{-6.17}$	1.14 (1005)
60202048004	-9.247±0.003	2.45±0.01	1.72 (1001)	2.31±0.01	0.33±0.02	1.04 (1000)	2.20±0.02	$37.22^{+2.94}_{-2.59}$	1.06 (1000)
60202048006	-9.261±0.002	2.49±0.01	1.75 (996)	2.37±0.01	0.31±0.02	1.13 (995)	2.26±0.02	$39.53^{+3.31}_{-2.89}$	1.16 (995)

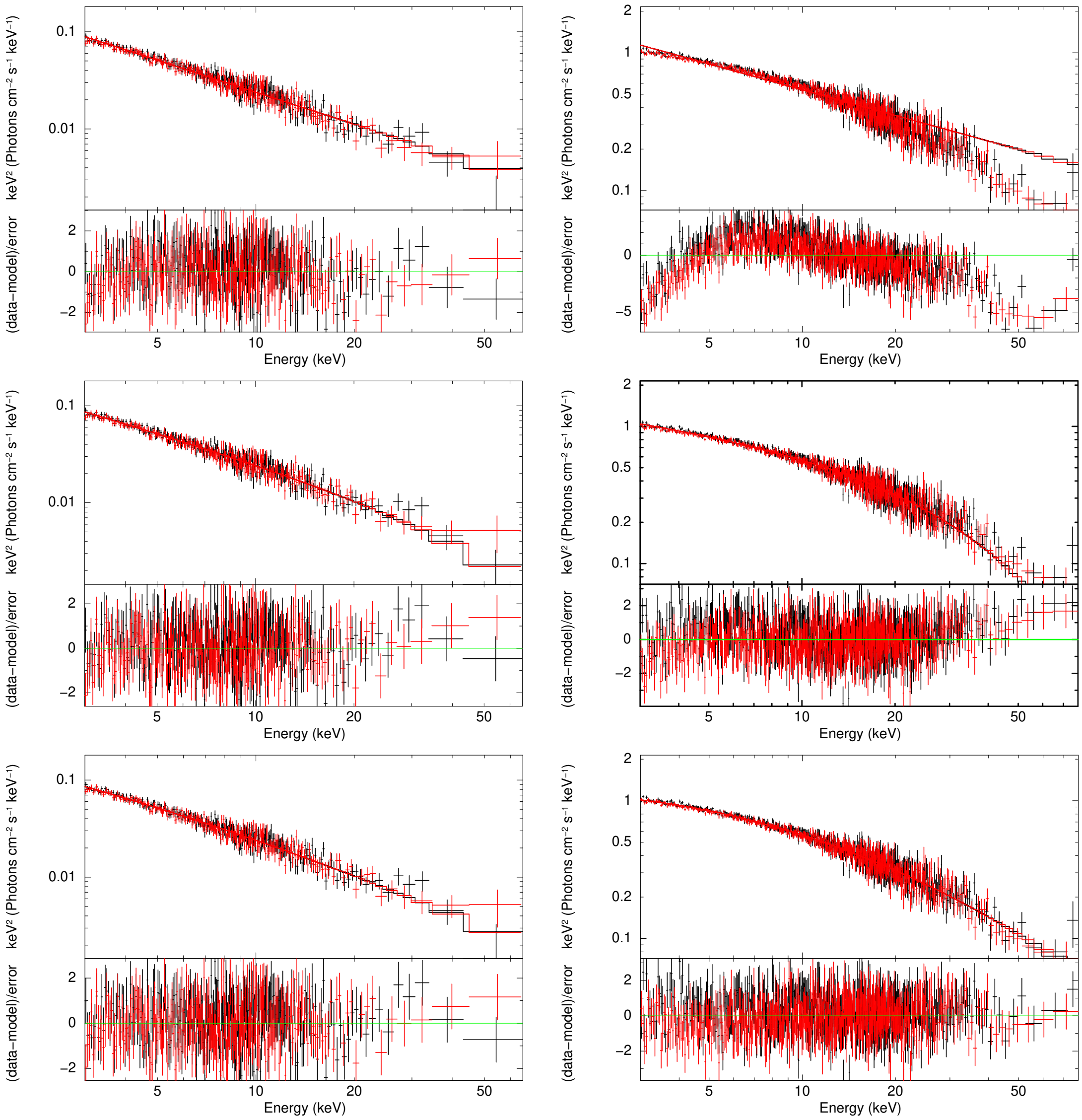

Figure 4.1: Spectral fits (*NuSTAR* alone) using the models PL in top panel, CPL in middle panel, and LP in bottom panel for the ObsIDs 60002023018 (low-flux state) and 60002023027 (high-flux state) are shown in the left and right panels, respectively. Significant curvature is apparent in the high flux state.

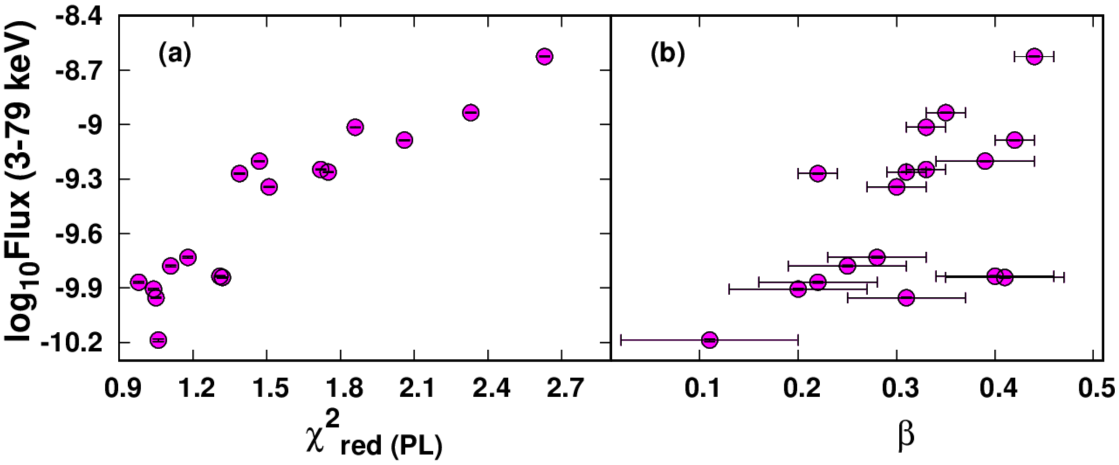

Figure 4.2: **(a)** Variation of flux with χ^2_{red} for PL fit with *NuSTAR* data, **(b)** Variation of flux with curvature β of LP fit with *NuSTAR* data.

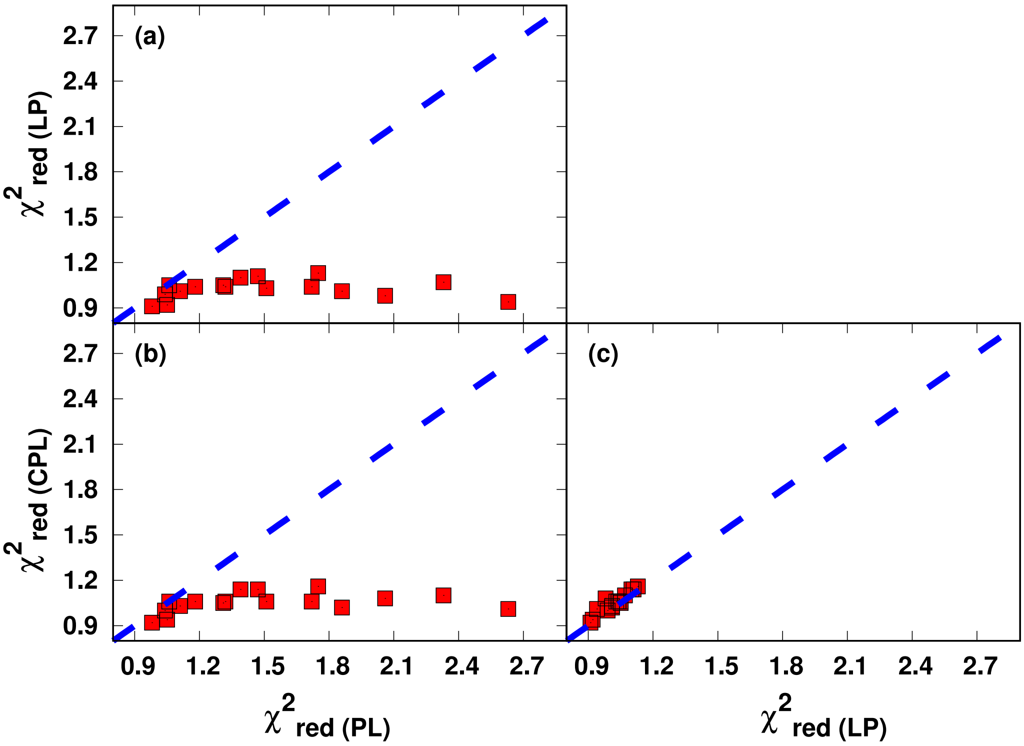

Figure 4.3: Scatter plots between the reduced chi-square values of *NuSTAR* data fitted with the PL, LP, and CPL models, along with the identity line.

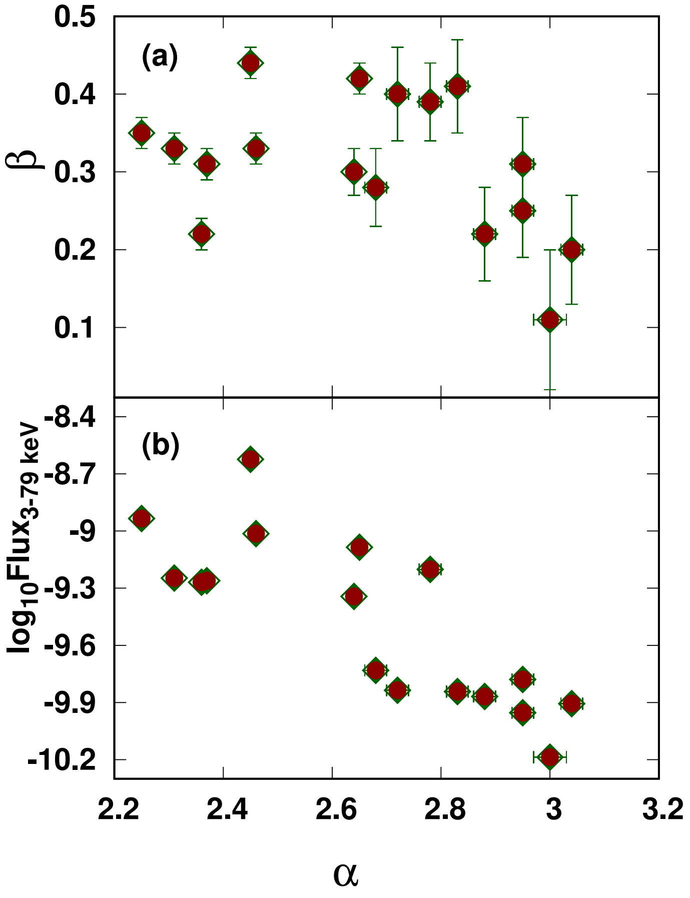

Figure 4.4: Scatter plots (*NuSTAR* alone) showing LP index α, along with **(a)** spectral curvature β, and **(b)** flux in the 3-79 keV range.

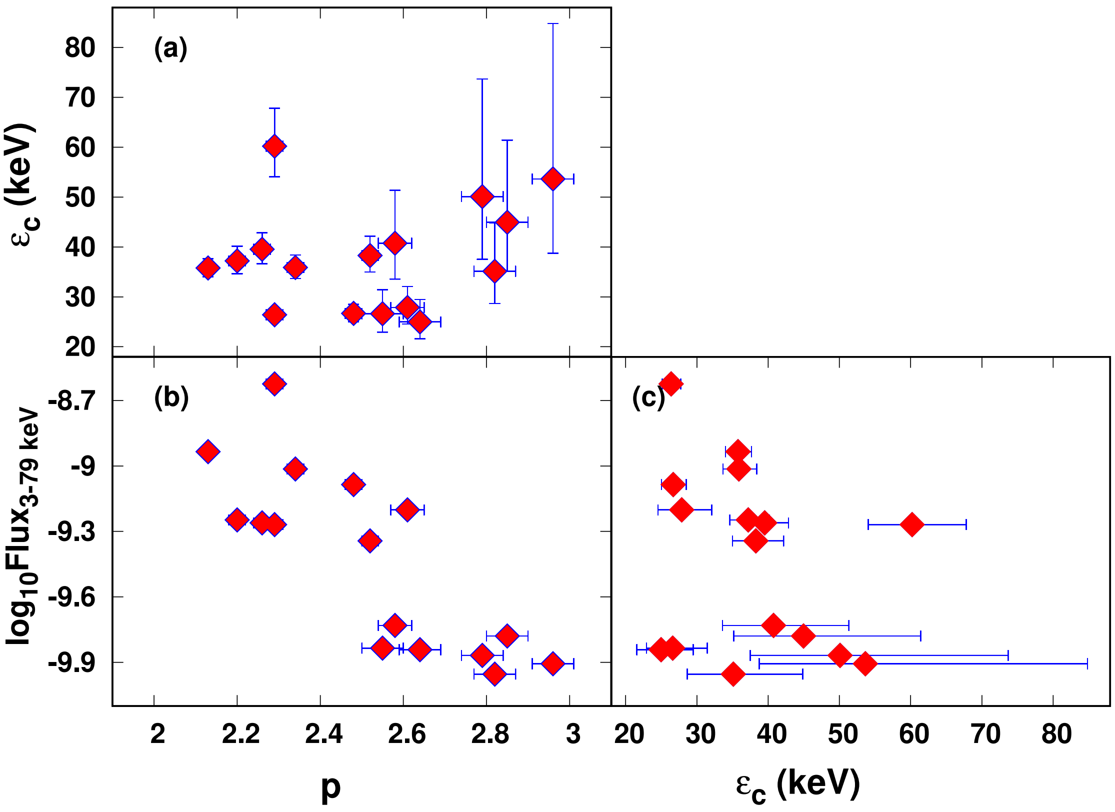

Figure 4.5: Scatter plots (*NuSTAR* alone) showing best-fit CPL model parameters: **(a)** index and cutoff energy, **(b)** index and flux, and **(c)** cutoff energy and flux.

Table 4.3: The best-fit parameters of combined spectrum from *Swift*-XRT and *NuSTAR* with a LP and a simple CPL model.

Obs.ID		Flux	LP (ϵ_0=5 keV)				CPL		
Swift	*NuSTAR*	(0.3-79 keV)	α	β	ϵ_p (keV)	χ^2_{red}(dof)	p	ϵ_c (keV)	χ^2_{red}(dof)
35014034	60002023006	-9.696±0.003	2.93±0.01	0.34±0.01	0.22±0.02	0.97 (962)	2.38±0.01	11.50±0.42	1.17 (962)
80050003	60002023010	-9.602±0.003	2.81±0.01	0.36±0.01	0.37±0.02	1.27 (1110)	2.23±0.01	10.37±0.30	1.40 (1110)
80050006	60002023014	-9.930±0.004	2.94±0.02	0.25±0.01	0.07±0.01	1.19 (848)	2.51±0.01	14.40±0.87	1.30 (848)
80050007	60002023016	-9.523±0.003	2.92±0.01	0.32±0.02	0.19±0.03	1.10 (822)	2.46±0.02	13.71±0.72	1.34 (822)
80050011	60002023018	-9.639±0.003	2.98±0.01	0.34±0.01	0.17±0.01	1.10 (1001)	2.42±0.01	10.73±0.38	1.35 (1001)
80050013	60002023020	-9.521±0.003	2.67±0.01	0.24±0.01	0.19±0.02	1.16 (1126)	2.29±0.01	16.97±0.69	1.20 (1126)
80050014	60002023022	-9.146±0.002	2.64±0.01	0.31±0.01	0.47±0.03	1.06 (1338)	2.23±0.01	16.45±0.46	1.62 (1338)
80050016	60002023024	-8.972±0.002	2.78±0.01	0.36±0.01	0.41±0.02	1.18 (1039)	2.23±0.01	11.93±0.38	1.41 (1039)
80050019	60002023027	-8.460±0.001	2.45±0.01	0.43±0.01	1.50±0.03	1.07 (1575)	1.91±1.91	12.16±12.16	2.11 (1575)
32792002	60002023029	-8.874±0.001	2.68±0.01	0.34±0.01	0.51±0.02	1.10 (1411)	2.21±0.01	14.15±0.31	1.52 (1411)
35014062	60002023033	-8.847±0.002	2.47±0.01	0.29±0.01	0.79±0.05	1.07 (1391)	2.19±0.01	22.72±0.83	1.33 (1391)
35014065	60002023035	-8.799±0.001	2.27±0.01	0.28±0.01	1.61±0.05	1.17 (1741)	1.96±0.01	21.77±0.52	1.45 (1741)
35014066	60002023037	-9.600±0.003	2.76±0.01	0.22±0.01	0.10±0.01	1.19 (1068)	2.39±0.01	17.67±0.77	1.14 (1068)
35014067	60002023039	-9.625±0.003	2.85±0.01	0.26±0.01	0.11±0.01	1.05 (1001)	2.43±0.01	14.71±0.65	1.21 (1001)
34228110	60202048002	-9.133±0.002	2.34±0.01	0.26±0.01	1.14±0.08	1.09 (1348)	2.12±0.01	28.88±1.44	1.50 (1348)
81926001	60202048004	-9.105±0.002	2.33±0.01	0.29±0.01	1.33±0.08	1.07 (1385)	2.05±0.01	23.45±0.92	1.29 (1385)
34228145	60202048006	-9.116±0.003	2.37±0.01	0.31±0.02	1.29±0.15	1.11 (1044)	2.25±0.02	37.69±2.64	1.18 (1044)

The neutral hydrogen column density N_H, inclusive of both HI and HII was fixed at $2.03 \times 10^{20} \mathrm{cm}^{-2}$ throughout the analysis. The best-fit parameters of these models are presented in Table 4.2. We observe that most of the low-flux states are well-fitted with a steep power-law model, yielding a photon index saturating at ~ 3, confirming the results by Baloković et al. (2016). In contrast, the high-flux states exhibit significant curvature and deviate from a simple power-law model (see Figure 4.1). The spectral fits using the PL, LP, and CPL models for a sample of low and high flux states are shown in Figure 4.1. Figure 4.3.1 illustrates the change in the reduced chi-square value of the PL fit (left) and the spectral curvature (right) as the flux increases.

Our analysis provides strong evidence for spectral curvature in the *NuSTAR* region, with a LP/CPL model clearly preferred over a pure PL model in high flux states. The plots between reduced chi-square values for the spectral fittings with the PL, LP, and CPL models (χ^2_{red}(PL), χ^2_{red}(LP), and χ^2_{red}(CPL)) are shown in Figure 4.3. Scatter plots showing the best-fit LP model parameters, and the flux, are depicted in Figure 4.4. The Spearman rank correlation study between the LP model parameters α and β yields a correlation coefficient, r_s= -0.41 with a null hypothesis probability, $p_s = 0.104$. This result is consistent with previous studies which reported that no significant correlation was observed (Sinha et al., 2015; Goswami et al., 2018). However, an anti-correlation is witnessed between α and the flux (r_s = -0.81, p_s <0.001), indicating that the spectra get harder during brighter states of the source. This harder when brighter behaviour of the source has already been reported earlier (Massaro et al., 2004, 2008; Sinha et al., 2015; Kapanadze et al., 2018a; Kapanadze et al., 2020). Scatter plots showing the best-fit CPL model parameters are depicted in Figure 4.5. Here no correlation is observed between p and ϵ_c ($r_s = 0.16$, $p_s = 0.556$), while a significant anti-correlation between p and flux (r_s = -0.79, p_s <0.001) is seen. This anti-correlation again consistent with harder when brighter behaviour of the source.

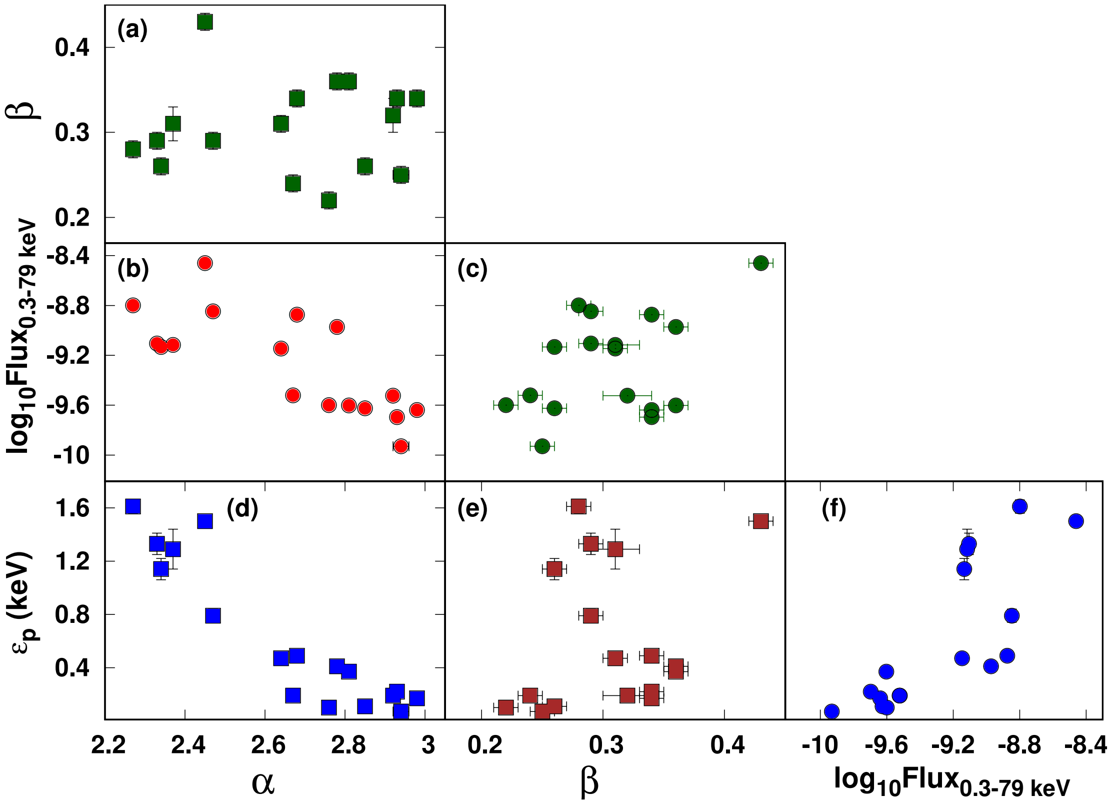

Figure 4.6: Scatter plots between the parameters obtained from LP fitting of combined *Swift*-XRT and *NuSTAR* data: **(a)** index (α) and curvature (β), **(b)** α and flux in 0.3 to 79 keV, **(c)** β and flux , **(d)** α and peak energy (ϵ_p), **(e)** β and ϵ_p, and **(f)** flux and ϵ_p.

4.3.2 Combined ***NuSTAR*** and ***Swift*-XRT regime**

In order to gain further insights, we also studied the broad X-ray spectra of Mkn 421 ranging from 0.3 to 79 keV using simultaneous *Swift*-XRT and *NuSTAR* observations, employing independently the log-parabola (LP) and simple exponential cutoff (CPL) models. These X-ray spectra exhibit significant curvature, and the LP model generally provides a better fit when compared to a simple CPL model. The best-fit parameters are presented in Table 4.3. The scatter plots between LP parameters and the flux are shown in Figure 4.6. We observe a strong negative correlation between α and ϵ_p (r_s = -0.86, p_s <0.001). Furthermore, we noted a strong negative correlation between α and flux (r_s = -0.80, p_s <0.001), and ϵ_p being significantly correlated with flux (r_s = 0.85, p_s <0.001). These correlations suggest that during flares, the spectral index hardens and the spectral peak moves towards higher energies. Again, we observe no correlation between α and β ($r_s = 0.17$, $p_s = 0.521$). Additionally, there was no significant correlation between β and peak energy, ϵ_p, ($r_s = 0.31$, $p_s = 0.227$).

The absence of a significant correlation among the LP parameters, even in the broad energy range studied here, indicates that the changes in spectral characteristics cannot simply be ascribed to the energy-dependence of the particle acceleration process as proposed by Massaro et al. (2004). Additionally, such a model is unable to account for the broadband SED of blazars (Massaro et al., 2004; Tramacere et al., 2009; Sinha et al., 2015). Hence, an alternate physically motivated choice could be a CPL type model. On the other hand, the foregoing analysis indicates that a simple (purely exponential) CPL model does not provide an improved fit to the broad X-ray spectra of the source, particularly in high flux states. To explore this further, we next study the broadband X-ray spectrum using a power-law with a modified exponential cutoff, as can be expected in shock-type acceleration scenarios (see Section 4.1).

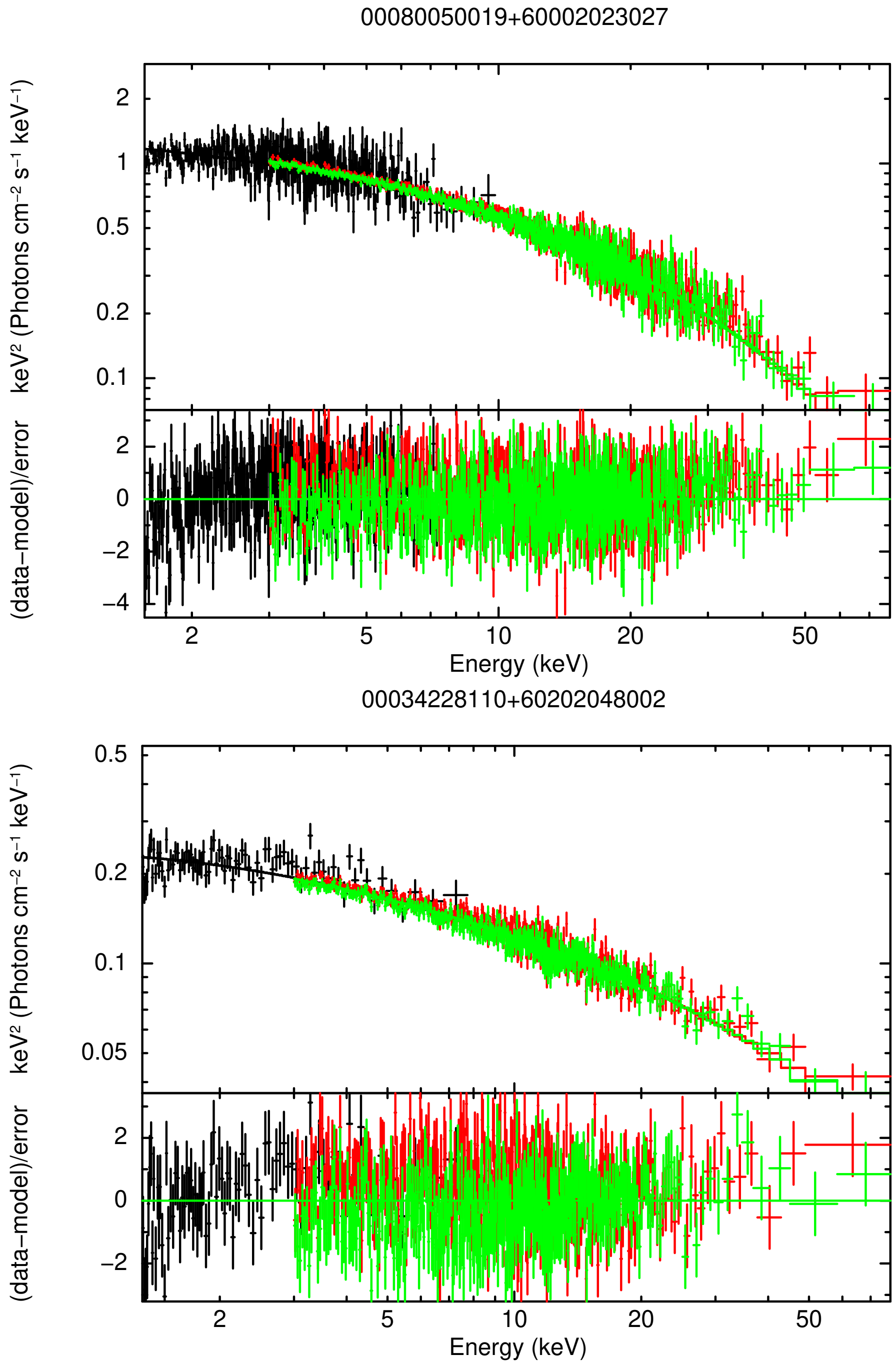

Figure 4.7: Spectral fit from ϵ_p-79 keV using the MCPL model for the obsID 00080050019+60002023027 (top panel) and 00034228110+60202048002 (bottom panel).

Table 4.4: Best fit parameters using the MCPL model (cooled p=2) for the energy range ϵ_p-79 keV.

Obs.ID		ϵ_p	ϵ_c	ζ	χ^2_{red}(dof)	Flux
Swift	*NuSTAR*	(keV)	(keV)			(ϵ_p-79 keV)
80050003	60002023010	0.37±0.02	2.64±0.16	0.54±0.01	1.20 (1106)	-9.621±0.003
80050014	60002023022	0.47±0.03	2.95±0.32	0.47±0.02	1.17 (1323)	-9.156±0.002
80050016	60002023024	0.41±0.02	2.63±0.27	0.52±0.02	1.18 (1030)	-8.988±0.003
80050019	60002023027	1.50±0.03	8.01±0.53	0.60±0.02	1.03 (1458)	-8.457±0.002
32792002	60002023029	0.49±0.02	3.54±0.28	0.52±0.02	1.10 (1394)	-8.888±0.002
35014062	60002023033	0.79±0.05	6.90±0.66	0.53±0.02	1.09 (1345)	-8.853±0.002
35014065	60002023035	1.61±0.05	20.58±0.66	0.71±0.03	1.05 (1613)	-8.807±0.002
34228110	60202048002	1.14±0.08	7.90±1.54	0.44±0.04	1.11 (1266)	-9.128±0.003
81926001	60202048004	1.33±0.08	14.96±1.01	0.62±0.04	1.06 (1285)	-9.109±0.003
34228145	60202048006	1.29±0.15	8.88±1.18	0.50±0.03	1.12 (1015)	-9.112±0.003

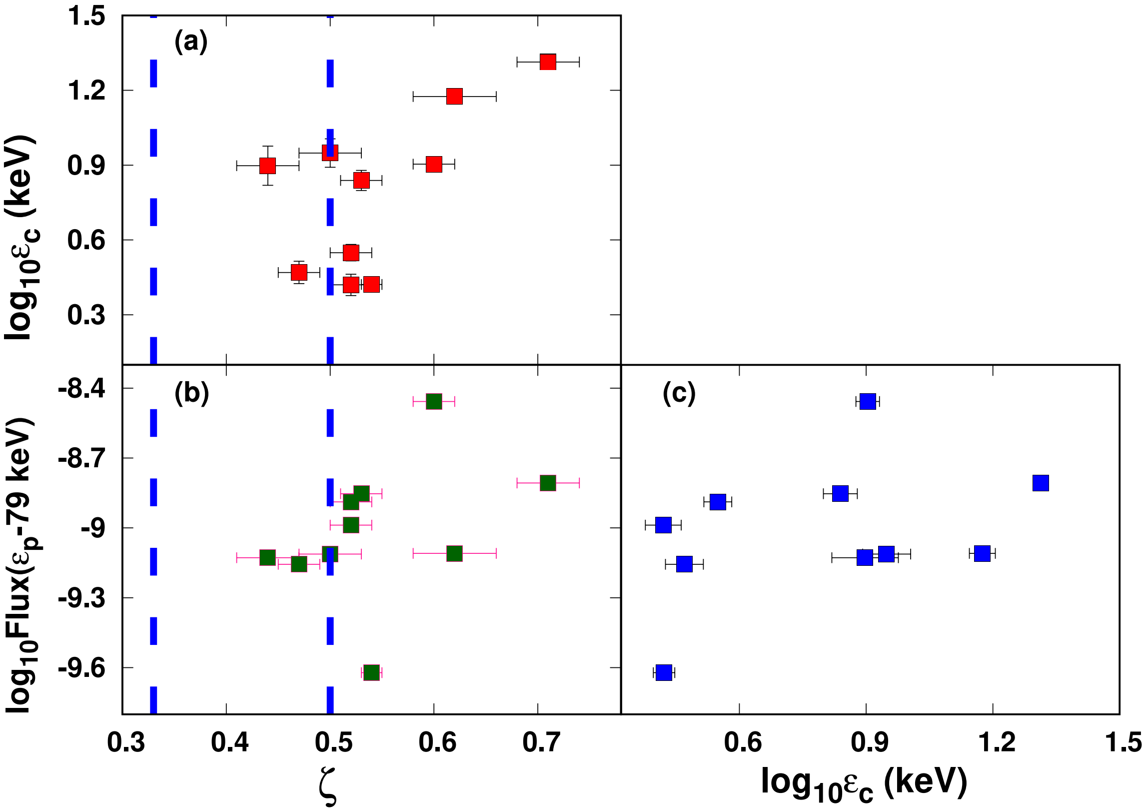

Figure 4.8: Scatter plots between best-fit parameters for the MCPL model (ϵ_p-79 keV). **(a)** ζ and cutoff energy (ϵ_c), **(b)** ζ and flux in ϵ_p-79 keV, and **(c)** ϵ_c and flux. The dotted vertical lines represent ζ corresponding to hard-sphere (0.33) and Bohm (0.5).

4.3.3 Probing a power-law with modified exponential cutoff

In the context of shock acceleration scenarios, the electron distribution exhibits a simple exponential cutoff form only when diffusion is independent of energy. The shape of the particle distribution deviates from this as the diffusion coefficient becomes energy-dependent, leading to a corresponding change in the cutoff region of the synchrotron spectral component, typically follows a sub-exponential shape (Zirakashvili & Aharonian, 2007; Fritz, 1989). In HBL sources such as Mkn 421, the maximum achievable electron energies are limited by synchrotron losses. The evolution of spectral index around the synchrotron (SED) peak does not support a simple cooling break origin of the peak frequency. It might be affected by the blending of different components (e.g., Baheeja et al., 2022). At hard X-rays, where the synchrotron spectrum declines, we may expect the emission to be more dominated by a single component, particularly during higher flux states. Additionally, the high-energy end of the spectrum is likely to be populated by a cooled electron distribution. To explore the spectral curvature towards high energies in more detail, we thus perform spectral fits to the X-ray data above the synchrotron SED peak (with $\epsilon_p > 0.3$ keV) using a modified CPL (MCPL) model

$$F(\epsilon) \propto \epsilon^{-p} \exp[-(\epsilon/\epsilon_{\rm c})^{\zeta}] \qquad \text{(MCPL)}\,, \tag{4.5}$$

where p represents the power-law index, ϵ_c characterizes the position of the cutoff energy, and the parameter ζ governs the steepness of the cutoff. This function is added as a local model in XSPEC, and we perform spectral fitting for the combined simultaneous *Swift*-XRT and *NuSTAR* observations from ϵ_p to 79 keV.

From 17 simultaneous *Swift*-XRT and *NuSTAR* observations available, we found only for 10 epochs the peak falls in between 0.3 and 79 keV. All of these epochs are during high-flux states, except obsID. 80050003+60002023010, and all these epochs are considered for the MCPL fit. The considered X-ray spectra did not allow us to constrain all parameters of the model. Hence, we performed a fitting with p fixed to a value 2, representing a cooled particle distribution. This choice may be appropriate since we are interested in the spectrum above ϵ_p where synchrotron losses dominate. The sample spectral fits of MCPL model are shown in Figure 4.7. The MCPL model represents well the spectrum above ϵ_p and the best-fit parameters ϵ_c and ζ are shown in Table 4.4. The scatter plots between the fitting parameters, and with the flux are shown in Figure 4.8. We performed a Spearman correlation analysis and did not find a significant correlation between the MCPL model parameters ϵ_c and ζ (r_s = 0.45, p_s = 0.192). Also, no significant correlations are observed between ϵ_c and flux (r_s = 0.42, p_s = 0.229), and between ζ and flux (r_s = 0.55, p_s = 0.102).

Constraining the ζ-parameter in the X-ray spectrum can provide insights into the parent particle distribution. In the case of synchrotron emission, the parameter ζ is linked to the primary particle distribution through the relation $\zeta = \frac{\beta_e}{\beta_e+2}$ (Fritz, 1989). Therefore, the value of ζ is expected to be 0.33 in the case of energy-independent diffusion ($\beta_e = 1$), while Bohm-type diffusion ($\beta_e = 2$) results in ζ=0.5. As can be seen from Table 4.4, the inferred ζ-values favour a Bohm-type behaviour.

4.4 Summary

We have conducted a detailed study of the X-ray spectra of Mkn 421 using simultaneous *Swift*-XRT and *NuSTAR* observations. Most of our observations considered are during high flux states (unlike Baloković et al. (2016) for example) and enables us to investigate the spectral curvature in the hard X-ray regime more rigorously. Our spectral study of *NuSTAR* observations using power-law (PL), log-parabolic (LP), and simple exponential cutoff power-law (CPL) models suggests that LP and CPL are clearly preferred over a simple PL. This provides strong evidence of spectral curvature in the 3-79 keV energy regime. We also examined the broad (*Swift*-XRT and *NuSTAR*) X-ray spectra, spanning from 0.3 to 79 keV with LP and CPL models, indicating that LP provides a better fit compared to CPL. However, the lack of a significant correlation between the LP parameters suggests that the variations in spectral characteristics cannot be attributed to the energy-dependence of the particle acceleration process.

The curvature in the X-ray spectrum is closely linked to the primary electron distribution. The acceleration of electrons at shocks is a favored mechanism for generating non-thermal particle distributions in astrophysical jets. In the presence of radiative losses like the synchrotron process, the accelerated electron distribution will be a broken power-law with a modified exponential cutoff at the maximum available electron energy. The resultant synchrotron spectrum from such a particle distribution will always be a power-law with a sub-exponential cutoff, and we found that a MCPL function can satisfactorily reproduce the data beyond the SED peak. Further, the results are consistent with a scenario where the hard X-ray spectrum is due to a cooled electron distribution, with the highest energy part shaped by Bohm-type diffusion.

Though the observed spectral curvature in the hard X-ray supports Bohm-type diffusion during flares in the jet, other possibilities are not yet ruled out. For instance, an energy-dependent escape time scale or the superposition of multiple broken power-law components might also contribute to spectral curvature. Since the highest-energy electrons are expected to probe the shock vicinity, X-ray spectral analysis along with dedicated polarization studies (e.g., Di Gesu et al., 2022) provides a powerful diagnostics of the underlying properties of jet flow. The signature of an electron distribution shaped by Bohm-type diffusion process could in principle be further probed by modeling the resultant γ-ray emission by inverse Compton scattering (Lefa et al., 2012), though in practice, this may be challenging to achieve with the current instrumentation (Romoli et al., 2017). The type of diffusion process can also have an impact on the temporal behaviour of the source. Hence, studying the light curve considering acceleration initiated by different diffusion processes will offer additional insights into the underlying characteristics.

Chapter 5

Long-term Multi-wavelength Spectral variations of blazar S5 0716+714

5.1 Introduction

S5 0716+714 is one among the most active blazars discovered in the Bonn-NRAO radio survey (Kuehr et al., 1981). The source is classified as an IBL (Giommi et al., 1999) and located at redshift, z = 0.31 (Nilsson et al., 2008). It has been extensively studied due to its significant variability on timescales ranging from hours to days across the entire electromagnetic spectrum (Raiteri et al., 2003; Rani et al., 2010; Larionov et al., 2013; Rani et al., 2010, 2013a,b; Gupta et al., 2012). Several optical monitoring campaigns of the source were carried out (Wagner et al., 1996; Rani et al., 2013b, 2015; Tripathi et al., 2024) and notably, a clear evidence of very short periodic oscillations (∼15 min) was reported (Rani et al., 2010). The optical colour versus magnitude plots of the source support a *bluer when brighter* trend (Rani et al., 2010; Tripathi et al., 2024) as well as a *redder when brighter* trend (Tripathi et al., 2024) during different epochs. A convex (concave-upward) X-ray spectrum of the source in the 0.1–10 keV band was observed by *BeppoSAX* (Giommi et al., 1999; Tagliaferri et al., 2003) and *XMM-Newton* (Foschini et al., 2006; Ferrero et al., 2006; Zhang, 2010). During the period of 2015 January–February, *Swift*'s X-ray telescope continuously monitored burst activity from this source and the 0.3–10 keV spectra were well fitted by a simple power-law function, with the spectral index reaching ~ 2.7 (Chandra et al., 2015). A convex hard X-ray spectrum indicates the presence of both synchrotron and the inverse Compton processes, whereas a power-law soft X-ray spectrum suggests a dominant synchrotron emission. Modeling the convex X-ray spectrum with a broken power-law function showed that the break energy shifted toward higher energies as flux increased, suggesting that synchrotron radiation played a dominant role during high flux states (Wierzcholska & Siejkowski, 2015). In γ-rays, the source was initially detected by *EGRET* (Lin et al., 1995), and later with the advent of high sensitivity instruments like *AGILE* (Chen et al., 2008), *MAGIC* (Anderhub et al., 2009), and *Fermi* (Abdo et al., 2009) it was regularly monitored. Notably, this is one of the bright blazars in the *Fermi*/LAT (Large Area Telescope) Bright AGN Sample (LBAS) and the spectra in the energy range 0.1–300 GeV exhibited a power-law shape (Abdo et al., 2010). However, in the Second LAT AGN catalog, the γ-ray spectrum is described using the log-parabola function due to the significant curvature observed (Ackermann et al., 2011). Nevertheless, the source is highly variable in γ-rays, the shortest variability times-cale being 1.5 hr (Geng et al., 2020).

The coordinated multi-wavelength observations of the source in optical and γ-ray frequencies suggest a significant correlation between optical and γ-ray fluxes. However, an orphan X-ray flare was also detected from the source, and this questions the validity of the co-spatial origin of X-ray and other bands (Rani et al., 2013b; Larionov et al., 2013). A multi-wavelength study of the source revealed that the characteristic variability timescales in radio, optical, X-ray, and γ-ray bands are comparable. The highest variability amplitude was found in optical and γ-ray regions, whereas it was lower in X-ray and radio regions (Liao et al., 2014). Further, a detailed multi-wavelength cross correlation function (CCF) analysis of the source was carried out by Wierzcholska & Siejkowski (2016) using the observations performed during January and February 2015. They showed strong correlations among fluxes in optical, UV and γ-ray bands with no appreciable time lag. However, no significant correlation was identified among X-ray flux and fluxes in other wavebands. The study also suggested a common region for the observed optical, UV, and γ-ray emissions. Studies on the broadband SED of the source found a simple SSC model is insufficient and favoured a combination of SSC and EC processes or a two-zone model (see, e.g., Rani et al., 2013b; Liao et al., 2014)

In spite of significant progress in the observational study of blazar S5 0716+714, a clear understanding of the physical scenario of the source during these multi-wavelength spectral variations has not been achieved. The availability of long-term multi-wavelength observations of the source in optical/UV, X-ray, and γ-ray wavelengths offers an excellent opportunity to perform a detailed spectral and temporal study. In particular, we analyze the simultaneous observations of the source by *Swift* and *Fermi*, spanning a period of $\sim$18 years, and perform a statistical study to identify the possible reasons for the spectral variations. The correlations between various spectral fit parameters are investigated under a scenario where the broadband SED shifts towards the blue side during high flux states. We also explore the long-term flux and spectral index distributions to determine whether these distributions have any connection with the correlation results. A broadband spectral study of the source, utilizing synchrotron, SSC, and EC processes, is also perform for the epochs with simultaneous *NuSTAR* observations. We further investigate the dominant source parameter responsible for the spectral variations using the best-fit model SED.

5.2 Observation and Data analysis

We conducted a detailed analysis of S5 0716+714 to investigate its spectral characteristics in differrent wavebands: optical/UV, X-ray, and γ-ray. We utilized all the observations of the source by *Swift*-UVOT, *Swift*-XRT, *NuSTAR* and *Fermi*-LAT telescopes till January 2023.

5.2.1 ***Swift*-XRT**

We conducted an X-ray spectral analysis of the source S5 0716+714 within the 0.3–10 keV range, utilizing all the data recorded from April 2005 to January 2023, totalling 361 observations. The X-ray spectra were obtained using the automated online tool *'Swift-XRT data products generator'*(Evans et al., 2009). This tool generates X-ray light curves, spectra, and images for any point source within the *Swift*-XRT field of view. It automatically selects source and background regions based on the count rate and corrects the products for instrumental artifacts, such as photon pile-up and CCD bad columns. The spectra were binned into groups of a minimum of 20 photons using *grppha* to improve χ^2 statistics.

All spectra were fitted independently using the power-law (PL) and log-parabola (LP) models within XSPEC. The neutral hydrogen column density was fixed at $N_H = 3.11 \times 10^{20}\,\mathrm{cm}^{-2}$ (Kalberla et al., 2005). We discarded all observations with degrees of freedom less than 4. We have also excluded all spectra which rendered a reduced chi-square (χ^2_{red}) value greater than 2. With these criteria, we obtained 302 spectra. F-test were performed to determine the statistical significance of the log-parabola model compared to the power-law model for each individual observation. The best-fit parameters for the power-law model and F-test details are provided in Table 5.1. In Table 5.2, we present the best-fit parameters of the log-parabola model for the 35 spectra for which the F-statistic value (F-value) was > 5 and the null hypothesis probability (P-value) < 0.05 (these observations are avoided in the correlation studies).

5.2.2 ***Swift*-UVOT**

We downloaded all *Swift*-UVOT (Ultra-Violet and Optical Telescope) observations of S5 0716+714 from the HEASARC archive. UVOT has three optical filters; u (3465 Å), b (4392 Å), and v (5468 Å), and three UV filters; uvw1 (2600 Å), uvm2 (2246 Å), and uvw2 (1928 Å). Standard data reduction procedures[1] were followed to obtain the spectral files. Multiple images in each filter

---

[1] `https://Swift.gsfc.nasa.gov/analysis/threads/uvot_thread_spectra.html`

Table 5.1: Table showing best-fit parameters of power-law spectral fitting of *Swift*-XRT observations.

ObsID	Exposure time (s)	Observation time (in MJD)	$\log_{10}$Flux ($\mathrm{ergs\,cm^{-2}\,s^{-1}}$)	Spectral index (α_{X})	χ^2_{red}(d.o.f)	F-value	P-value
35009001	18873.447	53462.04	-11.280±0.025	2.68±0.10	1.35(36)	3.14	0.085
35009002	7456.296	53600.62	-10.923±0.018	2.40±0.07	1.17(69)	17.00	0.000
35009003	5678.500	54375.70	-11.076±0.032	2.05±0.11	0.84(31)	5.89	0.024
35009004	2461.633	54396.69	-10.801±0.028	2.30±0.11	1.01(30)	7.18	0.012
35009005	1995.273	54397.63	-11.001±0.040	2.20±0.14	0.93(16)	1.29	0.274
35009006	2723.673	54398.18	-10.929±0.032	2.17±0.12	0.96(27)	9.47	0.005
35009007	2201.395	54399.51	-10.949±0.038	2.05±0.14	1.94(24)	8.19	0.009
35009008	1960.757	54400.37	-10.615±0.026	2.45±0.10	0.82(35)	2.83	0.102
35009009	1756.998	54401.33	-10.885±0.041	2.25±0.16	0.92(15)	3.36	0.088
35009012	2803.152	54407.20	-10.520±0.025	2.57±0.10	0.59(35)	0.12	0.733
35009013	1923.724	54410.15	-11.052±0.044	2.43±0.20	0.64(13)	8.96	0.011
35009014	2005.828	54413.15	-10.849±0.035	2.50±0.14	0.96(18)	0.08	0.780
35009015	2380.795	54417.10	-10.958±0.037	2.58±0.17	1.22(16)	2.65	0.124
35009016	1551.578	54577.62	-10.903±0.042	2.49±0.19	0.90(12)	4.73	0.052
35009017	2002.351	54584.75	-10.350±0.021	2.63±0.08	1.21(49)	0.15	0.697

(Table is available in its entirety in Appendix B, Table B.1).

Table 5.2: Table showing best-fit parameters of selected *Swift*-XRT observations using log-parabola model.

ObsID	Exposure time (s)	Observation time (in MJD)	$\log_{10}$Flux ($\mathrm{ergs\,cm^{-2}\,s^{-1}}$)	Spectral index (α_{X})	Spectral curvature β	χ^2_{red}(d.o.f)
35009002	7456.296	53600.62	-10.866±0.029	2.45±0.07	-0.46±0.17	0.95(68)
35009003	5678.500	54375.70	-11.012±0.060	2.12±0.11	-0.41±0.29	0.77(30)
35009004	2461.633	54396.69	-10.746±0.047	2.35±0.10	-0.43±0.25	0.84(29)
35009006	2723.673	54398.18	-10.864±0.051	2.25±0.11	-0.46±0.25	0.73(26)
35009007	2201.395	54399.51	-10.830±0.068	2.17±0.12	-0.67±0.28	1.49(23)
35009013	1923.724	54410.15	-10.899±0.146	2.38±0.16	-0.81±0.61	0.40(12)
35009070	1389.112	55566.48	-10.992±0.100	2.22±0.20	-0.67±0.44	0.58(9)
35009086	2324.264	55860.45	-10.723±0.058	2.15±0.12	-0.52±0.27	1.22(28)
35009088	1955.686	55862.45	-10.852±0.076	2.38±0.13	-0.66±0.37	0.88(17)
35009090	1078.077	55906.81	-10.694±0.102	2.21±0.20	-0.74±0.41	1.15(8)
32554001	4979.014	56185.82	-10.882±0.038	2.16±0.09	-0.36±0.19	1.00(45)
32554002	4677.188	56187.62	-11.001±0.066	2.03±0.13	-0.72±0.25	0.88(25)
35009153	6934.489	57044.29	-10.646±0.024	2.29±0.06	-0.21±0.14	0.93(88)
35009168	2478.112	57051.85	-10.669±0.056	2.18±0.10	-0.42±0.27	0.98(36)
35009170	6146.678	57052.99	-10.624±0.021	2.33±0.05	-0.34±0.12	1.18(134)

(Table is available in its entirety in Appendix B, Table B.2).

Table 5.3: Table showing best-fit parameters of power-law spectral fitting of *Swift*-UVOT observations.

ObsID	Exposure time (s)	Observation time (in MJD)	$\log_{10}$Flux ($\mathrm{ergs\,cm^{-2}\,s^{-1}}$)	Spectral index ($\alpha_{\mathrm{O/UV}}$)	χ^2_{red}(d.o.f)
35009002	7456.296	53600.62	-9.923±0.016	2.16±0.10	0.63(4)
35009004	2461.633	54396.69	-9.91±0.011	2.21±0.07	0.76(4)
35009006	2723.673	54398.18	-9.926±0.011	2.26±0.07	1.28(4)
35009007	2201.395	54399.51	-9.939±0.011	2.28±0.07	0.74(4)
35009008	1960.757	54400.37	-9.783±0.011	2.13±0.07	0.69(4)
35009009	1756.998	54401.33	-9.818±0.011	2.22±0.07	0.80(4)
35009012	2803.152	54407.20	-9.845±0.011	2.13±0.07	1.32(4)
35009013	1923.724	54410.15	-9.929±0.011	2.17±0.07	1.01(4)
35009014	2005.828	54413.15	-9.958±0.011	2.12±0.07	0.98(4)
35009015	2380.795	54417.10	-10.013±0.011	2.2±0.07	0.82(4)
35009016	1551.578	54577.62	-9.769±0.018	2.18±0.12	0.62(3)
35009017	2002.351	54584.75	-9.716±0.011	1.99±0.07	1.27(4)
35009018	4215.456	54585.83	-9.735±0.011	2.04±0.07	0.89(4)
35009020	1906.966	54588.69	-9.715±0.011	2.09±0.07	1.36(4)
35009021	2280.966	54798.81	-9.938±0.011	2.11±0.07	0.72(4)

(Table is available in its entirety in Appendix B, Table B.3).

were summed over the extensions using the *uvotimsum* tool for each observations. A circular region with a 5 arcsec radius centered at the source was used to extract the source counts. A circular region with a radius of about 20 arcsec, free from the source contamination, was used for background estimation. The spectral products for each filter were then generated using the *uvot2pha* tool.

To perform a power-law spectral fit in XSPEC, we considered only the observations for which images were available in at least four filters. We obtained 249 observations out of a total of 361. The optical/UV data were corrected for Galactic reddening using the UVRED model, with the parameter E_{B-V} fixed at 0.027 (Schlafly & Finkbeiner, 2011). We found that some observations required the addition of systematic error to achieve better fit statistics. We discarded those data which demands more than 5 percent of the systematic error to obtain χ^2_{red} less than 2. After these selection criteria, we got 235 UVOT observations, and the best-fit parameters of the spectral fit are provided in Table 5.3.

5.2.3 *NuSTAR*

The source S5 0716+714 was observed by *NuSTAR* on 2015 January 24 (MJD 57046.11) and on 2022 April 4 (MJD 59673.39). This epochs are marked with solid orange vertical lines in Figure 5.1. The observations were downloaded through NASA's HEASARC interface, and processed by using the software package NuSTARDAS (Version 2.1.1) within the HEASOFT environment (Version 6.29). For ObsID 90002003002 (MJD 57046.11), the source spectrum was extracted from a circular region with a 45 arcsec radius, while for ObsID 60701037002 (MJD 59673.39), a radius of 20 arcsec was used (low flux). Background estimation was performed using circular regions with radii of 70 arcsec and 50 arcsec, respectively, for ObsIDs 90002003002 and 60701037002. The *nuproduct* (Version 0.3.3) tool was employed to derive the source and background spectra after running *nupipeline* (Version 0.4.9) on each observation. Subsequently, the FPMA and FPMB source spectra were individually binned using the *grppha* tool to ensure a minimum of 30 counts per bin. The final spectra were fitted with an absorbed log-parabola model and the unabsorbed fluxes in the 3-79 keV energy range were used for the broadband spectral study.

5.2.4 *Fermi*-LAT

In this study, we have determined 2-day binned *Fermi*-LAT data in the energy range of 0.1-300 GeV to match the *Swift* observations. To perform data reduction, we employed *Fermitools* and followed the standard procedures[2]. Photons within a circular region of interest (ROI) with a 10 degree radius, centered on the position of S5 0716+714 were chosen. Only photon-like events falling under the category *evclass*=128 and *evtype*= 3 were included. Additionally, a zenith angle cut off (less than 90 degree) was employed to eliminate background γ-ray contamination originating from the Earth's limb. We conducted a binned likelihood analysis method to fit the data across the entire time interval. We used the standard templates iso_P8R3_SOURCE_V3_v1.txt

---

[2] `https://Fermi.gsfc.nasa.gov/ssc/data/analysis/scitools/`

and gll_iem_v07.fits as the isotropic background model and Galactic diffuse-emission model, respectively[3]. We included all γ-ray sources within a circular region of 20 degree radius from the central point in the fitting process, and their spectral characteristics were adopted from fourth Fermi Large Area Telescope (4FGL) catalogue. The parameters of all sources within the ROI were left as free variables, whereas those of sources outside the ROI were set to their catalogue values. To evaluate the significance of detecting each source within the ROI, we employed the test statistic (TS), defined as TS=$2\log(\mathcal{L})$, where $\mathcal{L}$ represents the likelihood parameter of the analysis. We froze the spectral parameters of all sources with TS < 25. The resulting output file was used as the input sky model for the unbinned likelihood analysis, which was then employed to determine the γ-ray flux and spectral index for the 2-day time bins that were simultaneous with *Swift* observations. We opted for the PowerLaw2 function to model the γ-ray spectrum of S5 0716+714 within each selected time bin, as it provided a good fit for these short time intervals. We started with the 'DRMNFB' optimizer, and sources with a TS value less than 9 were removed when they did not converge during the fitting process. Furthermore, for sources with TS values between 9 and 25, all parameters except the normalisation were held constant. The obtained fits were then optimized using the 'Newminuit'. The γ-ray spectrum of the source in the 4FGL catalogue is described by a log-parabola model. In order to determine whether there is a significant curvature in the γ-ray spectrum within the selected time bins, we computed the test statistics for both power-law ($\mathrm{TS_{pl}}$) and log-parabola ($\mathrm{TS_{lp}}$) functions. The significance of spectral curvature ($\mathrm{TS_c}$) is then calculated as $\mathrm{TS_c} = \mathrm{TS_{lp}}$ - $\mathrm{TS_{pl}}$. The best-fit parameters along with the TS values are provided in Table 5.4. A significant spectral curvature will result in a large positive value for $\mathrm{TS_c}$. Further, we produced a 3-day binned light curve for the entire period (till MJD 59975), and the obtained fluxes and indices were then used for the study of distribution of fluxes and indices.

---

[3] `https://fermi.gsfc.nasa.gov/ssc/data/access/lat/BackgroundModels.html`

Table 5.4: Table showing best-fit parameters of spectral fitting using a power-law model (along with TS values) for selected γ-ray observational data (2-day bins from *Fermi*-LAT) simultaneous with *Swift* observations.

$T_{\rm start}$ (MJD)	$T_{\rm stop}$ (MJD)	$\log_{10}$ Flux ($\rm photons\,cm^{-2}\,s^{-1}$)	Spectral index (α_γ)	$TS_{\rm pl}$	$TS_{\rm lp}$	$TS_{\rm c}$
54797	54799	-6.495±0.12	2.339±0.234	65.41	65.41	0.00
54805	54807	-6.578±0.14	1.956±0.203	55.66	56.26	0.60
54812	54814	-6.795±0.186	2.316±0.336	20.35	22.58	2.23
54819	54821	-6.776±0.165	2.161±0.269	26.58	26.97	0.39
54833	54835	-7.317±0.438	2.032±0.546	7.59	7.59	0.00
54849	54851	-7.023±0.271	2.509±0.555	7.46	7.83	0.37
54863	54865	-6.788±0.328	2.835±0.925	6.35	6.35	0.00
54866	54868	-7.172±0.400	1.905±0.503	18.75	18.75	0.00
54867	54869	-7.467±0.448	1.617±0.473	17.90	17.91	0.01
54873	54875	-7.133±0.329	2.194±0.498	7.59	5.51	-2.08
54877	54879	-7.462±0.451	1.669±0.499	12.54	13.48	0.94
54881	54883	-7.108±0.247	1.929±0.336	10.75	11.65	0.90
54883	54885	-7.131±0.328	2.118±0.569	8.89	8.89	0.00
54887	54889	-6.851±0.190	2.334±0.343	24.71	25.55	0.84
55119	55121	-6.536±0.106	2.098±0.180	81.68	82.82	1.14

(Table is available in its entirety in Appendix B, Table B.4).

5.3 Multi-wavelength analysis

The multi-wavelength light curve of the source S5 0716+714 from April 2005 to January 2023 (MJD 53461–59975) is shown in Figure 5.1. The approximate average flux values estimated in optical/UV (2–7 eV), X-ray (0.3–10 keV) and γ-ray (0.1–300 GeV) are $1.16\times10^{-10}\,\rm erg\,cm^{-2}s^{-1}$, $2.12\times10^{-11}\,\rm erg\,cm^{-2}s^{-1}$ and $2.24\times10^{-7}\,\rm phs\,cm^{-2}s^{-1}$, respectively. In Figure 5.2, the spectral indices in the respective waveband are plotted against time in MJD. The average photon spectral index in the optical/UV and X-ray bands ~ 2.22, while that in γ-ray is ~ 2.09. Figure 5.1 and 5.2 clearly show that the source exhibits significant fluctuation in flux and spectral indices across all energy bands.

5.3.1 Flux-Index Correlation

The scatter plots of the integrated fluxes in optical/UV, X-ray, and γ-ray energies with their corresponding photon indices $\alpha_{\rm O/UV}, \alpha_{\rm X}$ and α_γ, respectively, are shown in Figure 5.3. We observe a significant negative correlation between the optical/UV flux and $\alpha_{\rm O/UV}$. A Spearman rank correlation study between

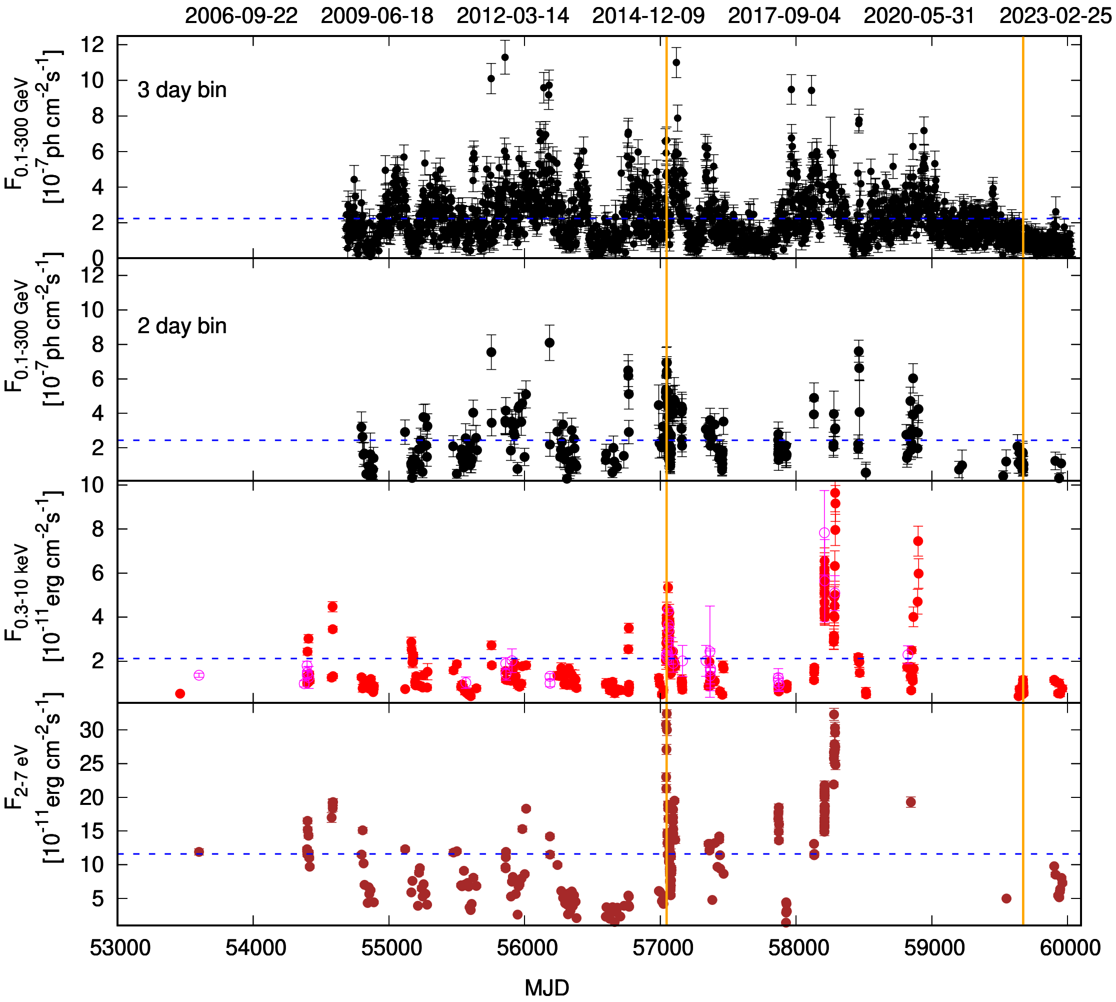

Figure 5.1: Multi-wavelength light curve of S5 0716+714. From top to bottom: panel 1 shows 3-day binned γ-ray light curve using *Fermi*-LAT observations in the energy range 0.1–300 GeV. Second panel shows 2-day binned γ-ray light curve simultaneous with *Swift* observations. X-ray light curve in 0.3–10 keV energy range using *Swift*-XRT observations is shown in panel 3 (red solid circles and magenta open circles correspond to the observations with power-law and log-parabola models, respectively) and optical/UV light curve in the 2–7 eV energy band using *Swift*-UVOT observations is given in the fourth panel. The dashed blue lines represent the average flux in each energy bands. The vertical line in orange colour represents the epochs where *NuSTAR* observations are available.

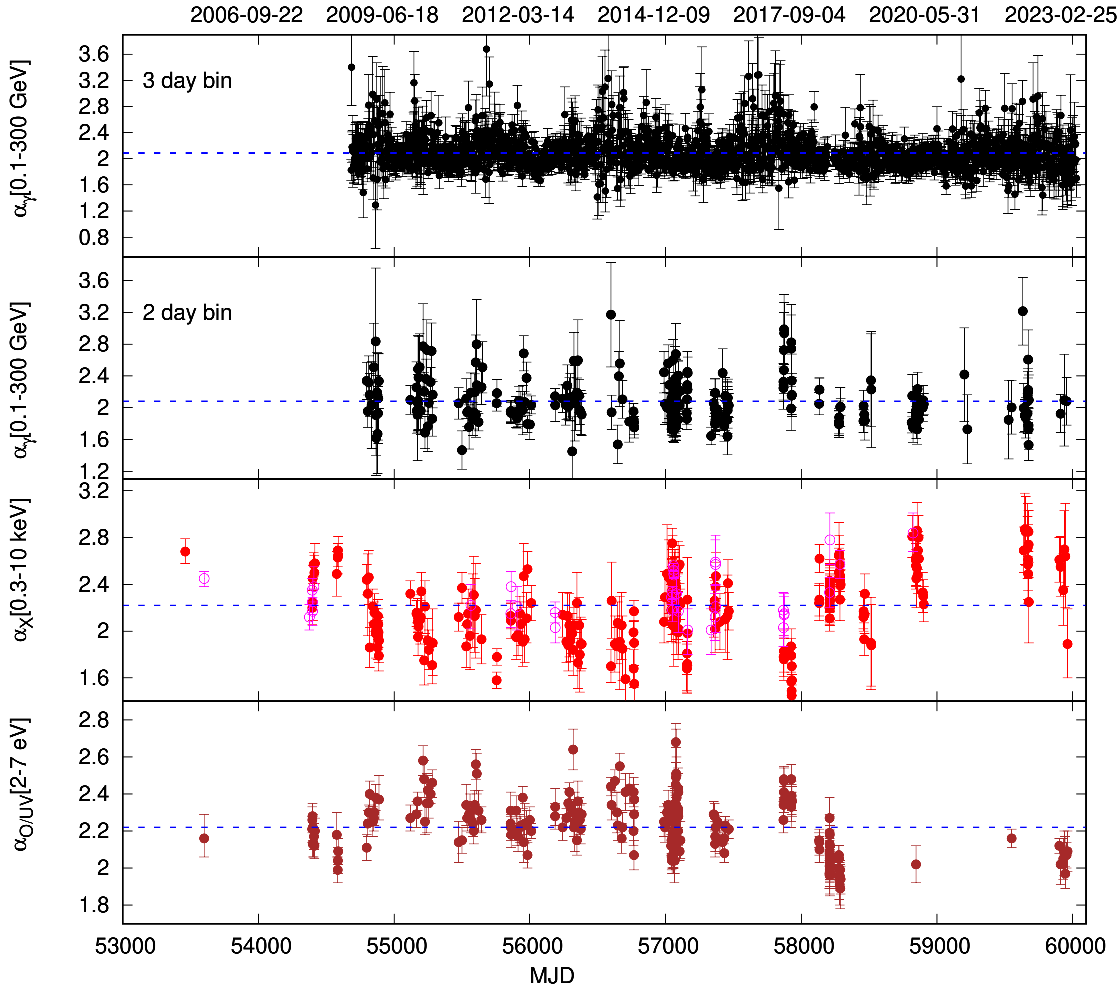

Figure 5.2: The spectral indices corresponding to the observations shown in Figure 5.1. Top panel shows the γ-ray index (α_γ) for 3-day binned data and the second panel is for 2-day binned data simultaneos with *Swift* observations, third panel is for X-ray ($\alpha_{\rm X}$), and fouth panel is for optical/UV ($\alpha_{\rm O/UV}$). The open circles in magenta colour are log-parabola index at 1 keV corresponding to the observations fitted by log-parabola model. The dashed blue lines represent the average spectral index in each energy band.

these quantities yield a correlation coefficient, r_s = -0.66 with a null hypothesis probability, $p_s < 0.0001$. This negative correlation suggests a *harder when brighter* behavior. Whereas, a mild positive correlation is observed between the X-ray flux in the 0.3 to 10 keV range and $\alpha_{\rm X}$ ($r_s = 0.38$, $p_s < 0.0001$), which implies a *softer when brighter* behavior of the source. These correlation are consistent with the broadband SED of the blazar shifting towards blue end during flux enhancement as shown in Figure 5.6. The spread of $\alpha_{\rm X}$ around 2 suggests the presence of both steep synchrotron and hard inverse Compton components in the X-ray band. Also, the number of observations with $\alpha_{\rm X}$ > 2 is high compared to those with $\alpha_{\rm X} < 2$, suggesting that the synchrotron spectral component often dominates in this energy range (Figure 5.6). The observed *softer when brighter* trend may then indicate a shift of the spectrum to high energies during an increase in flux (*bluer when brighter*) (Giommi et al., 1999). Similar behavior of the source in the X-ray region was also reported in earlier studies by measuring the hardness ratio (Giommi et al., 1999; Zhang, 2010; Wierzcholska & Siejkowski, 2015). In the γ-ray region, we did not find any significant correlation between flux and α_γ (r_s = -0.001, p_s = 0.987). However, Geng et al. (2020) reported a significant spectral hardening of the γ-ray spectrum with increase in flux during certain outbursts. The absence of such a correlation over a long period, regardless of the flux states, could also suggest that the source displays either *softer or harder when brighter* behaviour during different flaring events. Alternatively, the presence of a peak or a break in the γ-ray region can distroy the possible correlation. The latter inference is further asserted by the distribution of the γ-ray spectral index around 2 (bottom panel of Figure 5.3).

5.3.2 Flux-Flux Correlation

The scatter plots between the integrated fluxes of optical/UV, X-ray, and γ-ray energies are shown in Figure 5.4. A significant positive correlation is observed between the X-ray flux and optical/UV flux, with $r_s = 0.74$ and p_s < 0.0001, whereas a moderate correlation is observed between the X-ray and γ-ray flux ($r_s = 0.42$, $p_s < 0.0001$). A moderate correlation is also observed

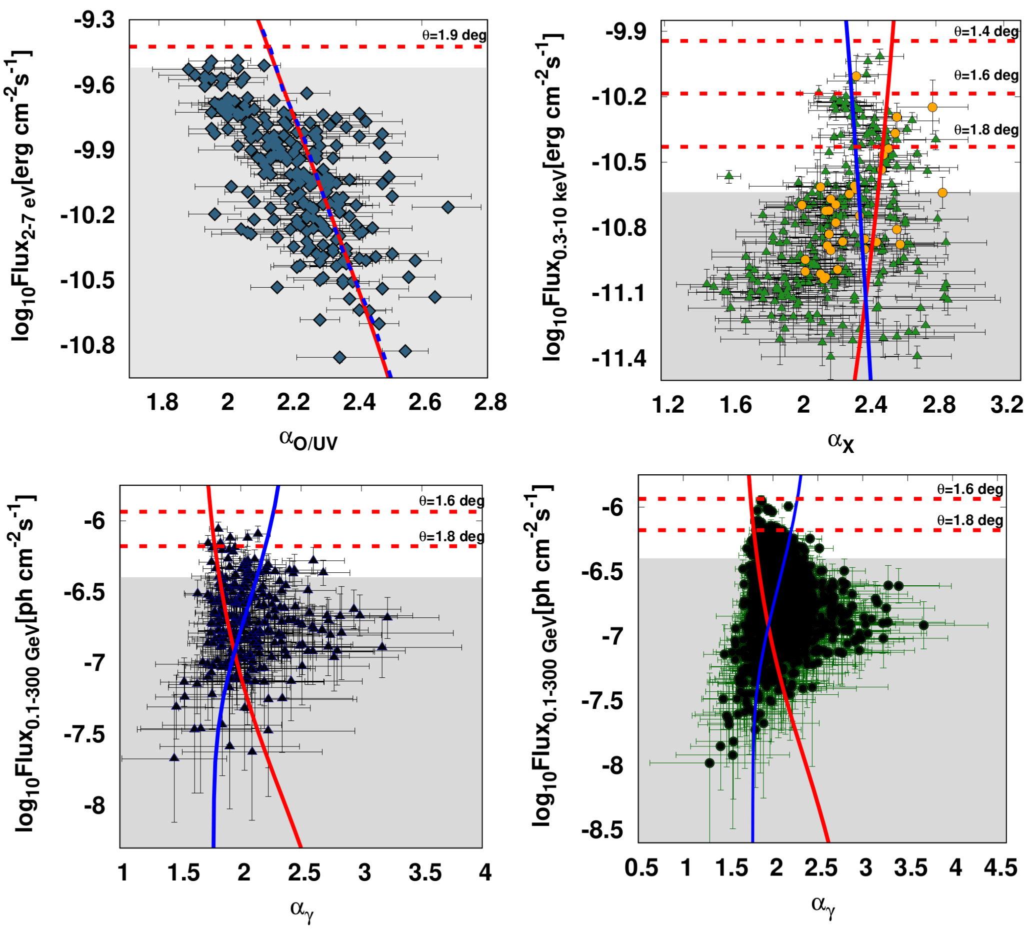

Figure 5.3: Scatter plots of the fluxes and indices in optical/UV, X-ray and γ-ray energies. The upper left panel is for optical/UV, the upper right is for X-ray (filled circles in orange colour correspond to the X-ray observations with log-parabola model), the lower left is for γ-ray in the 0.1-300 GeV energy range for 2-day binned data simultaneous with *Swift* observations, and the lower right is for 3-day binned γ-ray data for the entire epoch. The red and blue colour lines represent the flux-index relation in each energy-band assuming variation in bulk Lorentz factor and magnetic field, respectively. The top of the shaded regions represent the maximum attainable flux at a viewing angle of $\theta = 2$ degrees in each energy band (see Section 5.4).

between the optical/UV and γ-ray fluxes (r_s = 0.49, p_s < 0.0001). The latter correlation was also reported before, though it was performed for short time periods (Larionov et al., 2013; Rani et al., 2013b). This study identifies for the first time a strong correlation between optical/UV and X-ray flux over a long duration for the source S5 0716+714. These flux correlations are also consistent with the *bluer when brighter* behavior of the source which can be visualized from Figure 5.6.

5.3.3 Index-Index Correlation

The scatter plots illustrating the variations between the optical/UV, X-ray, and γ-ray indices are presented in Figure 5.5. In contrast to the positive correlation between X-ray and optical/UV fluxes, the *X-ray index shows a significant negative correlation with the optical/UV index.* The Spearman rank correlation analysis yielded a coefficient of r_s = -0.69, with p_s < 0.001. On the other hand, a mild correlation is found between the optical/UV and the γ-ray indices (r_s = 0.32, p_s < 0.001), while a mild negative correlation between the X-ray and γ-ray indices (r_s = -0.32, p_s = 0.001). The observed anti-correlation between the optical/UV and X-ray indices may be associated with the *harder when brighter* behaviour in optical/UV and *softer when brighter* behaviour in the X-ray region. This is again consistent with the spectrum shifting towards the blue end during high flux states (Figure 5.6).

To investigate whether the correlation between X-ray and optical/UV indices depends upon the flux state of the source, we repeated the study for those observations with X-ray flux above and below the average flux. Interestingly, we find that both these states supported the negative correlation; however, it is more prominent for low-flux states, the correlation coefficient being r_s = -0.72 (p_s < 0.001) while that for the high flux states is r_s = -0.42 (p_s < 0.001).

The power-law fit to the optical/UV spectrum mostly results with index $\alpha_{\mathrm{O/UV}} \gtrsim 2$. This indicates that the optical/UV emission mostly falls on the decaying part of the synchrotron spectral component. The X-ray spectral indices, on the other hand, have both cases with $\alpha_{\mathrm{X}} < 2$ and $\alpha_{\mathrm{X}} > 2$. This suggests that

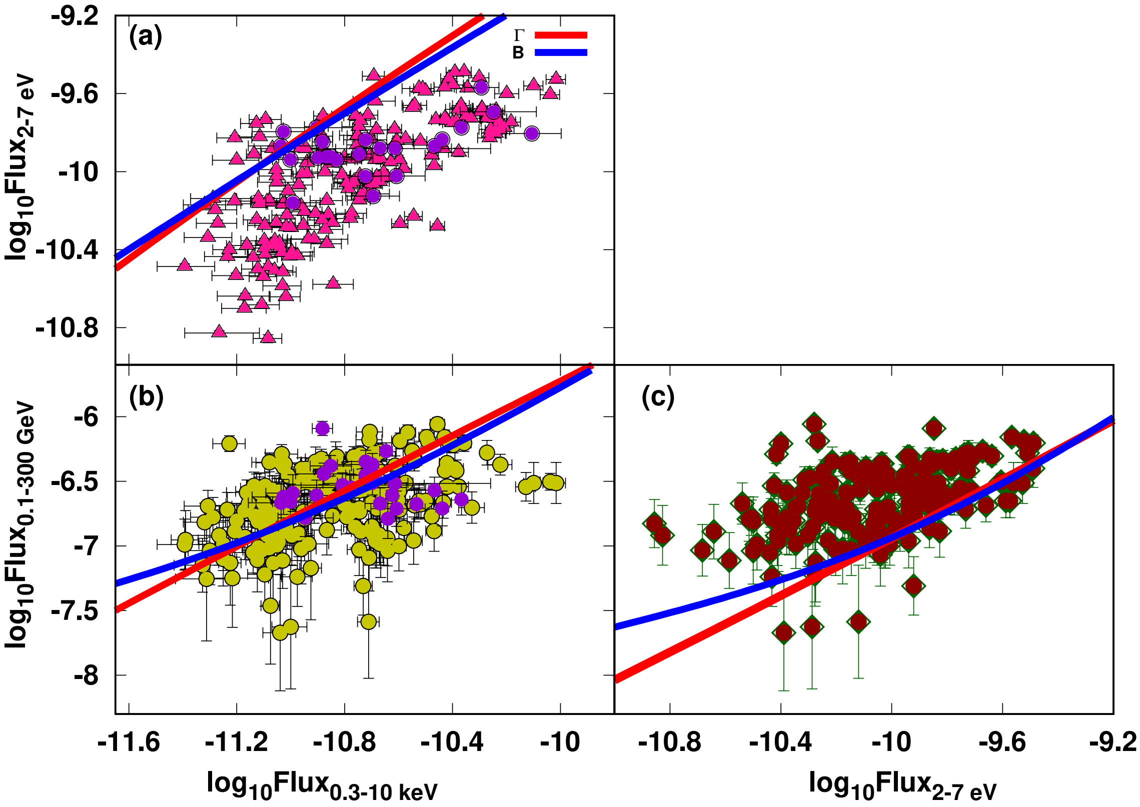

Figure 5.4: Scatter plots between fluxes in optical/UV, X-ray and γ-ray energies: **(a)** X-ray (0.3–10 keV)(Filled circles in violet colour correspond to the X-ray observations with the log-parabola model) and optical/UV (2–7 eV), **(b)** X-ray (0.3–10 keV) and γ-ray (0.1–300 GeV), and **(c)** Optical/UV (2–7 eV) and γ-ray (0.1–300 GeV). The red and blue colour lines represent the flux-flux relation assuming variation in bulk Lorentz factor (Γ) and magnetic field (B), respectively.

the X-ray energy region may fall either on the raising part of the Compton spectral component ($\alpha_{\mathrm{X}} < 2$) or decaying part of the synchrotron spectral component ($\alpha_{\mathrm{X}} > 2$). If we assume the underlying electron distribution is responsible for the broadband emission as a broken power-law, then $\alpha_{\mathrm{X}} > 2$ maps the high energy end of the particle distribution, while $\alpha_{\mathrm{X}} < 2$ maps the low energy end of the particle distribution. Since the condition $\alpha_{\mathrm{O/UV}} \gtrsim 2$ was true for majority of the observations, the optical region maps the particle distribution immediately after the break energy. In Figure 5.5 (a), we marked this region by vertical and horizontal dashed lines.

The correlation study between $\alpha_{\mathrm{O/UV}}$ and α_{X} for those observation having $\alpha_{\mathrm{X}} < 2$, resulted in a moderate negative correlation with r_s = -0.46 (p_s = 0.001). This result is consistent with the results obtained for blazar Mkn 421 (Baheeja et al., 2022). Such a correlation strongly disagrees with the radiative loss origin of a broken power-law electron distribution (Kardashev, 1962; Rybicki & Lightman, 1986). We also performed the $\alpha_{\mathrm{O/UV}} - \alpha_{\mathrm{X}}$ correlation study for the observations with $\alpha_{\mathrm{X}} > 2$. Again, we find a moderate negative correlation with r_s = -0.49 ($p_s < 0.0001$). This observed correlation may possibly be associated with the a shift in the spectrum towards blue side. For instance, shift towards the bluer end will harden the optical/UV index (optical/UV flux close to the peak) while softening the X-ray index (the X-ray flux falling at the synchrotron tail) as shown in Figure 5.6.

Our correlation analysis suggests that the dominant spectral changes encountered during different flux states may be associated with the shift in the SED towards bluer/redder end. Interestingly, this also indicates that the spectral variation in the blazar due to the changes in the underlying electron distribution may not be substantial. We explore the possible scenario under which these correlation results can be inferred in Section 5.4. The correlation between different observed quantities are summarized in Table 5.5.

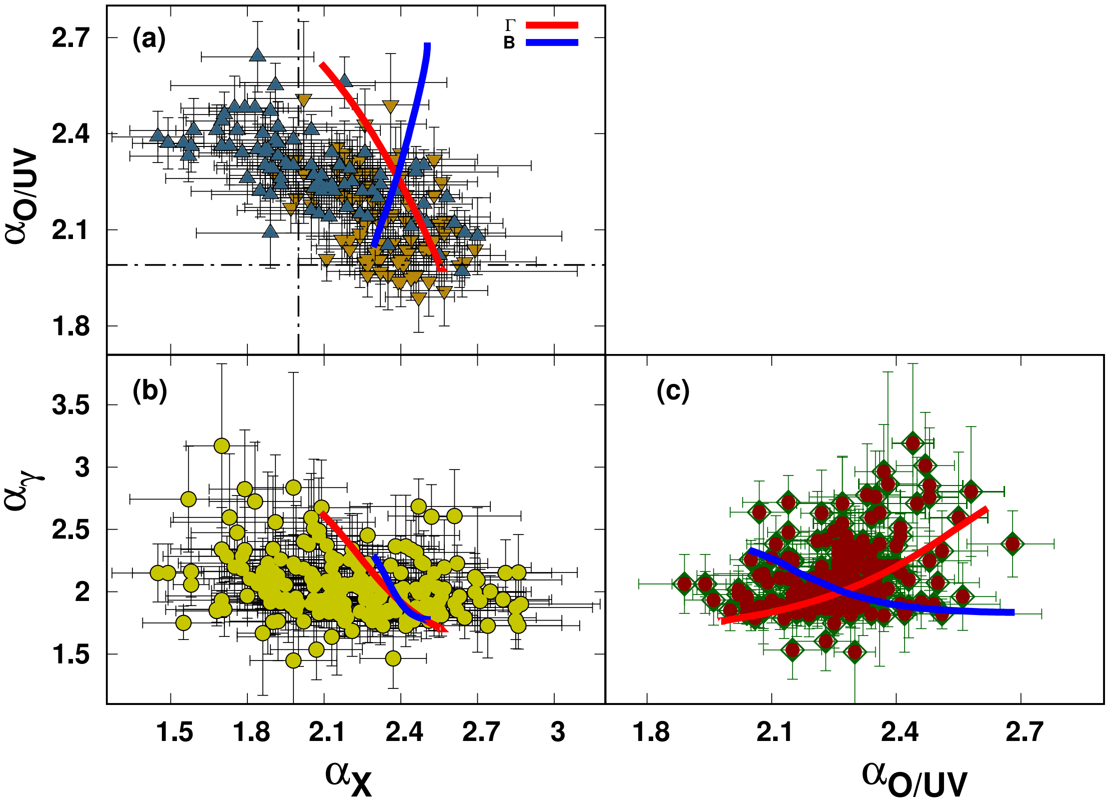

Figure 5.5: Scatter plots between the spectral indices: **(a)** X-ray (α_X)(filled triangles in dark-gray colour and filled inverted triangles in dark-yellow colour represent the observations with low and high X-ray fluxes, respectively.) and Optical/UV ($\alpha_\mathrm{O/UV}$), **(b)** X-ray (α_X) and γ-ray (α_γ), and **(c)** Optical/UV ($\alpha_\mathrm{O/UV}$) and γ-ray (α_γ). The red and blue colour lines represent the index-index relation with variation in Lorentz factor (Γ) and magnetic field (B), respectively.

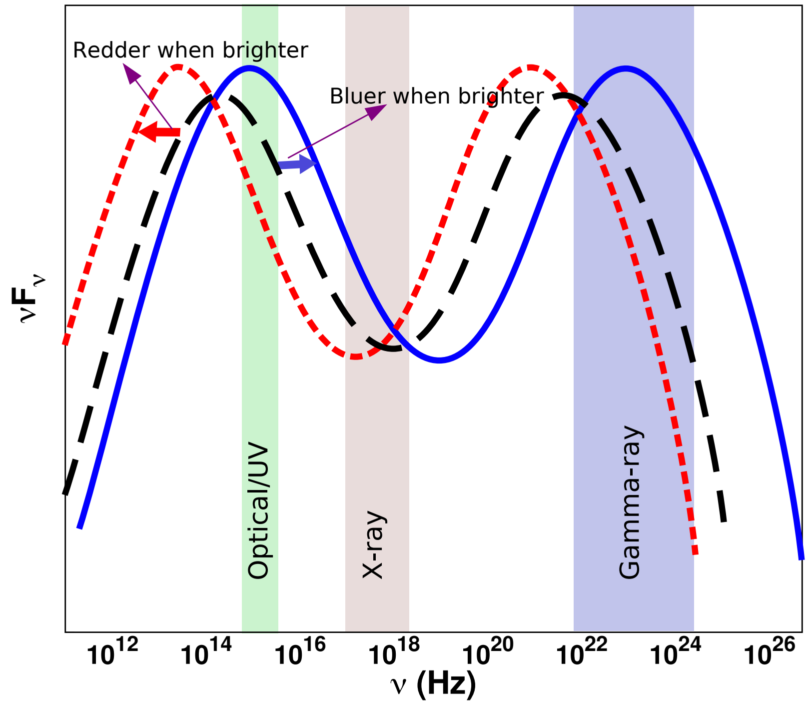

Figure 5.6: The shift of the SED towards the bluer and redder ends as the source becomes brighter is demonstrated. The hardening of the optical spectrum and the steepening of the X-ray spectrum are associated with the blue shift.

Table 5.5: Spearman correlation coefficient (r_s) and corresponding null hypothesis probability (p_s) of various relations among fluxes and indices.

	No.of data points	r_s	p_s
$\alpha_{\rm O/UV} - {\rm Flux}_{2-7\ \rm eV}$	235	-0.66	< 0.001
$\alpha_{\rm X} - {\rm Flux}_{0.3-10\ \rm keV}$	267	0.38	< 0.001
$\alpha_\gamma - {\rm Flux}_{0.1-300\ \rm GeV}$	252	-0.001	0.987
$\alpha_\gamma - {\rm Flux}_{0.1-300\ \rm GeV}$	1676	0.002	0.927
${\rm Flux}_{2-7\ \rm eV} - {\rm Flux}_{0.3-10\ \rm keV}$	184	0.74	< 0.001
${\rm Flux}_{0.1-300\ \rm GeV} - {\rm Flux}_{2-7\ \rm eV}$	175	0.49	< 0.001
${\rm Flux}_{0.1-300\ \rm GeV} - {\rm Flux}_{0.3-10\ \rm keV}$	209	0.42	< 0.001
$\alpha_{\rm O/UV} - \alpha_{\rm X}$	184	-0.69	< 0.001
$\alpha_\gamma - \alpha_{\rm O/UV}$	175	0.32	< 0.001
$\alpha_\gamma - \alpha_{\rm X}$	209	-0.32	0.001
$\alpha_{\rm O/UV} - \alpha_{\rm X} > 2$	139	-0.49	< 0.001
$\alpha_{\rm O/UV} - \alpha_{\rm X} < 2$	45	-0.46	0.001

5.3.4 Distribution of fluxes and indices

A long-term flux distribution study has the potential to understand the processess responsible for the flux variations in blazars. Studies conducted on blazar light curves across different energy bands largely support a log-normal variability (Vaughan et al., 2003; Romoli et al., 2018; Sinha et al., 2018; Rieger, 2019; Khatoon et al., 2020). Such a variability can be associated with the moving perturbation in the accretion disk (multiplicative process) or a large ensemble of mini-jets buried with in the blazar jet (Narayan & Piran, 2012). Alternatively, for a power-law spectrum, a log-normal variability in flux can be an outcome of normal variation in the photon index (Sinha et al., 2018; Khatoon et al., 2020). The flux distribution of certain blazar light curves also support a double log-normal behaviour (Sinha et al., 2018; Khatoon et al., 2020; Thekkoth et al., 2023).

To investigate the behaviour of the flux and spectral variability, we performed Anderson-Darling (AD) tests on the logarithm of fluxes and the spectral indices (Press et al., 1992). Under the AD test, a deviation of the given distribution from normality is prominent when the test statistics exceed a critical value. In Table 5.6, we present the details of the AD test for spectral indices and the logarithm of fluxes, with critical values calculated at a 5% significance level for the null hypothesis. From the AD test, we find that only the distributions of optical/UV and X-ray index satisfy the normal behaviour, while the distributions of the logarithm of fluxes in optical/UV, X-ray, and γ-ray energies, as well as the γ-ray index are inconclusive.

We extended the study on the distribution of indices and the logarithm of fluxes by analysing the corresponding histograms. These histograms were first fitted using a single Gaussian probability density function (PDF) defined as

$$f(x) = \frac{a_1}{\sqrt{2\pi\sigma^2}} \exp\left[-\frac{(x-\mu)^2}{2\sigma^2}\right] \tag{5.1}$$

where, a_1 is the normalisation factor, μ and σ are the mean and standard deviation of the distribution, respectively. In case of poor fit statistics, the fitting is repeated with a double Gaussian PDF given by

$$\begin{aligned} g(x) = &\frac{a_2}{\sqrt{2\pi\sigma_1^2}} \exp\left[-\frac{(x-\mu_1)^2}{2\sigma_1^2}\right] \\ +&\frac{1-a_2}{\sqrt{2\pi\sigma_2^2}} \exp\left[-\frac{(x-\mu_2)^2}{2\sigma_2^2}\right] \end{aligned} \tag{5.2}$$

where μ_1 and μ_2 are the means of the distribution with standard deviations σ_1 and σ_2, respectively. The histograms of the logarithm of fluxes and indices along with the best-fit PDF are shown in Figure 5.7. The parameters obtained from the fitting are provided in Table 5.7. Contrary to the AD test, we find the histogram of the logarithm of optical/UV fluxes can be well-fitted with a single Gaussian PDF with $\chi^2_{red} = 1.14$. A plausible reason for this can be the non-availability of high flux states that govern the tail of the distribution and which is evident from the histogram (top left panel of Figure 5.7). Since the AD test is sensitive to the tails of the distribution, the test results are inconclusive. The distributions of optical/UV and X-ray spectral indices, on the other hand, support a single Gaussian PDF with χ^2_{red} values 0.82 and 0.90, respectively. This is consistent with the conclusion drawn from the AD test. Nevertheless, if the results obtained from the histogram analysis were correct, then we could extend our inference that the log-normal variabitly of the optical/UV fluxes may be associated with the normal variations in the spectral index.

A single Gaussian PDF did not provide a satisfactory fit to the histogram of logarithm of X-ray fluxes ($\chi^2_{red} = 1.99$). Instead, the double Gaussian PDF was able to provide a better fit ($\chi^2_{red} = 1.47$). The double Gaussian behaviour of the logarithm of X-ray fluxes may be associated with the presence of two emission processes (synchrotron and SSC) active at this energy band. However, such a feature does not appear in the index distribution. Extending this study to hard X-rays (with predominant emission from SSC process) can probably provide a better answer to this unusual behaviour. At the γ-ray energies, the histograms of both indices and the logarithm of fluxes deviate from a Gaussian nature but can closely represent a double Gaussian PDF. The best fit reduced chi-squares obtained for a double Gaussian fit to indices and fluxes being 1.83 and 1.42, respectively. These fit results are better than the ones obtained for a single Gaussian fit (5.33 and 2.82, respectively). This is consistent with the conclusion drawn from the AD test as well.

Table 5.6: Anderson Darling test results of index/flux distributions in optical/UV, X-ray and γ-ray bands.

	Number of data points	Normal (Spectral index) AD(critical value)	Normal (Flux) AD(critical value)	Normal (log Flux) AD(critical value)
optical/UV	235	0.61 (0.774)	4.07 (0.774)	1.22 (0.774)
X-ray	267	0.32 (0.776)	15.59 (0.776)	2.33 (0.776)
γ-ray (0.1-300 GeV)	1676	29.31 (0.785)	34.73 (0.785)	4.62 (0.785)

Table 5.7: Best fit parameter values of the probability density functions fitted to the logarithm of flux and spectral indices in optical/UV, X-ray, and γ-ray.

	PDF	a_1/a_2	μ_1	σ_1	μ_2	σ_2	χ^2_{red}(d.o.f)
$\log_{10}\mathrm{Flux}_{2-7\ \mathrm{eV}}$	Gaussian	0.94±0.07	-10.00±0.02	0.30±0.02			1.14(21)
$\alpha_{\mathrm{O/UV}}$	Gaussian	0.96±0.06	2.21±0.01	0.16±0.01			0.82(17)
$\log_{10}\mathrm{Flux}_{0.3-10\ \mathrm{keV}}$	Gaussian	0.89±0.09	-10.82±0.04	0.34±0.04			1.99(22)
	Double Gaussian	0.16±0.06	-11.07±0.02	0.05±0.02	-10.78±0.04	0.34±0.03	1.47(20)
α_{X}	Gaussian	0.98±0.06	2.22±0.02	0.30±0.02			0.90(16)
$\log_{10}\mathrm{Flux}_{0.1-300\ \mathrm{GeV}}$	Gaussian	0.96±0.04	-6.73±0.04	0.27±0.01			2.82(25)
	Double Gaussian	0.64±0.24	-6.82±0.09	0.28±0.02	-6.56±0.03	0.18±0.04	1.42(23)
α_{γ}	Gaussian	0.92±0.05	2.06±0.01	0.19±0.01			5.33(25)
	Double Gaussian	0.75±0.05	2.03±0.01	0.15±0.02	2.25±0.04	0.34±0.02	1.83(23)

5.3.5 Broadband Spectral Energy Distribution

To examine the broadband emission mechanisms responsible for the optical/UV–X-ray–γ-ray emissions from S5 0716+714, we fitted the observed SED using synchrotron, SSC and EC processes. We considered only those epochs for which *NuSTAR* observations were available. Among the selected epochs, X-ray and gamma-ray flux during MJD 57045–57048 is large compared to the epoch MJD 59640–59699. To model the broadband SED, we considered the emission region to be a spherical blob of radius R and embedded with a tangled magnetic field B. The emission region is assumed to be populated homogeneously by a broken power-law electron distribution of the form

$$n(\gamma)\, d\gamma = K \times \left\{ \begin{array}{lll} \left(\frac{\gamma}{\gamma_b}\right)^{-p} d\gamma & \text{for} & \gamma_{\min} < \gamma < \gamma_b \\ \left(\frac{\gamma}{\gamma_b}\right)^{-q} d\gamma & \text{for} & \gamma_b < \gamma < \gamma_{\max} \end{array} \right. \quad \text{cm}^{-3} \tag{5.3}$$

where, p and q are the low and high energy indices, respectively of the broken power-law electron distribution, γ_b the break energy with K the corresponding number density, and $\gamma_{\min}$ and $\gamma_{\max}$ are the available minimum and maximum electron energies, respectively. The emission region is assumed to move down the blazar jet relativistically with a bulk Lorentz factor Γ at a viewing angle θ. The electron distribution undergoes energy losses through synchrotron, SSC, and EC processes. The source of external radiation field considered is the thermal IR photons from the dusty torus (EC/IR) at temperature T $\sim$ 1000 K (Ghisellini & Tavecchio, 2009; Błażejowski et al., 2000).

The observed synchrotron flux, after accounting for the relativistic and cosmological effects, can be estimated from the single particle emissivity (f_s), following Rybicki & Lightman (1986) as

$$F_{syn}(\nu) = \frac{4\pi\delta^3(1+z)}{3d_L^2} R^3 \frac{\sqrt{3}e^3 B}{16 m_e c^2} \int_{\gamma_{\min}}^{\gamma_{\max}} f_s(\nu/\kappa_1\gamma^2) n(\gamma) d\gamma, \tag{5.4}$$

The quantity κ_1 is given by

$$\kappa_1 = \frac{3e\delta B}{16 m_e c(1+z)}$$

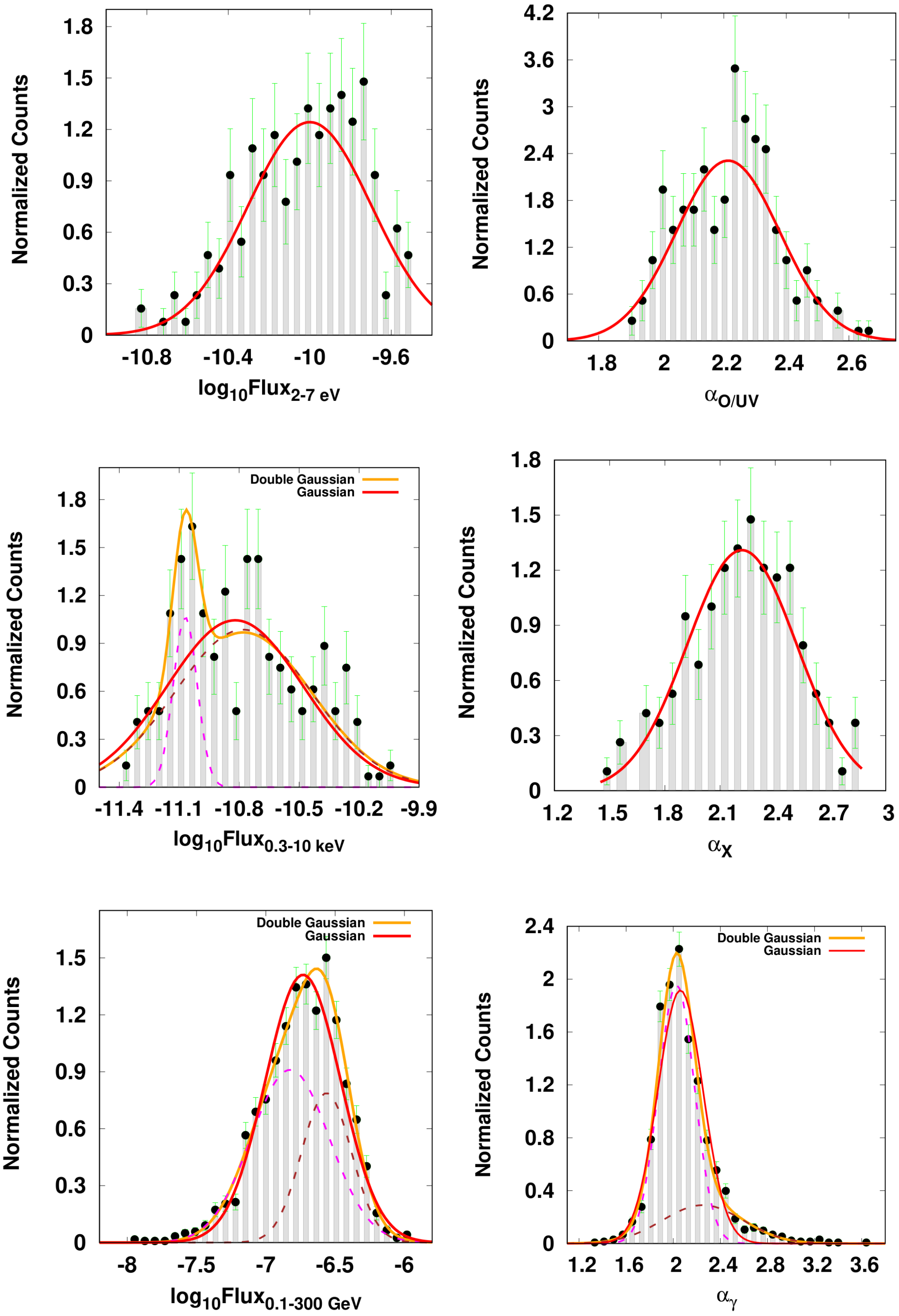

Figure 5.7: Histograms of logarithmic flux (left) and index (right) in optical/UV (top panel), X-ray (middle panel) and γ-ray (bottom panel) spectra of S5 0716+714. The solid red and orange curves represent the best fit single Gaussian function and double Gaussian function, respectively and dotted curves represent the two components of the double Gaussian function.

The observed SSC flux can be estimated (Blumenthal & Gould, 1970; Sahayanathan et al., 2018) as

$$F_{ssc}(\nu) = \frac{\delta^3(1+z)}{d_L^2}\pi R^3 \sigma_T \nu_s \int_{\gamma_{\min}}^{\gamma_{\max}} \frac{1}{\gamma^2} \int_{x_1}^{x_2} \frac{I_{syn}(\nu_i)}{\nu_i^2} f_c(\nu_i,\nu,\gamma) d\nu_i n(\gamma) d\gamma\,, \tag{5.5}$$

where ν_s is the frequency of the scattered photon, $I_{syn}(\nu_i)$ is the synchrotron intensity at photon frequency ν_i. The limits x_1 and x_2 are the minimum and maximum frequencies, respectively, of the synchrotron photons involved in the scattering process (Blumenthal & Gould, 1970; Jones, 1968)

$$x_1 = MAX\left[\nu_{syn}^{\min}, \frac{\nu_s}{4\gamma^2(1-h\nu_s/\gamma m_e c^2)}\right] \quad \text{and}$$

$$x_2 = MIN\left[\nu_{syn}^{\max}, \frac{\nu_s}{(1-h\nu_s/\gamma m_e c^2)}\right]\,.$$

The emissivity function f_c given by

$$f_c(\nu_i,\nu,\gamma) = 2r\log r + (1+2r)(1-r) + \frac{\zeta^2 r^2(1-r)}{2(1+\zeta r)}\,,$$

with

$$r = \frac{\nu_s}{4\nu_i\gamma^2(1-h\nu_s/\gamma m_e c^2)}\,,$$

and

$$\zeta = \frac{4h\nu_i\gamma}{m_e c^2}\,. \tag{5.6}$$

For $\Gamma \gg 1$, the observed EC flux can be obtained as (Dermer & Schlickeiser, 1993; Dermer & Menon, 2009; Finke, 2016)

$$F_{ec}(\nu) \approx \frac{\delta^3(1+z)}{8d_L^2} R^3 c\beta_\Gamma \sigma_T \nu \int_0^\infty d\nu_i^* \int_{\gamma_{\min}}^{\gamma_{\max}} \frac{U_{ph}^*}{\gamma^2\,\nu_i^{*2}} \phi(\gamma,\nu_s,\nu_i')n(\gamma)d\gamma\,, \tag{5.7}$$

where U_{ph}^* is target photon energy density at frequency ν_i^* measured in the rest frame of the AGN. The emissivity function ϕ is given by

$$\phi(\gamma, \nu_s, \nu_i') = \left[y + \frac{1}{y} + \frac{\nu_s^2}{\gamma^2 \nu_i'^2 y^2} - \frac{2\nu_s}{\gamma \nu_i' y} \right] , \tag{5.8}$$

with

$$y = 1 - \frac{h\nu_s}{\gamma m_e c^2} \; .$$

The broadband spectral fit is performed by coupling the numerical routines used for calculating the observed fluxes due to synchrotron, SSC, and EC processes with the statistical spectral fitting code XSPEC. The main parameters governing the observed broadband SED of the source are K, γ_b, p, q, B, R, Γ, θ, γ_min, γ_max and the energy density of the external target photon field U_{ph}^*. However, due to the limited information available in the narrow optical/UV, X-ray, and γ-ray energy bands, all these parameters cannot be simultaneously constrained satisfactorily. Nevertheless, additional constraints are imposed in the form of near equipartition between the non-thermal particle and magnetic field energy densities. We defined the equipartition parameter η as the ratio of magnetic field energy density (U_m) to electron energy density (U_e). The initial fit was performed for the low-flux state by letting the parameters p, q, γ_b, B, Γ, η, and U_{ph}^* free, while the parameters γ_min, γ_max, θ, and R were fixed at values 10, 10^6, 1.3 deg (see Section 5.4), and 4×10^{16} cm, respectively. However, the confidence intervals on the fit parameters were obtained only for p, q, γ_b, Γ, and B while the rest of the parameters were frozen to their best fit values. We found that the broadband SED of S5 0716+714 can be fitted reasonably well by considering synchrotron, SSC, and EC/IR processes and the corresponding source parameters are provided in Table 5.8. The model fit to the observed fluxes along with the residuals are shown in the upper panel of Figure 5.8.

We repeated the fitting for the high-flux state keeping the parameter values corresponding to the low-flux state as initial guess. The fitting was performed only on the parameters p, q, γ_b, B, Γ, and U^*_{ph} and the best-fit model parameters are provided in Table 5.8. The model fit to the observed fluxes, along with the residuals are shown in lower panel of Figure 5.8. Interestingly, we find the flux enhancement is predominatly associated with an increase in Γ which will blue-shift the spectrum. Hence this result is consistent with those from our correlation study; however, the absence of low energy information (infrared) and the plausible degeneracy among the source parameters does not let us assert this conclusion. Further, the increase in Γ did not cause a significant shift in the peak frequencies of the synchrotron and EC spectral component due to minor reduction in B and γ_b during the high flux states.

5.4 Discussion

The broadband non-thermal spectrum of blazar S5 0716+714 can be modeled assuming synchrotron and inverse Compton emission processes. The narrow band spectra in optical/UV, X-rays, and γ-rays show extreme flux and spectral variations. The broadband spectral modeling of the simultaneous multiwavelength observations during selected flux states provided hints about the plausible reasons for these spectral variations. However, a strong consensus regarding the origin of these variations is not possible. A detailed study of the long-term spectral variations of the source in different wavelengths has the potential to shed more light on the physics behind these spectral variations.

In an attempt to understand this, we perform detailed statistical and spectral studies of the blazar S5 0716+714 using its long-term observations in optical/UV, X-ray, and γ-ray. Our studies suggest that the source shows significant *harder when brighter* behavior in the optical/UV band and a mild *softer when brighter* behavior in the X-ray band. This behavior can be interpreted as an outcome of the broadband spectrum following a *bluer when brighter* trend, as shown in Figure 5.6. The plausible physical scenarios of the source that can initiate such a behavior are: (1) an increase in the jet Lorentz factor, and (2) an amplification of the magnetic field in the emission region. The latter scenario primarily affects the synchrotron and SSC components of the SED and may not have much effect on the EC. However, the variation in the SSC component can also lead to changes in the total Compton spectral component, and hence the behavior of the broadband SED under this condition is worth investigating. Since the jet is aligned to the observer at a small angle θ, the blue/red shift and the flux amplification will be governed by the Doppler factor δ rather than the Lorentz factor Γ alone. Therefore, the viewing angle will also affect the shift and amplification in the spectrum. Hence we performed this study using different values for θ (2, 1.8, 1.6, 1.4 and 1.3 degrees). The broadband spectral modeling of the source supports the first scenario mentioned above; however, a firm conclusion cannot be drawn by just reproducing the SED corresponding to two different flux states. Additionally, the variation in the rest of the source parameters (Table 5.8) did not result in a significant blue shift of the SED during the high flux state.

To investigate these two scenarios that can imitate the *bluer when brighter* behavior of the source, we selected the best-fit model spectrum corresponding to the period MJD 59640–59699 (low flux state) as a template SED and study the integrated fluxes at energies 2–7 eV, 0.3–10 keV, and 0.1–300 GeV. The study is performed by varying either Γ or B while freezing the rest of the parameters to their best-fit values. The average spectral indices are used for optical/UV and X-ray spectra, while for γ-ray, the spectral slope at 1 GeV is considered. The range of variation in this parameter (Γ or B) is selected such that they can reproduce the observed maximum and minimum integrated fluxes (Figure 5.3). Interestingly, this also imposes constraints on the jet viewing angle when the spectral variations are attributed to changes in the jet Lorentz factor alone. Since the Doppler factor for a given Γ peaks only at a certain value of θ, we find that the maximum observed flux can be obtained only when $\theta < 1.4$ degrees, irrespective of the choice of Γ. In Figure 5.3, we marked the maximum integrated flux in each energy band obtainable for different choices of θ as red dotted lines. Remarkably, this constraint on θ cannot be obtained by broadband spectral fitting of the source using synchrotron, SSC, and EC emission processes. In Figure 5.9, we show that the best-fit SED for $\theta = 2$ degrees, and in Table 5.9, we provide the best-fit parameters. Although the fit results in a $\chi^2_{red} = 1.81$, it fails to reproduce the maximum integrated fluxes (top of the shaded regions in each plot of Figure 5.3 represent the maximum attainable flux in different energy bands with $\theta = 2$ degrees).

For both the scenarios considered here (variation in Γ or B), the optical flux indicates a decreasing trend with its index, which is consistent with the observations (top left of Figure 5.3). However, the mild positive correlation observed between the X-ray flux and the indices is consistant with variation in Γ but not with B variation (top right of Figure 5.3). In the γ-ray band, variation in B predicts a mild positive trend between the flux and index, while Γ variation predicts a mild negative trend. However, the observed data do not support any such correlations. It is also possible that the correlation is not visible in the data due to counteracting variations in other source parameters. The observed positive correlations between optical/UV, X-ray, and γ-ray fluxes are consistent with the variations in Γ or B (Figure 5.4). Interestingly, the Γ variation predicts a negative correlation between the optical/UV and the X-ray spectral indices (Figure 5.5 (a)). This is strongly supported by the observations, whereas the trend predicted by B variation is opposite. The moderate positive correlation observed between the γ-ray and optical/UV indices is again supported only by the Γ variation. The mild negative correlation observed between the γ-ray and the X-ray spectral indices is supported under both scenarios. Hence, by comparing the correlation between the observed quantities with the trends predicted by the variations in B and Γ, we can conclude that the bluer when brighter behavior of the source during different flux states is predominantly associated with the variation in the bulk Lorentz factor of the blazar jet. We find that in many cases, the curves representing the trend between observed quantities show a moderate shift from a majority of the data points. This shift can be due to the choice of the template SED and can be reduced by modifying the base parameters.

Our study on flux and index distributions suggest that the index variation follows a normal behavior, whereas the fluxes follow a log-normal one. This can again be consistent with the *bluer when brighter* behavior of the source. During high flux states, the spectrum shifts towards the bluer end, and hence the spectral index measured at a given energy band will vary normally. This normal variation in the index can result in log-normal variation in the flux. This interpretation differs from the earlier reported ones where the normal variation in the indices are treated as a result of the fluctuation in the acceleration process (Sinha et al., 2018; Khatoon et al., 2020). Again, the observed *bluer when brighter* trend of the broadband SED cannot be easily comprehended with the effects of the underlying acceleration process. Our interpretation based on the Γ variation cannot explain the presence of double normal γ-ray index distribution as well as double log-normal γ-ray and X-ray flux distributions.

5.5 Summary

We performed a detailed long-term study of the blazar S5 0716+714, spanning from April 2005 to January 2023, in optical/UV, X-ray, and γ-ray wavelengths using *Swift*-UVOT/XRT and *Fermi*-LAT observations. The spectra in each waveband were fitted with a power-law/log-parabola model, and the correlation between the long-term variations in flux and spectral indices was examined. Our result indicates:

- A significant anti-correlation between flux and spectral index in the optical/UV range.
- A mild positive correlation between flux and index in the X-ray energy band.
- A significant correlation between the fluxes at optical/UV, X-ray, and γ-ray energies.
- The X-ray and optical/UV indices are anti-correlated.
- A mild correlation between optical/UV and γ-ray indices.
- A mild anti-correlation between X-ray and γ-ray indices.

The correlations support a *bluer when brighter* behavior of the source. The *bluer when brighter* behavior may suggest a variation in the bulk Lorentz factor. We also studied the distribution of fluxes and indices in these energy bands and found the following:

- The optical/UV fluxes followed a log-normal variability.
- The X-ray and the γ-ray fluxes indicate a double log-normal variability.
- The optical/UV and X-ray index distributions support a normal behavior.
- The γ-ray index distribution suggests a double normal behavior.

Our study suggests that the log-normal flux variability of the source may be associated with a normal variations in the spectral indices. When combined with our correlation study, the *bluer when brighter* trend of the source results in normal variation in the optical/UV, X-ray, and γ-ray indices, which in turn produce log-normal variability in the fluxes (Figure 5.6). The limited information available did not allow us to draw conclusions strongly on the double normal/double log-normal behavior of the indices/fluxes.

We also studied the broadband spectral energy distribution for two different flux states during which simultaneous observations by *NuSTAR* were available. The broadband spectra can be well fitted using synchrotron, SSC, and EC processes during both states. The γ-ray emission can be explained by the EC scattering of infrared photons from the dust torus. Our results from spectral fitting suggest that the flux enhancement of the source is primarily linked to an increase in the bulk Lorentz factor of the blazar jet. The increase in the bulk Lorentz factor of the jet can also be a plausible reason for the *bluer when brighter* trend of the source. This was further confirmed by varying the bulk Lorentz factor of the low flux state SED (template SED) and comparing the results with the correlation studies. However, the wide spread in the data around the model curve suggests that different flux states may be associated with variations in parameters besides the bulk Lorentz factor. This procedure also allows us to draw constraints on the jet viewing angle as $\theta \lesssim 1.4$ degrees, though this estimate depends on the choice of the template SED considered.

The statistical and spectral analysis of blazar S5 0716+714 leads us to conclude that the variability of the source is predominantly associated with changes in the bulk Lorentz factor of the jet. This study can be extended to other blazars to draw a global picture regarding AGN variability. The blazar emission zone falls within a few Schwarzschild radii ($\sim$ parsecs) of the central black hole,

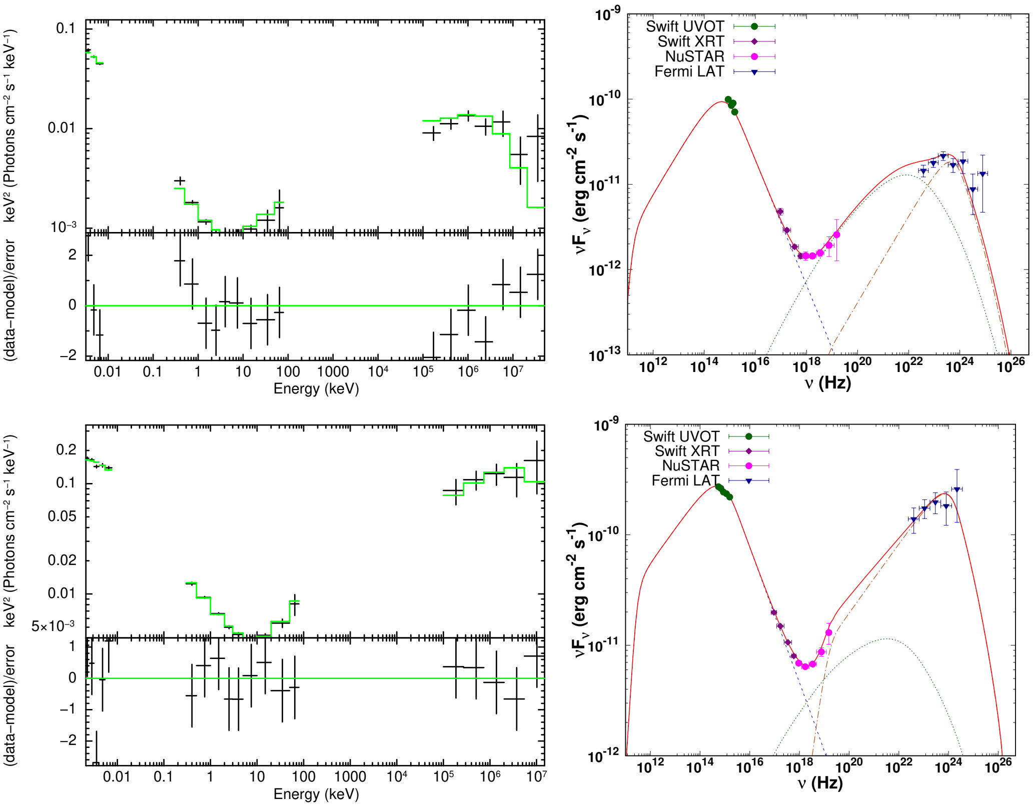

Figure 5.8: The upper panel shows broadband SED fitting of S5 0716+714 during the epoch MJD 59640–59699 (low-flux state) and the lower panel is for the epoch MJD 57045–57048 (high-flux state). Left panel: The unfolded spectrum with residuals obtained from XSPEC fitting. Right panel: Synchrotron, SSC, and EC/IR components are represented by dashed curve, dotted curve, and dashed dotted curve, respectively. The solid red curve represents the sum of the three components.

which cannot be resolved through radio interferometry studies. The ejection of superluminal knots from the jets of radio galaxies also supports the variations in the jet Lorentz factor, but at a length scale much farther away from the blazar emission zone (D'arcangelo et al., 2009; Jorstad et al., 2017; Kun et al., 2023).

Table 5.8: Best fit values of the model parameters from broadband SED fitting.

Parameter	59640–59699 (low-flux state)	57045–57048 (high-flux state)
p	$1.979^{+0.096}_{-0.100}$	$2.367^{+0.070}_{-0.090}$
q	$4.466^{+0.038}_{-0.027}$	$4.223^{+0.027}_{-0.027}$
log γ_b	$3.598^{+0.018}_{-0.013}$	$3.533^{+0.030}_{-0.029}$
B (in Gauss)	$0.613^{+0.026}_{-0.021}$	$0.579^{+0.026}_{-0.024}$
η	0.3	0.3
Γ	$12.04^{+0.91}_{-1.04}$	$25.73^{+3.48}_{-3.11}$
R (in cm)	4×10^{16}	4×10^{16}
log $\gamma_{\rm min}$	1	1
log $\gamma_{\rm max}$	6	6
θ (in degree)	1.3	1.3
T (in kelvin)	1000	1000
Doppler Factor, δ_D	22.38	38.38
U^*_{ph} (erg/cm^3)	7.57×10^{-6}	1.06×10^{-5}
χ^2/d.o.f	25.49/14	20.21/14

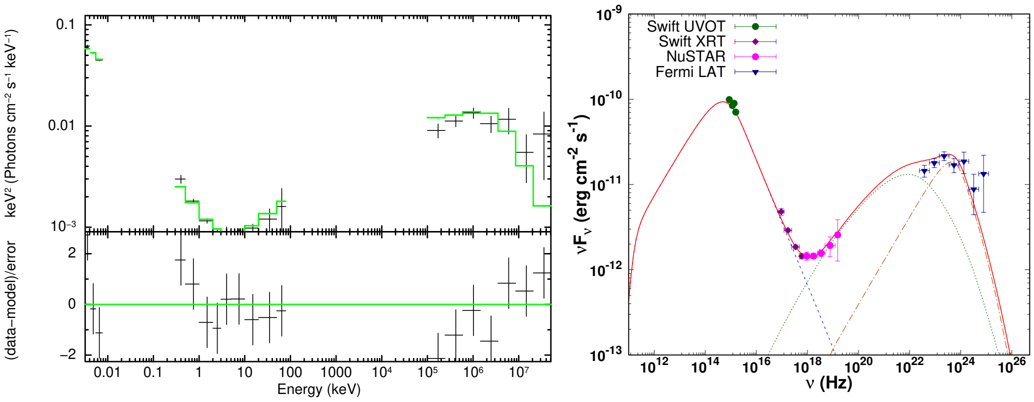

Figure 5.9: The broadband SED fitting of S5 0716+714 during the epoch MJD 59640–59699 (low-flux state) with viewing angle, $\theta = 2$ degree. The labels are same as that of Figure 5.8.

Table 5.9: Best fit values of the model parameters from broadband SED fitting for the epoch MJD 59640–59699 with $\theta = 2$ degree.

Parameter	59640–59699 (low-flux state)
p	$1.968^{+0.098}_{-0.088}$
q	$4.462^{+0.041}_{-0.026}$
$\log \gamma_b$	$3.597^{+0.018}_{-0.013}$
B (in Gauss)	$0.611^{+0.028}_{-0.019}$
η	0.3
Γ	$13.72^{+1.62}_{-1.46}$
R (in cm)	4×10^{16}
$\log \gamma_{\rm min}$	1
$\log \gamma_{\rm max}$	6
θ (in degree)	2
T (in kelvin)	1000
Doppler Factor, δ_D	22.3
U^*_{ph} (erg/cm^3)	7.57×10^{-6}
χ^2/d.o.f	25.41/14

Chapter 6

Summary and Future Prospects

The spectral energy distribution (SED) of blazars shows a double-humped structure: the low-energy peak (IR to X-ray) is attributed to synchrotron emission by relativistic electrons, while the origin of the high-energy peak (MeV to TeV gamma-rays) remains uncertain. Modeling the broadband SED of blazars often suggests that the emitting electron distribution follows a broken power-law. A power-law electron distribution can result from Fermi-type acceleration of the relativistic electrons in the jet. The radiative loss (synchrotron/IC) of a power-law electron distribution can result in a broken power-law electron distribution, with the power-law indices differing by one. Consequently, the photon spectrum will exhibit a broken power-law, with the high- and low-energy spectral indices differing by 0.5. However, SED modeling of blazars often contradicts this inference, with the index difference found to be significantly larger than 0.5. Additionally, recent high-resolution observations have revealed a mild/strong curvature in the X-ray spectra of high-energy-peaked blazars (HBLs). In the first part of this thesis we thoroughly investigated the radiative loss interpretation of the broken power-law electron distribution by studying the spectrum around the synchrotron peak of the blazar Mkn 421. Further, a dedicated study is carried out to understand the spectral curvature in the X-ray spectrum of the blazar.

The synchrotron peak energy of Mkn 421 falls into the soft X-ray regime, while the hard X-ray energy band probes the decline of the synchrotron spectral component. A detailed analysis of the source around the synchrotron SED peak is presented in Chapter 3. We utilized all the observations of the source by *Swift*-XRT from 2008 to 2019 in the 0.3 to 10.0 keV energy range to obtain the characteristic photon energy (where the spectral index changes significantly) and the corresponding spectral indices. The X-ray spectra in this energy range can be well fitted by both a log-parabola and a smooth broken power-law function. Our analysis using the smooth broken power-law spectral fit reveals strong anti-correlation between the spectral indices both before and after the characteristic photon energy. Additionally, the spectral curvature observed at this energy indicates an anti-correlation with the low-energy spectral index, while showing a positive correlation with the high-energy spectral index. These results contradict the interpretation based on radiative losses for the characteristic photon energy. To explore alternative explanations, we consider scenarios where the underlying particle distribution is described either by a power-law with an exponential cut-off or by a power-law with a gradual decline at the maximum electron energy rather than a sharp cut-off. We find that these scenarios can reproduce the anti-correlation between the spectral indices, even though they deviate from the observations. A more comprehensive understanding of the origin and evolution of the radiating particle distribution is necessary to match the observed results.

In Chapter 4 we have thoroughly examined the curvature in the X–ray spectrum of Mkn 421 using simultaneous observations from *Swift*-XRT (0.3-10 keV) and *NuSTAR* (3-79 keV) telescopes. The curvature in blazar spectrum has the potential to understand the particle dynamics in jets. Our spectral analysis of *NuSTAR* observations alone employing a power-law (PL), log-parabola (LP), and simple exponential cutoff power-law (CPL) models, indicates a clear preference for LP and CPL models over the simple PL. This strongly supports the presence of spectral curvature in the X-ray spectra even beyond the synchrotron peak. The 0.3 to 79 keV broad X-ray spectral anlysis using simultaneous *Swift*-XRT and *NuSTAR* observations with LP and CPL models, indicating that LP provides a better fit compared to CPL. However, the absence of a significant correlation between the LP parameters implies that the variations in spectral characteristics cannot be attributed to the energy dependence of the particle acceleration process. To explore this further, we then studied the broadband X-ray spectrum using a power-law with a modified exponential cutoff (MCPL) model. In the presence of synchrotron losses, shock acceleration can result in a power-law particle distribution with a modified exponential cutoff. The resulting synchrotron spectrum from such a particle distribution will always be a power-law with a sub-exponential cutoff. We found that an MCPL function can satisfactorily fit the data beyond the SED peak. Additionally, the results obtained were consistent with a scenario where particle acceleration is mediated through Bohm-type diffusion and the spectra beyond the synchrotron peak is modulated by the radiative loss process.

In the latter part of the thesis, in Chapter 5, we conducted a comprehensive long-term study of the blazar S5 0716+714, covering the period from April 2005 to January 2023, across optical/UV, X-ray, and γ-ray wavelengths using *Swift*-UVOT/XRT and *Fermi*-LAT observations. The spectra in each waveband were fitted with power-law/log-parabola models, and we examined the correlation between long-term variations in flux and spectral indices. We found (1) a significant anti-correlation between flux and spectral index in the optical/UV range, (2) a mild positive correlation between flux and index in the X-ray regime, (3) the fluxes at optical/UV and X-ray, optical/UV and γ-ray, and X-ray and γ-ray energies are positively correlated, (4) X-ray and optical/UV indices are significantly anti-correlated, and (5) γ-ray indices are mildly correlated positively with optical/UV indices and mildly anti-correlated with X-ray indices. These correlation results support the *bluer when brighter* behavior of the source. Further, the flux and index distribution studies in these energy bands shows (1) the optical/UV fluxes indicates a log-normal variability, (2) the X-ray and the γ-ray fluxes support a double log-normal variability, (3) the optical/UV and X-ray index distributions follow a Gaussian behavior and (4) the γ-ray index distribution follow a double Gaussian behavior. When combining the findings of flux and index distributions with their correlation results, the *bluer when brighter* behavior of the source results in Gaussian variations in the spectral indices across different energy bands. These variations, in turn, contribute to log-normal variability in the fluxes. The broadband spectral energy distribution was analysed for two different flux states, during which simultaneous observations by *NuSTAR* were available. The broadband SED of these states were effectively modeled using synchrotron, SSC (Synchrotron Self-Compton), and EC (External Compton) processes. The γ-ray emission can be attributed to the EC scattering of infrared photons from the dust torus. The results of broadband spectral fitting indicate that the enhancement in the flux of the source is mainly associated with an increase in the bulk Lorentz factor of the blazar jet. The increase in the bulk Lorentz factor of the jet may also explain the *bluer when brighter* behaviour of the source. Additionally, we find that the model curves corresponding to variations in the bulk Lorentz factor have the potential to explain the observed correlations between the spectral parameters. Thus, this study concludes that the spectral changes of the blazar S5 0716+714 are primarily linked to variations in the bulk Lorentz factor of the jet.

6.1 Future plans

- In Chapter 3, we found that the simple scenario, where the electron distribution is accelerated at a shock front with constant acceleration time-scale and escape time-scale, fails to explain the observed relation between the photon indices before and after the peak. We plan to incorporate energy dependence into acceleration time-scale and escape time-scale; this may make it possible to modify the correlation and reduce the deviation from the observations.
- In Chapter 4, we found that the spectral curvature observed in the hard X-ray spectra of Mkn 421 supports the presence of Bohm-type diffusion during flares in the jet. We plan to extend this study to other HBL sources that show significant curvature (e.g., Mkn 501) to probe the turbulence properties in the jet in more detail.
- In Chapter 5, we find that model curves based on variations in the bulk Lorentz factor can potentially explain the observed correlations between the spectral parameters of the source S5 0716+714. However, the large scatter in the data around the model curve indicates that differ-

ent flux states may be influenced by variations in parameters other than the bulk Lorentz factor. We plan to simulate the observed scatter in multi-wavelength flux-flux, flux-index, and index-index plots by varying multiple parameters simultaneously to determine the limits on different parameters and propose an idea about the most important parameters causing the spectral changes and the observed correlations.

- We plan a detailed, multi-wavelength, long term spectral study of a large number of FSRQs, HBLs, IBLs, and LBLs in order to understand the significant parameters responsible for the spectral variations in blazars.
- A detailed temporal and spectral study of blazars, especially the sources that remained in a low-flux state for a long period and have recently undergone gamma-ray flares, is planned. We aim to perform broadband spectral modeling of these sources during different gamma-ray activity states to understand the primary factors causing the gamma-ray flares. Additionally, we plan to study the flux distribution for the the different epochs in detail, along with the flux distributions separately for quiescent and flaring phases, in order to uncover the possible physics behind these flares.

Chapter 7

Recommendations

- Using a large number of *Swift*-XRT observations of Mkn 421 corresponding to different flux states, our statistical analysis reveals a strong anti-correlation between the spectral indices before and after (Γ_{low} and Γ_{high}) the synchrotron (SED) peak. This result does not support a radiative loss interpretation of a broken power-law distribution of photons around the synchrotron (SED) peak.
- A simple scenario where the electron distribution resulting from the assumptions of constant acceleration time-scale and escape time-scale can not match with the observations. However, a deeper understanding of the origin and evolution of the radiating particle distribution is needed to satisfactorily match the observed results.
- X-ray spectral analysis of Mkn 421 using *NuSTAR* observations reveals that, during periods of low flux, the hard X-ray spectra are best represented by a steep power-law. However, the spectrum exhibits significant curvature during its high flux states. The persistance of curvature even after the synchrotron peak, makes it challenging to attribute this solely to the spectral transition occurring at the peak of the synchrotron component.
- The results of the X-ray spectral analysis above the synchrotron SED peak using a modified cut-off power-law model (MCPL) is able to pro-

vide some inferences on the diffusion properties in the jet. Extending similar study to a large sample of blazars is expected to provide us more informations on the turbulent properties in the jet.

- A long-term multi-wavelength statistical and spectral analysis of the blazar S5 0716+714 leads us to conclude that the observed correlation among fluxes and indices in different wave bands supports a *bluer when brighter behaviour* of the source. The correlation studies of multi-wavelength spectral parameters will have the potential to provide insights in to the physics of blazars.
- In the case of blazar S5 0716+714 we find that the model curves corresponding to variations in the bulk Lorentz factor of the jet have the potential to explain the observed correlations and hence the *bluer when brighter behaviour* of the source. Extending this type of study to a large sample of sources in different classes of blazars is expected to improve our understanding about the significant parameters (bulk Lorentz factor, magnetic field, break energy, etc.) responsible for the spectral variations in each classes.

Appendix A

Appendix 1

Table A.1: Best fit parameters of spectral fitting using *eplogpar* model and *sbpl* model

ObsID	Date of Obs.	Exposure	*eplogpar*			*sbpl*			$\mathrm{Flux}_{0.3-10.0\,\mathrm{kev}}$
		(sec)	ϵ_p (keV)	β	χ^2_{red}(dof)	Γ_{low}	Γ_{high}	χ^2_{red}(dof)	($10^{-10}\mathrm{erg\,cm^{-2}s^{-1}}$)
(1)	(2)	(3)	(4)	(5)	(6)	(7)	(8)	(9)	(10)
30352053-Orb2	2008-01-16	575.100	$0.42^{+0.07}_{-0.08}$	0.28±0.05	1.04(305)	1.36±0.12	2.54±0.02	1.06(305)	20.00±0.28
30352054	2008-01-16	1134.085	$0.42^{+0.04}_{-0.05}$	0.30±0.03	1.08(394)	1.33±0.10	2.57±0.01	1.12(394)	15.26±0.15
30352056	2008-01-17	944.126	$0.43^{+0.05}_{-0.07}$	0.34±0.04	0.95(322)	1.29±0.12	2.61±0.02	1.00(322)	13.54±0.17
30352055-Orb1	2008-01-17	394.900	$0.64^{+0.07}_{-0.08}$	0.45±0.08	1.11(227)	1.29±0.12	2.69±0.04	1.12(227)	10.00±0.21
30352055-Orb2	2008-01-17	362.600	$0.60^{+0.05}_{-0.04}$	0.49±0.06	1.09(260)	1.22±0.10	2.73±0.03	1.12(260)	15.04±0.26
30352058	2008-01-18	889.108	$0.57^{+0.04}_{-0.04}$	0.33±0.04	1.07(378)	1.38±0.07	2.59±0.02	1.10(378)	14.88±0.16
30352059	2008-01-19	919.112	$0.43^{+0.04}_{-0.04}$	0.34±0.04	1.04(359)	1.22±0.12	2.62±0.01	1.06(359)	13.73±0.15
30352060	2008-02-06	753.060	$0.60^{+0.05}_{-0.06}$	0.26±0.03	1.13(429)	1.48±0.06	2.51±0.02	1.15(429)	24.33±0.24
30352066	2008-02-10	1174.100	$0.74^{+0.03}_{-0.03}$	0.30±0.03	1.17(467)	1.46±0.04	2.55±0.02	1.18(467)	20.85±0.18
30352068	2008-02-11	1868.208	$0.46^{+0.03}_{-0.05}$	0.25±0.02	1.10(495)	1.44±0.06	2.52±0.01	1.14(495)	18.61±0.14
30352069	2008-02-11	949.085	$0.48^{+0.04}_{-0.06}$	0.28±0.03	0.96(422)	1.40±0.08	2.54±0.01	0.98(422)	18.53±0.18
30352071-Seg1	2008-02-12	699.700	$0.50^{+0.08}_{-0.07}$	0.24±0.04	1.14(381)	1.49±0.09	2.49±0.02	1.17(381)	18.90±0.22
30352071-Seg2	2008-02-12	763.700	$0.50^{+0.08}_{-0.07}$	0.23±0.03	1.10(394)	1.49±0.08	2.48±0.02	1.12(394)	19.17±0.21
30352072	2008-02-13	979.112	$0.41^{+0.06}_{-0.07}$	0.23±0.03	1.05(412)	1.45±0.10	2.49±0.01	1.07(412)	18.91±0.20
30352073	2008-02-13	629.107	$0.54^{+0.07}_{-0.09}$	0.25±0.04	0.98(352)	1.47±0.09	2.51±0.02	1.00(352)	19.13±0.25
30352074-Orb1	2008-02-14	790.900	$0.63^{+0.08}_{-0.11}$	0.20±0.04	1.05(378)	1.56±0.08	2.44±0.03	1.06(378)	22.21±0.28
30352074-Orb2	2008-02-14	422.700	$0.74^{+0.11}_{-0.14}$	0.24±0.06	0.93(273)	1.51±0.10	2.49±0.04	0.93(273)	22.38±0.45
30352075	2008-02-14	1529.124	$0.66^{+0.05}_{-0.06}$	0.23±0.03	1.10(489)	1.53±0.05	2.47±0.02	1.11(489)	18.30±0.15
30352077	2008-02-15	1589.125	$0.72^{+0.07}_{-0.09}$	0.24±0.04	0.93(375)	1.51±0.07	2.48±0.03	0.93(375)	17.03±0.21
30352079	2008-02-16	1228.244	$0.47^{+0.06}_{-0.08}$	0.26±0.04	1.12(365)	1.43±0.10	2.52±0.02	1.14(365)	16.74±0.20
30352081-Orb1	2008-03-13	461.000	$0.49^{+0.07}_{-0.10}$	0.32±0.06	1.05(276)	1.30±0.14	2.59±0.03	1.04(276)	11.75±0.21
30352083	2008-04-02	894.619	$0.54^{+0.08}_{-0.11}$	0.20±0.04	0.97(382)	1.55±0.09	2.45±0.02	0.99(382)	13.39±0.17
30352085	2008-04-03	1139.622	$3.11^{+0.33}_{-0.26}$	0.21±0.02	1.17(574)	1.55±0.01	2.47±0.05	1.17(574)	30.00±0.25
30352086	2008-04-03	1159.607	$1.35^{+0.05}_{-0.06}$	0.26±0.03	1.02(511)	1.51±0.03	2.49±0.03	1.02(511)	24.79±0.22
30352087-Orb1	2008-04-04	360.000	$1.67^{+0.18}_{-0.15}$	0.21±0.04	0.97(358)	1.56±0.05	2.44±0.06	0.97(358)	24.45±0.38
30352087-Orb2	2008-04-04	758.300	$1.31^{+0.08}_{-0.08}$	0.21±0.03	1.17(457)	1.57±0.04	2.43±0.03	1.17(457)	23.45±0.25
30352088	2008-04-05	1139.210	$4.10^{+0.86}_{-0.89}$	0.11±0.03	1.07(503)	1.67±0.02	2.36±0.08	0.08(503)	20.00±0.21
30352089	2008-04-06	1019.621	$1.67^{+0.09}_{-0.09}$	0.24±0.03	1.04(481)	1.53±0.03	2.47±0.04	1.04(481)	20.00±0.20
30352091	2008-04-08	1074.608	$1.76^{+0.17}_{-0.14}$	0.19±0.03	1.16(447)	1.59±0.04	2.41±0.05	1.16(447)	23.17±0.28
30352093	2008-04-09	2197.915	$1.22^{+0.05}_{-0.06}$	0.20±0.02	1.06(533)	1.58±0.03	2.43±0.02	1.06(533)	17.13±0.14

ObsID	Date of Obs.	Exposure	*eplogpar*			*sbpl*			$\mathrm{Flux}_{0.3-10.0\,\mathrm{kev}}$
		(sec)	ϵ_p (keV)	β	χ^2_{red} (dof)	Γ_{low}	Γ_{high}	χ^2_{red} (dof)	($10^{-10}\mathrm{erg\,cm^{-2}s^{-1}}$)
30352094-Orb1	2008-04-11	690.400	$0.75^{+0.07}_{-0.09}$	0.25±0.04	1.02(346)	1.51±0.07	2.49±0.03	1.03(346)	23.09±0.32
30352094-Orb2	2008-04-11	1120.000	$0.59^{+0.13}_{-0.12}$	0.18±0.06	0.95(284)	1.55±0.12	2.43±0.04	0.95(284)	11.48±0.22
30352095	2008-04-13	2917.377	$0.70^{+0.03}_{-0.05}$	0.26±0.02	1.12(514)	1.49±0.04	2.50±0.02	1.15(514)	11.56±0.09
31202001-Orb1	2008-05-02	901.600	$0.47^{+0.08}_{-0.08}$	0.19±0.06	1.06(281)	1.50±0.10	2.45±0.03	1.06(281)	6.65±0.12
30352097	2008-05-04	734.619	$1.03^{+0.08}_{-0.10}$	0.21±0.04	1.04(386)	1.56±0.05	2.44±0.04	1.04(386)	16.74±0.22
30352098-Orb1	2008-05-05	1146.000	$0.54^{+0.04}_{-0.06}$	0.25±0.03	1.16(461)	1.47±0.06	2.51±0.02	1.19(461)	19.42±0.17
30352098-Orb2	2008-05-05	846.200	$0.48^{+0.05}_{-0.07}$	0.27±0.03	1.08(398)	1.42±0.09	2.53±0.02	1.10(398)	17.84±0.19
31202003	2008-05-07	1569.056	$0.41^{+0.04}_{-0.06}$	0.26±0.03	1.00(419)	1.41±0.09	2.53±0.01	1.04(419)	13.32±0.12
30352100-Orb1	2008-11-08	943.800	$0.50^{+0.05}_{-0.06}$	0.36±0.04	1.16(330)	1.29±0.10	2.63±0.02	1.19(330)	10.00±0.13
30352102-Orb1	2008-12-03	874.800	$0.75^{+0.05}_{-0.06}$	0.38±0.04	1.12(339)	1.38±0.07	2.62±0.03	1.14(339)	10.71±0.14
30352102-Orb2	2008-12-03	1614.000	$0.69^{+0.03}_{-0.04}$	0.41±0.03	1.10(400)	1.34±0.05	2.65±0.02	1.15(400)	10.00±0.10
30352104	2009-01-12	794.227	$1.03^{+0.06}_{-0.07}$	0.34±0.05	1.11(327)	1.44±0.06	2.57±0.04	1.12(327)	10.69±0.16
30352105	2009-01-13	769.621	$0.79^{+0.08}_{-0.11}$	0.25±0.05	1.05(320)	1.51±0.08	2.49±0.04	1.05(320)	10.66±0.17
30352107	2009-01-27	929.225	$0.87^{+0.08}_{-0.10}$	0.24±0.04	1.00(349)	1.53±0.07	2.47±0.04	1.01(349)	10.00±0.15
30352124	2009-04-11	533.855	$0.53^{+0.06}_{-0.08}$	0.33±0.05	0.93(294)	1.36±0.11	2.59±0.03	0.94(294)	12.81±0.20
30352125	2009-04-14	1019.226	$0.53^{+0.06}_{-0.08}$	0.26±0.04	1.14(364)	1.44±0.09	2.52±0.02	1.15(364)	11.18±0.14
30352129	2009-04-22	724.224	$0.57^{+0.08}_{-0.10}$	0.28±0.05	1.07(294)	1.43±0.11	2.54±0.03	1.07(294)	9.13±0.15
30352151	2009-05-27	974.447	$0.45^{+0.06}_{-0.08}$	0.30±0.05	1.07(317)	1.29±0.13	2.57±0.02	1.07(317)	8.46±0.12
31540001-Orb1	2009-11-14	669.800	$1.75^{+0.17}_{-0.14}$	0.19±0.03	1.06(431)	1.58±0.04	2.42±0.05	1.06(431)	21.76±0.27
31540001-Orb3	2009-11-14	185.700	$1.61^{+0.28}_{-0.20}$	0.31±0.10	1.09(191)	1.46±0.09	2.54±0.11	1.09(191)	11.36±0.38
31540002-Orb1	2009-11-15	602.600	$2.01^{+0.27}_{-0.20}$	0.20±0.04	0.96(377)	1.56±0.04	2.44±0.06	0.96(377)	17.24±0.26
31540002-Orb3	2009-11-15	209.700	$1.84^{+0.24}_{-0.22}$	0.24±0.07	1.19(255)	1.53±0.06	2.47±0.09	1.19(255)	18.51±0.45
30352160	2009-12-09	1024.454	$0.45^{+0.06}_{-0.08}$	0.30±0.05	1.06(318)	1.33±0.13	2.57±0.02	1.07(318)	8.39±0.12
30352161	2009-12-11	969.613	$0.52^{+0.06}_{-0.08}$	0.29±0.04	1.00(328)	1.41±0.10	2.55±0.02	1.02(328)	9.41±0.13
30352162	2009-12-13	994.602	$0.59^{+0.04}_{-0.06}$	0.38±0.04	0.95(332)	1.32±0.08	2.64±0.02	0.97(332)	10.00±0.12
30352163-Seg1	2009-12-15	498.600	$0.80^{+0.05}_{-0.07}$	0.35±0.05	1.10(316)	1.41±0.07	2.59±0.03	1.12(316)	15.28±0.23
30352163-Seg2	2009-12-15	490.800	$0.82^{+0.05}_{-0.07}$	0.37±0.05	1.16(317)	1.40±0.07	2.61±0.03	1.17(317)	15.14±0.23
30352167	2009-12-25	1164.605	$0.76^{+0.05}_{-0.06}$	0.29±0.03	1.02(420)	1.46±0.05	2.53±0.02	1.03(420)	14.16±0.15
30352168-Seg1	2009-12-27	597.800	$0.88^{+0.08}_{-0.10}$	0.26±0.05	1.16(332)	1.51±0.07	2.49±0.04	1.16(332)	13.32±0.20
30352168-Seg2	2009-12-27	584.800	$1.17^{+0.07}_{-0.08}$	0.29±0.05	1.05(347)	1.49±0.05	2.51±0.04	1.06(347)	14.10±0.22

ObsID	Date of Obs.	Exposure	*eplogpar*			*sbpl*			$\mathrm{Flux}_{0.3-10.0\,\mathrm{kev}}$
		(sec)	ϵ_p (keV)	β	χ^2_{red} (dof)	Γ_{low}	Γ_{high}	χ^2_{red} (dof)	($10^{-10}\mathrm{erg\,cm^{-2}s^{-1}}$)
30352170	2009-12-31	1174.448	$1.32^{+0.05}_{-0.06}$	0.24±0.03	1.14(491)	1.53±0.03	2.47±0.03	1.15(491)	21.64±0.20
30352173-Seg1	2010-01-06	499.700	$1.16^{+0.08}_{-0.09}$	0.27±0.05	1.08(349)	1.50±0.05	2.50±0.04	1.08(349)	16.90±0.26
30352173-Seg2	2010-01-06	459.100	$1.33^{+0.07}_{-0.08}$	0.34±0.05	1.18(338)	1.44±0.05	2.57±0.04	1.18(338)	16.81±0.27
30352178-Seg1	2010-01-14	699.600	$1.15^{+0.06}_{-0.06}$	0.31±0.03	1.17(419)	1.47±0.04	2.54±0.03	1.17(419)	20.96±0.24
30352178-Seg2	2010-01-14	592.400	$1.15^{+0.07}_{-0.07}$	0.28±0.04	1.01(400)	1.49±0.04	2.51±0.03	1.02(400)	21.17±0.27
30352179-Seg1	2010-01-15	498.600	$1.63^{+0.08}_{-0.08}$	0.33±0.04	1.12(402)	1.44±0.03	2.56±0.04	1.12(402)	22.89±0.30
30352179-Seg2	2010-01-15	497.000	$1.72^{+0.09}_{-0.08}$	0.35±0.04	1.17(402)	1.42±0.03	2.58±0.04	1.17(402)	23.03±0.30
30352182	2010-01-16	939.454	$1.27^{+0.14}_{-0.15}$	0.21±0.06	1.06(300)	1.56±0.07	2.44±0.06	1.06(300)	15.53±0.31
30352187	2010-01-20	704.617	$1.53^{+0.15}_{-0.13}$	0.18±0.04	1.05(402)	1.60±0.04	2.40±0.05	1.05(402)	16.87±0.23
31540008	2010-01-21	1059.621	$0.68^{+0.09}_{-0.12}$	0.20±0.04	1.09(362)	1.56±0.08	2.44±0.03	1.10(362)	10.55±0.14
31540010	2010-01-23	1109.454	$0.72^{+0.08}_{-0.10}$	0.25±0.05	0.93(335)	1.51±0.08	2.49±0.03	0.94(335)	7.62±0.11
30352188	2010-01-24	1124.621	$0.81^{+0.21}_{-0.22}$	0.11±0.05	0.95(308)	1.69±0.12	2.31±0.06	0.95(308)	12.25±0.24
30352189	2010-01-27	1104.609	$0.83^{+0.05}_{-0.07}$	0.33±0.04	1.08(360)	1.42±0.06	2.57±0.03	1.08(360)	9.42±0.13
30352196-Seg1	2010-02-05	598.200	$1.63^{+0.15}_{-0.16}$	0.19±0.04	1.12(354)	1.58±0.05	2.42±0.06	1.12(354)	33.36±0.53
30352196-Seg2	2010-02-05	585.200	$1.60^{+0.16}_{-0.14}$	0.22±0.05	1.18(345)	1.55±0.05	2.45±0.06	1.19(345)	33.15±0.54
30352200	2010-02-10	1014.608	$1.07^{+0.06}_{-0.08}$	0.29±0.04	0.99(358)	1.48±0.05	2.52±0.04	0.99(358)	10.00±0.14
30352203-Seg1	2010-02-12	596.200	$1.20^{+0.06}_{-0.07}$	0.28±0.04	1.05(390)	1.49±0.04	2.52±0.04	1.05(390)	20.00±0.26
30352203-Seg2	2010-02-12	510.600	$1.25^{+0.06}_{-0.07}$	0.30±0.04	1.18(373)	1.47±0.05	2.53±0.04	1.18(373)	20.00±0.28
30352205	2010-02-15	929.527	$0.85^{+0.06}_{-0.08}$	0.23±0.03	0.99(412)	1.53±0.05	2.47±0.03	1.00(412)	18.57±0.21
30352206-Seg1	2010-02-16	598.100	$3.46^{+0.38}_{-0.32}$	0.21±0.03	1.18(514)	1.54±0.02	2.49±0.06	1.17(514)	35.70±0.38
30352206-Seg2	2010-02-16	586.900	$3.38^{+0.36}_{-0.31}$	0.22±0.03	1.09(505)	1.53±0.02	2.49±0.06	1.09(505)	34.99±0.38
30352207	2010-02-17	1064.609	$6.58^{+1.41}_{-1.44}$	0.17±0.03	0.99(515)	1.58±0.01	2.51±0.14	1.00(515)	46.21±0.56
30352208	2010-02-18	607.231	$2.42^{+0.48}_{-0.30}$	0.19±0.04	1.09(384)	1.57±0.04	2.43±0.07	1.09(384)	31.27±0.49
30352212	2010-02-24	1419.578	$3.10^{+0.30}_{-0.39}$	0.18±0.03	1.07(496)	1.58±0.02	2.43±0.06	1.07(496)	17.93±0.20
30352213	2010-02-25	884.617	$4.07^{+0.78}_{-0.77}$	0.14±0.03	1.07(485)	1.63±0.02	2.40±0.08	1.06(485)	20.00±0.23
30352214	2010-02-26	1389.166	$4.43^{+0.64}_{-0.47}$	0.22±0.02	1.14(578)	1.52±0.01	2.57±0.07	1.11(578)	24.95±0.22
30352215	2010-02-27	1278.909	$4.06^{+0.73}_{-0.69}$	0.15±0.03	0.93(496)	1.61±0.02	2.43±0.08	0.92(496)	18.46±0.21
30352217-Seg1	2010-03-02	498.900	$5.94^{+1.20}_{-0.80}$	0.17±0.04	1.09(436)	1.58±0.02	2.55±0.17	1.08(436)	25.35±0.37
30352219	2010-03-04	899.620	$2.25^{+0.36}_{-0.24}$	0.19±0.04	1.07(417)	1.57±0.03	2.43±0.06	1.07(417)	24.84±0.35
30352221	2010-03-06	1194.607	$3.01^{+0.88}_{-0.52}$	0.13±0.03	1.07(452)	1.65±0.03	2.35±0.07	1.07(452)	14.65±0.18
30352222	2010-03-07	1189.619	$4.37^{+1.02}_{-0.98}$	0.16±0.04	1.06(390)	1.60±0.03	2.44±0.13	1.06(390)	14.78±0.25

ObsID	Date of Obs.	Exposure	*eplogpar*			*sbpl*			Flux$_{0.3-10.0\,\mathrm{kev}}$
		(sec)	ϵ_p (keV)	β	χ^2_{red} (dof)	Γ_{low}	Γ_{high}	χ^2_{red} (dof)	($10^{-10}\mathrm{erg\,cm^{-2}s^{-1}}$)
30352224	2010-03-09	969.617	$4.40^{+0.76}_{-0.53}$	0.23±0.03	1.07(520)	1.50±0.01	2.60±0.09	1.05(520)	23.30±0.25
30352226	2010-03-11	944.696	$1.50^{+0.09}_{-0.09}$	0.24±0.03	1.06(433)	1.53±0.04	2.47±0.04	1.07(433)	16.25±0.19
30352227	2010-03-12	1014.446	$1.72^{+0.09}_{-0.09}$	0.24±0.03	1.00(491)	1.53±0.03	2.47±0.04	1.00(491)	22.23±0.22
30352228	2010-03-14	959.448	$0.45^{+0.07}_{-0.09}$	0.26±0.04	0.96(326)	1.42±0.12	2.53±0.02	0.98(326)	10.00±0.14
30352233	2010-03-20	1344.621	$0.73^{+0.07}_{-0.09}$	0.22±0.04	0.94(387)	1.54±0.07	2.46±0.03	0.95(387)	9.38±0.11
30352234	2010-03-21	1039.564	$0.62^{+0.12}_{-0.16}$	0.15±0.04	1.01(366)	1.62±0.09	2.38±0.03	1.01(366)	10.00±0.14
30352235	2010-03-22	1009.448	$0.66^{+0.06}_{-0.07}$	0.33±0.05	0.99(328)	1.40±0.08	2.58±0.03	1.00(328)	8.76±0.12
30352236	2010-03-23	979.606	$0.66^{+0.15}_{-0.21}$	0.17±0.06	0.78(283)	1.60±0.12	2.40±0.04	0.78(283)	8.55±0.17
30352237-Seg1	2010-03-25	497.500	$1.28^{+0.16}_{-0.17}$	0.18±0.06	0.99(298)	1.59±0.07	2.41±0.06	0.99(298)	12.23±0.24
30352237-Seg2	2010-03-25	592.600	$1.30^{+0.13}_{-0.14}$	0.20±0.05	1.09(324)	1.57±0.06	2.43±0.06	1.09(324)	12.48±0.22
30352238	2010-03-27	1049.452	$1.70^{+0.10}_{-0.10}$	0.27±0.04	0.97(431)	1.49±0.03	2.51±0.04	0.98(431)	14.52±0.18
30352239	2010-03-29	1009.634	$2.42^{+0.35}_{-0.24}$	0.24±0.04	0.95(395)	1.52±0.03	2.48±0.07	0.95(395)	15.11±0.23
30352240	2010-03-31	1024.625	$1.60^{+0.11}_{-0.11}$	0.24±0.04	1.06(413)	1.53±0.04	2.47±0.05	1.06(413)	12.42±0.16
30352241	2010-03-31	691.235	$1.48^{+0.14}_{-0.13}$	0.25±0.05	1.05(317)	1.52±0.05	2.48±0.06	1.05(317)	10.50±0.19
30352242	2010-04-01	849.555	$0.90^{+0.09}_{-0.11}$	0.24±0.05	0.92(317)	1.53±0.07	2.48±0.04	0.93(317)	8.84±0.14
31202006	2010-04-02	1069.602	$0.97^{+0.08}_{-0.10}$	0.21±0.04	1.00(379)	1.56±0.06	2.45±0.04	1.01(379)	10.00±0.14
31202007	2010-04-03	869.227	$1.65^{+0.14}_{-0.12}$	0.27±0.05	1.08(342)	1.50±0.05	2.50±0.06	1.08(342)	11.76±0.20
31202008	2010-04-05	808.992	$0.66^{+0.21}_{-0.35}$	0.13±0.07	1.02(262)	1.63±0.16	2.36±0.06	1.02(262)	7.77±0.18
31202009-Seg1	2010-04-07	581.400	$0.71^{+0.19}_{-0.30}$	0.23±0.11	1.10(183)	1.51±0.19	2.47±0.07	1.10(183)	7.77±0.27
31202009-Seg2	2010-04-07	519.900	$0.92^{+0.20}_{-0.29}$	0.24±0.11	1.11(171)	1.52±0.17	2.48±0.10	1.11(171)	8.12±0.31
31202015	2010-04-23	789.448	$0.62^{+0.08}_{-0.11}$	0.24±0.05	0.99(317)	1.49±0.09	2.49±0.03	0.99(317)	10.00±0.15
31202017	2010-04-28	884.609	$1.38^{+0.08}_{-0.09}$	0.25±0.04	1.16(409)	1.52±0.04	2.48±0.04	1.17(409)	14.05±0.18
31202018	2010-04-29	994.752	$1.71^{+0.11}_{-0.10}$	0.25±0.03	1.12(444)	1.52±0.03	2.48±0.04	1.12(444)	15.18±0.18
31202019-Seg1	2010-05-02	598.300	$1.27^{+0.12}_{-0.12}$	0.21±0.05	1.00(334)	1.56±0.05	2.44±0.05	1.00(334)	13.36±0.22
31202019-Seg2	2010-05-02	589.000	$1.46^{+0.11}_{-0.13}$	0.25±0.05	0.99(339)	1.52±0.05	2.48±0.05	0.99(339)	13.64±0.23
31202020	2010-05-03	1194.428	$0.59^{+0.06}_{-0.08}$	0.24±0.04	1.11(391)	1.50±0.07	2.49±0.02	1.12(391)	12.24±0.14
31202021-Seg1	2010-05-04	399.700	$1.26^{+0.09}_{-0.09}$	0.31±0.05	1.08(304)	1.47±0.06	2.54±0.05	1.08(304)	15.03±0.27
31202021-Seg2	2010-05-04	399.700	$1.23^{+0.10}_{-0.10}$	0.27±0.05	0.98(304)	1.50±0.06	2.50±0.05	0.99(304)	15.18±0.28
31202021-Seg3	2010-05-04	373.900	$1.20^{+0.09}_{-0.10}$	0.29±0.06	0.88(295)	1.48±0.06	2.52±0.05	0.88(295)	15.13±0.28
31202022	2010-05-05	1194.454	$1.89^{+0.14}_{-0.12}$	0.23±0.03	1.01(469)	1.54±0.03	2.46±0.04	1.01(469)	15.49±0.17

ObsID	Date of Obs.	Exposure	*eplogpar*			*sbpl*			$\mathrm{Flux}_{0.3-10.0\,\mathrm{kev}}$
		(sec)	ϵ_p (keV)	β	χ^2_{red} (dof)	Γ_{low}	Γ_{high}	χ^2_{red} (dof)	($10^{-10}\mathrm{erg\,cm^{-2}s^{-1}}$)
31202023	2010-05-06	1014.460	$3.23^{+0.78}_{-0.47}$	0.16±0.03	1.11(468)	1.60±0.02	2.41±0.07	1.11(468)	16.50±0.20
31202026	2010-05-09	1149.455	$0.68^{+0.03}_{-0.04}$	0.42±0.03	0.99(410)	1.32±0.05	2.67±0.02	1.03(410)	14.41±0.14
31202027	2010-05-10	954.443	$0.44^{+0.05}_{-0.06}$	0.35±0.05	1.03(316)	1.25±0.13	2.62±0.02	1.06(316)	9.37±0.12
31202028	2010-05-11	994.607	$0.87^{+0.04}_{-0.06}$	0.31±0.04	1.07(409)	1.45±0.05	2.55±0.03	1.08(409)	14.07±0.16
31202029	2010-05-14	854.617	$0.44^{+0.08}_{-0.10}$	0.28±0.05	1.01(292)	1.36±0.15	2.54±0.02	1.02(292)	7.52±0.12
31202031	2010-05-20	1124.602	$0.73^{+0.07}_{-0.09}$	0.25±0.04	0.99(348)	1.49±0.07	2.50±0.03	0.99(348)	8.46±0.12
31202033	2010-05-26	1009.618	$0.53^{+0.12}_{-0.15}$	0.17±0.04	0.94(340)	1.58±0.11	2.40±0.03	0.95(340)	10.00±0.15
31202034	2010-05-29	1164.461	$0.42^{+0.05}_{-0.06}$	0.33±0.04	0.96(330)	1.21±0.14	2.61±0.02	0.96(330)	8.56±0.11
31202050	2010-12-13	999.639	$0.49^{+0.04}_{-0.06}$	0.45±0.05	1.15(291)	1.19±0.12	2.71±0.02	1.18(291)	7.55±0.11
31202140	2012-05-31	1069.606	$0.43^{+0.05}_{-0.06}$	0.29±0.04	1.17(377)	1.37±0.10	2.56±0.01	1.18(377)	12.85±0.14
35014054	2013-03-23	974.451	$0.55^{+0.08}_{-0.11}$	0.16±0.03	1.01(439)	1.60±0.07	2.39±0.02	1.02(439)	18.46±0.19
35014056	2013-03-30	1074.607	$1.07^{+0.07}_{-0.08}$	0.24±0.04	1.06(407)	1.53±0.05	2.47±0.04	1.07(407)	25.92±0.33
80050019-Orb1	2013-04-12	436.900	$1.88^{+0.10}_{-0.09}$	0.40±0.04	1.24(419)	1.38±0.03	2.62±0.05	1.24(419)	58.70±0.77
80050019-Orb5	2013-04-12	1516.000	$1.60^{+0.05}_{-0.05}$	0.35±0.02	1.22(554)	1.43±0.02	2.57±0.02	1.23(554)	53.70±0.41
35014065-Orb3	2013-04-17	1497.000	$1.86^{+0.17}_{-0.13}$	0.14±0.02	1.12(561)	1.65±0.02	2.35±0.04	1.12(561)	25.43±0.20
35014079	2013-12-05	1034.449	$0.45^{+0.06}_{-0.08}$	0.27±0.04	1.17(352)	1.43±0.10	2.55±0.02	1.18(352)	10.67±0.13
35014081-Seg1	2013-12-09	498.600	$1.04^{+0.08}_{-0.10}$	0.25±0.04	1.11(343)	1.53±0.06	2.48±0.04	1.12(343)	17.07±0.26
35014082	2013-12-11	1054.607	$0.76^{+0.06}_{-0.08}$	0.22±0.03	1.11(430)	1.54±0.06	2.46±0.03	1.11(430)	15.62±0.17
35014083-Seg1	2013-12-13	408.500	$2.13^{+0.54}_{-0.30}$	0.15±0.04	1.03(358)	1.63±0.05	2.37±0.07	1.03(358)	21.05±0.34
35014083-Seg2	2013-12-13	459.000	$1.91^{+0.22}_{-0.17}$	0.23±0.04	1.17(354)	1.53±0.04	2.47±0.06	1.17(354)	19.42±0.31
35014106	2014-02-14	1029.617	$0.77^{+0.04}_{-0.06}$	0.27±0.03	1.12(459)	1.50±0.05	2.51±0.02	1.15(459)	20.00±0.19
35014107	2014-02-15	554.444	$0.43^{+0.08}_{-0.10}$	0.22±0.04	1.05(335)	1.46±0.13	2.48±0.02	1.06(335)	29.23±0.41
35014125	2014-04-01	324.617	$0.48^{+0.12}_{-0.16}$	0.26±0.08	0.99(222)	1.44±0.19	2.52±0.04	1.00(222)	9.47±0.23
35014154-Seg1	2015-01-02	499.200	$0.77^{+0.10}_{-0.13}$	0.21±0.04	0.99(334)	1.56±0.08	2.44±0.04	0.99(334)	17.11±0.26
35014154-Seg2	2015-01-02	473.300	$0.97^{+0.10}_{-0.12}$	0.21±0.04	0.94(340)	1.57±0.07	2.43±0.04	0.95(340)	17.59±0.27
35014157-Orb1	2015-01-06	564.800	$0.76^{+0.07}_{-0.09}$	0.29±0.05	1.19(321)	1.46±0.08	2.54±0.03	1.19(321)	14.01±0.21
35014157-Orb2	2015-01-06	445.500	$1.12^{+0.09}_{-0.10}$	0.25±0.05	1.19(316)	1.52±0.06	2.48±0.05	1.18(316)	15.63±0.26
35014160-Seg1	2015-01-13	395.600	$1.31^{+0.22}_{-0.21}$	0.14±0.05	1.03(313)	1.65±0.08	2.35±0.07	1.03(313)	16.16±0.30
35014160-Seg2	2015-01-13	554.400	$1.22^{+0.13}_{-0.14}$	0.17±0.04	1.15(359)	1.61±0.06	2.39±0.05	1.15(359)	16.57±0.25
35014161-Seg1	2015-01-15	398.000	$0.76^{+0.11}_{-0.09}$	0.31±0.06	0.99(283)	1.44±0.09	2.55±0.04	0.99(283)	13.50±0.25
35014161-Seg2	2015-01-15	460.100	$0.78^{+0.09}_{-0.08}$	0.33±0.05	1.09(298)	1.42±0.08	2.57±0.04	1.09(298)	13.65±0.23

ObsID	Date of Obs.	Exposure	*eplogpar*			*sbpl*			$\text{Flux}_{0.3-10.0\,\text{kev}}$
		(sec)	ϵ_p (keV)	β	χ^2_{red} (dof)	Γ_{low}	Γ_{high}	χ^2_{red} (dof)	($10^{-10}\text{erg}\,\text{cm}^{-2}\text{s}^{-1}$)
35014162-Seg1	2015-01-17	400.700	$0.72^{+0.13}_{-0.12}$	0.09±0.05	1.10(301)	1.71±0.09	2.29±0.06	1.11(301)	14.39±0.27
35014162-Seg2	2015-01-17	301.300	$0.77^{+0.13}_{-0.12}$	0.17±0.06	1.11(265)	1.60±0.08	2.40±0.05	1.11(265)	14.57±0.31
35014162-Seg3	2015-01-17	262.100	$1.06^{+0.51}_{-0.32}$	0.11±0.07	1.10(257)	1.70±0.08	2.30±0.08	1.11(257)	14.94±0.36
35014163	2015-01-18	969.448	$0.54^{+0.06}_{-0.08}$	0.29±0.04	1.13(346)	1.42±0.09	2.55±0.02	1.15(346)	11.35±0.15
35014164-Seg1	2015-01-19	500.300	$0.93^{+0.07}_{-0.06}$	0.34±0.04	0.93(347)	1.43±0.06	2.58±0.03	0.94(347)	18.50±0.26
35014164-Seg2	2015-01-19	475.800	$1.05^{+0.06}_{-0.05}$	0.42±0.05	1.14(343)	1.37±0.05	2.64±0.03	1.15(343)	18.14±0.26
35014165-Orb1	2015-01-21	742.900	$1.21^{+0.13}_{-0.14}$	0.22±0.06	0.97(288)	1.55±0.08	2.45±0.06	0.98(288)	10.00±0.21
35014166-Seg1	2015-01-21	500.900	$1.23^{+0.15}_{-0.16}$	0.15±0.05	1.19(345)	1.63±0.07	2.37±0.05	1.20(345)	17.51±0.28
35014166-Seg2	2015-01-21	498.700	$0.97^{+0.15}_{-0.20}$	0.14±0.04	1.18(344)	1.66±0.08	2.35±0.05	1.19(344)	17.60±0.28
35014166-Seg3	2015-01-21	462.100	$1.34^{+0.18}_{-0.17}$	0.16±0.05	1.02(335)	1.62±0.07	2.38±0.06	1.02(335)	17.77±0.30
35014167	2015-01-24	329.457	$0.83^{+0.17}_{-0.25}$	0.18±0.07	0.92(252)	1.59±0.13	2.41±0.06	0.92(252)	13.11±0.31
35014168	2015-01-25	1134.604	$0.47^{+0.08}_{-0.11}$	0.21±0.04	1.10(361)	1.51±0.11	2.46±0.02	1.11(361)	10.52±0.14
35014170	2015-01-29	1004.619	$0.56^{+0.05}_{-0.07}$	0.33±0.04	1.13(333)	1.39±0.09	2.59±0.02	1.16(333)	9.45±0.13
35014173	2015-02-06	874.619	$1.62^{+0.21}_{-0.17}$	0.24±0.06	1.06(290)	1.53±0.06	2.47±0.08	1.06(290)	10.66±0.23
35014174	2015-02-09	824.621	$0.67^{+0.05}_{-0.07}$	0.29±0.04	1.08(374)	1.45±0.07	2.54±0.02	1.10(374)	14.31±0.17
35014175	2015-02-11	914.109	$6.06^{+1.50}_{-1.80}$	0.13±0.03	1.05(475)	1.64±0.02	2.45±0.13	0.13(475)	18.46±0.22
35014176	2015-02-13	994.609	$2.02^{+0.49}_{-0.28}$	0.12±0.04	1.08(418)	1.67±0.05	2.33±0.06	1.08(418)	18.65±0.25
35014177	2015-02-15	709.448	$0.91^{+0.09}_{-0.11}$	0.21±0.04	1.02(356)	1.56±0.07	2.45±0.04	1.02(356)	13.07±0.19
35014178	2015-02-17	189.635	$0.66^{+0.08}_{-0.08}$	0.27±0.07	0.87(191)	1.45±0.11	2.53±0.06	0.87(191)	11.00±0.34
35014185	2015-03-08	844.630	$1.20^{+0.05}_{-0.06}$	0.29±0.03	0.95(426)	1.48±0.04	2.52±0.03	0.96(426)	20.00±0.23
35014186	2015-03-11	835.035	$0.54^{+0.07}_{-0.10}$	0.23±0.04	1.05(367)	1.48±0.09	2.49±0.02	1.05(367)	15.18±0.19
35014188-Seg1	2015-03-15	497.400	$0.82^{+0.12}_{-0.10}$	0.21±0.04	1.10(342)	1.56±0.07	2.44±0.04	1.10(342)	17.05±0.26
35014188-Seg2	2015-03-15	494.300	$0.80^{+0.11}_{-0.10}$	0.22±0.05	1.19(338)	1.54±0.07	2.46±0.04	1.19(338)	16.92±0.26
35014190	2015-03-19	949.460	$0.55^{+0.05}_{-0.06}$	0.37±0.05	0.99(318)	1.28±0.10	2.64±0.02	1.00(318)	10.00±0.13
35014194	2015-03-27	1004.615	$0.87^{+0.04}_{-0.06}$	0.28±0.03	1.02(458)	1.48±0.04	2.52±0.02	1.04(458)	20.00±0.19
35014199	2015-04-03	1119.620	$0.57^{+0.05}_{-0.07}$	0.32±0.04	1.03(360)	1.40±0.08	2.58±0.02	1.06(360)	13.40±0.16
35014201-Seg1	2015-04-07	399.400	$0.41^{+0.08}_{-0.10}$	0.23±0.07	0.99(240)	1.36±0.14	2.50±0.03	0.98(240)	10.00±0.22
35014201-Seg2	2015-04-07	409.600	$0.46^{+0.08}_{-0.10}$	0.26±0.07	0.99(242)	1.37±0.14	2.53±0.03	0.99(242)	10.00±0.21
35014202	2015-04-09	919.066	$0.89^{+0.05}_{-0.07}$	0.28±0.04	1.17(399)	1.49±0.05	2.51±0.03	1.18(399)	15.90±0.19
35014203-Seg1	2015-04-11	600.200	$1.21^{+0.06}_{-0.08}$	0.29±0.04	1.05(376)	1.49±0.05	2.52±0.04	1.06(376)	18.44±0.25

ObsID	Date of Obs.	Exposure	*eplogpar*			*sbpl*			$\text{Flux}_{0.3-10.0\,\text{kev}}$
		(sec)	ϵ_p (keV)	β	χ^2_{red} (dof)	Γ_{low}	Γ_{high}	χ^2_{red} (dof)	($10^{-10}\text{erg}\,\text{cm}^{-2}\text{s}^{-1}$)
35014203-Seg2	2015-04-11	527.400	$1.28^{+0.08}_{-0.09}$	0.27±0.04	1.11(360)	1.51±0.05	2.50±0.04	1.11(360)	18.82±0.27
35014204	2015-04-13	829.443	$1.20^{+0.04}_{-0.05}$	0.33±0.03	1.15(431)	1.45±0.04	2.56±0.03	1.16(431)	19.35±0.22
35014208	2015-04-17	619.617	$0.62^{+0.11}_{-0.15}$	0.18±0.05	1.09(335)	1.57±0.10	2.42±0.03	1.09(335)	14.31±0.22
35014212	2015-04-22	954.599	$0.66^{+0.06}_{-0.08}$	0.24±0.03	0.97(410)	1.51±0.06	2.49±0.02	0.98(410)	15.81±0.17
35014214	2015-04-29	969.605	$0.43^{+0.06}_{-0.08}$	0.26±0.04	0.98(365)	1.41±0.11	2.52±0.02	1.01(365)	12.65±0.15
92204003	2015-05-05	1020.032	$0.76^{+0.08}_{-0.11}$	0.21±0.04	1.00(380)	1.56±0.07	2.44±0.03	1.01(380)	11.82±0.15
35014216	2015-05-06	1019.626	$0.75^{+0.12}_{-0.17}$	0.14±0.04	0.98(384)	1.64±0.08	2.36±0.04	0.99(384)	11.59±0.16
35014218	2015-05-08	1094.610	$0.50^{+0.08}_{-0.10}$	0.28±0.05	1.16(301)	1.40±0.13	2.54±0.02	1.17(301)	6.47±0.10
35014219	2015-05-10	1079.617	$0.44^{+0.09}_{-0.12}$	0.22±0.05	1.12(318)	1.49±0.13	2.47±0.02	1.13(318)	7.49±0.11
35014226	2015-05-24	464.195	$0.70^{+0.06}_{-0.08}$	0.44±0.07	1.11(245)	1.33±0.11	2.68±0.04	1.14(245)	9.27±0.18
92204006	2015-06-02	908.953	$0.70^{+0.05}_{-0.06}$	0.33±0.04	1.03(355)	1.41±0.07	2.58±0.02	1.04(355)	12.43±0.16
35014242	2015-12-14	1069.451	$0.68^{+0.03}_{-0.04}$	0.47±0.04	1.04(391)	1.26±0.06	2.71±0.02	1.07(391)	14.41±0.14
35014243	2015-12-17	1014.618	$0.45^{+0.06}_{-0.07}$	0.27±0.04	1.13(376)	1.41±0.10	2.53±0.02	1.15(376)	12.69±0.14
34228001	2015-12-21	2009.225	$0.63^{+0.09}_{-0.11}$	0.15±0.03	1.10(466)	1.62±0.06	2.38±0.02	1.10(466)	10.64±0.11
35014251	2015-12-27	984.454	$0.68^{+0.05}_{-0.07}$	0.31±0.04	1.16(371)	1.42±0.07	2.56±0.02	1.17(371)	12.17±0.15
34228006	2015-12-30	989.620	$0.98^{+0.04}_{-0.06}$	0.27±0.03	1.18(464)	1.50±0.04	2.51±0.02	1.19(464)	20.61±0.20
34228007	2015-12-31	949.447	$0.73^{+0.05}_{-0.06}$	0.26±0.03	1.19(443)	1.50±0.05	2.50±0.02	1.17(443)	21.09±0.21
34228009	2016-01-03	1069.614	$0.46^{+0.03}_{-0.04}$	0.40±0.03	1.18(381)	1.18±0.09	2.67±0.01	1.20(381)	14.65±0.14
35014254	2016-01-04	984.660	$0.48^{+0.03}_{-0.05}$	0.35±0.03	1.08(404)	1.30±0.08	2.62±0.01	1.15(404)	17.75±0.17
92399004-Seg1	2016-05-26	597.000	$1.31^{+0.11}_{-0.12}$	0.20±0.04	1.09(368)	1.57±0.05	2.43±0.05	1.09(368)	16.35±0.24
92399004-Seg2	2016-05-26	541.600	$1.29^{+0.13}_{-0.13}$	0.18±0.04	1.19(354)	1.59±0.06	2.41±0.05	1.19(354)	16.15±0.25
92399006-Seg1	2016-06-09	495.600	$1.89^{+0.28}_{-0.20}$	0.21±0.05	1.19(337)	1.56±0.05	2.44±0.07	1.19(337)	28.95±0.49
92399006-Seg2	2016-06-09	492.400	$1.82^{+0.30}_{-0.20}$	0.19±0.05	1.06(327)	1.58±0.05	2.42±0.07	1.06(327)	27.31±0.49
34228080	2016-06-12	909.621	$0.75^{+0.09}_{-0.12}$	0.18±0.04	1.02(400)	1.59±0.07	2.41±0.03	1.03(400)	13.85±0.17
34228108	2017-01-02	899.461	$0.85^{+0.07}_{-0.09}$	0.24±0.04	0.90(363)	1.52±0.06	2.48±0.03	0.90(363)	11.50±0.16
34228109	2017-01-03	974.617	$0.43^{+0.08}_{-0.08}$	0.21±0.05	1.00(309)	1.46±0.08	2.46±0.02	0.99(309)	7.91±0.12
34228110-Orb3	2017-01-04	848.300	$1.37^{+0.10}_{-0.09}$	0.26±0.04	1.17(354)	1.51±0.04	2.49±0.05	1.18(354)	10.78±0.16
34228110-Orb5	2017-01-04	785.300	$1.25^{+0.10}_{-0.09}$	0.26±0.05	1.01(344)	1.51±0.05	2.49±0.05	1.02(344)	10.79±0.17
34228116	2017-01-10	964.617	$0.79^{+0.08}_{-0.11}$	0.20±0.04	1.20(390)	1.57±0.07	2.43±0.03	1.20(390)	13.38±0.17
34228118	2017-01-19	1114.621	$0.92^{+0.08}_{-0.10}$	0.22±0.04	1.19(369)	1.54±0.06	2.46±0.03	1.20(369)	10.00±0.13
81926001	2017-01-31	1008.000	$1.32^{+0.19}_{-0.17}$	0.13±0.04	1.05(379)	1.66±0.05	2.34±0.05	1.05(379)	10.57±0.15

ObsID	Date of Obs.	Exposure	*eplogpar*			*sbpl*			$\mathrm{Flux}_{0.3-10.0\,\mathrm{kev}}$
		(sec)	ϵ_p (keV)	β	χ^2_{red} (dof)	Γ_{low}	Γ_{high}	χ^2_{red} (dof)	($10^{-10}\mathrm{erg\,cm^{-2}s^{-1}}$)
34228128	2017-02-01	844.610	$0.85^{+0.32}_{-0.64}$	0.07±0.05	1.03(304)	1.75±0.15	2.25±0.07	1.03(304)	8.91±0.17
34228127	2017-02-01	844.619	$0.76^{+0.11}_{-0.12}$	0.08±0.04	1.02(356)	1.74±0.11	2.26±0.05	1.02(356)	11.55±0.18
34228129	2017-02-01	964.442	$0.74^{+0.15}_{-0.16}$	0.12±0.04	1.06(372)	1.67±0.09	2.33±0.04	1.06(372)	11.36±0.16
34228126	2017-02-01	789.617	$0.91^{+0.16}_{-0.16}$	0.12±0.04	1.16(346)	1.67±0.09	2.33±0.05	1.16(346)	11.30±0.18
34228131	2017-02-01	1049.157	$0.49^{+0.10}_{-0.10}$	0.18±0.04	0.97(346)	1.56±0.11	2.42±0.03	0.97(346)	9.40±0.13
34228159	2017-03-14	1034.621	$0.43^{+0.08}_{-0.08}$	0.19±0.04	1.01(336)	1.50±0.11	2.44±0.02	1.01(336)	10.00±0.14
34228161	2017-03-19	1004.621	$0.65^{+0.11}_{-0.15}$	0.15±0.04	1.02(373)	1.62±0.08	2.38±0.03	1.03(373)	12.64±0.17
31630004	2017-04-15	864.515	$1.53^{+0.08}_{-0.08}$	0.30±0.04	1.10(398)	1.47±0.04	2.53±0.04	1.10(398)	16.81±0.22
31630007	2017-04-18	904.617	$0.57^{+0.09}_{-0.12}$	0.21±0.04	1.00(322)	1.54±0.10	2.45±0.03	1.01(322)	9.35±0.14
31630009	2017-04-21	1008.341	$0.44^{+0.08}_{-0.08}$	0.17±0.04	0.95(357)	1.54±0.12	2.42±0.02	0.95(357)	10.68±0.14
92412001	2017-04-23	1173.083	$0.97^{+0.08}_{-0.10}$	0.22±0.04	1.06(358)	1.55±0.06	2.45±0.04	1.07(358)	10.92±0.16
31630010	2017-04-24	889.621	$0.73^{+0.11}_{-0.15}$	0.18±0.04	1.02(346)	1.59±0.08	2.41±0.04	1.02(346)	10.00±0.15
93249001	2017-04-25	1119.607	$0.75^{+0.07}_{-0.10}$	0.23±0.04	1.12(376)	1.54±0.07	2.47±0.03	1.13(376)	10.67±0.14
93249002	2017-04-26	1009.610	$0.56^{+0.14}_{-0.19}$	0.15±0.05	1.05(314)	1.61±0.12	2.38±0.03	1.05(314)	10.72±0.18
93249004	2017-04-28	1029.447	$0.49^{+0.09}_{-0.12}$	0.21±0.04	1.08(334)	1.53±0.11	2.45±0.02	1.10(334)	9.03±0.13
92412002	2017-04-30	1029.460	$0.54^{+0.14}_{-0.18}$	0.13±0.04	0.98(366)	1.66±0.10	2.35±0.03	0.98(366)	10.86±0.15
93249005	2017-05-01	959.454	$0.58^{+0.12}_{-0.16}$	0.15±0.04	1.13(376)	1.63±0.09	2.37±0.03	1.14(376)	12.57±0.17
92412004-Seg1	2017-05-14	597.600	$1.23^{+0.29}_{-0.28}$	0.11±0.05	1.14(320)	1.70±0.08	2.30±0.07	1.14(320)	11.13±0.20
31630014	2017-05-22	999.607	$1.04^{+0.10}_{-0.12}$	0.19±0.04	1.08(361)	1.59±0.06	2.42±0.04	1.08(361)	10.00±0.14
92412006	2017-05-28	908.952	$3.95^{+0.98}_{-0.92}$	0.12±0.04	1.19(425)	1.65±0.03	2.38±0.10	1.18(425)	14.12±0.19
93249012	2017-06-27	1084.390	$0.54^{+0.09}_{-0.12}$	0.20±0.04	1.16(335)	1.56±0.10	2.44±0.03	1.18(335)	8.46±0.12
31202147	2017-12-19	1079.110	$0.60^{+0.08}_{-0.10}$	0.18±0.03	1.15(434)	1.60±0.07	2.41±0.02	1.17(434)	16.32±0.17
31202212-Seg1	2018-03-14	495.800	$1.17^{+0.18}_{-0.21}$	0.13±0.04	1.08(348)	1.67±0.07	2.33±0.05	1.08(348)	19.37±0.30
31202212-Seg2	2018-03-14	499.000	$1.27^{+0.16}_{-0.17}$	0.15±0.04	1.04(348)	1.64±0.06	2.36±0.05	1.04(348)	20.00±0.31
31202213	2018-03-15	279.457	$1.07^{+0.13}_{-0.15}$	0.22±0.06	0.97(271)	1.55±0.09	2.45±0.06	0.97(271)	17.32±0.37
31202214	2018-03-16	394.713	$1.05^{+0.23}_{-0.31}$	0.11±0.05	1.09(306)	1.69±0.10	2.31±0.06	1.09(306)	16.81±0.31
31202215-Seg1	2018-03-17	596.300	$0.88^{+0.07}_{-0.10}$	0.29±0.05	1.17(311)	1.48±0.07	2.53±0.04	1.18(311)	12.02±0.19
31202215-Seg-2	2018-03-17	454.600	$0.86^{+0.09}_{-0.11}$	0.29±0.06	1.11(279)	1.48±0.09	2.52±0.04	1.12(279)	12.02±0.22
31202216	2018-03-18	1074.608	$1.13^{+0.11}_{-0.13}$	0.24±0.06	1.04(296)	1.54±0.07	2.47±0.05	1.05(296)	12.78±0.24
31202231-Seg1	2018-04-18	495.200	$1.33^{+0.28}_{-0.33}$	0.12±0.06	1.05(293)	1.68±0.08	2.32±0.08	1.05(293)	10.89±0.22
31202231-Seg2	2018-04-18	517.400	$1.06^{+0.25}_{-0.20}$	0.14±0.06	1.18(296)	1.65±0.08	2.35±0.06	1.18(296)	10.76±0.21

ObsID	Date of Obs.	Exposure (sec)	*eplogpar* ϵ_p (keV)	*eplogpar* β	*eplogpar* χ^2_{red} (dof)	*sbpl* $\Gamma_{\rm low}$	*sbpl* $\Gamma_{\rm high}$	*sbpl* χ^2_{red} (dof)	$\rm Flux_{0.3-10.0\,kev}$ ($10^{-10}\rm erg\,cm^{-2}s^{-1}$)
31202239-Orb1	2018-05-20	522.100	$0.62^{+0.11}_{-0.10}$	0.36±0.08	1.12(224)	1.36±0.14	2.61±0.04	1.12(224)	7.34±0.17
94151014	2018-11-28	1054.619	$0.53^{+0.06}_{-0.08}$	0.26±0.04	1.09(373)	1.47±0.08	2.51±0.02	1.11(373)	12.13±0.14
31630030	2019-01-23	969.617	$0.57^{+0.09}_{-0.10}$	0.10±0.04	1.16(339)	1.71±0.12	2.30±0.04	1.17(339)	10.00±0.16
31630042	2019-02-24	944.445	$0.48^{+0.07}_{-0.09}$	0.21±0.04	1.08(395)	1.54±0.09	2.46±0.02	1.11(395)	15.16±0.17
31630045	2019-03-02	1019.617	$0.78^{+0.07}_{-0.09}$	0.20±0.03	1.13(428)	1.57±0.06	2.43±0.03	1.14(428)	16.73±0.18
31630046	2019-03-04	1109.617	$0.79^{+0.10}_{-0.13}$	0.15±0.03	0.98(431)	1.63±0.06	2.37±0.03	0.98(431)	14.22±0.16
31630052	2019-03-23	409.617	$1.50^{+0.22}_{-0.18}$	0.19±0.06	1.16(298)	1.58±0.07	2.42±0.07	1.16(298)	13.68±0.27
31630053	2019-03-25	409.621	$1.84^{+0.43}_{-0.25}$	0.15±0.05	1.01(341)	1.64±0.06	2.36±0.07	1.01(341)	24.82±0.43
31630054-Orb1	2019-03-28	695.200	$0.74^{+0.12}_{-0.17}$	0.16±0.04	1.02(338)	1.62±0.09	2.39±0.04	1.03(338)	15.57±0.24
31630054-Orb2	2019-03-28	233.500	$1.23^{+0.16}_{-0.16}$	0.22±0.07	1.09(265)	1.56±0.08	2.44±0.07	1.09(265)	22.55±0.51
31630055	2019-03-29	883.052	$1.92^{+0.17}_{-0.14}$	0.26±0.04	1.06(386)	1.50±0.04	2.50±0.05	1.06(386)	18.89±0.27
31630078	2019-06-06	939.617	$0.44^{+0.09}_{-0.12}$	0.21±0.04	1.08(321)	1.52±0.12	2.46±0.02	1.10(321)	9.31±0.13
11445001	2019-06-13	999.621	$0.75^{+0.09}_{-0.13}$	0.17±0.04	1.02(393)	1.60±0.07	2.40±0.03	1.03(393)	12.23±0.15
11445006	2019-06-22	1009.871	$1.16^{+0.08}_{-0.09}$	0.21±0.04	1.04(406)	1.56±0.05	2.44±0.04	1.04(406)	12.74±0.16

Appendix B

Appendix 2

Table B.1: Table showing the best-fit parameters of power-law fitting of *Swift*-XRT observations.

ObsID	Exposure time (sec)	Observation time (in MJD)	Log_{10}Flux ($\text{ergs}\,\text{cm}^{-2}\,\text{s}^{-1}$)	Spectral index (α_X)	χ^2_{red}(d.o.f)	F-value	P-value
35009001	18873.447	53462.040	-11.280±0.025	2.68±0.10	1.35(36)	3.14	0.0851
35009002	7456.296	53600.620	-10.923±0.018	2.40±0.07	1.17(69)	17.00	0.0001
35009003	5678.500	54375.700	-11.076±0.032	2.05±0.11	0.84(31)	5.89	0.0215
35009004	2461.633	54396.690	-10.801±0.028	2.30±0.11	1.01(30)	7.18	0.0120
35009005	1995.273	54397.630	-11.001±0.040	2.20±0.14	0.93(16)	1.29	0.2738
35009006	2723.673	54398.180	-10.929±0.032	2.17±0.12	0.96(27)	9.47	0.0049
35009007	2201.395	54399.510	-10.949±0.038	2.05±0.14	1.94(24)	8.19	0.0088
35009008	1960.757	54400.370	-10.615±0.026	2.45±0.10	0.82(35)	2.83	0.1018
35009009	1756.998	54401.330	-10.885±0.041	2.25±0.16	0.92(15)	3.36	0.0880
35009012	2803.152	54407.200	-10.520±0.025	2.57±0.10	0.59(35)	0.12	0.7333
35009013	1923.724	54410.150	-11.052±0.044	2.43±0.20	0.64(13)	8.96	0.0112
35009014	2005.828	54413.150	-10.849±0.035	2.50±0.14	0.96(18)	0.08	0.7794
35009015	2380.795	54417.100	-10.958±0.037	2.58±0.17	1.22(16)	2.65	0.1243
35009016	1551.578	54577.620	-10.903±0.042	2.49±0.19	0.90(12)	4.73	0.0523
35009017	2002.351	54584.750	-10.350±0.021	2.63±0.08	1.21(49)	0.15	0.6974
35009018	4215.456	54585.830	-10.462±0.015	2.69±0.06	0.81(83)	0.01	0.9349
35009020	1906.966	54588.690	-10.880±0.032	2.65±0.16	1.31(21)	4.88	0.0389
35009021	2280.966	54798.810	-10.895±0.033	2.44±0.13	1.12(20)	0.61	0.4453
35009022	930.894	54806.900	-11.115±0.089	2.32±0.36	1.33(4)	0.02	0.9071
35009023	1442.916	54813.660	-11.054±0.059	2.46±0.23	1.79(6)	1.32	0.3020
35009024	1410.050	54820.360	-11.088±0.056	1.86±0.17	1.57(10)	0.07	0.8000
35009026	1974.480	54843.730	-11.042±0.041	2.21±0.14	0.77(14)	0.07	0.7925
35009027	1476.231	54850.290	-10.961±0.055	2.06±0.19	0.75(12)	3.53	0.0869
35009028	1927.047	54855.630	-11.126±0.046	2.16±0.16	1.46(13)	0.00	0.9965
35009029	1535.146	54864.670	-10.948±0.064	1.98±0.21	1.57(11)	0.39	0.5467
35009030	2306.189	54867.070	-10.925±0.039	2.00±0.13	1.14(21)	1.97	0.1757
35009032	3555.498	54874.690	-11.065±0.033	1.99±0.10	1.31(27)	0.20	0.6583
35009033	2604.626	54876.900	-11.052±0.039	2.02±0.13	0.77(21)	3.48	0.0767
35009034	4628.971	54878.630	-11.075±0.033	1.86±0.10	0.78(32)	1.57	0.2198
35009035	2462.866	54880.450	-11.062±0.039	2.13±0.14	1.02(19)	0.87	0.3642

ObsID	Exposure time (sec)	Observation time (in MJD)	Log_{10}Flux ($\mathrm{ergs\,cm^{-2}\,s^{-1}}$)	Spectral index (α_X)	χ^2_{red}(d.o.f)	F-value	P-value
35009036	2860.081	54882.050	-11.124±0.039	1.96±0.12	0.47(20)	0.35	0.5593
35009037	3245.926	54884.120	-11.224±0.040	2.06±0.13	0.67(17)	0.02	0.8974
35009038	3228.851	54886.000	-11.142±0.040	1.99±0.13	0.75(21)	0.86	0.3659
35009039	2489.205	54888.000	-11.096±0.046	1.79±0.13	0.49(16)	0.06	0.8100
35009040	1006.000	54889.070	-11.059±0.061	1.92±0.19	0.67(7)	0.03	0.8724
35009041	5573.671	55120.410	-11.136±0.027	2.32±0.10	1.01(34)	3.54	0.0689
35009042	1543.201	55165.120	-10.544±0.032	2.15±0.11	0.89(27)	0.48	0.4938
90082001	1892.669	55167.000	-10.599±0.027	2.16±0.09	0.85(37)	0.16	0.6953
35009043	1188.458	55172.880	-10.711±0.039	2.15±0.13	1.86(20)	0.03	0.8649
35009044	1318.462	55176.550	-10.709±0.051	1.95±0.16	0.76(15)	1.55	0.2336
35009045	3152.005	55177.020	-10.692±0.027	2.08±0.09	0.92(42)	0.31	0.5812
35009046	4230.887	55178.030	-10.641±0.020	2.11±0.07	0.97(66)	1.32	0.2555
35009047	4088.793	55179.030	-10.642±0.021	2.07±0.07	0.84(61)	0.08	0.7821
35009048	2679.155	55180.050	-10.666±0.026	2.04±0.08	0.79(40)	0.73	0.3990
35009050	1314.979	55193.340	-10.977±0.055	2.10±0.21	1.28(10)	4.59	0.0609
90082002	2536.228	55196.020	-11.045±0.042	2.12±0.14	1.01(18)	0.94	0.3462
35009051	1306.307	55200.840	-10.878±0.041	2.34±0.16	1.25(15)	0.17	0.6887
35009053	1647.407	55221.670	-11.051±0.071	1.75±0.21	1.25(11)	2.36	0.1554
35009054	1075.660	55228.020	-11.052±0.061	2.21±0.23	0.93(8)	0.00	0.9900
35009057	1358.063	55249.160	-11.096±0.060	1.92±0.19	1.15(9)	0.09	0.7678
35009058	1065.602	55256.050	-10.866±0.058	1.84±0.17	1.46(10)	0.14	0.7174
35009061	1943.154	55281.040	-11.097±0.057	1.71±0.16	0.65(11)	0.07	0.7975
35009062	1168.212	55284.300	-10.819±0.089	1.90±0.28	0.62(4)	0.43	0.5587
35009063	1699.779	55475.640	-10.801±0.036	2.12±0.12	0.68(20)	0.31	0.5826
35009064	2106.123	55501.060	-10.731±0.033	2.37±0.13	0.62(24)	3.08	0.0926
35009065	1326.358	55531.580	-11.080±0.064	1.87±0.18	1.27(8)	1.90	0.2106
35009066	1113.069	55538.260	-11.029±0.058	2.06±0.21	0.55(9)	–	–
35009067	1321.345	55545.820	-11.088±0.058	2.15±0.21	0.85(9)	0.74	0.4137
35009069	1218.050	55559.600	-11.208±0.096	1.96±0.29	0.53(5)	0.00	0.9811
35009070	1389.112	55566.480	-11.101±0.054	2.08±0.20	1.00(10)	8.34	0.0179

ObsID	Exposure time (sec)	Observation time (in MJD)	Log_{10}Flux ($\mathrm{ergs\,cm^{-2}\,s^{-1}}$)	Spectral index (α_X)	χ^2_{red}(d.o.f)	F-value	P-value
35009071	1252.922	55580.830	-11.288±0.085	2.18±0.32	0.72(5)	3.95	0.1177
35009072	1318.219	55587.240	-11.319±0.078	2.31±0.33	1.54(5)	2.13	0.2180
35009073	897.610	55594.130	-11.235±0.078	2.13±0.31	0.96(4)	1.93	0.0408
35009075	1180.939	55602.290	-11.393±0.111	2.18±0.41	0.82(4)	–	–
35009081	1183.066	55643.850	-11.116±0.064	1.93±0.21	1.48(8)	–	–
35009083	3963.168	55756.100	-10.566±0.029	1.58±0.07	0.98(49)	0.64	0.4279
35009084	4184.871	55758.310	-10.743±0.026	1.78±0.07	0.69(50)	0.49	0.4874
35009085	2164.898	55859.190	-10.810±0.032	2.13±0.11	0.59(26)	2.29	0.1424
35009086	2324.264	55860.450	-10.804±0.034	2.05±0.12	1.46(29)	6.77	0.0147
35009087	2136.213	55861.450	-10.940±0.041	2.09±0.15	1.26(19)	4.85	0.0409
35009088	1955.686	55862.450	-10.950±0.037	2.34±0.15	1.17(18)	7.11	0.0163
35009089	978.219	55899.250	-10.953±0.060	1.95±0.19	1.92(8)	–	–
35009090	1078.077	55906.810	-10.822±0.057	2.10±0.23	1.72(9)	5.51	0.0469
35009091	952.768	55913.020	-10.786±0.059	1.97±0.18	1.17(10)	0.36	0.5625
35009093	1085.661	55927.370	-10.729±0.044	2.15±0.15	1.44(16)	0.01	0.9277
35009094	1068.087	55934.400	-10.883±0.051	2.06±0.18	1.22(11)	1.77	0.2132
35009095	955.275	55948.260	-11.030±0.068	1.91±0.21	0.57(7)	0.11	0.7493
35009096	1017.948	55955.680	-11.022±0.058	2.47±0.27	1.24(7)	1.64	0.2472
35009097	1376.499	55962.480	-11.079±0.060	1.93±0.20	0.99(9)	2.35	0.1637
35009099	822.392	55976.530	-11.010±0.061	2.11±0.21	0.67(6)	0.02	0.8806
35009100	1122.904	55983.330	-10.752±0.036	2.53±0.14	0.49(16)	1.18	0.2944
35009103	1341.387	56011.280	-10.742±0.038	2.24±0.15	0.68(20)	4.16	0.0556
32554001	4979.014	56185.820	-10.933±0.025	2.09±0.09	1.16(46)	8.40	0.0058
32554002	4677.188	56187.620	-11.133±0.040	1.83±0.13	1.48(26)	18.74	0.0002
35009104	1188.083	56242.410	-10.873±0.054	2.14±0.19	0.47(9)	0.08	0.7910
35009107	970.322	56269.350	-10.774±0.055	1.91±0.18	1.71(12)	1.99	0.1859
35009108	798.231	56276.410	-10.846±0.057	2.13±0.19	0.72(8)	0.22	0.6504
35009109	1025.481	56283.640	-10.872±0.065	1.88±0.22	1.93(10)	4.75	0.0572
35009110	942.744	56291.970	-11.017±0.081	2.05±0.27	1.58(4)	–	–
35009111	872.684	56298.320	-10.866±0.054	1.92±0.18	1.35(10)	1.19	0.3042

ObsID	Exposure time (sec)	Observation time (in MJD)	Log_{10}Flux ($\mathrm{ergs\,cm^{-2}\,s^{-1}}$)	Spectral index (α_X)	χ^2_{red}(d.o.f)	F-value	P-value
35009112	1105.716	56312.300	-11.039±0.058	1.98±0.17	1.08(8)	4.12	0.0819
35009113	1012.945	56319.300	-10.842±0.074	1.84±0.22	0.55(8)	0.58	0.4714
35009114	963.334	56325.180	-10.779±0.048	2.05±0.15	0.98(12)	0.37	0.5530
35009117	1023.065	56347.470	-10.860±0.062	2.24±0.25	0.72(6)	2.85	0.1522
35009118	967.814	56354.080	-10.996±0.083	1.73±0.22	1.89(6)	3.20	0.1338
35009119	905.132	56364.190	-11.053±0.070	2.05±0.23	0.42(4)	0.25	0.6535
35009120	878.229	56368.660	-10.913±0.125	1.80±0.32	0.40(4)	4.46	0.1252
35009121	985.370	56375.130	-10.934±0.075	1.89±0.23	0.58(7)	0.79	0.4088
35009122	1083.081	56382.080	-11.107±0.065	1.89±0.21	0.70(7)	0.87	0.3859
35009123	1865.524	56598.420	-11.018±0.053	1.70±0.14	0.73(11)	2.94	0.0136
35009124	1058.078	56602.420	-11.004±0.076	2.26±0.32	1.37(4)	0.97	0.4289
35009125	1088.200	56627.390	-11.171±0.080	1.89±0.24	0.88(5)	0.49	0.5223
35009127	1444.190	56642.010	-11.083±0.053	1.87±0.15	1.06(10)	0.58	0.4660
35009128	1108.224	56648.590	-10.975±0.055	2.07±0.18	1.41(10)	0.54	0.4814
35009130	1072.918	56662.920	-11.265±0.149	1.91±0.41	0.50(4)	1.03	0.4169
35009131	990.378	56676.760	-11.203±0.085	2.05±0.29	0.59(4)	0.06	0.8228
35009132	1022.975	56682.300	-11.139±0.089	1.85±0.27	0.97(5)	0.85	0.4090
35009133	858.081	56704.430	-11.169±0.089	1.59±0.25	0.48(4)	0.03	0.8876
35009136	1978.260	56764.630	-10.595±0.030	1.99±0.09	1.00(36)	1.37	0.2498
35009137	2492.758	56765.030	-11.227±0.058	1.68±0.16	0.76(11)	0.03	0.8554
35009138	1995.813	56767.960	-10.456±0.026	2.17±0.09	1.35(40)	0.01	0.9375
35009139	1985.835	56768.760	-11.033±0.059	1.90±0.19	1.83(11)	0.70	0.4225
35009140	1928.229	56769.630	-11.095±0.062	1.55±0.16	1.08(11)	0.19	0.6686
35009141	1288.740	56989.680	-10.908±0.051	2.08±0.18	0.78(11)	0.45	0.5176
35009142	1080.642	56995.940	-11.014±0.052	2.29±0.21	1.17(9)	1.90	0.2053
35009143	925.192	57011.030	-11.307±0.089	2.49±0.44	1.54(4)	4.17	0.1510
35009145	1055.574	57023.210	-11.162±0.069	2.46±0.31	0.42(4)	0.89	0.4162
35009147	995.396	57041.090	-10.692±0.039	2.26±0.14	1.10(16)	0.03	0.8674
35009148	1108.173	57042.750	-10.687±0.075	2.18±0.27	1.31(4)	0.15	0.7225
35009149	987.873	57043.410	-10.666±0.057	2.24±0.21	0.49(6)	0.02	0.8896

ObsID	Exposure time (sec)	Observation time (in MJD)	Log_{10}Flux ($\mathrm{ergs\,cm^{-2}\,s^{-1}}$)	Spectral index (α_X)	χ^2_{red}(d.o.f)	F-value	P-value
35009152	1639.746	57044.020	-10.549±0.032	2.29±0.13	1.43(25)	3.72	0.0656
35009153	6934.489	57044.290	-10.671±0.016	2.26±0.06	0.98(89)	5.77	0.0184
35009154	1002.631	57045.010	-10.430±0.036	2.33±0.13	1.06(18)	0.78	0.3908
35009157	1693.479	57047.130	-10.357±0.026	2.51±0.10	1.12(34)	0.34	0.5624
35009158	6581.760	57047.220	-10.403±0.014	2.50±0.05	1.06(98)	0.36	0.5523
35009159	1496.858	57048.720	-10.413±0.029	2.42±0.10	1.20(28)	4.05	0.0900
35009160	1496.857	57048.860	-10.490±0.046	2.51±0.19	1.54(10)	0.03	0.8681
35009161	1496.858	57049.650	-10.496±0.028	2.35±0.10	0.87(31)	1.17	0.2884
35009162	1004.054	57050.010	-10.541±0.027	2.75±0.13	1.28(31)	3.20	0.0835
35009167	3173.149	57051.260	-10.703±0.024	2.05±0.08	0.94(50)	3.90	0.0539
35009164	204.550	57051.660	-10.528±0.094	2.41±0.44	1.87(4)	–	–
35009168	2478.112	57051.850	-10.735±0.028	2.13±0.10	1.10(37)	5.40	0.0259
35009169	5493.422	57052.270	-10.607±0.014	2.29±0.05	1.09(122)	4.50	0.0359
35009170	6146.678	57052.990	-10.665±0.014	2.27±0.05	1.31(135)	15.22	0.0002
35009171	5504.335	57054.460	-10.597±0.013	2.32±0.05	0.98(139)	3.07	0.0820
35009172	1084.621	57055.440	-10.574±0.027	2.35±0.10	0.93(35)	0.69	0.4117
35009173	1074.455	57056.310	-10.272±0.018	2.52±0.07	0.78(64)	0.15	0.6988
35009174	1495.582	57057.640	-10.421±0.026	2.36±0.10	0.80(33)	0.38	0.5443
35009175	2069.218	57058.520	-10.428±0.016	2.49±0.06	1.04(89)	2.29	0.1335
35009176	5398.273	57058.650	-10.386±0.009	2.51±0.04	1.00(173)	3.17	0.0768
35009177	13683.906	57059.050	-10.381±0.006	2.55±0.02	1.11(244)	12.81	0.0004
35009178	12432.057	57060.050	-10.451±0.007	2.50±0.03	1.10(228)	9.00	0.0030
35009179	12270.371	57061.040	-10.486±0.007	2.47±0.03	1.11(217)	13.26	0.0003
33627001	549.653	57061.570	-10.610±0.121	2.10±0.40	0.99(4)	0.56	0.5088
33627002	509.023	57061.580	-10.596±0.054	2.38±0.22	0.69(9)	1.21	0.3030
35009180	16025.651	57062.050	-10.545±0.007	2.47±0.03	1.04(229)	5.54	0.0194
33627003	439.617	57062.370	-10.517±0.047	2.27±0.18	0.92(12)	0.77	0.4004
33627004	449.247	57062.370	-10.631±0.063	2.39±0.25	0.75(7)	4.95	0.0678
35009181	1124.441	57063.960	-10.580±0.028	2.42±0.11	1.36(34)	0.10	0.7579
35009182	979.681	57064.300	-10.468±0.029	2.55±0.12	0.80(27)	0.86	0.3629

ObsID	Exposure time (sec)	Observation time (in MJD)	$\mathrm{Log_{10}Flux}$ $(\mathrm{ergs\,cm^{-2}\,s^{-1}})$	Spectral index (α_X)	χ^2_{red}(d.o.f)	F-value	P-value
35009184	649.453	57066.030	-10.377±0.036	2.24±0.13	1.33(23)	0.01	0.9229
35009185	4607.684	57066.090	-10.422±0.011	2.51±0.04	1.12(159)	0.61	0.4376
35009186	4467.523	57066.100	-10.418±0.011	2.50±0.04	0.90(149)	0.29	0.5894
35009190	1488.192	57067.910	-10.434±0.030	2.31±0.11	0.80(28)	0.06	0.8133
35009187	999.749	57068.290	-10.477±0.024	2.53±0.10	0.81(43)	3.57	0.0657
35009188	834.558	57068.820	-10.643±0.032	2.56±0.14	0.90(23)	1.14	0.2970
35009189	1029.620	57069.950	-10.699±0.032	2.40±0.14	1.34(27)	2.65	0.1157
35009192	1079.491	57070.220	-10.702±0.038	2.53±0.17	0.68(18)	1.23	0.2830
35009193	1099.454	57070.750	-10.740±0.033	2.40±0.13	0.63(25)	0.41	0.5294
35009194	879.460	57071.090	-10.694±0.034	2.42±0.13	0.82(23)	0.37	0.5497
35009195	1064.444	57071.680	-10.672±0.031	2.38±0.13	1.04(28)	2.08	0.1604
35009196	1027.095	57072.010	-10.681±0.041	2.20±0.15	0.89(16)	0.00	0.9525
35009197	481.940	57072.750	-10.686±0.062	2.23±0.25	0.97(7)	1.64	0.2475
35009198	1025.790	57073.010	-10.655±0.040	2.27±0.15	0.85(17)	0.00	0.9613
35009199	1117.293	57073.610	-10.670±0.035	2.28±0.12	0.99(20)	0.09	0.7648
35009200	1022.454	57074.140	-10.746±0.041	2.24±0.15	1.38(15)	0.02	0.9040
35009203	710.102	57075.670	-10.844±0.061	2.09±0.19	1.52(6)	1.32	0.3034
35009205	781.743	57076.540	-10.744±0.056	2.21±0.18	1.86(8)	4.39	0.0680
35009206	733.549	57077.070	-10.744±0.047	2.38±0.18	0.95(10)	0.04	0.8449
35009207	1046.904	57077.800	-10.666±0.036	2.36±0.15	1.46(19)	2.05	0.1697
35009208	1054.669	57078.070	-10.629±0.035	2.29±0.13	0.42(19)	0.84	0.3724
35009209	812.427	57078.740	-10.766±0.070	2.18±0.25	0.75(7)	0.01	0.9238
35009210	771.710	57079.000	-10.702±0.068	2.02±0.22	0.44(7)	2.39	0.1732
35009211	952.450	57079.730	-10.792±0.046	2.16±0.15	0.79(11)	2.66	0.1337
35009212	1236.105	57080.130	-10.747±0.041	2.14±0.14	0.97(17)	0.08	0.7839
35009213	1178.465	57080.530	-10.726±0.043	2.24±0.18	1.09(15)	7.77	0.0145
35009216	431.248	57091.940	-10.613±0.070	2.21±0.28	0.85(6)	3.13	0.1370
35009217	862.276	57092.200	-10.682±0.073	1.99±0.23	0.62(5)	0.59	0.4866
35009218	639.157	57092.670	-10.680±0.051	2.55±0.21	0.51(7)	0.02	0.9008
35009220	667.287	57093.660	-10.747±0.061	2.26±0.24	0.58(8)	0.22	0.6525

ObsID	Exposure time (sec)	Observation time (in MJD)	Log$_{10}$Flux (ergs cm^{-2} s^{-1})	Spectral index (α_X)	χ^2_{red}(d.o.f)	F-value	P-value
35009221	1019.102	57094.190	-10.794±0.048	2.07±0.17	0.75(12)	6.21	0.0299
35009222	786.395	57094.930	-10.752±0.063	2.02±0.22	0.86(8)	1.26	0.2981
35009224	1080.645	57103.700	-10.714±0.037	2.57±0.16	1.59(16)	0.03	0.8690
35009225	1469.268	57110.280	-10.754±0.035	2.23±0.13	0.65(20)	0.80	0.3820
92197001	952.304	57156.260	-10.983±0.069	1.70±0.21	0.62(7)	2.79	0.1457
92197002	953.906	57157.590	-10.935±0.069	1.68±0.20	0.60(7)	1.21	0.3135
92197003	965.776	57158.320	-11.026±0.064	1.81±0.18	1.09(7)	0.87	0.3857
92197004	1017.427	57159.720	-11.037±0.091	1.72±0.25	0.72(6)	1.37	0.2951
92197005	937.445	57160.380	-10.988±0.088	2.27±0.36	1.38(4)	1.61	0.2937
92197006	1052.448	57161.520	-11.156±0.079	1.98±0.27	1.23(5)	0.50	0.5175
92197007	995.918	57162.980	-10.888±0.072	1.78±0.23	1.92(10)	7.60	0.0222
35009226	812.497	57336.490	-10.888±0.072	1.78±0.23	1.92(10)	7.60	0.0222
35009227	952.773	57355.060	-11.068±0.061	2.20±0.25	1.44(6)	2.64	0.1652
35009228	992.886	57361.570	-10.705±0.047	2.26±0.16	1.18(11)	1.64	0.2289
92197008	1085.823	57365.360	-10.965±0.058	2.02±0.20	0.95(9)	1.35	0.2781
35009229	1017.958	57365.700	-10.940±0.070	2.14±0.27	1.26(8)	7.58	0.0284
35009230	737.141	57366.420	-11.045±0.059	2.19±0.20	0.68(6)	0.38	0.5653
92197010	1009.852	57367.220	-10.994±0.053	2.57±0.27	1.32(7)	6.71	0.0412
92197011	987.458	57368.150	-11.018±0.058	2.68±0.31	1.27(5)	6.36	0.0653
35009231	1038.017	57368.620	-10.881±0.048	2.38±0.20	1.05(10)	0.66	0.4361
92197012	957.387	57369.210	-11.043±0.069	2.06±0.26	1.97(8)	6.34	0.0399
92197013	965.913	57370.670	-10.873±0.046	2.47±0.19	0.55(10)	1.16	0.3088
35009233	764.723	57401.470	-10.963±0.073	2.08±0.24	0.92(5)	0.47	0.5314
35009239	802.888	57439.000	-11.200±0.082	2.10±0.28	0.50(4)	2.12	0.2411
92197017	1031.045	57456.700	-11.327±0.108	2.13±0.37	0.68(4)	–	–
92197021	1002.450	57460.550	-10.744±0.045	2.41±0.20	0.89(14)	3.68	0.0774
35009241	964.900	57466.590	-10.778±0.045	2.17±0.16	1.09(13)	0.37	0.5537
93250001	2096.693	57868.150	-11.060±0.050	1.93±0.17	1.02(16)	6.50	0.0222
93250002	2139.387	57869.150	-11.115±0.052	2.04±0.19	1.20(15)	21.73	0.0004
93250003	2191.368	57870.410	-11.127±0.055	1.78±0.17	1.64(13)	4.37	0.0584

ObsID	Exposure time (sec)	Observation time (in MJD)	Log_{10}Flux ($\mathrm{ergs\,cm^{-2}\,s^{-1}}$)	Spectral index (α_{X})	χ^2_{red}(d.o.f)	F-value	P-value
93250004	1938.074	57871.670	-11.093±0.058	1.76±0.18	1.64(13)	3.32	0.0933
93250005	1993.391	57872.670	-11.207±0.063	1.83±0.18	0.63(9)	1.01	0.3444
93250006	1928.111	57873.130	-11.149±0.053	2.09±0.19	0.78(12)	5.44	0.0396
93250007	1919.272	57874.660	-11.214±0.062	1.91±0.22	1.89(10)	10.09	0.0113
93250008	1975.634	57925.160	-11.084±0.051	1.87±0.15	0.65(12)	0.11	0.7468
93250009	2100.088	57926.280	-11.101±0.049	1.79±0.14	1.29(14)	0.01	0.9148
93250010	1920.046	57927.080	-11.098±0.085	1.57±0.23	0.71(8)	1.50	0.2602
93250011	2054.410	57928.740	-11.072±0.054	1.49±0.14	0.62(12)	0.17	0.6874
93250012	1912.296	57929.000	-11.060±0.068	1.45±0.18	0.97(11)	0.97	0.3474
93250013	1928.803	57930.000	-11.122±0.055	1.70±0.16	1.05(12)	1.17	0.3029
93250014	2249.037	57931.790	-11.029±0.049	1.58±0.13	0.49(16)	–	–
93250015	1993.299	58132.000	-10.943±0.040	2.24±0.15	0.86(18)	1.98	0.1771
93250016	1970.728	58133.600	-10.829±0.036	2.27±0.14	1.29(21)	1.61	0.2193
93250017	1797.195	58134.000	-10.766±0.029	2.62±0.12	0.77(25)	0.36	0.5528
35009247	1325.082	58208.230	-10.240±0.035	2.32±0.13	0.75(20)	0.04	0.8393
35009245	1384.638	58208.300	-10.260±0.031	2.27±0.11	1.11(27)	0.57	0.4568
35009242	846.630	58208.500	-10.262±0.042	2.21±0.16	1.10(15)	4.02	0.0647
35009249	1086.192	58208.570	-10.240±0.036	2.20±0.14	1.22(21)	4.69	0.0427
35009244	1022.459	58208.630	-10.225±0.037	2.24±0.14	0.53(20)	3.77	0.0672
35009251	1021.548	58208.770	-10.229±0.038	2.33±0.16	1.40(19)	5.35	0.0327
10635019	907.059	58209.030	-10.208±0.036	2.20±0.12	0.84(20)	0.14	0.7144
10635001	585.799	58209.100	-10.258±0.041	2.34±0.17	0.82(15)	3.93	0.0674
10635009	1051.412	58209.300	-10.183±0.035	2.11±0.11	1.03(23)	1.04	0.3186
10635011	1019.938	58209.360	-10.227±0.061	2.27±0.22	0.92(6)	1.60	0.2618
10635006	1020.631	58209.490	-10.243±0.029	2.32±0.11	1.12(28)	0.00	0.9874
10635015	647.047	58209.630	-10.367±0.040	2.43±0.17	1.05(15)	2.42	0.1422
10635018	1155.657	58209.700	-10.291±0.031	2.30±0.12	1.39(28)	4.52	0.0428
10635012	1097.297	58209.760	-10.238±0.032	2.31±0.12	0.87(26)	1.09	0.3055
10635017	530.264	58209.900	-10.294±0.050	2.37±0.20	0.71(9)	1.18	0.3083
10635008	1023.041	58210.090	-10.293±0.054	2.32±0.21	1.73(8)	0.16	0.6994

ObsID	Exposure time (sec)	Observation time (in MJD)	$\mathrm{Log_{10}Flux}$ ($\mathrm{ergs\,cm^{-2}\,s^{-1}}$)	Spectral index (α_X)	χ^2_{red}(d.o.f)	F-value	P-value
10635005	1037.289	58210.160	-10.331±0.032	2.43±0.13	1.54(24)	0.45	0.5103
10635010	485.879	58210.240	-10.378±0.045	2.39±0.18	1.46(13)	0.11	0.7438
10635002	947.293	58210.300	-10.368±0.030	2.40±0.11	0.78(27)	0.97	0.3337
10635020	800.366	58210.360	-10.362±0.037	2.41±0.16	1.29(17)	2.74	0.1174
10635007	790.331	58210.430	-10.375±0.055	2.87±0.29	1.36(6)	5.18	0.0719
10635013	1067.129	58210.690	-10.399±0.035	2.32±0.14	1.27(21)	0.69	0.4176
10635004	977.017	58210.960	-10.386±0.040	2.20±0.13	1.39(16)	0.43	0.5220
10635027	1095.160	58211.420	-10.261±0.034	2.35±0.13	0.63(21)	0.01	0.9244
10635024	530.590	58211.500	-10.244±0.045	2.26±0.16	0.58(13)	1.57	0.2337
10635030	929.760	58276.670	-10.540±0.044	2.44±0.18	1.22(13)	0.01	0.9294
10635031	715.793	58277.870	-10.500±0.052	2.50±0.20	0.71(7)	0.92	0.3754
10635032	469.912	58278.000	-10.524±0.056	2.65±0.28	1.16(6)	0.20	0.6742
10635033	960.813	58279.250	-10.391±0.031	2.46±0.12	0.80(23)	0.09	0.7614
10635034	928.927	58280.380	-10.310±0.037	2.66±0.16	1.37(16)	0.00	0.9556
10635035	999.133	58281.050	-10.511±0.031	2.51±0.13	1.40(24)	2.47	0.1296
10635036	1149.940	58282.510	-10.398±0.038	2.57±0.17	0.87(16)	0.27	0.6117
10635037	962.266	58283.040	-10.345±0.039	2.45±0.17	1.29(16)	0.44	0.5160
10635038	1012.459	58284.770	-10.199±0.044	2.27±0.18	1.49(16)	4.23	0.0576
10635039	999.876	58285.770	-10.367±0.033	2.57±0.15	1.22(21)	5.72	0.0267
10635040	987.287	58286.030	-10.301±0.036	2.44±0.16	1.02(17)	2.23	0.1548
10635041	1085.819	58287.690	-10.016±0.035	2.47±0.13	1.27(19)	0.02	0.8821
10635042	916.713	58288.680	-10.099±0.034	2.39±0.12	0.62(19)	0.78	0.3879
10635043	812.286	58289.810	-10.038±0.035	2.40±0.13	0.91(20)	0.24	0.6314
10635044	1986.423	58458.150	-10.662±0.029	2.12±0.10	0.68(32)	3.80	0.0602
10635045	1048.040	58459.410	-10.681±0.044	2.17±0.17	1.63(18)	2.56	0.1283
10635046	1045.541	58463.390	-10.707±0.047	1.93±0.14	1.50(15)	0.56	0.4657
10635047	1130.795	58466.380	-10.708±0.046	2.14±0.16	1.68(14)	0.00	0.9948
10635048	1110.736	58468.370	-10.833±0.044	2.32±0.17	0.77(13)	0.26	0.6209
10635049	1038.022	58514.260	-11.216±0.134	1.90±0.40	0.56(3)	2.67	0.2441
10635050	1077.876	58516.260	-11.312±0.118	1.88±0.35	0.87(3)	0.35	0.6157

ObsID	Exposure time (sec)	Observation time (in MJD)	$\mathrm{Log}_{10}\mathrm{Flux}$ ($\mathrm{ergs\,cm^{-2}\,s^{-1}}$)	Spectral index (α_{X})	χ^2_{red}(d.o.f)	F-value	P-value
10635052	967.817	58818.390	-10.761±0.039	2.81±0.18	1.17(14)	0.63	0.4420
10635053	786.065	58823.380	-10.702±0.042	2.88±0.20	0.87(12)	5.60	0.0374
10635054	892.583	58843.310	-10.886±0.054	2.61±0.25	0.50(7)	0.19	0.6814
32554003	992.891	58846.090	-10.760±0.040	2.56±0.18	0.95(14)	3.89	0.0704
10635055	1017.963	58846.360	-10.874±0.048	2.63±0.24	0.88(10)	1.62	0.2348
10635056	1048.019	58848.350	-11.172±0.056	2.45±0.25	1.73(7)	0.50	0.5066
10635057	1933.619	58851.480	-10.602±0.025	2.54±0.10	1.01(36)	0.81	0.3751
10635058	929.872	58854.120	-10.869±0.049	2.86±0.23	0.85(8)	0.96	0.3604
10635059	1868.259	58857.240	-10.910±0.037	2.48±0.16	0.59(18)	0.73	0.4038
10635060	2164.737	58860.090	-10.959±0.033	2.69±0.16	1.71(20)	2.74	0.1145
10635061	483.367	58863.690	-10.397±0.041	2.80±0.19	1.24(12)	0.06	0.8172
10635062	989.475	58866.140	-10.782±0.043	2.62±0.19	1.33(11)	0.00	0.9831
10635063	980.351	58896.160	-10.328±0.046	2.33±0.17	0.76(12)	1.53	0.2421
10635064	1020.470	58899.210	-10.128±0.035	2.30±0.14	0.70(19)	2.53	0.1291
10635065	958.020	58902.190	-10.223±0.043	2.23±0.15	0.96(14)	0.71	0.4135
96041003	2268.861	59639.460	-11.390±0.047	2.69±0.19	1.22(9)	0.13	0.7263
96041004	1097.283	59646.430	-11.132±0.060	2.87±0.30	1.22(5)	3.85	0.1213
96041005	927.451	59653.060	-11.115±0.063	2.85±0.29	0.81(6)	0.01	0.9244
96041006	914.720	59667.020	-11.174±0.062	2.71±0.26	0.53(6)	3.40	0.1245
96041007	1032.296	59668.400	-11.058±0.057	2.86±0.22	0.57(7)	0.34	0.5817
96041009	907.279	59670.600	-11.303±0.077	2.57±0.33	1.99(4)	–	–
96041010	911.375	59671.390	-10.940±0.057	2.61±0.26	0.68(8)	0.14	0.7209
96041011	842.294	59672.040	-10.996±0.055	2.49±0.22	1.12(9)	0.14	0.7188
89272001	1597.288	59673.700	-11.084±0.044	2.85±0.17	1.19(13)	0.96	0.3472
96041014	1132.463	59675.160	-11.253±0.061	2.74±0.28	1.72(7)	2.97	0.1358
96041015	886.675	59676.220	-11.247±0.087	2.25±0.35	1.18(4)	0.79	0.4400
96879002	1334.456	59901.500	-10.943±0.044	2.61±0.19	1.16(25)	0.66	0.4258
96879003	914.457	59911.240	-10.970±0.053	2.55±0.25	1.21(17)	4.37	0.0530
96879004	1222.224	59930.410	-11.267±0.081	2.35±0.30	0.91(12)	0.02	0.9008
96879005	675.848	59938.430	-11.002±0.068	2.70±0.32	0.61(11)	3.60	0.0395
96879007	772.017	59946.180	-11.284±0.104	2.64±0.44	1.66(7)	0.09	0.7797
96879009	940.248	59962.060	-11.119±0.085	1.89±0.29	0.90(13)	0.64	0.4380

Table B.2: Table showing the best-fit parameters of selected *Swift*-XRT observations using log-parabola model.

ObsID	Exposure time (s)	Observation time (in MJD)	Log_{10}Flux ($\text{ergs}\,\text{cm}^{-2}\,\text{s}^{-1}$)	Spectral index (α_X)	Spectral curvature β	χ^2_{red}(d.o.f)
35009002	7456.296	53600.62	-10.866±0.029	2.45±0.07	-0.46±0.17	0.95(68)
35009003	5678.5	54375.70	-11.012±0.060	2.12±0.11	-0.41±0.29	0.77(30)
35009004	2461.633	54396.69	-10.746±0.047	2.35±0.10	-0.43±0.25	0.84(29)
35009006	2723.673	54398.18	-10.864±0.051	2.25±0.11	-0.46±0.25	0.73(26)
35009007	2201.395	54399.51	-10.830±0.068	2.17±0.12	-0.67±0.28	1.49(23)
35009013	1923.724	54410.15	-10.899±0.146	2.38±0.16	-0.81±0.61	0.40(12)
35009070	1389.112	55566.48	-10.992±0.100	2.22±0.20	-0.67±0.44	0.58(9)
35009086	2324.264	55860.45	-10.723±0.058	2.15±0.12	-0.52±0.27	1.22(28)
35009088	1955.686	55862.45	-10.852±0.076	2.38±0.13	-0.66±0.37	0.88(17)
35009090	1078.077	55906.81	-10.694±0.102	2.21±0.20	-0.74±0.41	1.15(8)
32554001	4979.014	56185.82	-10.882±0.038	2.16±0.09	-0.36±0.19	1.00(45)
32554002	4677.188	56187.62	-11.001±0.066	2.03±0.13	-0.72±0.25	0.88(25)
35009153	6934.489	57044.29	-10.646±0.024	2.29±0.06	-0.21±0.14	0.93(88)
35009168	2478.112	57051.85	-10.669±0.056	2.18±0.10	-0.42±0.27	0.98(36)
35009170	6146.678	57052.99	-10.624±0.021	2.33±0.05	-0.34±0.12	1.18(134)
35009177	13683.906	57059.05	-10.367±0.009	2.56±0.02	-0.15±0.06	1.06(243)
35009178	12432.057	57060.05	-10.438±0.010	2.52±0.03	-0.14±0.07	1.06(227)
35009179	12270.371	57061.04	-10.467±0.011	2.49±0.03	-0.18±0.08	1.05(216)
35009180	16025.651	57062.05	-10.534±0.010	2.48±0.03	-0.11±0.07	1.02(228)
35009213	1178.465	57080.53	-10.608±0.095	2.32±0.16	-0.71±0.43	0.75(14)
35009221	1019.102	57094.19	-10.722±0.082	2.17±0.18	-0.49±0.39	0.52(11)
92197007	995.918	57162.98	-10.697±0.130	2.01±0.21	-0.89±0.43	1.16(9)
35009226	812.497	57336.49	-10.697±0.130	2.01±0.21	-0.89±0.43	1.16(9)
35009229	1017.958	57365.70	-10.614±0.267	2.12±0.20	-1.14±0.71	0.69(7)
92197010	1009.852	57367.22	-10.877±0.105	2.59±0.20	-0.85±0.53	0.73(6)
92197011	987.458	57368.15	-10.808±0.198	2.57±0.22	-1.19±0.81	0.61(4)
92197012	957.387	57369.21	-10.777±0.185	2.21±0.22	-1.15±0.58	1.18(7)
93250001	2096.693	57868.15	-10.947±0.100	2.03±0.16	-0.58±0.39	0.76(15)
93250002	2139.387	57869.15	-10.904±0.124	2.18±0.16	-0.98±0.42	0.51(14)
93250006	1928.111	57873.13	-11.036±0.121	2.14±0.18	-0.59±0.49	0.57(11)
93250007	1919.272	57874.66	-11.027±0.116	2.15±0.20	-0.97±0.42	0.99(9)
35009251	1021.548	58208.77	-10.106±0.095	2.33±0.13	-0.70±0.40	1.14(18)
10635007	790.331	58210.43	-10.248±0.124	2.78±0.21	-1.03±0.68	0.80(5)
10635039	999.876	58285.77	-10.293±0.063	2.57±0.12	-0.60±0.36	1.00(20)
10635053	786.065	58823.38	-10.640±0.071	2.84±0.16	-0.66±0.48	0.63(11)

Table B.3: Best-fit parameters for power-law fitting of *Swift*-UVOT observations.

ObsID	Exposure time (s)	Observation time (in MJD)	Log$_{10}$Flux (ergs cm^{-2} s^{-1})	Spectral index ($\alpha_{\mathrm{O/UV}}$)	χ^2_{red}(d.o.f)
35009002	7456.296	53600.62	-9.923±0.016	2.16±0.10	0.63(4)
35009004	2461.633	54396.69	-9.910±0.011	2.21±0.07	0.76(4)
35009006	2723.673	54398.18	-9.926±0.011	2.26±0.07	1.28(4)
35009007	2201.395	54399.51	-9.939±0.011	2.28±0.07	0.74(4)
35009008	1960.757	54400.37	-9.783±0.011	2.13±0.07	0.69(4)
35009009	1756.998	54401.33	-9.818±0.011	2.22±0.07	0.80(4)
35009012	2803.152	54407.20	-9.845±0.011	2.13±0.07	1.32(4)
35009013	1923.724	54410.15	-9.929±0.011	2.17±0.07	1.01(4)
35009014	2005.828	54413.15	-9.958±0.011	2.12±0.07	0.98(4)
35009015	2380.795	54417.10	-10.013±0.011	2.20±0.07	0.82(4)
35009016	1551.578	54577.62	-9.769±0.018	2.18±0.12	0.62(3)
35009017	2002.351	54584.75	-9.716±0.011	1.99±0.07	1.27(4)
35009018	4215.456	54585.83	-9.735±0.011	2.04±0.07	0.89(4)
35009020	1906.966	54588.69	-9.715±0.011	2.09±0.07	1.36(4)
35009021	2280.966	54798.81	-9.938±0.011	2.11±0.07	0.72(4)
35009022	930.894	54806.90	-9.822±0.012	2.24±0.07	1.15(4)
35009023	1442.916	54813.66	-9.990±0.007	2.30±0.04	0.73(4)
35009024	1410.050	54820.36	-10.155±0.012	2.40±0.07	1.14(4)
35009026	1974.480	54843.73	-10.366±0.012	2.25±0.08	0.78(4)
35009027	1476.231	54850.29	-10.177±0.012	2.27±0.07	1.03(4)
35009028	1927.047	54855.63	-10.247±0.011	2.30±0.07	1.32(4)
35009029	1535.146	54864.67	-10.206±0.012	2.38±0.07	0.92(4)
35009040	1006.000	54889.07	-10.355±0.018	2.37±0.11	1.48(4)
35009041	5573.671	55120.41	-9.911±0.011	2.27±0.07	1.04(4)
35009042	1543.201	55165.12	-10.230±0.012	2.29±0.07	1.23(4)
35009043	1188.458	55172.88	-10.120±0.007	2.36±0.05	1.84(4)
35009052	867.522	55214.32	-10.410±0.013	2.58±0.08	1.24(4)
35009053	1647.407	55221.67	-10.055±0.017	2.48±0.10	1.91(4)
35009054	1075.660	55228.02	-10.023±0.012	2.25±0.07	1.45(4)
35009056	822.426	55242.13	-10.188±0.022	2.35±0.16	1.06(2)
35009057	1358.063	55249.16	-10.277±0.012	2.42±0.08	0.94(4)
35009058	1065.602	55256.05	-10.149±0.012	2.35±0.08	0.87(4)
35009059	1331.516	55270.00	-10.246±0.008	2.40±0.05	1.35(4)
35009061	1943.154	55281.04	-10.392±0.012	2.46±0.08	1.19(4)
35009063	1699.779	55475.64	-9.929±0.016	2.14±0.11	0.63(4)
35009064	2106.123	55501.06	-9.921±0.011	2.15±0.07	1.02(4)
35009065	1326.358	55531.58	-10.158±0.017	2.34±0.11	0.79(4)
35009066	1113.069	55538.26	-10.167±0.012	2.27±0.07	1.08(4)
35009068	1243.216	55552.17	-10.041±0.012	2.29±0.07	1.02(4)
35009069	1218.050	55559.60	-10.151±0.012	2.30±0.07	1.03(4)
35009070	1389.112	55566.48	-10.159±0.012	2.26±0.07	1.28(4)
35009071	1252.922	55580.83	-10.138±0.012	2.24±0.07	1.37(4)
35009072	1318.219	55587.24	-10.170±0.012	2.20±0.07	1.02(4)
35009073	897.610	55594.13	-10.436±0.013	2.34±0.08	0.94(4)
35009075	1180.939	55602.29	-10.486±0.013	2.56±0.08	1.12(4)
35009077	942.744	55610.05	-10.379±0.018	2.51±0.11	1.17(4)
35009079	1015.460	55622.08	-10.093±0.017	2.31±0.11	0.76(4)
35009081	1183.066	55643.85	-10.165±0.012	2.26±0.07	1.49(4)
35009085	2164.898	55859.19	-10.017±0.011	2.24±0.07	0.92(4)
35009086	2324.264	55860.45	-10.024±0.016	2.31±0.10	0.77(4)

ObsID	Exposure time (s)	Observation time (in MJD)	Log$_{10}$Flux (ergs cm^{-2} s^{-1})	Spectral index ($\alpha_{\mathrm{O/UV}}$)	χ^2_{red}(d.o.f)
35009087	2136.213	55861.45	-9.955±0.011	2.22±0.07	1.14(4)
35009088	1955.686	55862.45	-9.923±0.011	2.18±0.07	1.16(4)
35009089	978.219	55899.25	-10.277±0.012	2.31±0.08	0.98(4)
35009090	1078.077	55906.81	-10.126±0.012	2.20±0.08	1.07(4)
35009091	952.768	55913.02	-10.088±0.012	2.17±0.08	1.26(4)
35009093	1085.661	55927.37	-10.114±0.012	2.22±0.08	0.97(4)
35009094	1068.087	55934.40	-10.248±0.008	2.23±0.05	1.64(4)
35009095	955.275	55948.26	-10.586±0.010	2.38±0.06	1.91(4)
35009096	1017.948	55955.68	-10.168±0.017	2.14±0.11	0.91(4)
35009097	1376.499	55962.48	-10.150±0.017	2.24±0.11	1.08(4)
35009099	822.392	55976.53	-10.100±0.012	2.23±0.08	0.96(4)
35009100	1122.904	55983.33	-9.816±0.011	2.07±0.07	0.83(4)
35009101	1012.620	56000.07	-10.065±0.012	2.26±0.08	1.01(4)
35009103	1341.387	56011.28	-9.738±0.007	2.20±0.04	1.99(4)
32554001	4979.014	56185.82	-9.848±0.011	2.28±0.07	0.93(4)
32554002	4677.188	56187.62	-9.938±0.016	2.33±0.10	0.73(4)
35009104	1188.083	56242.41	-10.002±0.011	2.22±0.07	0.99(4)
35009107	970.322	56269.35	-10.214±0.008	2.27±0.05	1.88(4)
35009109	1025.481	56283.64	-10.296±0.012	2.35±0.08	0.87(4)
35009110	942.744	56291.97	-10.284±0.008	2.41±0.05	2.00(4)
35009111	872.684	56298.32	-10.370±0.013	2.33±0.08	1.10(4)
35009112	1105.716	56312.30	-10.389±0.008	2.30±0.05	0.84(4)
35009113	1012.945	56319.30	-10.578±0.018	2.64±0.11	1.80(4)
35009114	963.334	56325.18	-10.240±0.008	2.22±0.05	1.96(4)
35009115	581.690	56331.25	-10.275±0.022	2.25±0.16	0.36(2)
35009116	546.585	56337.25	-10.500±0.011	2.29±0.08	1.34(2)
35009117	1023.065	56347.47	-10.220±0.012	2.15±0.08	1.51(4)
35009118	967.814	56354.08	-10.413±0.018	2.36±0.12	0.81(4)
35009119	905.132	56364.19	-10.262±0.012	2.30±0.08	1.09(4)
35009120	878.229	56368.66	-10.347±0.012	2.26±0.08	1.21(4)
35009121	985.370	56375.13	-10.346±0.012	2.21±0.08	1.46(4)
35009122	1083.081	56382.08	-10.683±0.010	2.29±0.06	1.70(4)
35009123	1865.524	56598.42	-10.642±0.009	2.44±0.05	0.83(4)
35009124	1058.078	56602.42	-10.434±0.013	2.34±0.08	1.33(4)
35009125	1088.200	56627.39	-10.701±0.010	2.47±0.06	1.34(4)
35009127	1444.190	56642.01	-10.489±0.017	2.30±0.11	1.29(4)
35009128	1108.224	56648.59	-10.432±0.012	2.23±0.08	0.96(4)
35009130	1072.918	56662.92	-10.827±0.011	2.55±0.07	1.01(4)
35009131	990.378	56676.76	-10.533±0.013	2.16±0.08	1.30(4)
35009132	1022.975	56682.30	-10.440±0.013	2.22±0.08	1.47(4)
35009133	858.081	56704.43	-10.638±0.014	2.41±0.10	0.43(3)
35009135	1110.731	56732.58	-10.409±0.013	2.43±0.08	1.45(4)
35009136	1978.260	56764.63	-10.267±0.012	2.20±0.08	1.08(4)
35009137	2492.758	56765.03	-10.400±0.012	2.41±0.08	0.99(4)
35009138	1995.813	56767.96	-10.280±0.012	2.07±0.08	1.20(4)
35009139	1985.835	56768.76	-10.416±0.013	2.29±0.08	1.42(4)
35009140	1928.229	56769.63	-10.424±0.012	2.37±0.08	1.06(4)
35009141	1288.740	56989.68	-10.215±0.012	2.25±0.08	0.83(4)
35009142	1080.642	56995.94	-10.223±0.012	2.22±0.08	1.26(4)
35009143	925.192	57011.03	-10.338±0.009	2.30±0.05	0.65(4)
35009144	1070.615	57019.35	-10.314±0.012	2.34±0.08	1.13(4)
35009145	1055.574	57023.21	-10.379±0.012	2.28±0.08	0.98(4)

ObsID	Exposure time (s)	Observation time (in MJD)	Log$_{10}$Flux (ergs cm^{-2} s^{-1})	Spectral index ($\alpha_{\mathrm{O/UV}}$)	χ^2_{red}(d.o.f)
35009146	832.423	57029.00	-10.271±0.009	2.31±0.05	1.17(4)
35009147	995.396	57041.09	-9.511±0.007	2.12±0.05	1.60(4)
35009148	1108.173	57042.75	-9.639±0.011	2.25±0.07	1.22(4)
35009152	1639.746	57044.02	-9.672±0.011	2.15±0.07	1.22(4)
35009154	1002.631	57045.01	-9.567±0.011	2.06±0.07	0.86(4)
35009157	1693.479	57047.13	-9.489±0.007	2.04±0.04	0.95(4)
35009159	1496.858	57048.72	-9.523±0.011	2.04±0.07	1.14(4)
35009167	3173.149	57051.26	-9.833±0.016	2.18±0.11	0.62(4)
35009168	2478.112	57051.85	-9.880±0.016	2.34±0.10	0.76(4)
35009169	5493.422	57052.27	-9.841±0.011	2.28±0.07	1.07(4)
35009171	5504.335	57054.46	-9.939±0.011	2.19±0.07	0.90(4)
35009172	1084.621	57055.44	-9.833±0.011	2.15±0.07	1.09(4)
35009173	1074.455	57056.31	-9.724±0.011	2.07±0.07	1.12(4)
35009174	1495.582	57057.64	-9.738±0.007	2.05±0.05	1.49(4)
35009175	2069.218	57058.52	-9.726±0.011	2.04±0.07	0.86(4)
35009177	13683.906	57059.05	-9.774±0.012	2.08±0.08	0.81(3)
35009178	12432.057	57060.05	-9.835±0.016	2.10±0.10	0.91(4)
35009179	12270.371	57061.04	-9.869±0.016	2.15±0.10	0.86(4)
35009181	1124.441	57063.96	-9.985±0.007	2.13±0.05	1.47(4)
35009182	979.681	57064.30	-9.970±0.007	2.12±0.05	1.17(4)
35009184	649.453	57066.03	-9.901±0.021	2.08±0.16	1.10(2)
35009190	1488.192	57067.91	-9.882±0.011	2.04±0.07	0.89(4)
35009187	999.749	57068.29	-9.916±0.015	2.21±0.10	1.33(2)
35009188	834.558	57068.82	-10.030±0.016	2.25±0.10	0.55(2)
35009189	1029.620	57069.95	-10.053±0.025	2.27±0.16	1.08(2)
35009192	1079.491	57070.22	-10.061±0.016	2.32±0.10	1.57(2)
35009193	1099.454	57070.75	-10.122±0.016	2.34±0.10	0.78(2)
35009194	879.460	57071.09	-10.064±0.016	2.21±0.10	0.66(2)
35009195	1064.444	57071.68	-10.033±0.016	2.32±0.10	1.04(2)
35009196	1027.095	57072.01	-10.028±0.016	2.31±0.10	0.59(2)
35009197	481.940	57072.75	-9.939±0.019	2.28±0.12	1.01(2)
35009198	1025.790	57073.01	-10.007±0.016	2.24±0.10	0.77(2)
35009199	1117.293	57073.61	-10.052±0.016	2.23±0.10	1.12(2)
35009200	1022.454	57074.14	-10.146±0.016	2.32±0.10	1.04(2)
35009201	1082.254	57074.60	-10.202±0.016	2.25±0.10	0.77(2)
35009202	693.083	57075.21	-10.260±0.018	2.45±0.12	0.94(2)
35009203	710.102	57075.67	-10.262±0.017	2.27±0.11	1.53(2)
35009204	697.188	57076.07	-10.164±0.018	2.68±0.11	1.86(2)
35009205	781.743	57076.54	-10.021±0.016	2.28±0.11	0.96(2)
35009207	1046.904	57077.80	-9.934±0.026	2.49±0.16	0.93(2)
35009208	1054.669	57078.07	-9.951±0.015	2.19±0.10	0.78(2)
35009209	812.427	57078.74	-10.053±0.017	2.34±0.10	1.83(2)
35009210	771.710	57079.00	-10.114±0.039	2.51±0.25	1.73(2)
35009211	952.450	57079.73	-10.058±0.016	2.30±0.10	0.81(2)
35009213	1178.465	57080.53	-10.023±0.017	2.50±0.10	1.24(2)
35009214	289.196	57081.20	-10.034±0.020	2.26±0.13	1.10(2)
35009215	207.101	57081.66	-10.038±0.021	2.38±0.13	1.64(2)
35009216	431.248	57091.94	-9.860±0.009	2.20±0.07	1.76(2)
35009217	862.276	57092.20	-9.786±0.016	2.32±0.10	0.92(2)
35009219	789.267	57093.26	-9.739±0.017	2.30±0.10	0.37(2)
35009220	667.287	57093.66	-9.769±0.018	2.43±0.11	0.42(2)
35009221	1019.102	57094.19	-9.837±0.016	2.41±0.10	0.55(2)

ObsID	Exposure time (s)	Observation time (in MJD)	Log$_{10}$Flux (ergs cm^{-2} s^{-1})	Spectral index ($\alpha_{\mathrm{O/UV}}$)	χ^2_{red}(d.o.f)
35009222	786.395	57094.93	-9.814±0.025	2.28±0.16	1.01(2)
35009224	1080.645	57103.70	-9.711±0.007	2.09±0.05	1.06(4)
35009225	1469.268	57110.28	-9.863±0.016	2.15±0.10	0.79(4)
35009227	952.773	57355.06	-9.882±0.012	2.29±0.07	1.29(4)
35009228	992.886	57361.57	-9.917±0.012	2.28±0.07	0.94(4)
35009229	1017.958	57365.70	-9.882±0.011	2.13±0.07	1.30(4)
35009230	737.141	57366.42	-9.896±0.012	2.17±0.08	1.30(4)
35009231	1038.017	57368.62	-9.885±0.007	2.22±0.05	1.46(4)
35009232	937.729	57382.49	-10.322±0.008	2.25±0.05	1.76(4)
35009233	764.723	57401.47	-9.880±0.012	2.15±0.07	1.15(4)
35009236	759.707	57420.28	-10.014±0.008	2.14±0.05	1.51(4)
35009237	398.201	57433.28	-9.864±0.013	2.16±0.08	1.16(4)
35009238	516.499	57434.02	-9.847±0.008	2.08±0.05	1.47(4)
35009239	802.888	57439.00	-9.942±0.008	2.23±0.05	1.54(4)
35009240	411.059	57441.00	-10.026±0.009	2.22±0.06	1.51(4)
35009241	964.900	57466.59	-10.063±0.008	2.21±0.05	1.90(4)
93250002	2139.387	57869.15	-9.775±0.011	2.26±0.07	1.03(4)
93250003	2191.368	57870.41	-9.753±0.007	2.34±0.04	1.87(4)
93250004	1938.074	57871.67	-9.733±0.011	2.41±0.07	1.22(4)
93250005	1993.391	57872.67	-9.827±0.011	2.48±0.07	0.76(4)
93250006	1928.111	57873.13	-9.868±0.011	2.47±0.07	0.71(4)
93250007	1919.272	57874.66	-9.795±0.011	2.37±0.07	1.18(4)
93250008	1975.634	57925.16	-10.856±0.020	2.35±0.13	1.12(4)
93250009	2100.088	57926.28	-10.539±0.013	2.48±0.08	1.13(4)
93250010	1920.046	57927.08	-10.355±0.012	2.33±0.08	1.28(4)
93250011	2054.410	57928.74	-10.379±0.012	2.37±0.08	0.76(4)
93250012	1912.296	57929.00	-10.507±0.013	2.39±0.08	0.97(4)
93250013	1928.803	57930.00	-10.500±0.008	2.36±0.05	1.30(4)
93250014	2249.037	57931.79	-10.515±0.012	2.36±0.08	0.94(4)
93250015	1993.299	58132.00	-9.883±0.007	2.15±0.04	1.50(4)
93250016	1970.728	58133.60	-9.943±0.011	2.14±0.07	1.22(4)
93250017	1797.195	58134.00	-9.936±0.011	2.10±0.07	0.84(4)
35009248	911.748	58208.03	-9.825±0.011	1.97±0.08	1.00(4)
35009247	1325.082	58208.23	-9.804±0.007	2.01±0.05	1.34(4)
35009245	1384.638	58208.30	-9.802±0.011	1.96±0.07	1.07(4)
35009242	846.630	58208.50	-9.827±0.017	2.27±0.11	0.95(4)
35009249	1086.192	58208.57	-9.787±0.017	2.19±0.10	1.46(4)
35009244	1022.459	58208.63	-9.786±0.016	2.09±0.11	1.45(4)
35009251	1021.548	58208.77	-9.805±0.007	2.08±0.05	1.42(4)
10635019	907.059	58209.03	-9.775±0.012	2.07±0.08	0.86(4)
10635001	585.799	58209.10	-9.784±0.012	2.13±0.08	0.89(4)
10635009	1051.412	58209.30	-9.746±0.011	2.01±0.07	1.07(4)
10635011	1019.938	58209.36	-9.744±0.007	2.01±0.05	1.77(4)
10635006	1020.631	58209.49	-9.700±0.011	2.01±0.08	1.01(4)
10635015	647.047	58209.63	-9.674±0.012	2.03±0.08	1.08(4)
10635018	1155.657	58209.70	-9.676±0.011	2.03±0.07	0.84(4)
10635012	1097.297	58209.76	-9.686±0.007	2.01±0.05	1.47(4)
10635017	530.264	58209.90	-9.695±0.008	2.06±0.05	1.72(4)
10635008	1023.041	58210.09	-9.683±0.016	1.97±0.11	0.74(4)
10635005	1037.289	58210.16	-9.727±0.016	2.18±0.10	1.26(4)
10635010	485.879	58210.24	-9.681±0.012	2.00±0.08	0.95(4)
10635002	947.293	58210.30	-9.661±0.011	2.01±0.07	1.00(4)

ObsID	Exposure time (s)	Observation time (in MJD)	Log$_{10}$Flux ($\mathrm{ergs\,cm^{-2}\,s^{-1}}$)	Spectral index ($\alpha_{\mathrm{O/UV}}$)	χ^2_{red}(d.o.f)
10635020	800.366	58210.36	-9.689±0.008	1.99±0.05	1.72(4)
10635007	790.331	58210.43	-9.693±0.012	1.98±0.08	1.35(4)
10635013	1067.129	58210.69	-9.750±0.016	2.12±0.11	1.15(4)
10635004	977.017	58210.96	-9.743±0.011	2.04±0.08	0.95(4)
10635027	1095.160	58211.42	-9.727±0.016	1.96±0.11	1.06(4)
10635024	530.590	58211.50	-9.729±0.008	2.00±0.05	1.51(4)
10635030	929.760	58276.67	-9.660±0.007	2.07±0.05	1.81(4)
10635031	715.793	58277.87	-9.588±0.012	2.05±0.08	1.02(4)
10635032	469.912	58278.00	-9.574±0.008	2.00±0.05	1.24(4)
10635033	960.813	58279.25	-9.491±0.011	1.96±0.07	1.13(4)
10635035	999.133	58281.05	-9.576±0.016	1.94±0.11	0.78(4)
10635036	1149.940	58282.51	-9.555±0.016	1.91±0.11	0.81(4)
10635037	962.266	58283.04	-9.572±0.011	1.96±0.07	0.96(4)
10635038	1012.459	58284.77	-9.601±0.007	1.99±0.05	1.16(4)
10635039	999.876	58285.77	-9.569±0.007	1.99±0.05	1.46(4)
10635040	987.287	58286.03	-9.519±0.011	1.95±0.07	0.96(4)
10635041	1085.819	58287.69	-9.528±0.016	1.89±0.11	0.81(4)
10635042	916.713	58288.68	-9.561±0.007	1.94±0.05	1.12(4)
10635043	812.286	58289.81	-9.606±0.011	1.94±0.08	1.23(4)
32554003	992.891	58846.09	-9.714±0.016	2.02±0.10	1.17(4)
10635069	1050.020	59549.48	-10.303±0.008	2.16±0.05	0.68(4)
96879002	1334.456	59901.50	-10.010±0.007	2.12±0.04	1.68(4)
96879003	914.457	59911.24	-10.069±0.016	2.02±0.11	1.13(4)
96879004	1222.224	59930.41	-10.265±0.016	2.05±0.11	0.80(4)
96879005	675.848	59938.43	-10.287±0.019	2.08±0.12	0.65(3)
96879006	579.477	59943.32	-10.221±0.012	2.09±0.08	1.56(4)
96879007	772.017	59946.18	-10.196±0.012	1.97±0.08	1.03(4)
96879008	912.450	59954.44	-10.094±0.011	2.07±0.07	1.37(4)
96879009	940.248	59962.06	-10.138±0.016	2.09±0.11	0.94(4)

Table B.4: Best-fit parameters of spectral fitting using a power-law model for selected gamma-ray observational data (2-day bins) simultaneous with *Swift* observations.

$T_{\rm start}$ MJD	$T_{\rm stop}$ MJD	$\mathrm{Log_{10}Flux}$ $(\mathrm{phs\,cm^{-2}\,s^{-1}})$	Spectral index (α_γ)	$TS_{\rm pl}$	$TS_{\rm lp}$	$TS_{\rm c}$
54797	54799	-6.495±0.120	2.339±0.234	65.41	65.41	0.00
54805	54807	-6.578±0.140	1.956±0.203	55.66	56.26	0.60
54812	54814	-6.795±0.186	2.316±0.336	20.35	22.58	2.23
54819	54821	-6.776±0.165	2.161±0.269	26.58	26.97	0.39
54833	54835	-7.317±0.438	2.032±0.546	7.59	7.59	0.00
54849	54851	-7.023±0.271	2.509±0.555	7.46	7.83	0.37
54863	54865	-6.788±0.328	2.835±0.925	6.35	6.35	0.00
54866	54868	-7.172±0.400	1.905±0.503	18.75	18.75	0.00
54867	54869	-7.467±0.448	1.617±0.473	17.90	17.91	0.01
54873	54875	-7.133±0.329	2.194±0.498	7.59	5.51	-2.08
54877	54879	-7.462±0.451	1.669±0.499	12.54	13.48	0.94
54881	54883	-7.108±0.247	1.929±0.336	10.75	11.65	0.90
54883	54885	-7.131±0.328	2.118±0.569	8.89	8.89	0.00
54887	54889	-6.851±0.190	2.334±0.343	24.71	25.55	0.84
55119	55121	-6.536±0.106	2.098±0.180	81.68	82.82	1.14
55164	55166	-6.959±0.183	2.255±0.321	23.27	24.56	1.29
55165	55167	-7.001±0.192	1.962±0.282	28.88	29.14	0.26
55171	55173	-7.587±0.437	1.909±0.577	5.04	8.48	3.44
55175	55177	-7.091±0.257	2.054±0.361	18.14	18.46	0.32
55176	55178	-6.882±0.213	2.488±0.424	14.39	14.65	0.26
55177	55179	-7.038±0.240	2.088±0.376	11.80	12.36	0.56
55178	55180	-6.941±0.214	2.072±0.344	21.13	21.13	0.00
55179	55181	-6.949±0.295	2.380±0.520	14.06	14.06	0.00
55186	55188	-6.870±0.211	2.511±0.418	11.18	11.55	0.37
55195	55197	-6.971±0.202	1.962±0.300	28.75	28.75	0.00
55213	55215	-6.960±0.237	2.773±0.535	7.11	0.00	-7.11
55220	55222	-6.718±0.142	2.202±0.245	38.55	38.64	0.09
55227	55229	-6.996±0.176	1.686±0.204	52.46	53.24	0.78
55234	55236	-6.614±0.127	2.362±0.250	42.07	43.38	1.31
55241	55243	-6.701±0.150	2.728±0.379	24.19	24.19	0.00
55248	55250	-7.219±0.246	1.764±0.317	19.79	21.77	1.98
55255	55257	-6.422±0.084	2.060±0.147	162.92	162.92	0.00
55268	55270	-6.426±0.092	2.323±0.183	107.69	107.69	0.00
55275	55277	-6.667±0.130	2.714±0.353	27.44	28.75	1.31
55280	55282	-6.830±0.160	1.860±0.218	41.45	41.69	0.24
55283	55285	-6.486±0.095	2.164±0.168	102.13	103.20	1.07
55474	55476	-6.680±0.127	2.054±0.197	67.25	68.11	0.86
55500	55502	-7.309±0.226	1.466±0.241	42.29	48.38	6.09
55530	55532	-6.820±0.152	2.115±0.250	30.67	33.59	2.92
55537	55539	-6.716±0.125	1.941±0.183	76.35	76.68	0.33
55544	55546	-6.917±0.175	1.958±0.248	29.05	30.01	0.96
55551	55553	-7.068±0.243	1.757±0.277	33.63	33.63	0.00
55565	55567	-6.592±0.142	2.190±0.248	50.51	50.51	0.00
55579	55581	-6.778±0.154	1.854±0.206	74.67	74.67	0.00
55586	55588	-6.817±0.147	1.941±0.209	40.09	43.75	3.66
55593	55595	-6.720±0.135	2.196±0.229	42.34	42.26	-0.08
55600	55602	-6.648±0.152	2.570±0.345	30.14	30.14	0.00
55601	55603	-6.990±0.197	1.906±0.279	32.21	32.66	0.45
55607	55609	-6.913±0.240	2.799±0.565	9.38	6.36	-3.02
55609	55611	-6.861±0.204	2.282±0.331	18.72	19.11	0.39

$T_{\rm start}$ MJD	$T_{\rm stop}$ MJD	$\rm Log_{10}Flux$ ($\rm phs\,cm^{-2}\,s^{-1}$)	Spectral index (α_γ)	$TS_{\rm pl}$	$TS_{\rm lp}$	$TS_{\rm c}$
55621	55623	-6.394±0.079	1.818±0.111	227.96	232.01	4.05
55642	55644	-6.589±0.122	2.259±0.221	63.44	63.44	0.00
55649	55651	-6.729±0.147	2.508±0.323	22.27	23.80	1.53
55755	55757	-6.122±0.058	2.057±0.099	346.18	346.31	0.13
55757	55759	-6.461±0.096	2.183±0.173	99.21	99.90	0.69
55858	55860	-6.447±0.090	1.951±0.138	145.97	147.63	1.66
55859	55861	-6.453±0.089	1.956±0.137	150.91	150.98	0.07
55860	55862	-6.461±0.088	1.934±0.135	163.86	165.01	1.15
55861	55863	-6.381±0.079	1.957±0.126	207.31	211.01	3.70
55898	55900	-6.734±0.136	1.945±0.194	64.40	65.00	0.60
55905	55907	-6.453±0.085	1.866±0.124	171.16	171.58	0.42
55912	55914	-6.480±0.085	1.893±0.127	173.36	174.90	1.54
55919	55921	-6.535±0.105	2.088±0.174	107.98	107.98	0.00
55926	55928	-6.564±0.117	1.951±0.166	101.05	101.05	0.00
55933	55935	-6.473±0.099	2.048±0.158	117.74	118.77	1.03
55947	55949	-7.112±0.216	1.969±0.312	21.57	26.68	5.11
55954	55956	-6.366±0.089	2.684±0.221	77.67	81.50	3.83
55961	55963	-6.354±0.073	2.071±0.129	170.11	170.78	0.67
55975	55977	-6.456±0.096	2.373±0.201	98.71	98.71	0.00
55982	55984	-6.338±0.076	1.794±0.104	260.71	260.99	0.28
55999	56001	-6.832±0.148	1.789±0.191	61.62	61.62	0.00
56010	56012	-6.293±0.067	2.034±0.113	215.60	224.30	8.70
56184	56186	-6.092±0.055	2.143±0.102	368.34	369.67	1.33
56186	56188	-6.658±0.137	2.031±0.206	67.30	67.91	0.61
56241	56243	-6.532±0.100	2.113±0.173	93.55	93.55	0.00
56262	56264	-6.831±0.174	2.037±0.257	36.02	36.02	0.00
56268	56270	-6.721±0.138	2.063±0.215	52.27	54.54	2.27
56275	56277	-6.630±0.128	2.278±0.261	39.13	39.13	0.00
56282	56284	-6.474±0.087	2.010±0.143	135.48	136.46	0.98
56290	56292	-6.855±0.172	2.107±0.269	25.91	26.26	0.35
56297	56299	-6.877±0.193	2.130±0.298	30.91	30.91	0.00
56311	56313	-7.672±0.449	1.449±0.434	19.82	19.84	0.02
56324	56326	-6.745±0.158	2.593±0.356	25.31	25.31	0.00
56330	56332	-7.128±0.304	2.056±0.475	18.28	18.28	0.00
56336	56338	-7.039±0.256	2.163±0.453	8.70	8.41	-0.29
56346	56348	-6.520±0.100	2.189±0.184	89.73	89.98	0.25
56353	56355	-6.920±0.232	2.596±0.511	10.42	10.54	0.12
56363	56365	-6.598±0.118	2.149±0.210	70.19	70.24	0.05
56367	56369	-6.704±0.121	1.967±0.179	80.97	80.97	0.00
56374	56376	-6.984±0.190	1.940±0.278	33.26	34.99	1.73
56381	56383	-7.034±0.200	1.913±0.264	24.21	28.36	4.15
56597	56599	-6.890±0.211	3.171±0.658	7.79	9.11	1.32
56601	56603	-6.785±0.150	1.941±0.217	54.83	54.83	0.00
56647	56649	-7.239±0.229	1.537±0.243	49.33	50.63	1.30
56654	56656	-6.698±0.149	2.396±0.313	33.05	33.05	0.00
56661	56663	-6.918±0.231	2.557±0.541	10.50	10.50	0.00
56681	56683	-7.052±0.157	2.104±0.237	32.79	34.17	1.38
56731	56733	-6.815±0.199	1.825±0.259	16.89	24.69	7.80
56763	56765	-6.188±0.062	1.953±0.099	267.61	267.61	0.00
56764	56766	-6.209±0.061	1.846±0.090	376.57	376.60	0.03
56766	56768	-6.059±0.050	1.814±0.074	532.16	532.16	0.00
56767	56769	-6.291±0.074	1.758±0.101	300.37	300.37	0.00

T_{start} MJD	T_{stop} MJD	$\mathrm{Log}_{10}\mathrm{Flux}$ ($\mathrm{phs\,cm^{-2}\,s^{-1}}$)	Spectral index (α_γ)	TS_{pl}	TS_{lp}	TS_{c}
56768	56770	-6.536±0.101	1.751±0.134	148.38	148.42	0.04
56988	56990	-6.348±0.113	2.445±0.260	57.67	57.67	0.00
56994	56996	-6.645±0.164	2.046±0.257	33.71	33.93	0.22
57010	57012	-6.692±0.122	2.001±0.189	60.12	62.65	2.53
57018	57020	-6.490±0.102	2.557±0.234	63.70	63.70	0.00
57022	57024	-6.587±0.098	2.025±0.161	105.10	106.31	1.21
57028	57030	-6.679±0.137	2.286±0.249	46.61	47.96	1.35
57040	57042	-6.281±0.073	2.060±0.124	184.55	184.87	0.32
57041	57043	-6.305±0.068	2.060±0.120	216.99	217.26	0.27
57042	57044	-6.272±0.068	2.116±0.125	201.56	201.77	0.21
57043	57045	-6.268±0.065	1.895±0.099	306.52	306.65	0.13
57044	57046	-6.159±0.055	1.730±0.075	512.01	513.55	1.54
57046	57048	-6.205±0.065	1.905±0.099	303.06	303.10	0.04
57047	57049	-6.192±0.058	1.768±0.081	422.29	422.44	0.15
57048	57050	-6.158±0.057	1.833±0.085	416.07	416.32	0.25
57049	57051	-6.341±0.079	2.002±0.128	184.47	184.47	0.00
57050	57052	-6.672±0.121	1.905±0.176	83.70	84.82	1.12
57051	57053	-6.606±0.103	1.849±0.150	132.32	135.74	3.42
57053	57055	-6.721±0.127	1.756±0.181	76.34	79.22	2.88
57054	57056	-6.512±0.129	1.855±0.207	65.98	65.73	-0.25
57055	57057	-6.280±0.095	2.602±0.257	57.17	59.16	1.99
57056	57058	-6.359±0.083	2.210±0.159	116.95	116.95	0.00
57057	57059	-6.419±0.083	1.840±0.119	190.88	190.99	0.11
57058	57060	-6.642±0.120	1.784±0.156	103.23	103.23	0.00
57059	57061	-6.710±0.135	1.873±0.184	85.52	85.53	0.01
57060	57062	-6.570±0.101	1.923±0.149	126.97	128.66	1.69
57061	57063	-6.677±0.114	1.962±0.172	72.99	80.29	7.30
57062	57064	-6.861±0.135	1.727±0.167	67.11	69.42	2.31
57063	57065	-6.885±0.157	1.835±0.201	49.87	50.22	0.35
57065	57067	-6.541±0.103	2.080±0.175	82.82	82.82	0.00
57066	57068	-6.665±0.121	1.849±0.170	71.55	73.13	1.58
57067	57069	-6.771±0.123	1.812±0.167	68.70	74.63	5.93
57068	57070	-6.849±0.148	1.972±0.218	39.44	41.11	1.67
57069	57071	-6.889±0.182	2.151±0.295	25.42	25.65	0.23
57070	57072	-6.913±0.216	2.365±0.409	16.53	16.53	0.00
57071	57073	-6.961±0.210	2.256±0.371	20.32	20.32	0.00
57072	57074	-6.984±0.165	1.808±0.216	37.37	38.29	0.92
57073	57075	-7.028±0.201	1.841±0.257	22.38	23.64	1.26
57074	57076	-6.768±0.169	2.674±0.382	15.99	16.26	0.27
57075	57077	-6.709±0.140	2.340±0.273	34.16	35.23	1.07
57076	57078	-6.572±0.097	1.843±0.138	140.25	141.07	0.82
57077	57079	-6.562±0.093	1.763±0.123	154.82	157.27	2.45
57078	57080	-6.776±0.130	1.819±0.173	62.50	64.69	2.19
57079	57081	-6.712±0.137	2.020±0.205	56.16	56.16	0.00
57080	57082	-6.364±0.082	2.158±0.146	135.35	135.85	0.50
57090	57092	-6.380±0.077	2.061±0.134	160.49	161.62	1.13
57091	57093	-6.403±0.075	1.849±0.109	210.80	214.70	3.90
57092	57094	-6.323±0.076	2.046±0.127	164.08	164.53	0.45
57093	57095	-6.348±0.087	2.404±0.184	87.92	89.27	1.35
57102	57104	-6.318±0.115	2.024±0.181	74.20	75.33	1.13
57109	57111	-6.329±0.088	2.211±0.164	118.86	118.88	0.02
57155	57157	-6.504±0.092	1.932±0.139	134.95	135.62	0.67

T_{start} MJD	T_{stop} MJD	$\mathrm{Log_{10}Flux}$ ($\mathrm{phs\,cm^{-2}\,s^{-1}}$)	Spectral index (α_γ)	TS_{pl}	TS_{lp}	TS_{c}
57156	57158	-6.508±0.090	1.858±0.131	198.39	198.61	0.22
57157	57159	-6.389±0.081	2.104±0.144	181.86	182.03	0.17
57158	57160	-6.357±0.082	2.284±0.163	139.41	140.90	1.49
57159	57161	-6.605±0.125	2.452±0.255	47.00	48.13	1.13
57160	57162	-6.673±0.129	2.227±0.232	33.95	34.29	0.34
57161	57163	-6.370±0.085	2.435±0.202	89.78	89.78	0.00
57335	57337	-6.512±0.095	1.643±0.111	199.34	200.78	1.44
57354	57356	-6.565±0.106	2.058±0.173	94.14	94.62	0.48
57360	57362	-6.558±0.107	1.993±0.163	93.45	94.27	0.82
57364	57366	-6.517±0.097	2.185±0.178	91.75	91.78	0.03
57365	57367	-6.573±0.098	1.795±0.133	151.17	152.14	0.97
57366	57368	-6.443±0.083	1.820±0.118	213.12	213.72	0.60
57367	57369	-6.530±0.096	1.851±0.139	161.06	161.30	0.24
57368	57370	-6.549±0.103	1.878±0.151	140.19	140.40	0.21
57369	57371	-6.554±0.104	1.989±0.164	100.54	100.64	0.10
57370	57372	-6.674±0.117	1.927±0.172	70.77	76.02	5.25
57381	57383	-6.589±0.113	1.971±0.169	85.19	85.26	0.07
57400	57402	-6.474±0.082	1.829±0.112	218.05	218.12	0.07
57419	57421	-6.700±0.155	2.437±0.304	27.84	32.48	4.64
57432	57434	-6.862±0.152	1.772±0.194	60.35	62.63	2.28
57433	57435	-6.727±0.129	1.817±0.174	82.85	85.63	2.78
57438	57440	-6.804±0.134	1.901±0.191	55.98	59.40	3.42
57439	57441	-6.721±0.130	2.150±0.230	47.92	48.70	0.78
57453	57455	-6.817±0.161	2.076±0.251	34.76	34.76	0.00
57454	57456	-6.878±0.156	1.846±0.208	51.27	51.27	0.00
57455	57457	-7.150±0.209	1.639±0.233	45.18	45.18	0.00
57456	57458	-7.082±0.212	1.968±0.296	22.89	26.75	3.86
57457	57459	-6.973±0.201	2.027±0.285	24.01	24.76	0.75
57458	57460	-6.776±0.149	2.124±0.236	33.69	34.92	1.23
57459	57461	-6.735±0.125	2.029±0.199	60.80	60.87	0.07
57465	57467	-6.452±0.092	2.028±0.152	118.25	118.50	0.25
57867	57869	-6.784±0.144	2.247±0.265	34.18	34.54	0.36
57868	57870	-6.610±0.119	2.326±0.230	53.02	54.45	1.43
57869	57871	-6.554±0.110	2.286±0.205	69.80	72.61	2.81
57870	57872	-6.718±0.146	2.474±0.298	30.94	32.54	1.60
57871	57873	-6.886±0.202	2.725±0.474	10.49	11.18	0.69
57872	57874	-6.666±0.144	2.987±0.439	19.00	19.36	0.36
57873	57875	-6.621±0.135	2.937±0.388	24.31	24.32	0.01
57924	57926	-6.828±0.186	1.989±0.274	24.64	24.95	0.31
57925	57927	-6.672±0.159	2.823±0.475	16.45	17.08	0.63
57926	57928	-6.805±0.168	2.743±0.424	14.23	16.44	2.21
57927	57929	-6.782±0.136	2.151±0.233	43.22	46.49	3.27
57929	57931	-6.811±0.190	2.340±0.336	27.88	25.42	-2.46
57930	57932	-6.792±0.172	2.161±0.272	28.62	29.11	0.49
58131	58133	-6.404±0.086	2.049±0.140	142.42	143.66	1.24
58132	58134	-6.310±0.078	2.227±0.147	135.31	135.61	0.30
58275	58277	-6.687±0.127	1.821±0.171	86.49	86.49	0.00
58276	58278	-6.651±0.131	1.792±0.168	75.18	75.18	0.00
58278	58280	-6.402±0.145	1.877±0.207	50.39	50.39	0.00
58286.5	58289	-6.513±0.158	2.010±0.243	51.98	56.28	4.30
58289	58291	-6.504±0.065	2.009±0.104	933.94	937.38	3.44
58457	58459	-6.654±0.104	1.833±0.148	661.22	668.49	7.27

T_{start} MJD	T_{stop} MJD	Log_{10}Flux ($\mathrm{phs\,cm^{-2}\,s^{-1}}$)	Spectral index (α_γ)	TS_{pl}	TS_{lp}	TS_{c}
58458	58460	-6.711±0.127	2.023±0.197	45.07	45.09	0.02
58462	58464	-6.119±0.037	1.914±0.058	7.28	7.30	0.02
58465	58467	-6.179±0.045	1.841±0.068	5.03	7.11	2.08
58467	58469	-6.390±0.195	1.838±0.246	144.53	150.73	6.20
58513	58515	-7.250±0.380	2.344±0.585	34.85	36.52	1.67
58515	58517	-7.255±0.479	2.230±0.730	58.87	58.97	0.10
58812	58814	-6.559±0.094	1.813±0.131	215.38	215.38	0.00
58817	58819	-6.852±0.163	2.150±0.267	134.87	135.18	0.31
58822	58824	-6.790±0.153	1.750±0.185	80.74	84.75	4.01
58842	58844	-6.326±0.074	1.908±0.110	45.25	45.54	0.29
58845	58847	-6.572±0.102	1.963±0.153	88.32	88.64	0.32
58847	58849	-6.728±0.126	1.770±0.156	63.26	64.10	0.84
58850	58852	-6.647±0.146	2.036±0.226	130.45	132.30	1.85
58853	58855	-6.521±0.154	1.728±0.187	291.49	301.03	9.54
58856	58858	-6.531±0.117	2.236±0.211	219.53	219.58	0.05
58859	58861	-6.405±0.087	2.119±0.152	70.81	74.72	3.91
58862	58864	-6.219±0.061	1.938±0.098	79.58	81.76	2.18
58865	58867	-6.409±0.078	1.853±0.114	155.56	161.19	5.63
58895	58897	-6.704±0.121	2.001±0.179	6.56	6.56	0.00
58898	58900	-6.543±0.111	2.092±0.188	7.30	7.30	0.00
58901	58903	-6.372±0.080	2.045±0.135	5.79	9.66	3.87
59201	59203	-7.129±0.278	2.417±0.589	21.24	22.46	1.22
59223	59225	-7.007±0.395	1.727±0.434	18.02	19.81	1.79
59526	59528	-7.435±0.358	1.846±0.492	22.33	22.33	0.00
59548	59550	-6.918±0.242	2.003±0.335	62.75	62.91	0.16
59631	59633	-6.682±0.144	3.215±0.427	23.57	23.78	0.21
59638	59640	-6.954±0.226	1.995±0.312	29.92	30.47	0.55
59645	59647	-6.767±0.143	1.902±0.201	19.67	20.12	0.45
59652	59654	-7.010±0.202	1.874±0.257	25.62	25.62	0.00
59666	59668	-6.930±0.176	1.927±0.253	14.90	14.90	0.00
59667	59669	-6.932±0.187	2.154±0.305	19.67	21.36	1.69
59668	59670	-6.946±0.198	2.083±0.291	30.18	33.59	3.41
59669	59671	-7.036±0.264	2.195±0.382	47.91	51.93	4.02
59670	59672	-6.760±0.163	2.607±0.373	61.36	65.49	4.13
59671	59673	-6.775±0.151	2.223±0.266	35.43	35.89	0.46
59672	59674	-7.018±0.178	1.771±0.228	28.28	28.28	0.00
59673	59675	-7.133±0.171	1.531±0.195	17.07	17.37	0.30
59674	59676	-7.100±0.209	1.728±0.259	44.39	45.41	1.02
59675	59677	-6.987±0.204	2.097±0.314	6.52	6.20	-0.32
59910	59912	-6.905±0.178	1.924±0.239	25.78	25.77	-0.01
59937	59939	-7.626±0.479	2.095±0.579	34.72	34.72	0.00
59953	59955	-6.961±0.212	2.081±0.301	55.68	55.85	0.17

Bibliography

Abdo, A. A., Ackermann, M., Ajello, M., et al. 2009, ApJ, 700, 597

Abdo, A. A., Ackermann, M., Agudo, I., et al. 2010, ApJ, 716, 30

Abdo, A. A., Ackermann, M., Ajello, M., et al. 2011, The Astrophysical Journal, 736, 131

Abdo, A. A., Ackermann, M., Ajello, M., et al. 2011, ApJ, 736, 131

Acciari, V. A., Aliu, E., Aune, T., et al. 2009, ApJ, 703, 169

Acciari, V. A., Aliu, E., Arlen, T., et al. 2011, ApJ, 738, 25

Ackermann, M., Ajello, M., Allafort, A., et al. 2011, The Astrophysical Journal, 743, 171

Ackermann, M., Ajello, M., Albert, A., et al. 2015, ApJ, 799, 86

Ackermann, M., Anantua, R., Asano, K., et al. 2016, ApJ, 824, L20

Aleksić, J., Alvarez, E. A., Antonelli, L. A., et al. 2012, A&A, 542, A100

Anderhub, H., Antonelli, L. A., Antoranz, P., et al. 2009, ApJ, 704, L129

Antonucci, R. 1993, ARA&A, 31, 473

Arnaud, K. A. 1996, in Astronomical Society of the Pacific Conference Series, Vol. 101, Astronomical Data Analysis Software and Systems V, ed. G. H. Jacoby & J. Barnes, 17

Atwood, W. B., Abdo, A. A., Ackermann, M., et al. 2009, ApJ, 697, 1071

Bagchi, J., Vivek, M., Vikram, V., et al. 2014, ApJ, 788, 174

Baheeja, C., Sahayanathan, S., Rieger, F. M., Jagan, S. K., & Ravikumar, C. D. 2022, MNRAS, 514, 3074

Baheeja, C., Sahayanathan, S., Rieger, F. M., & Ravikumar, C. D. 2024, Phys. Rev. D, 109, 103039

Baheeja, C., Thekkoth, A., Sahayanathan, S., Ravikumar, C. D., & Bhatt, N. 2024, PASA, 41, e103

Baloković, M., Paneque, D., Madejski, G., et al. 2016, ApJ, 819, 156

Baloković , M., Paneque, D., Madejski, G., et al. 2016, The Astrophysical Journal, 819, 156

Barthelmy, S. D., Barbier, L. M., Cummings, J. R., et al. 2005, Space Sci. Rev., 120, 143

Bartoli, B., Bernardini, P., Bi, X. J., et al. 2016, ApJS, 222, 6

Begelman, M. C., Blandford, R. D., & Rees, M. J. 1984, Reviews of Modern Physics, 56, 255

Begelman, M. C., Blandford, R. D., & Rees, M. J. 1984, Rev. Mod. Phys., 56, 255

Begelman, M. C., Fabian, A. C., & Rees, M. J. 2008, MNRAS, 384, L19

Bell, A. R. 1978, MNRAS, 182, 147

Bhagwan, J., Gupta, A. C., Papadakis, I. E., & Wiita, P. J. 2014, Monthly Notices of the Royal Astronomical Society, 444, 3647

Biteau, J., & Giebels, B. 2012, A&A, 548, A123

Blandford, R., & Eichler, D. 1987, Physics Reports, 154, 1

Blandford, R. D., & Königl, A. 1979, ApJ, 232, 34

Blandford, R. D., & Ostriker, J. P. 1978, ApJ, 221, L29

Blandford, R. D., & Payne, D. G. 1982, MNRAS, 199, 883

Blandford, R. D., & Znajek, R. L. 1977, MNRAS, 179, 433

Błażejowski, M., Sikora, M., Moderski, R., & Madejski, G. M. 2000, ApJ, 545, 107

Blumenthal, G. R., & Gould, R. J. 1970, Reviews of Modern Physics, 42, 237

Blumenthal, G. R., & Gould, R. J. 1970, Rev. Mod. Phys., 42, 237

Böttcher, M., & Dermer, C. D. 2010, ApJ, 711, 445

Böttcher, M., Reimer, A., Sweeney, K., & Prakash, A. 2013, ApJ, 768, 54

Burbidge, G. R. 1956, ApJ, 124, 416

Burrows, D. N., Hill, J. E., Nousek, J. A., et al. 2005, Space Sci. Rev., 120, 165

Carini, M. T., Miller, H. R., & Goodrich, B. D. 1990, AJ, 100, 347

Carini, M. T., Miller, H. R., Noble, J. C., & Goodrich, B. D. 1992, AJ, 104, 15

Celotti, A., & Ghisellini, G. 2008, Monthly Notices of the Royal Astronomical Society, 385, 283

Cerruti, M. 2020, Galaxies, 8, 72

Chandra, S., Zhang, H., Kushwaha, P., et al. 2015, The Astrophysical Journal, 809, 130

Chen, A. W., D'Ammando, F., Villata, M., et al. 2008, A&A, 489, L37

Chen, L. 2014, The Astrophysical Journal, 788, 179

Cortina, J., & CTAO LST Collaboration. 2023, The Astronomer's Telegram, 16381, 1

Costamante, L., & Ghisellini, G. 2002, A&A, 384, 56

D'arcangelo, F. D., Marscher, A. P., Jorstad, S. G., et al. 2009, ApJ, 697, 985

Dermer, C. D., & Menon, G. 2009, High Energy Radiation from Black Holes: Gamma Rays, Cosmic Rays, and Neutrinos

Dermer, C. D., & Schlickeiser, R. 1993, ApJ, 416, 458

Dermer, C. D., Schlickeiser, R., & Mastichiadis, A. 1992, A&A, 256, L27

Di Gesu, L., Donnarumma, I., Tavecchio, F., et al. 2022, ApJ, 938, L7

Di Gesu, L., Marshall, H. L., Ehlert, S. R., et al. 2023, Nature Astronomy, 7, 1245

Dondi, L., & Ghisellini, G. 1995, MNRAS, 273, 583

Evans, P. A., Beardmore, A. P., Page, K. L., et al. 2009, MNRAS, 397, 1177

Fan, J. H. 2003, ApJ, 585, L23

Fan, J. H., Cheng, K. S., Zhang, L., & Liu, C. H. 1997, A&A, 327, 947

Fan, J. H., Yang, J. H., Liu, Y., et al. 2016, The Astrophysical Journal Supplement Series, 226, 20

Fermi, E. 1949a, Physical Review, 75, 1169

—. 1949b, Physical Review, 75, 1169

Ferrero, E., Wagner, S. J., Emmanoulopoulos, D., & Ostorero, L. 2006, A&A, 457, 133

Finke, J. D. 2016, ApJ, 830, 94

Foschini, L., Tagliaferri, G., Pian, E., et al. 2006, A&A, 455, 871

Fossati, G., Maraschi, L., Celotti, A., Comastri, A., & Ghisellini, G. 1998, MNRAS, 299, 433

Fossati, G., Celotti, A., Chiaberge, M., et al. 2000, The Astrophysical Journal, 541, 166

Fossati, G., Buckley, J. H., Bond, I. H., et al. 2008, The Astrophysical Journal, 677, 906

Fritz, K. D. 1989, A&A, 214, 14

Gasparyan, S., Bégué, D., & Sahakyan, N. 2022, MNRAS, 509, 2102

Gaur, H., Chen, L., Misra, R., et al. 2017, The Astrophysical Journal, 850, 209

Geng, X., Zeng, W., Rani, B., et al. 2020, The Astrophysical Journal, 904, 67

Ghisellini, G., Celotti, A., & Costamante, L. 2002, A&A, 386, 833

Ghisellini, G., Celotti, A., Fossati, G., Maraschi, L., & Comastri, A. 1998, MNRAS, 301, 451

Ghisellini, G., Padovani, P., Celotti, A., & Maraschi, L. 1993, ApJ, 407, 65

Ghisellini, G., Righi, C., Costamante, L., & Tavecchio, F. 2017, MNRAS, 469, 255

Ghisellini, G., & Svensson, R. 1991, MNRAS, 252, 313

Ghisellini, G., & Tavecchio, F. 2009, MNRAS, 397, 985

Ghisellini, G., Tavecchio, F., Foschini, L., & Ghirlanda, G. 2011, MNRAS, 414, 2674

Ghisellini, G., Tavecchio, F., Maraschi, L., Celotti, A., & Sbarrato, T. 2014, Nature, 515, 376

Giebels, B., & Degrange, B. 2009, A&A, 503, 797

Giommi, P., Massaro, E., Chiappetti, L., et al. 1999, A&A, 351, 59

Goswami, P., Sahayanathan, S., Sinha, A., & Gogoi, R. 2020, MNRAS, 499, 2094

Goswami, P., Sahayanathan, S., Sinha, A., & Gogoi, R. 2020, Monthly Notices of the Royal Astronomical Society, 499, 2094–2103

Goswami, P., Sahayanathan, S., Sinha, A., Misra, R., & Gogoi, R. 2018, Monthly Notices of the Royal Astronomical Society, 480, 2046

Guilbert, P. W., Fabian, A. C., & Rees, M. J. 1983, MNRAS, 205, 593

Gupta, A. C., Krichbaum, T. P., Wiita, P. J., et al. 2012, MNRAS, 425, 1357

Harrison, F. A., Craig, W. W., Christensen, F. E., et al. 2013, ApJ, 770, 103

Heidt, J., & Wagner, S. J. 1996, A&A, 305, 42

Horan, D., Acciari, V. A., Bradbury, S. M., et al. 2009, The Astrophysical Journal, 695, 596

IceCube Collaboration, Aartsen, M. G., Ackermann, M., et al. 2018, Science, 361, eaat1378

Jagan, S. K., Sahayanathan, S., Misra, R., Ravikumar, C. D., & Jeena, K. 2018, MNRAS, 478, L105

Jones, F. C. 1968, Phys. Rev., 167, 1159

Jorstad, S. G., Marscher, A. P., Morozova, D. A., et al. 2017, ApJ, 846, 98

Kalberla, P. M. W., Burton, W. B., Hartmann, D., et al. 2005, A&A, 440, 775

Kalberla, P. M. W., Burton, W. B., Hartmann, D., et al. 2005, Astronomy Astrophysics, 440, 775–782

Kapanadze, B., Dorner, D., Romano, P., et al. 2017, The Astrophysical Journal, 848, 103

Kapanadze, B., Vercellone, S., Romano, P., et al. 2018a, ApJ, 858, 68

Kapanadze, B., Dorner, D., Vercellone, S., et al. 2016, ApJ, 831, 102

Kapanadze, B., Vercellone, S., Romano, P., et al. 2018b, ApJ, 854, 66

Kapanadze, B., Gurchumelia, A., Dorner, D., et al. 2020, The Astrophysical Journal Supplement Series, 247, 27

Kardashev, N. S. 1962, Soviet Ast., 6, 317

Kataoka, J., & Stawarz, Ł. 2016, ApJ, 827, 55

Kataoka, J., & Stawarz, Ł. 2016, The Astrophysical Journal, 827, 55

Kellermann, K. I., Sramek, R., Schmidt, M., Shaffer, D. B., & Green, R. 1989, AJ, 98, 1195

Khatoon, R., Shah, Z., Misra, R., & Gogoi, R. 2020, MNRAS, 491, 1934

Kirk, J. G., & Dendy, R. O. 2001, Journal of Physics G Nuclear Physics, 27, 1589

Kirk, J. G., Rieger, F. M., & Mastichiadis, A. 1998, A&A, 333, 452

Krawczynski, H., Hughes, S. B., Horan, D., et al. 2004, The Astrophysical Journal, 601, 151

Kuehr, H., Witzel, A., Pauliny-Toth, I. I. K., & Nauber, U. 1981, A&AS, 45, 367

Kun, E., Britzen, S., Frey, S., Gabányi, K. É., & Gergely, L. Á. 2023, MNRAS, 526, 4698

Landau, R., Golisch, B., Jones, T. J., et al. 1986, ApJ, 308, 78

Larionov, V. M., Jorstad, S. G., Marscher, A. P., et al. 2013, ApJ, 768, 40

Larionov, V. M., Jorstad, S. G., Marscher, A. P., et al. 2013, The Astrophysical Journal, 768, 40

Lefa, E., Kelner, S. R., & Aharonian, F. A. 2012, ApJ, 753, 176

Lemoine, M. 2019, Phys. Rev. D, 99, 083006

Liao, N. H., Bai, J. M., Liu, H. T., et al. 2014, The Astrophysical Journal, 783, 83

Lin, Y. C., Bertsch, D. L., Dingus, B. L., et al. 1995, ApJ, 442, 96

Longair, M. S. 2011, High Energy Astrophysics

Mankuzhiyil, N., Ansoldi, S., Persic, M., et al. 2012, The Astrophysical Journal, 753, 154

Marscher, A. P., & Gear, W. K. 1985a, ApJ, 298, 114

—. 1985b, ApJ, 298, 114

Martí-Vidal, I., Muller, S., Vlemmings, W., Horellou, C., & Aalto, S. 2015, Science, 348, 311

Massaro, E., Perri, M., Giommi, P., & Nesci, R. 2004, A&A, 413, 489

Massaro, F., Tramacere, A., Cavaliere, A., Perri, M., & Giommi, P. 2008, A&A, 478, 395

Mattox, J. R., Bertsch, D. L., Chiang, J., et al. 1996, ApJ, 461, 396

Miller, H. R., Carini, M. T., & Goodrich, B. D. 1989, Nature, 337, 627

Miller, P., Rawlings, S., & Saunders, R. 1993, MNRAS, 263, 425

Narayan, R., & Piran, T. 2012, MNRAS, 420, 604

Nenkova, M., Ivezić, Ž., & Elitzur, M. 2002, ApJ, 570, L9

Nilsson, K., Pursimo, T., Sillanpää, A., Takalo, L. O., & Lindfors, E. 2008, A&A, 487, L29

Noble, J. C., & Miller, H. R. 1996, in Astronomical Society of the Pacific Conference Series, Vol. 110, Blazar Continuum Variability, ed. H. R. Miller, J. R. Webb, & J. C. Noble, 30

Peterson, B. M. 1997, An Introduction to Active Galactic Nuclei

Press, W. H., Teukolsky, S. A., Vetterling, W. T., & Flannery, B. P. 1992, Numerical recipes in FORTRAN. The art of scientific computing

Raiteri, C. M., Villata, M., Tosti, G., et al. 2003, A&A, 402, 151

Rani, B., Gupta, A. C., Joshi, U. C., Ganesh, S., & Wiita, P. J. 2010, ApJ, 719, L153

Rani, B., Gupta, A. C., Joshi, U. C., Ganesh, S., & Wiita, P. J. 2010, The Astrophysical Journal Letters, 719, L153

Rani, B., Krichbaum, T. P., Lott, B., Fuhrmann, L., & Zensus, J. A. 2013a, Advances in Space Research, 51, 2358

Rani, B., Krichbaum, T. P., Marscher, A. P., et al. 2015, A&A, 578, A123

Rani, B., Gupta, A. C., Strigachev, A., et al. 2010, MNRAS, 404, 1992

Rani, B., Krichbaum, T. P., Fuhrmann, L., et al. 2013b, A&A, 552, A11

Rees, M. J. 1966, Nature, 211, 468

—. 1984, ARA&A, 22, 471

Reynolds, S. P. 2009, The Astrophysical Journal, 703, 662

Rieger, F. M. 2019, Galaxies, 7, 28

Rieger, F. M., Bosch-Ramon, V., & Duffy, P. 2007, Ap&SS, 309, 119

Rieger, F. M., Bosch-Ramon, V., & Duffy, P. 2007, Astrophysics and Space Science, 309, 119

Rodrigues, X., Paliya, V. S., Garrappa, S., et al. 2024, A&A, 681, A119

Roming, P. W. A., Kennedy, T. E., Mason, K. O., et al. 2005, Space Sci. Rev., 120, 95

Romoli, C., Chakraborty, N., Dorner, D., Taylor, A. M., & Blank, M. 2018, Galaxies, 6, 135

Romoli, C., Taylor, A. M., & Aharonian, F. 2017, Astroparticle Physics, 88, 38

Rybicki, G. B., & Lightman, A. P. 1986, Radiative Processes in Astrophysics, 400

Sahakyan, N. 2018, ApJ, 866, 109

Sahayanathan, S. 2008, MNRAS, 388, L49

Sahayanathan, S., Sinha, A., & Misra, R. 2018, Research in Astronomy and Astrophysics, 18, 035

Sambruna, R. M., Barr, P., Giommi, P., et al. 1994, ApJS, 95, 371

Schlafly, E. F., & Finkbeiner, D. P. 2011, The Astrophysical Journal, 737, 103

Schwartz, D. A. 2002, ApJ, 569, L23

Sembay, S., Edelson, R., Markowitz, A., Griffiths, R. G., & Turner, M. J. L. 2002, ApJ, 574, 634

Seyfert, C. K. 1943, ApJ, 97, 28

Shakura, N. I., & Sunyaev, R. A. 1973, A&A, 24, 337

Shu, F. H. 1991, The physics of astrophysics. Volume 1: Radiation.

Sikora, M., & Begelman, M. C. 2013, ApJ, 764, L24

Sikora, M., Begelman, M. C., & Rees, M. J. 1994, ApJ, 421, 153

Sinha, A., Khatoon, R., Misra, R., et al. 2018, MNRAS, 480, L116

Sinha, A., Sahayanathan, S., Acharya, B. S., et al. 2017, ApJ, 836, 83

Sinha, A., Sahayanathan, S., Acharya, B. S., et al. 2017, The Astrophysical Journal, 836, 83

Sinha, A., Shukla, A., Misra, R., et al. 2015, Astronomy Astrophysics, 580, A100

Sinha, A., Shukla, A., Misra, R., et al. 2015, A&A, 580, A100

Soldi, S., Türler, M., Paltani, S., et al. 2008, A&A, 486, 411

Tagliaferri, G., Ravasio, M., Ghisellini, G., et al. 2003, A&A, 400, 477

Takalo, L. O., Sillanpaeae, A., & Nilsson, K. 1994, A&AS, 107, 497

Tavecchio, F., Maraschi, L., & Ghisellini, G. 1998, The Astrophysical Journal, 509, 608

Thekkoth, A., Sahayanathan, S., Shah, Z., Paliya, V. S., & Ravikumar, C. D. 2023, MNRAS, 526, 6364

Tramacere, A., Giommi, P., Perri, M., Verrecchia, F., & Tosti, G. 2009, A&A, 501, 879

Tramacere, A., Massaro, E., & Taylor, A. M. 2011, ApJ, 739, 66

Tramacere, A., Massaro, F., & Cavaliere, A. 2007a, A&A, 466, 521

Tramacere, A., Giommi, P., Massaro, E., et al. 2007b, A&A, 467, 501

Tripathi, T., Gupta, A. C., Takey, A., et al. 2024, MNRAS, 527, 5220

Urry, C. M., & Padovani, P. 1995, PASP, 107, 803

Uttley, P., McHardy, I. M., & Vaughan, S. 2005, MNRAS, 359, 345

Vaughan, S., Edelson, R., Warwick, R. S., & Uttley, P. 2003, MNRAS, 345, 1271

Wagner, S. J., Witzel, A., Heidt, J., et al. 1996, AJ, 111, 2187

Weidinger, M., & Spanier, F. 2015, A&A, 573, A7

Wierzcholska, A., & Siejkowski, H. 2015, MNRAS, 452, L11

—. 2016, MNRAS, 458, 2350

Yan, D., Zhang, L., Yuan, Q., Fan, Z., & Zeng, H. 2013, The Astrophysical Journal, 765, 122

Zech, A., & Lemoine, M. 2021, A&A, 654, A96

Zhang, Y. H. 2010, The Astrophysical Journal, 713, 180

Zirakashvili, V. N., & Aharonian, F. 2007, A&A, 465, 695